

Conferences and Symposia

THE 12th INTERNATIONAL CONFERENCE OF THE SLOVENIAN SOCIETY FOR NON-DESTRUCTIVE TESTING

APPLICATION OF CONTEMPORARY NON-DESTRUCTIVE TESTING IN ENGINEERING

4 - 6 September 2013, SLOVENIA

CONFERENCE PROCEEDINGS

Edited by J. Grum and T. Kek and Published by the Slovenian Society for Non-Destructive
Testing, Aškerčeva 6, 1000 Ljubljana, Slovenia

Articles from the AE Sessions (* indicates a keynote paper)

A LOW FREQUENCY LAMB-WAVES BASED STRUCTURAL HEALTH MONITORING OF AN
AERONAUTICAL CARBON FIBRE REINFORCED POLYMER COMPOSITE,*
M. Carboni, A. Gianneo, M. Giglio S1

FROM ACOUSTIC EMISSION TESTING (AT) TO ACOUSTIC MONITORING,*
P. Tscheliesnig S21

THE NEW HIGHER ORDER SPECTRAL TECHNIQUES FOR NON-LINEARITY MONITORING OF
STRUCTURES AND MACHINERY,*
L. Gelman S28

ASSESSMENT OF INFRASTRUCTURES BY MEANS OF PASSIVE AND POSITIVE ELASTIC
WAVES APPROACHES,*
T. Shiotani, Y. Kobayashi, S. Momoki S33

ACTUAL POSSIBILITIES OF DAMAGE EVALUATION OF MACHINES WITH ROTATING
PARTS BY ACOUSTIC EMISSION,
P. Mazal, L. Nohal, F. Hort S52

A STUDY ON THE PERFORMANCE OF ACOUSTIC EMISSION AND LOW FREQUENCY
VIBRATION METHODS TO THE REAL-TIME CONDITION MONITORING OF RAILWAY AXLES,
M. Carboni, S. Bruni, D. Crivelli, M. Guagliano, P. Rolek S60

NEW PROSPECTS TO USE ACOUSTIC EMISSION DURING SCRATCH TESTING FOR PROBING
FUNDAMENTAL MECHANISMS OF PLASTIC DEFORMATION,
A. Danyuk, D. Merson, A. Vinogradov S68

MONITORING OF AUTONOMOUS HEALING PROCESS OF CONCRETE BY ACOUSTIC
EMISSION AND DIGITAL IMAGE CORRELATION,
E. Tsangouri, K. Van Tittelboom, N. De Belie, D.G. Aggelis, D. Van Hemelrijck S76

CLUSTERING OF AE SIGNAL AMPLITUDES BY MEANS OF FUZZY C-MEANS ALGORITHM,
R. Svečko, A. Hančič, D. Kusić, J. Grum S83

ENHANCEMENT OF EFFICIENCY OF TRIBOLOGICAL TESTING BY USING ACOUSTIC
EMISSION MEASUREMENTS,
I. Rastegaev, D. Merson, A. Vinogradov S91

WAVELET BASED APPROACH TO ACOUSTIC EMISSION PHASE PICKING, E. Pomponi, A. Vinogradov	S98
ARC WELDING PROCESS MONITORING BY AUDIBLE SOUND, I. Polajnar, Z. Bergant, J. Grum	S103
THE SYSTEM OF AE CONTROL AND DIAGNOSTICS OF TECHNICAL STATUS OF ELECTRIC SWITCH MECHANISM, S.V. Altynbaev, V.S. Fadeev, N.A. Semashko	S113
STATISTICAL EVALUATION OF INJECTION MOLDING PROCESS PARAMETERS IMPACT ON THE DETECTED ACOUSTIC EMISSION EVENTS, D. Kusić, R. Svečko, A. Hančič, T. Kek, J. Grum	S118
TESTING PRESSURE VESSEL WITH ACOUSTIC EMISSION, G. Gavranić, T. Kek, J. Grum	S126
ACOUSTIC EMISSION MONITORING OF FRACTURE PROCESS STAGES IN HYDROGEN EMBRITTLED HIGH-CARBON STEEL E. Merson, D. Merson, A. Vinogradov	S134
EFFECT OF TEMPERATURE ON MICROSTRUCTURE EVOLUTION IN TRIP/TWIP STEELS DURING TENSILE DEFORMATION M. Linderov, C. Segel, A. Vinogradov, A. Weidner, H. Biermann	S142
INVESTIGATING THE PRESENCE OF CRACKS IN TOOL STEEL INSERTS BY USING ACOUSTIC EMISSION METHOD T. Kek, D. Kusić, R. Svečko, A. Hančič, J. Grum	S150
ACOUSTIC EMISSION DURING SHORT-TERM ELECTROCHEMICAL CORROSION TESTING: LSP EFFECT ON PITTING CORROSION U. Trdan, J. Grum	S158
DETECTION AND PROCESSING OF SOUND SIGNALS IN STEEL QUENCHING F. Ravnik, J. Grum	S165

A LOW FREQUENCY LAMB-WAVES BASED STRUCTURAL HEALTH MONITORING OF AN AERONAUTICAL CARBON FIBRE REINFORCED POLYMER COMPOSITE

M. Carboni^{1*}, A. Gianneo¹, M. Giglio¹

¹Department of Mechanical Engineering – Politecnico di Milano
Via La Masa 1, 20156 Milano, Italy
michele.carboni@polimi.it, andrea.gianneo@mail.polimi.it, marco.giglio@polimi.it

ABSTRACT

Carbon Fiber Reinforced Polymer composites have been developed since the '60s and allow the design of resistant and innovative lightweight primary structures, replacing traditional metallic materials. However, their intensive structural use remains limited due, between also other factors, to several peculiar damage mechanisms able to quickly degrade the mechanical properties and requiring high maintenance costs due to service interruptions needed for carrying out periodical non-destructive testing inspections. One solution, more and more suggested and proposed in the literature, is then to apply a structural health monitoring approach. The present paper investigates such possibility focusing on the application of the "Design of Experiment" methodology to the performance of Lamb ultrasonic waves-based monitoring carried out using piezoelectric transducers bonded on the surface of aeronautical laminates. The choice of a Design Of Experiment approach is based on the well-known fact that the success of an ultrasonic monitoring approach is mostly based on the knowledge of the most influencing factors, but also that the today published research studies usually consider them individually. A rigorous factorial design method is then applied in order to study the influence of different operative factors. Since the worst type of damage in a composite structure is a delamination, the research is particularly focused on this kind of defect obtained both artificially, using Teflon patches, and naturally, by suitable mechanical impacts.

Key words: Design of Experiment, Lamb Ultrasonic Waves, Structural Health Monitoring, Carbon Fiber Reinforced Polymer Composite

1. Introduction

Carbon Fiber Reinforced Polymer (CFRP) composites have been developed since the '60s and allow the design of resistant and innovative light weight primary structures, replacing traditional metallic materials, due to their high strength-weight and moduli-weight ratios, excellent fatigue strength as well as fatigue damage tolerance; another advantage is their non-corroding behaviour. However, their intensive structural use remains limited due to, among other factors, several peculiar damage mechanisms, which are able to quickly degrade the mechanical properties and result in high maintenance costs caused by the service interruptions required for carrying out periodical non-destructive testing (NDT) inspections. An increasingly proposed solution in the

literature is the application of a structural health monitoring (SHM) approach, which, in the aeronautical field, has shown, according to Chang [1], the potentiality of decreasing the overall costs of NDT by 30%. The present paper investigates this possibility by focusing on the application of the “Design of Experiment” (DOE) methodology to the performance of Lamb ultrasonic wave-based SHM, using piezoelectric (PZT) transducers surface bonded onto aeronautical CFRP laminates. The choice of a DOE approach is based on the well-known fact that the success of an ultrasonic SHM approach requires the knowledge of the most influencing factors and their mutual influences, which up to now have not been studied, but have been considered individually in the published research. In particular, a rigorous 2^k factorial design method is applied to study the influence of the following factors on a SHM approach: the frequency of excitation, the dimension and the position of the defects and the inspection approach (pulse-echo or pitch-catch). Since the worst type of damage in a composite structure is delamination, this research particularly focuses on this kind of defect, obtained both artificially by using Teflon patches and naturally by mechanical impacts. To this aim, the experimental elastic moduli of CFRP unidirectional (UD) laminas and of a quasi-isotropic laminate, necessary for defining the propagation of the elastic wave, are firstly determined and this information is subsequently used to simulate the Lamb wave dispersive propagation properties through the semi-analytical finite element (SAFE) approach. Information about the dispersive behaviour of such waves is needed to best fit the Lamb wave-based SHM methodology to the target structure and to thereby allow the design of all aspects of the SHM process, i.e. the way to activate and receive diagnostic signals, the type of PZT transducers, etc. Finally, the DOE approach is applied to different composite laminate panels, and the sampled data are analysed by the discrete and continuous wavelet transforms. The CFRP system adopted in this research is a quasi-isotropic 17 ply layup $[0/+45/0/-45/90/-45/0/+45/90]_s$, one of the most representative carbon fibre laminates in the aeronautical field, as Toso et al. [2] show in their EASA framework, made of UD pre-preg SAATI EH-550/T800S laminas.

2. Experiments on CFRP UD laminas and the quasi-isotropic laminate

Since the propagative properties of an elastic wave depend on both physical and elastic properties, the first necessary step is the definition of the effective elastic moduli of the UD laminas constituting the target quasi-isotropic carbon-fibre laminate. CFRP laminas belong to a special class of orthotropic materials, called transversely isotropic. In particular, their mechanical behaviour $\sigma = [C]\epsilon$ requires five independent elastic constants: E_{11} , E_{22} , G_{12} , ν_{12} and ν_{23} , being 1 the in-plane direction along the fibres, 2 the in-plane direction transverse to the fibre and 3 the out-of plane direction. According to ASTM-D 3039 [3] and 3518 [4], experimental static tensile tests were carried out on four different types of coupons (each composed by five specimens): UD 0° , UD 90° , UD $\pm 45^\circ$ and the quasi-isotropic layup. The first three coupon types allowed the definition of the in-plane tensile properties E_{11} , E_{22} , ν_{12} , ν_{21} and, in a simplified way, the in-plane shear response G_{12} . The fourth coupon was used to evaluate the elastic properties of the quasi-isotropic laminate: E_{xx} , E_{yy} and ν_{xy} , being x and y the in-plane coordinates of the laminate (x aligned to the 0° lamina and y to the 90° one).

An electro-mechanical tensile test machine MTS-Alliance RT/100 (maximum load 100 kN), an extensometer and two half Wheatstone bridges, dedicated to the longitudinal and transversal strains and compensated for temperature effects by “dummy” gages, formed the basis of the experimental setup. The strain gauges were of the type CEA06250UT350. Figure 1 shows the shape, stress-strain curves (obtained from extensometer data) and the typical failure mode of the different specimens, while Table 1 summarises the experimental elastic moduli of the laminas constituting the quasi-isotropic laminate. In the latter, μ stands for the mean value, σ for the standard deviation and CV is defined by the ASTM-D 3039 [3] as the sample coefficient of variation (σ/μ), respectively.

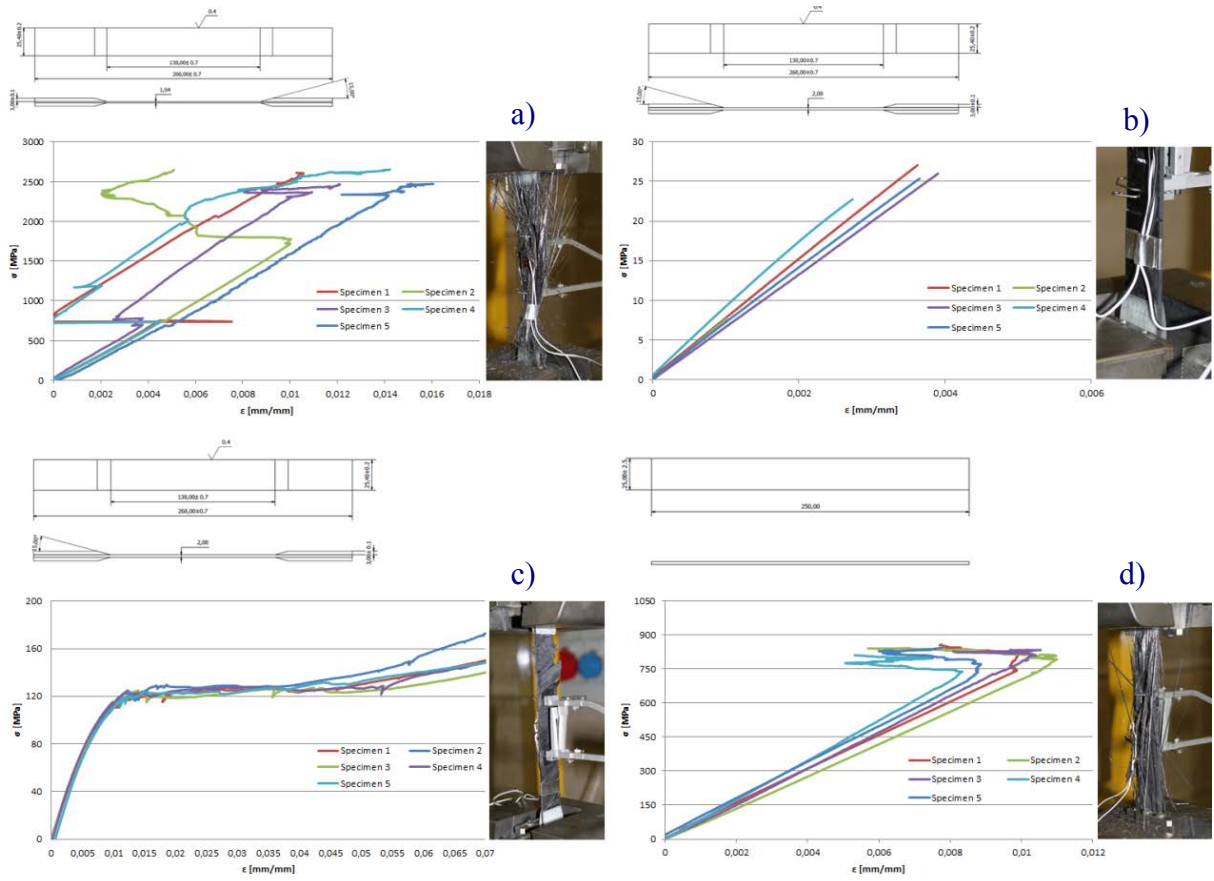


Figure 1: Experimental tensile stress-strain curves and the corresponding failure modes: a) UD 0°; b) UD 90°; c) UD ±45°; d) quasi-isotropic layup.

Table 1: Experimental in-plane properties of the UD laminas and the quasi-isotropic laminate.

	E_{11} [GPa]	ν_{12}	E_{22} [GPa]	ν_{21}	G_{12} [GPa]	E_{xx} [GPa]	ν_{xy}
μ	159,420	0,323	8,120	0,018	4,68	70,020	0,371
σ	2,471	0,019	0,432	0,001	0,342	1,033	0,002
CV [%]	1,550	5,795	5,326	7,480	7,309	1,475	0,560

3. Semi-analytical finite element simulation and design of the SHM process

The semi-analytical finite element (SAFE) approach is a useful and powerful method for numerical modelling of guided wave propagation in composite laminates of arbitrary layup and cross-sectional geometry, where usually the traditional FEM method requires high computational costs and may result in numerical failure, especially with very short wavelengths, as discussed by Bartoli et al. [5]. The SAFE approach adopts a finite element bi-dimensional discretization of the cross-sectional area (Fig. 2a) since the displacements along the wave propagation direction are assumed to be in the harmonic-plane way. Moreover, the typical plane geometry of CFRP laminates allows further simplification in terms of mono-dimensional simulations. Results, in terms of multiple modes and dispersion properties, can be obtained in a numerically stable manner by the eigenvalue and eigenvector problem expressed by Eqs. (1) and (2); more details can be found in [5]. Two quadratic 1-D finite elements have been used to model each of the 17 laminas constituting the quasi-isotropic laminate, following the convergence studies by Bartoli et al. [5] for dispersive solutions. Each element has three degrees of freedom (dof) per node, associated to the displacements U_x , U_y , U_z (Fig. 2b).

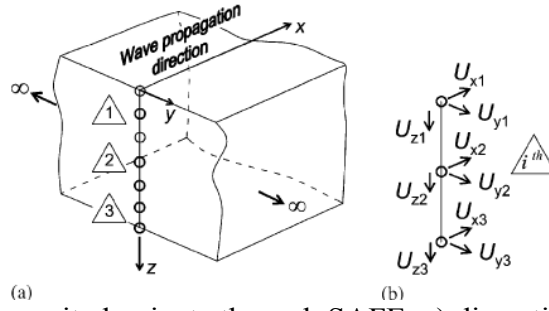


Figure 2: Modelling a composite laminate through SAFE: a) discretization along the thickness, b) degrees of freedom of a 1-D quadratic element.

$$\{[K_{tot1}] + ik[K_{tot2}] + k^2[K_{tot3}] - \omega^2[M_{tot}]\}\mathbf{u} = 0 \implies \{[K_{tot}] - \omega^2[M_{tot}]\}\mathbf{u} = 0 \quad (1)$$

$$[M_{tot}]^{-1}[K_{tot}]\mathbf{u} = \omega^2[I]\mathbf{u} \quad (2)$$

Figure 3 shows the dispersion curves, in terms of phase velocities C_p , obtained using, as input to SAFE, the experimental results shown in Table 1. Considering the quasi-isotropic layup and to quantify its anisotropy level, four different directions of Lamb wave propagation (0° , 30° , 60° and 90° with respect to the x coordinate of the laminate) were simulated. The quasi-isotropic behaviour of the laminate and an essential parameter for the SHM process can be noted. The latter is the so-called “cut-off frequency” $f_{\text{cut-off}}$, which outlines the extension of the non-dispersive region, where only three fundamental Lamb wave modes can exist (S_0 , A_0 and SH_0) and whose dispersive behaviour is restrained (i.e. the velocity is almost constant in this range, apart for the A_0 wave close to the origin). Figures 3a to d show no substantial differences between the $f_{\text{cut-off}}$ parameter, whose value is about 380 kHz, since the quasi-isotropic stacking sequence minimises the anisotropy level of the laminate. This behaviour is concurrently shown in Figure 4, which shows the phase velocities of the Lamb wave modes in a polar diagram.

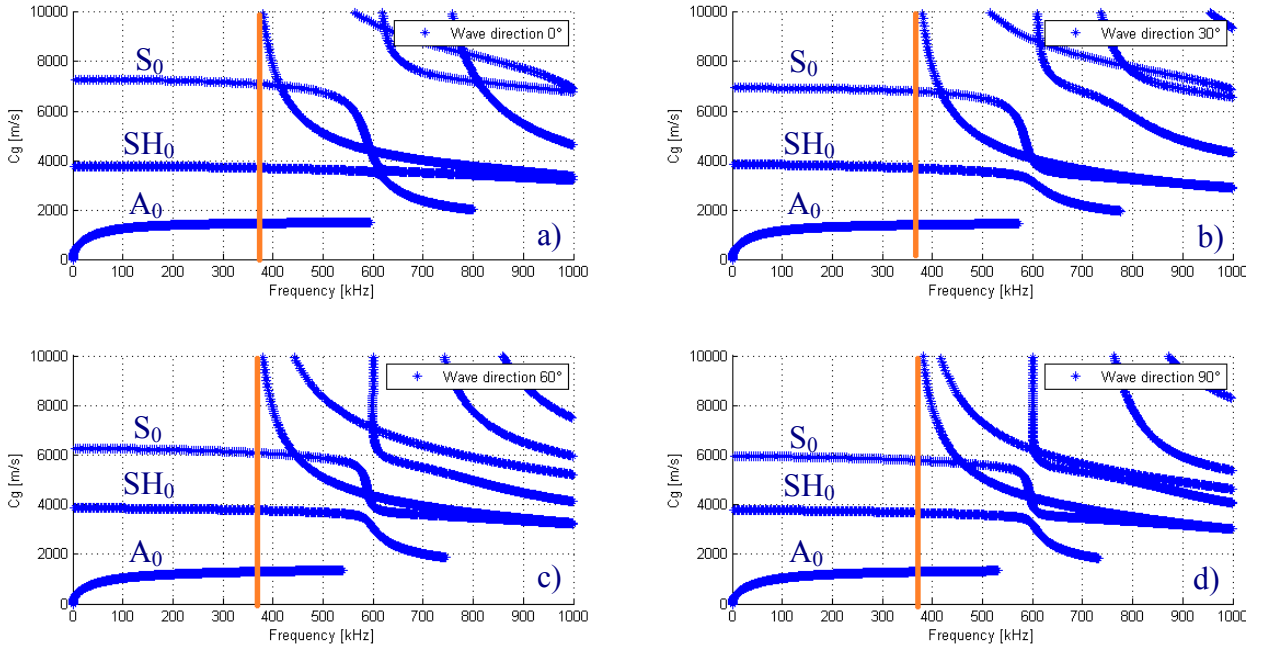


Figure 3: SAFE dispersion curves for the target quasi-isotropic laminate expressed as $C_p(\mathbf{f})$: a) 0° ; b) 30° ; c) 60° ; d) 90° . (Wave propagation with respect to the x coordinate of the laminate)

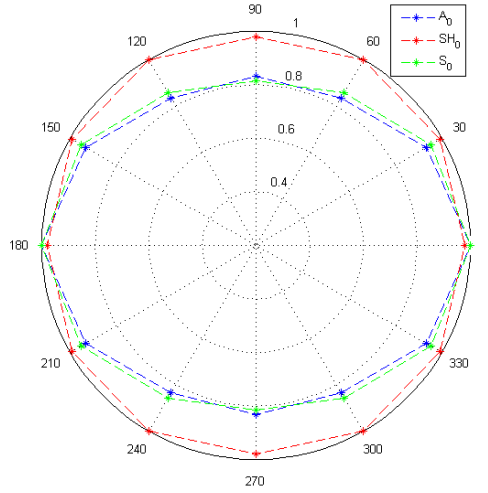


Figure 4: Polar diagram of the phase velocities, at 100 kHz, of the quasi-isotropic laminate. The values are normalized with respect to themselves.

Having determined the cut-off frequency, the PZT ceramic that best suits the present Lamb wave-based SHM process was chosen and enabled the design of the transducer. In particular, the actuating signal, the expected received Lamb waves, the in-plane and out-of-plane resonant frequencies and, consequently, the geometrical features of the PZT were chosen so to optimise both the actuating ($f < f_{\text{cut-off}}$) and receiving (adequately far away from the resonant frequencies) stages. The aforementioned properties of the PZT PIC255, finally adopted in the present research, are reported in Table 2, while Figure 5 shows the chosen piezoelectric transducer.

Table 2: Piezoelectric properties of PZT PIC255 [6].

T_{curie} [°C]	350	g_{31} [Vm/N]	$-11.3 \cdot 10^{-3}$
k_p	0.62	g_{33} [Vm/N]	$25 \cdot 10^{-3}$
k_t	0.47	N_p [Hzm]	2000
d_{31} [C/N]	$-180 \cdot 10^{-12}$	N_t [Hzm]	2000
d_{33} [C/N]	$400 \cdot 10^{-12}$		



Figure 5: Detail of the adopted PZT transducer.

As it will be clear in the following Sections, the interest is here focused onto the fundamental asymmetrical mode A_0 excited at very low frequency, much below the cut-off frequency, so Figures 6 and 7 summarise the main propagation features of this particular mode, in a restrained range of actuation: [0;150] kHz. In particular, Figures 6 and 7 show, respectively, its dispersion properties expressed as the group velocity, i.e. the wave-packet velocity, and the wavelength λ against frequency through the well-known expression:

$$\lambda = \frac{2\pi}{k} \quad (3)$$

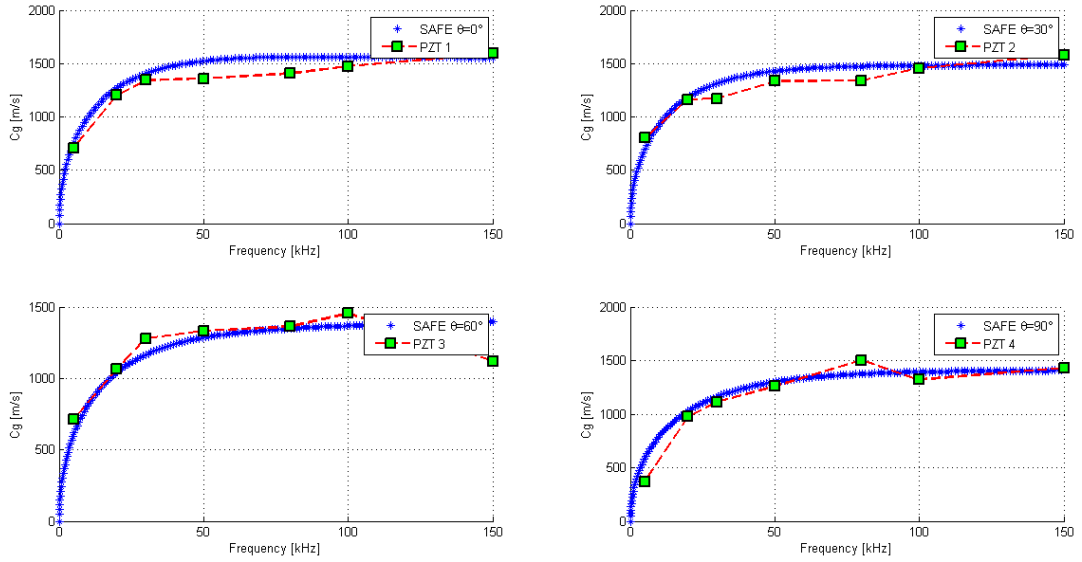


Figure 6: Comparison between the numerical SAFE group velocity values C_g of the fundamental A_0 mode and the experimental ones.

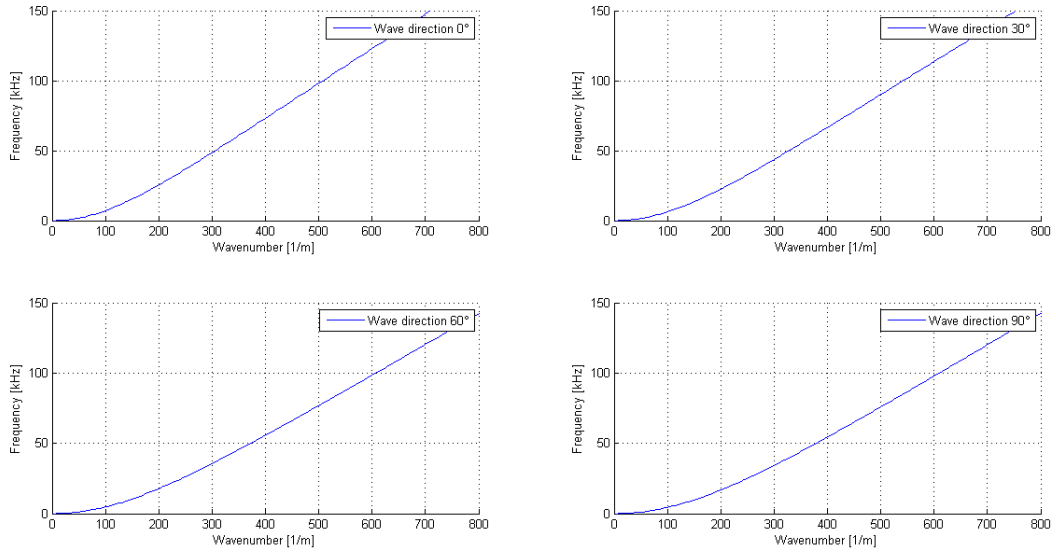


Figure 7: Dispersive relationship of A_0 mode expressed as frequency function of wavenumber for different wave propagation directions (with respect to the 0° aligned fibre).

Additionally, the experimental A_0 group velocity is super imposed to the numerical one in Figure 6. Top this aim, four PZTs (named PZT1, PZT2, PZT3 and PZT4) were bonded onto a CFRP laminate (Fig. 8) with a step of 30° with respect to the x coordinate of the laminate. The received signals, from an actuator positioned in the middle of the laminate, were processed through the Hilbert transform in order to extract C_g values according to:

$$C_g = \frac{\Delta x}{tof} \quad (4)$$

where Δx is the wave propagation path from the actuator to the sensor and “tof” the related time of flight. The experimental evidence shows good agreement with numerical values, hence the validation of SAFE is achieved given that the first numerical output are k and ω (Eqs. (1) and (2)) values from which the group velocities are defined as

$$C_p \stackrel{\text{def}}{=} \frac{\partial \omega}{\partial k} \cong \frac{\Delta \omega}{\Delta k} \quad (5)$$

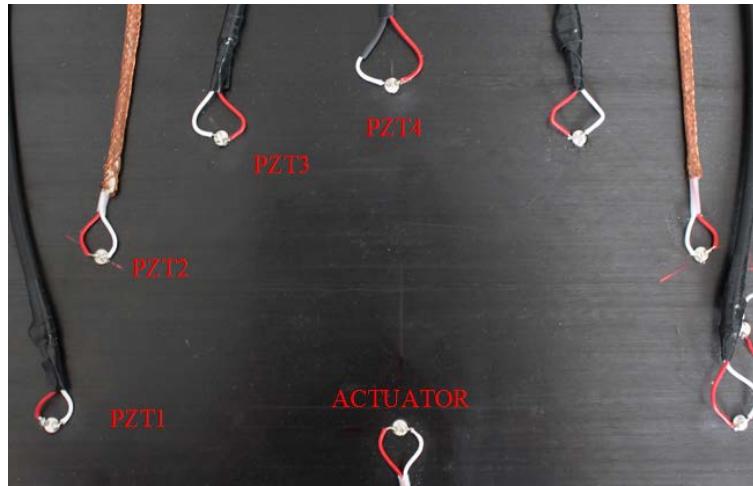


Figure 8: Experimental setup for SAFE validation: four PZT receivers equally spaced of 30° and a central actuator driven @ 30 V peak-to-peak.

4. A “Design Of Experiment” approach

The DOE approach essentially consists of a preliminary experimental stage and of a secondary stage dedicated to the design of an experimental plan and the analysis of the ensuing experimental results.

4.1 Preliminary experimental stage

As Montgomery (2005) said: “the success of an experimental research is founded, more than 90%, on an early stage of laboratory work”. This requires initially a better understanding of the physical phenomenon, in a composite material, causing the Lamb wave propagation and, consequently, of the development of the best experimental setup and of the way of conducting the experiments; regarding the first aspect, Figure 9 displays the developed measurement and acquisition systems.

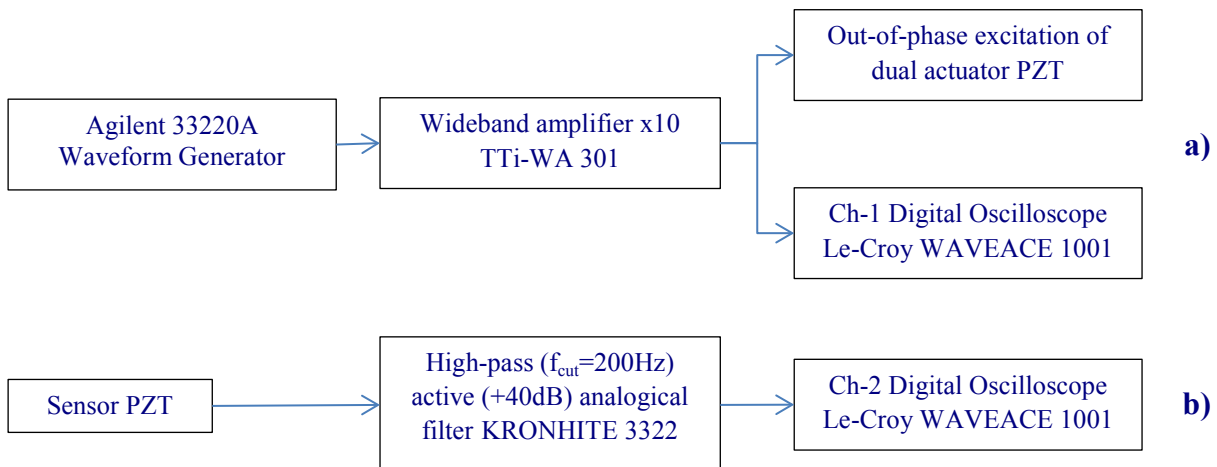


Figure 9: Detail of the measurement chain (a) and of the acquisition system (b).

Concerning the latter, a PZT transducer fixed onto a host structure generates simultaneously both symmetric and anti-symmetric modes, which superimpose and influence each other making the interpretation, of the diagnostic signal, a troublesome task. At present, most mode selection approaches are based on the rationale that a desired wave mode can be enhanced while other undesired modes minimised, by mutual interactions of an array of appropriately placed PZTs, in the resultant signal. Su and Ye (2004) assert to be able to selectively activate a desired Lamb

mode energising, in-phase (symmetric mode S_i) or out-of-phase (anti-symmetric mode A_i), a pair of PZT transducers symmetrically bonded on the upper and lower surfaces of a quasi-isotropic composite laminate. Actually, this approach seemed here to just enhance a specific mode at a given frequency, but it wasn't able to cancel wave modes completely. An alternative method, proposed here, turns out to be particularly efficacious at low frequency, and it's based on the following experimental evidence: actuating a single PZT within [0;50] kHz, a pure A_0 mode seems to be generated (Fig. 10a), whose magnitude can be further enhanced out-of-phase energising a couple of PZTs (Fig 10b). At the same time, the S_0 mode is almost hidden within the electrical noise and tends to become significant as 50 kHz are approached, but still with one order of magnitude lower than the A_0 mode. All these preliminary tests have been carried out on the quasi-isotropic circular laminate shown in Figure 11, as explained in detail by Gianneo (2012).

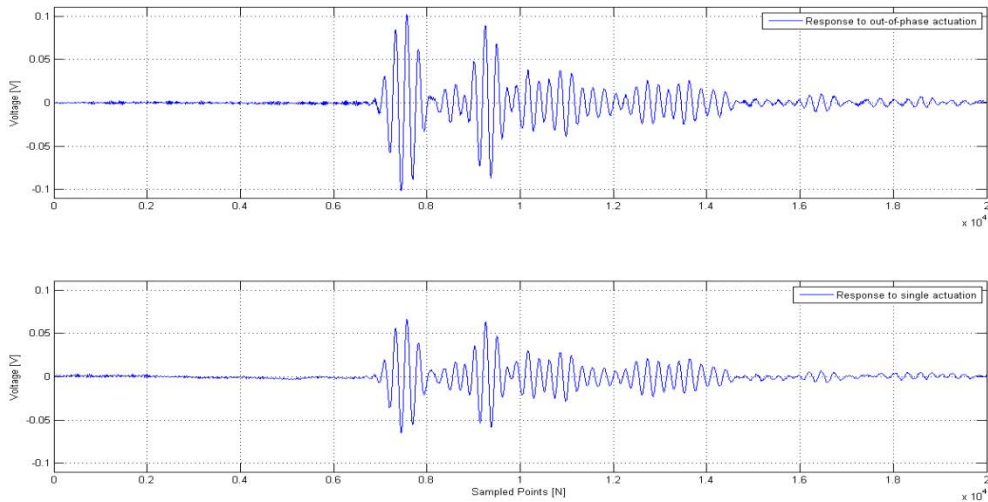


Fig. 10: Effect of the adopted PZT actuation strategy: a) the signal in response to a pair of PZTs excited out-of-phase; b) signal response to a single PZT excitation.

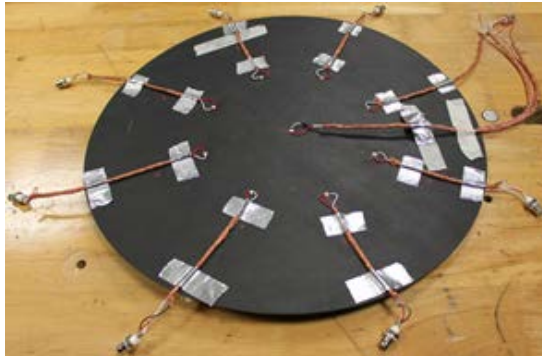


Figure 11: Quasi-isotropic circular laminate target for the preliminary experimental stage.

In particular, the aforementioned tuning approach is experimentally validated in Figure 12, where the peak-to-peak amplitude ratio $\left(\frac{A_0}{S_0}\right)_{pk-pk}$ for the different wave propagation paths corresponding to the PZT1, PZT2, PZT3 and PZT4 transducers shown in Figure 8. The higher values (approximately equal to 50 dB) can be reached, as could be expected, out-of-phase energising the PZTs, since a flexural mode is induced into the laminate. However, it's interesting to emphasize that, in the low frequency range, the way of actuation always gives a stronger fundamental anti-symmetrical mode rather than a symmetrical one, even though an in-phase actuation is applied, unlike what is usually reported in the literature. The peak-to-peak ratio keeps higher than 0 dB until 50 kHz and, above this point, it's possible to visualize the common trend enclosed in a bandwidth around 0 dB. For completeness, Figure 13 reports the difference,

in dB and at 50 kHz, between out-of-phase and in-phase actuations, whose maximum is reached at 60°.

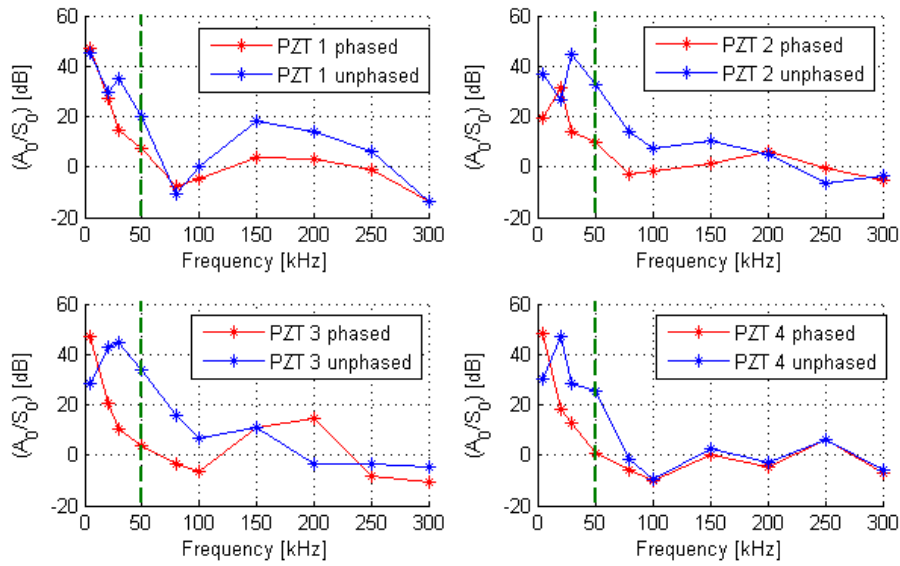


Figure 12: Amplitude ratio of the two fundamentals Lamb wave modes (A_0, S_0) obtained driving the PZT transducers in-phase and out-of-phase.

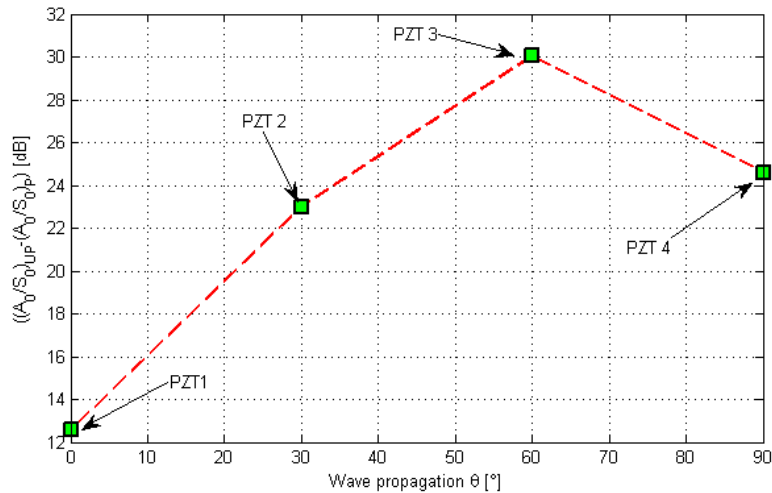


Figure 13: Difference between the amplitude ratio of the two fundamentals Lamb wave modes (A_0, S_0) energised out-of-phase and in-phase @ 50 kHz, as a function of the wave propagation direction.

This experimental evidence opens the promising possibility of conducting a NDE and a SHM via PZT wafers bonded onto the surface of a CFRP laminate only using, as diagnostic wave, the fundamental asymmetrical A_0 , simplifying the interpretation of the signal waves received from the PZT sensors. In the following subchapters a DOE is established to verify the performance of such an approach based onto the A_0 mode.

4.2 Design of Experiment for artificial delaminations

With the aim to study the influence of k factors on an SHM process founded onto a pair of PZT actuators symmetrically bonded to the upper and lower surfaces of the laminate and out-of-phase energised in the low frequency range, an experimental screening plane with a factorial 2^k design was chosen, thus taking into account both the principal and interactional effects. The design factors, established amongst many others classified as constant and noise factors, are: the

frequency of excitation, the position and the dimension of the delamination defects. In particular, the 8 and 24 mm defect dimensions were chosen compatibly to the SAFE's dispersion curves $f(k)$ of Figure 7, the frequency range of actuation and the well-known necessary (but not sufficient) relationship suggested in literature to guarantee an interaction between an ultrasonic wave and a defect:

$$d > \frac{\lambda}{4} \quad (6)$$

where d is a characteristic dimension of the defect and λ is the wavelength. Since the wavelength decreases with frequency, it's immediate to establish, from Figure 7, that a reasonable minimum detectable defect size is 7.85 mm @ 25kHz, rounded up to 8 mm. The defects were located, via circular Teflon patches during the manufacturing process, between the first and second ply, and the sixteenth and seventeenth ply (respectively at a distance of 0.125 mm and 2 mm from the upper surface). Despite the possibility of carrying out a NDE at the lowest excitation frequency into the aforementioned range, since it's impossible to achieve a benchmark signal of the artificially delaminated panels, the frequency is set across the upper boundary 50kHz, so at 45 and 60 kHz to avoid the mutual scattering interference between boundaries and defects as well. Furthermore, as the experimental scatter can potentially hide the significance of the factors under investigation, their levels were sufficiently spaced to prevent such circumstance. The chosen factors were coded, as usually by ANOVA, with a low and a high level so that i.e. 45 kHz is associated to -1 (low level) and 60 kHz to +1 (high level). Table 3 provides all the adopted codifications.

Table 3: High and low level codifications used in the ANOVA analysis.

Considered factor	Value	Code for ANOVA
Frequency [kHz]	45	-1
	60	+1
Position from the first ply [mm]	2	-1
	0.125	+1
Dimension [mm]	8	-1
	24	+1

Two CFRP laminates ("Plate-1" and "Plate-2"), compliant with the data reported in Table 1, were set up with eight PZT transducers along the diagonal lines of the panels: four dedicated to the Pulse-Eco (PE) technique and the remaining to the Pitch-Catch (PC) one. Radiographic testing (28 kV and 5 mA for 30 s) was then performed, on each plate, to check the position and the dimension, after the manufacturing process, of the Teflon patches with respect to PE and PC transducers. Figure 14 and Table 4 show the results as regards the example case of Plate-2. It is worth noticing that knowing the exact position of the artificial delaminations allows to compare the information to the one coming from PE, hence an accuracy of detection is obtained. On the contrary, the PC can only provide the interaction with a defect, without any information about its location.

The designed plan was carried out driving a pair PZT actuators out-of-phase, in agreement with a 5.5 cycles sinusoidal tone burst 30 V peak-to-peak modulated with a Hanning window. Two groups of time records (45 and 60 kHz) were sampled, one for each of the two artificially defected composite panels, according to the measurement chain aforementioned in Fig. 9a. The sampled data were processed using the discrete wavelet transform (DWT, wavelet Daubechies 6th level, db6) for de-noising the signal and the continuous one (CWT, wavelet Morlet, morl) to evaluate the percentage of energy for each coefficient of the adopted wavelet transform. In order to extract the feature of the diagnostic signal in response to artificial defects, the CWT

coefficient corresponding to the maximum energy of the scalogram, along the scale axis, was then considered. The extracted signal were represented through their energy envelope, i.e. the Hilbert transform, an approach aimed at canvassing a Lamb wave signal in the time domain in terms of its energy distribution. Figure 15 gives an example of the complete digital signal processing performed in the following subchapters.

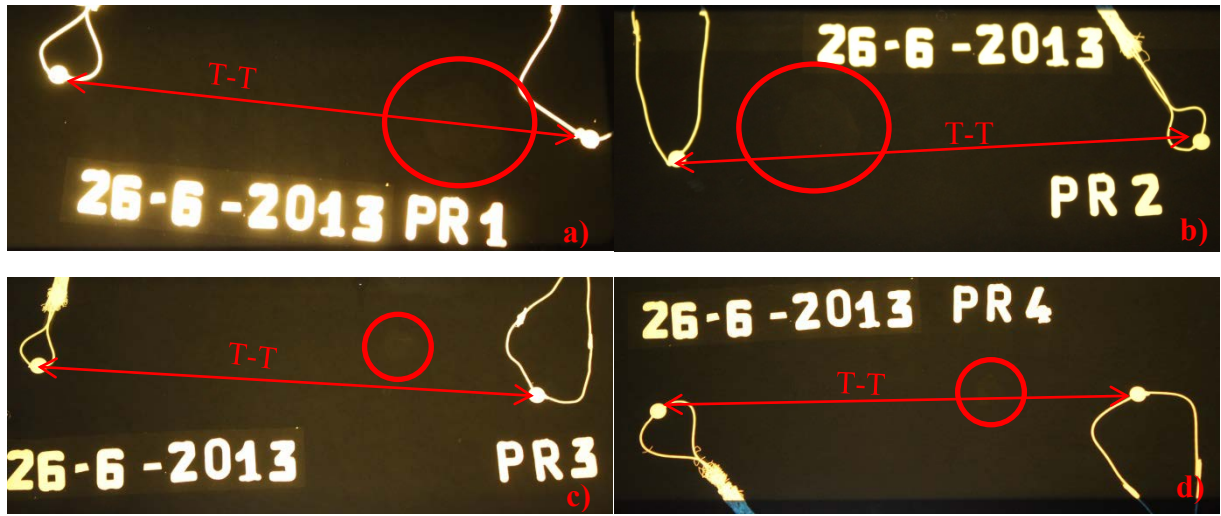


Figure 14: Radiographic testing of the artificially-delaminated Plate-2: a) and b) 24 mm patches; c) and d) 8 mm patches. The presence of delamination is highlighted through red ellipses.

Table 4: Evaluated distance from PZT transducers and dimensions of artificial Teflon patches. Nomenclature according to Figure 14.

	N° of pixel	Distance [mm]		N° of pixel	Distance [mm]
RX-1			RX-3		
T-T	2953.8	156.00	T-T	2412.6	155.00
T-Delamination	1993	105.26	T-Delamination	1674.9	107.61
Delamination size	453.8	23.9	Delamination size	146.8	9.4
RX-2			RX-4		
T-T	2980	157.00	T-T	2906.4	153.00
T-Delamination	1947	102.6	T-Delamination	1942.3	102.3
Delamination size	435	22.9	Delamination size	141.8	7.5

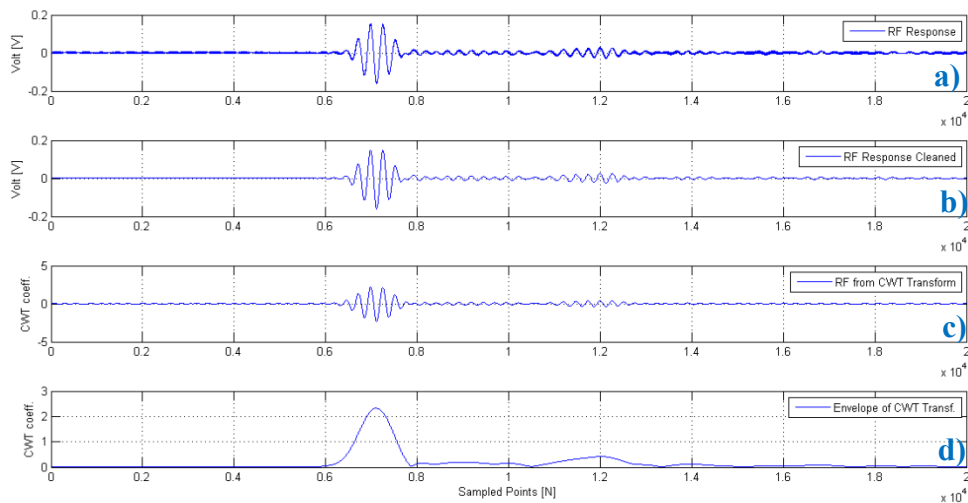


Figure 15: Processing of Lamb Wave signals: a) noisy sampled signal in time domain; b) de-noised signal (DWT, db6); c) scalogram wavelet coefficient (CWT, morl) corresponding to the central frequency of actuation; d) energy envelope of the extracted CWT coefficient.

4.3 Analysis of experimental results from PE

For the Pulse-Echo method, the evaluation of damage response to the diagnostic signal was achieved by evaluating its reflection coefficient R , that is the ratio of the largest magnitude of the damage-reflected first wave component captured by the sensor to that of the incident wave. Figure 16 gives an example of the acquired PZT response to a 24 mm artificial defect: the blue line stands for the response to an artificial delamination in the radio-frequency domain extracted from the CWT, the red one represents its Hilbert transform.

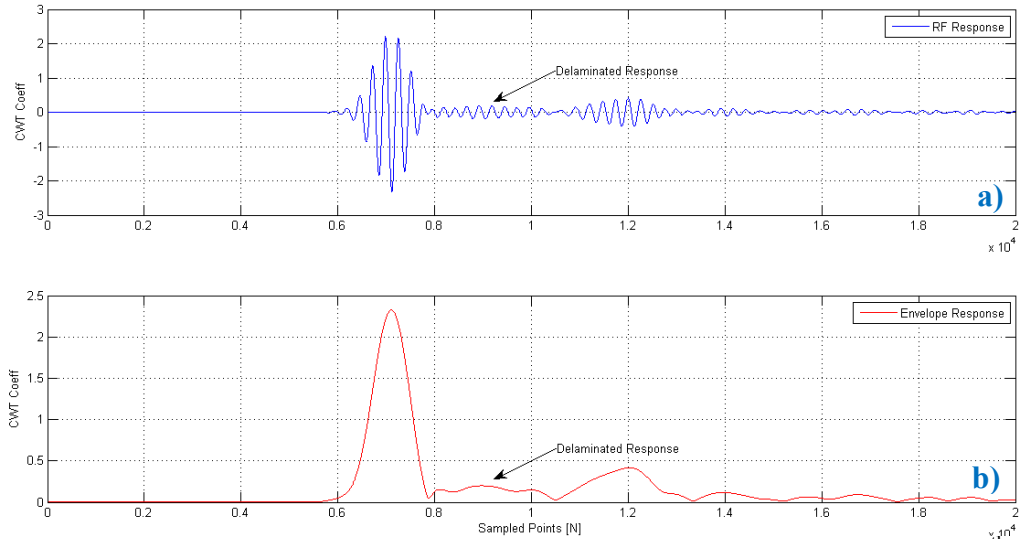


Figure 16: Pulse-Echo response to a 24 mm delamination positioned between the 16th and the 17th ply @45kHz, from Plate-1: a) radio-frequency representation; b) Hilbert transform. Data from CWT coefficient.

The main effects and interaction plot are a first tool of synthesis: in this case, Figure 17 outlines, as key factors, the dimension and the interaction frequency-dimension and, in a weaker way, the dimension and the interaction dimension-position. Anyway, these results are subjective and an analysis of variance (ANOVA) needs to be performed to highlight their impact with respect to the scatter of the method.

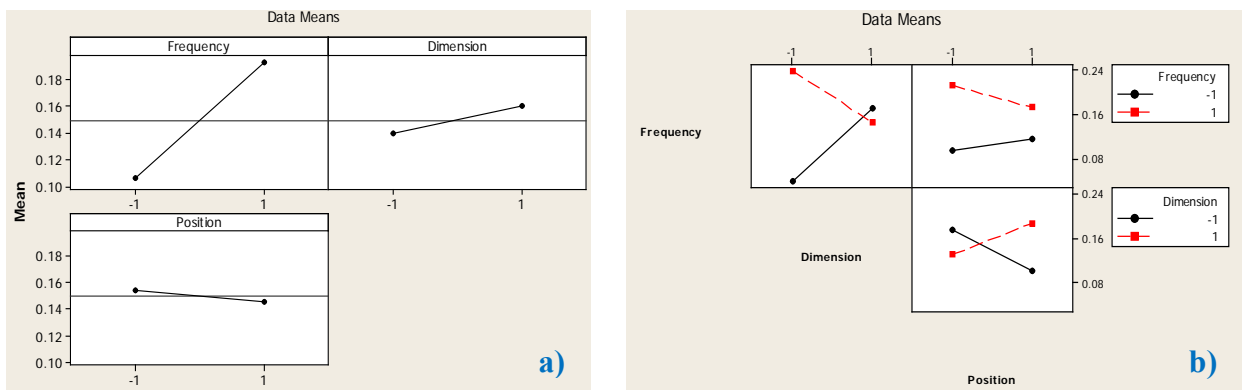


Figure 17: Main effects (a) and interaction plot (b) of the studied factors: frequency, dimension and position of artificial delaminations.

Table 5 summarises the ANOVA analysis of the complete model considering a fixed level of significance (α -value) equal to 10%. It is pointed out that the interaction frequency-dimension seems to significantly influence the Pulse-Echo SHM process. Moreover, Figure 18 shows the hypotheses of the 2^k factorial plan on the residuals: normality, homogeneity of variance, absence of structure and independence from run-order are all passed. As a result, a lowered model, only containing the previously highlighted interaction, could be considered. The results, summarised in Table 6, fits the experimental evidence better than the complete one since the R^2_{adj} parameter

gets higher. The hypotheses about the residuals normality, the homogeneity of variance and the absence of any structure, as shown in Figure 19, are Also overcome.

Table 5: ANOVA report of the complete model: response versus frequency, dimension, position.

Estimated Effects and Coefficients for Response (coded units)						
Term	Effect	Coef	SE Coef	T	P	
Constant		0.14952	0.03025	4.94	0.001	
Frequency	0.08687	0.04344	0.03025	1.44	0.189	
Dimension	0.02073	0.01036	0.03025	0.34	0.741	
Position	-0.00903	-0.00451	0.03025	-0.15	0.885	
Frequency*Dimension	-0.11245	-0.05622	0.03025	-1.86	0.100	
Frequency*Position	-0.03075	-0.01537	0.03025	-0.51	0.625	
Dimension*Position	0.06505	0.03252	0.03025	1.08	0.314	
Frequency*Dimension*Position	0.00283	0.00141	0.03025	0.05	0.964	
S = 0.121001 PRESS = 0.468522						
R-Sq = 46.92% R-Sq(pred) = 0.00% R-Sq(adj) = 0.48%						

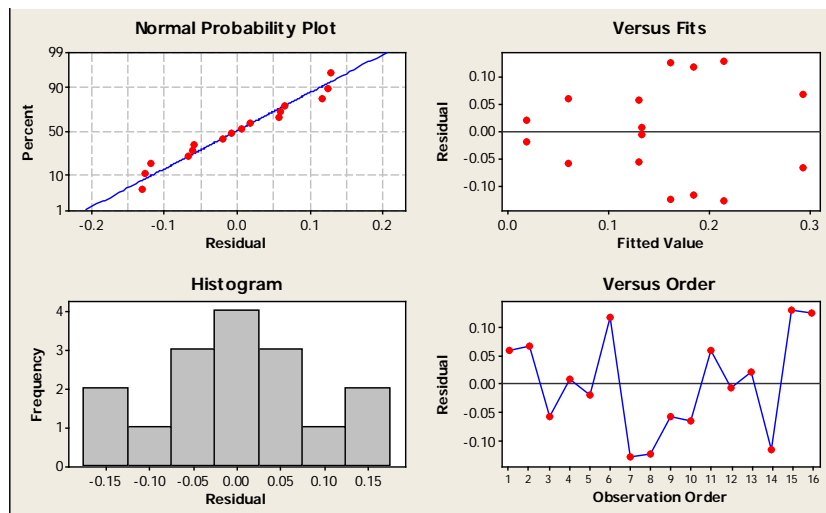


Figure 18: Check about the residuals hypotheses for the response of the complete 2^k factorial plan.

Table 6: ANOVA report of the lowered model: response versus frequency, dimension and their interaction.

Estimated Effects and Coefficients for Response (coded units)						
Term	Effect	Coef	SE Coef	T	P	
Constant		0.14952	0.02683	5.57	0.000	
Frequency	0.08687	0.04344	0.02683	1.62	0.131	
Dimension	0.02073	0.01036	0.02683	0.39	0.706	
Frequency*Dimension	-0.11245	-0.05622	0.02683	-2.10	0.058	
S = 0.107314 PRESS = 0.245683						
R-Sq = 37.38% R-Sq(pred) = 0.00% R-Sq(adj) = 21.72%						

Concerning the PE technique, it can be concluded that the interaction frequency-dimension is highly significant, since its p-value is lower than the imposed significance level. In addition, also the frequency, as a stand-alone factor, seems to be significant, but the experimental evidence isn't so strong to justify such conclusion due to the p-value higher than the α one. The position and the interactions between the other factors don't seem to be significant. Furthermore, on the base of the coefficients of Table 6 and what is shown in Figure 17b, the PE performance with respect to a high dimension level (i.e. a big defect) is quite independent from the actuation

frequency, while it can be enhanced working at a low frequency level for small defects (low dimension level).

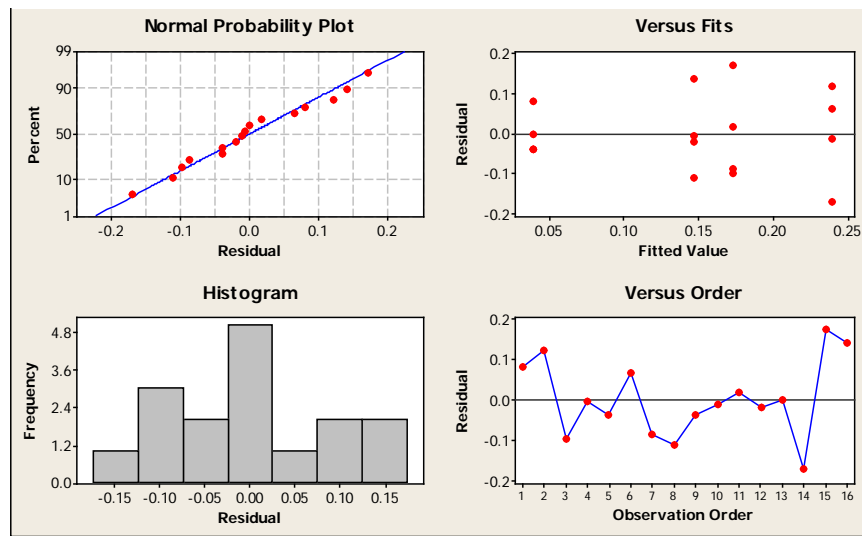


Figure 19: Check about the residuals hypothesis for the response of the lowered 2^k factorial plan.

4.4 Analysis of experimental results from PC

Regarding the Pitch-Catch configuration, the transmission coefficient T (i.e. the ratio of the A_0 peak wave component propagating across the damage and captured by the sensor to that of the incident wave) is chosen as the relevant response from the delamination. Figure 20 shows an example of the sampled data: the green line stands for the incident wave without defect interaction, while the red one represents the response of the wave passing through the delamination. Their envelopes are also given: the blue dots of Figures 20c and d highlight the A_0 mode shape before and after the defect interaction.

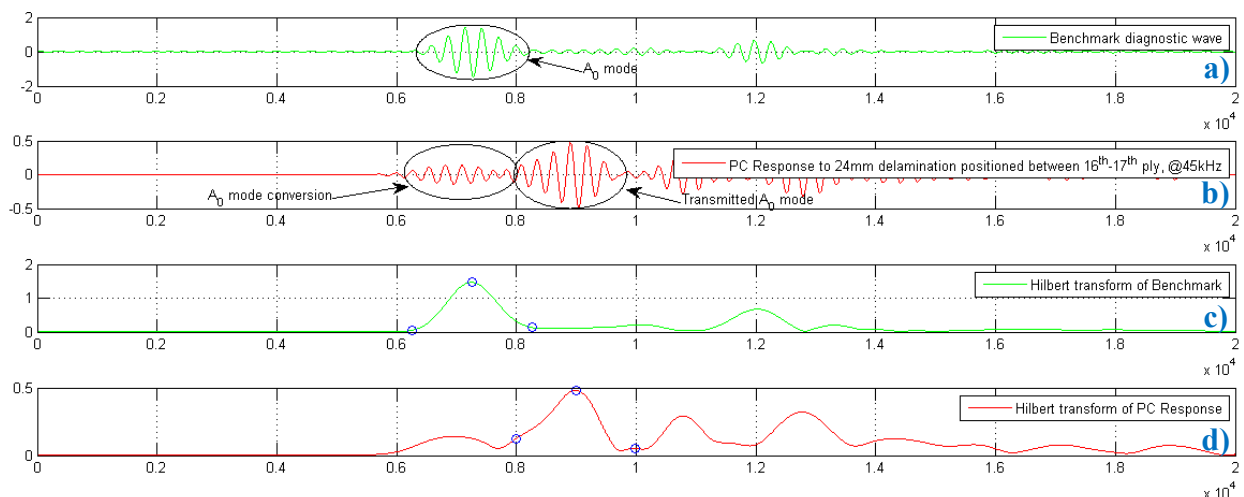


Figure 20: Example of PC response caused by a 24 mm delamination positioned between the 16th and the 17th ply @45kHz, from Plate-1: a) benchmark diagnostic wave; b) transmitted wave across the delamination; c) and d) corresponding envelopes.

The main effects and interaction plot of Figure 21 outline a strong dependency from dimension, with respect to the other main factors and a weak interaction between frequency and position. In particular, the ANOVA analysis, again with $\alpha=10\%$ and reported in Table 7, points out the dimension as the only potential key factor influencing the Pitch-Catch SHM process. Moreover, Figure 22 shows the effectiveness hypothesis of the 2^k factorial plan about the residuals: all the checks resulted to be satisfied.

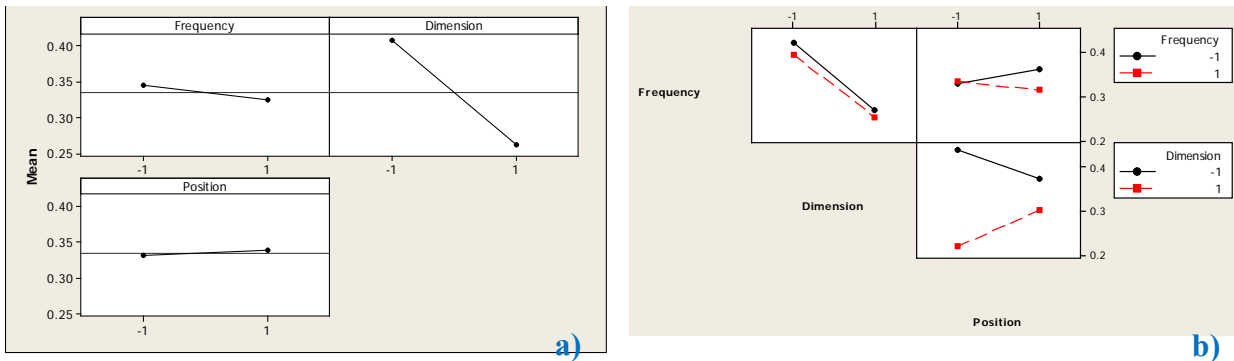


Figure 21: Main effects (a) and interaction plot (b) of the studied factors: frequency, dimension and position of artificial delaminations.

Table 7: ANOVA report of the complete model: response versus frequency, dimension, position.

Estimated Effects and Coefficients for Response (coded units)						
Term	Effect	Coef	SE Coef	T	P	
Constant		0.33439	0.02979	11.23	0.000	
Frequency	-0.02031	-0.01016	0.02979	-0.34	0.742	
Dimension	-0.14621	-0.07311	0.02979	-2.45	0.040	
Position	0.00714	0.00357	0.02979	0.12	0.908	
Frequency*Dimension	0.00579	0.00289	0.02979	0.10	0.925	
Frequency*Position	-0.02626	-0.01313	0.02979	-0.44	0.671	
Dimension*Position	0.07419	0.03709	0.02979	1.25	0.248	
Frequency*Dimension*Position	0.01129	0.00564	0.02979	0.19	0.854	
S = 0.119150 PRESS = 0.454296						
R-Sq = 49.83% R-Sq(pred) = 0.00% R-Sq(adj) = 5.92%						

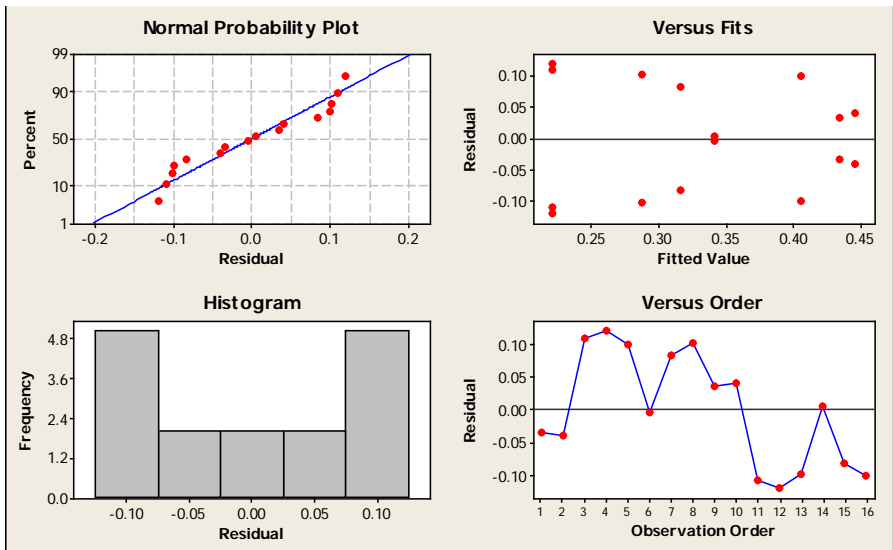


Figure 22: Check about the residuals hypotheses for the response of the complete 2^k factorial plan.

Again, a lowered model was then considered: the ANOVA report of Table 8 fits the experimental evidence better since the R^2_{adj} parameter gets higher. Moreover, the hypotheses about the residuals normality, the homogeneity of variance and the absence of any structure, as shown in Figure 23, are again overcome.

In summary the PC response to an artificial delamination defect is influenced only by its extension, hence, regardless of the diagnostic wave excitation frequency and the relative position of the defect along the thickness of a CFRP laminate, abrupt changes in the amplitude response signal to diagnostic wave occur when the A_0 mode is transmitted through delaminations.

Table 8: ANOVA report of the lowered model: response versus dimension.

Estimated Effects and Coefficients for Response (coded units)						
Term	Effect	Coef	SE Coef	T	P	
Constant		0.33439	0.02508	13.34	0.000	
Dimension	-0.14621	-0.07311	0.02508	-2.92	0.011	
S = 0.100302 PRESS = 0.183962						
R-Sq = 37.78% R-Sq(pred) = 18.73% R-Sq(adj) = 33.33%						

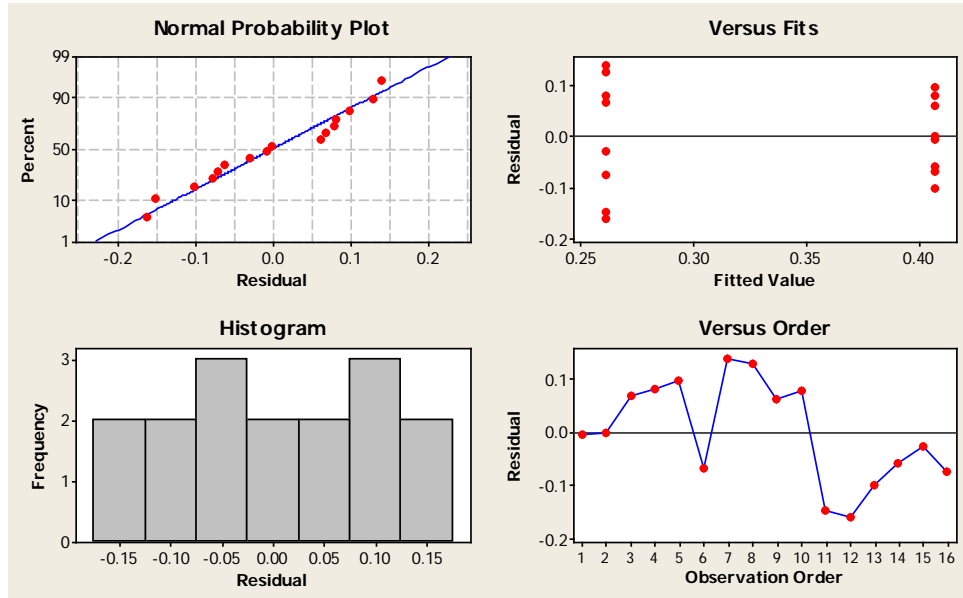


Figure 23: Check about the residuals hypotheses for the response of the lowered 2^k factorial plan.

5. Performance of the suggested SHM process from natural delaminations

After taking into account the factors potentially influencing the performance of the suggested SHM approach, its performance was then evaluated with respect to natural delaminations, established through drop weight impact tests. In particular, the interest was to perform low-velocity impacts, since they can cause a significant amount of internal delamination without evidence at the surface. This type of damage is often referred to Barely Visible Impact Damage (BVID) and can cause a significant degradation of structural properties: if the damaged laminate is subjected to high compressive loading, buckling failure may occur. Boeing [11] defines BVID as: “small damages which cannot be found during heavy maintenance general visual inspections using typical lighting conditions from a distance of five feet”.

Impact tests were performed in accordance to ASTM D7136 [12], using a 25.4 mm diameter hemispherical striker tip impactor (Fig. 24), whose mass is about 1.2 Kg, guided by an impact device consisting in the cylindrical tube mechanism shown in Figure 25a. This device is equipped, as shown in Figure 25b, with a laser triangulation Mel M7L sensor in order to measure the real impact velocity. Figure 26 provides an example of the acquired impactor profile during a test and used to determine the real velocity at the impact.

The target CFRP plate, illustrated in Figure 27, presents four randomised impact locations according to Table 9, which shows the effective impact energies selected to achieve a BVID. A detail of the highest energy impacted region is also given. It is worth noticing that none of the common visible damaged modes, listed in ASTM D7136 [12], are visible, hence the barely condition is achieved despite of the 20 J application.

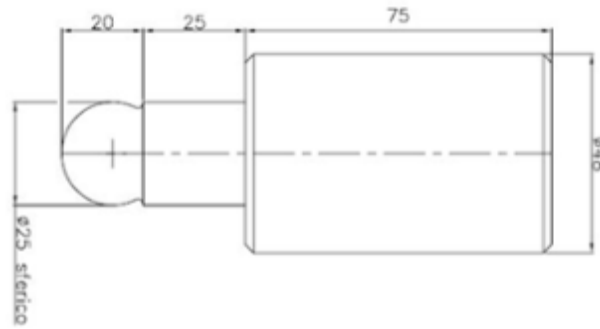


Figure 24: Impactor with hemispherical striker tip whose mass is about 1.2 Kg.

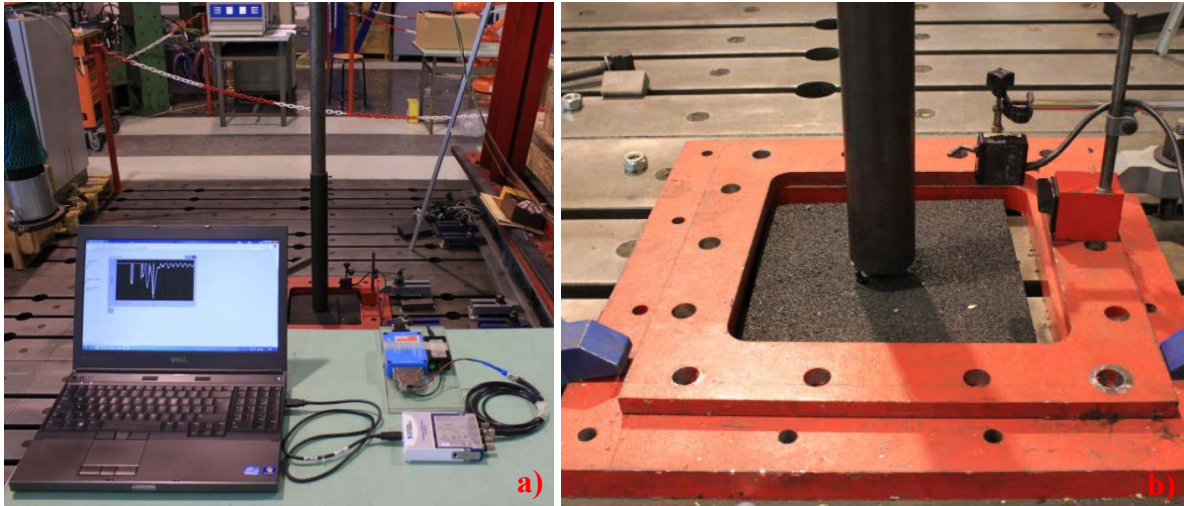


Figure 25: Detail of the experimental setup used during drop weight impact test: a) measurement chain and impact device system; b) laser triangulation for impact velocity calculation.

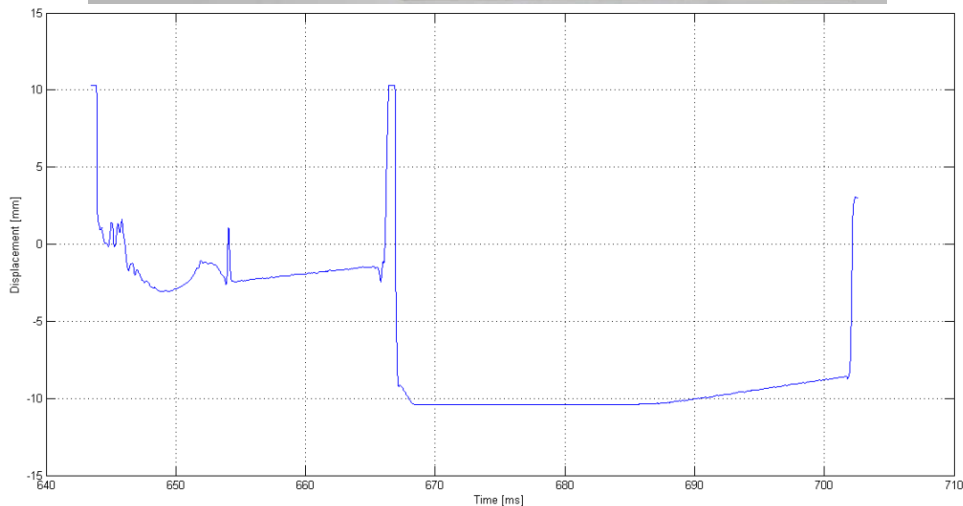


Figure 26: Superposition of the impactor shape from laser triangulation to the real one.

Table 9: Effective BVID energies applied to the target CFRP laminate.

Nominal Impact Energy [J]	Drop Height [m]	Measured Impact Velocity [m/s]	Effective Impact Energy [J]
5	0.4	2.03	2.8
10	0.8	3.7	8.1
15	1.2	4.8	13.8
20	1.7	5.9	20.8

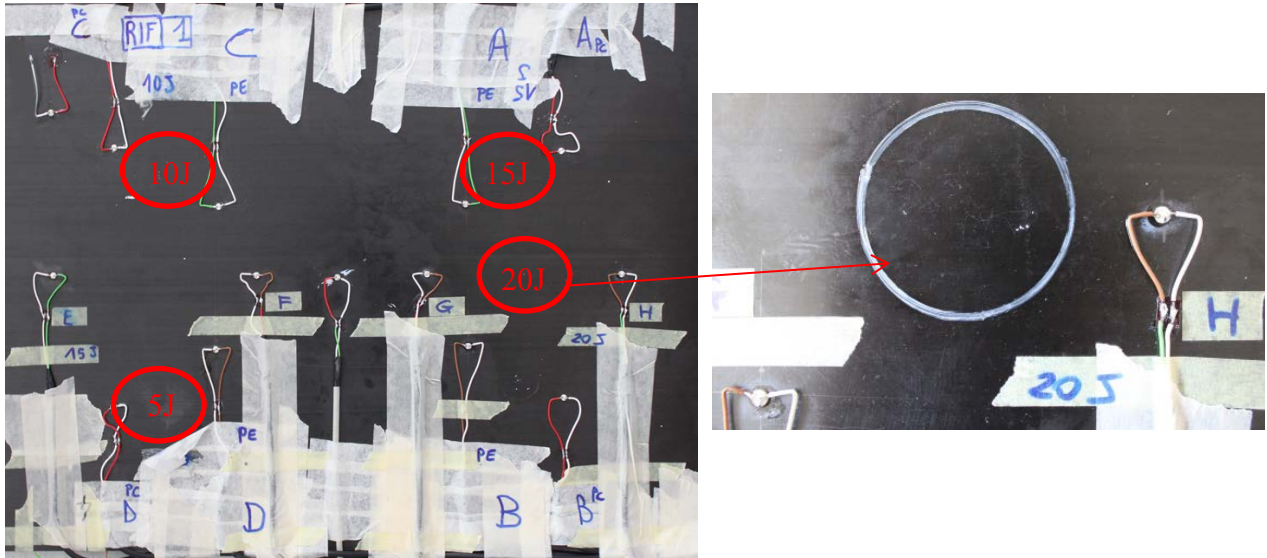


Figure 27: Target CFRP laminate used for the drop weight impact tests: red ellipses identify the impact zones at different energy.

Once again, the laminate is instrumented with a central pair of PZT actuators out-of-phase energised at 45 and 60 kHz and an array of PZT sensors to perform the PC and PE SHM techniques. The sampled data were then digital processed in the same way as in the previous Sections and the results obtained from the natural delaminations are summarised in the main effect and interaction plot shown in Figure 28. In this case, the design factors are limited to the impact energy and the excitation frequency. This because a natural delamination due to an impact tends to develop involving more plies and to be a much more complicated damage, so to make the concept of position (as here defined) meaningless. The comparison of results was then possible assimilating the impact energy directly to the extension of damage, as a consequence of its characteristic dimension. Furthermore, a rigorous ANOVA analysis could not be performed since the number of replications per factor level were limited to one (since just one is the impacted CFRP laminate): there were not enough degrees of freedom to estimate the error/variance.

In any case, some elements of similarity into the response to the same SHM sensor network with respect to artificial defects could be found. In particular, the Pulse-Echo method underlines the same kind of interaction frequency-dimension, or correspondingly frequency-impact energy, from which the response was maximised driving the PZT at high frequency for small defect (low energy), whereas it was almost steady interacting with wide defect. The main discrepancy consisted in the apparent, since the variance of the process couldn't be estimated, significance of the energy and frequency as stand-alone factors. Their influence, onto the reflection factor, could be attributed to the fact that a BVID damage is much more complicated than a simple delamination simulated through a Teflon patch, indeed is the combination of three types of damage [13]: matrix cracks, fibre fractures and delamination, each of those contribute to the global response.

On the contrary, as pointed out through the DOE approach, the Pitch-Catch, characterized by its transmission factor T , was mainly influenced by the extension of the defect (similarly the impact energy): the higher the extension, the lower the transmission coefficient. Hence, in that case, the complex damage mechanism seems not to affect the final response.

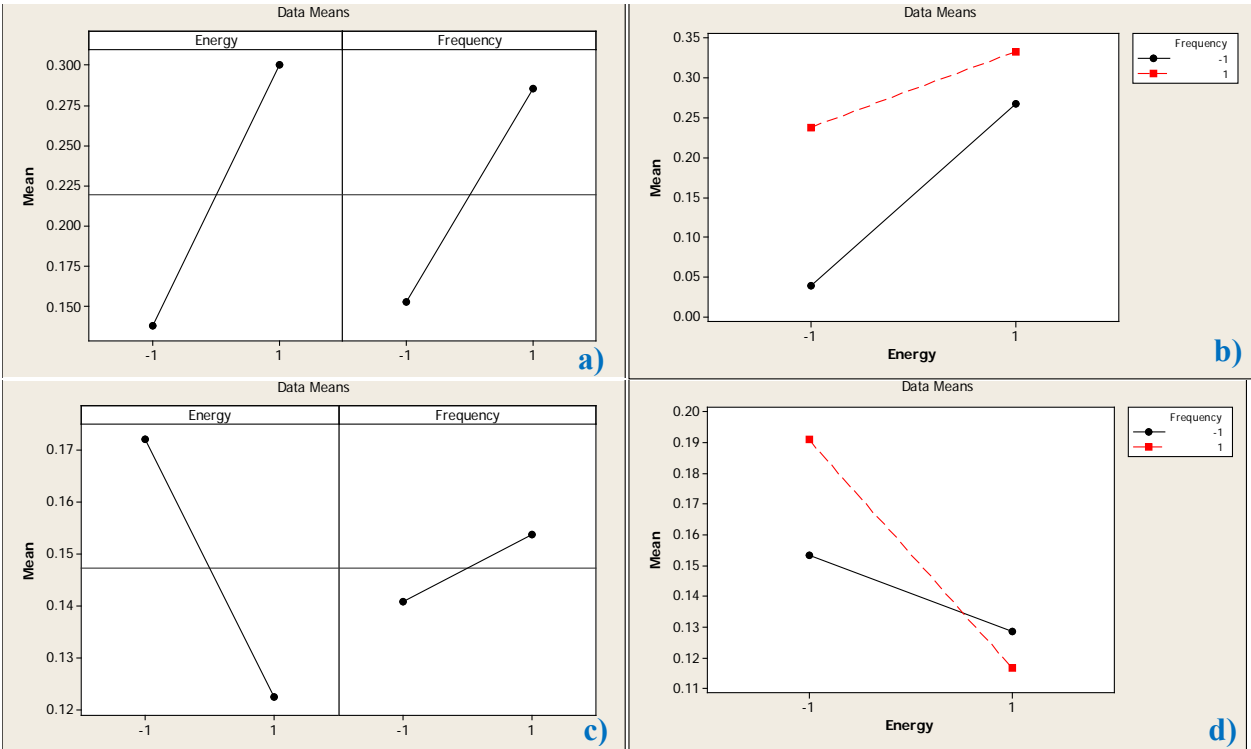


Figure 28: Impact tests results summarized in the main effects and interaction plot: (a) and (b) reflection factor for Pulse-Echo and (c) and (d) Transmission one for Pitch-Catch.

6. Concluding remarks

A new way for tuning Lamb waves, based on the actuation at a very low frequency [0;50] kHz and able to give back mainly the fundamental A_0 mode, was observed and characterised up to 100 kHz, above which the A_0 mode is no longer the only significant one. This frequency range simplifies the interpretation of the diagnostic signal waves received from PZT sensors, since only one mode significantly propagates and interacts with the host structure. Moreover, its magnitude, with respect to the other modes, and its SNR can be successfully enhanced using a pair of PZT actuators symmetrically bonded onto the upper and lower surfaces of the composite laminate. Further studies are required to verify if a strong mode conversion can occur within this low frequency range.

The performance and the potentially influencing factors of the proposed SHM process, both in the Pulse-Echo and in the Pitch-Catch configurations of the PZT transducers, were studied considering a quasi-isotropic composite laminate prone to artificial defects and natural delaminations obtained by low-velocity impact tests. The actuation frequency was chosen across the limit value equal to 50 kHz due to the closest boundary condition able to mask useful response signals. Anyway, the proposed SHM process could be encouraging for vast structures since, at low frequency, lower attenuation coefficient are achievable.

Some elements of similarity between the response to an artificial defect and a natural delamination could be found: the PC response is almost reliant on the damage extension inside the laminate, while the PE one seems to recognise the complex damage mechanism induced by an impact damage. This opens the promising possibility to extract, from the response signal, additional information about the nature of damage, since a fingerprint could be identified on the

differences between the response to a pure delamination (the artificial one) and a natural one which typically consists of multiple delaminations through the thickness together with matrix cracks and fibre fractures. Moreover, known the key factors and how they play a role in the NDE, essential information is here supplied with the aim to design an optimized SHM PZT sensor network.

7. Acknowledgements

The authors would like to thank Mr. R. Galeazzi for the active help given to the present research.

8. References

- [1] Chang F.K., 1999, Structural Health Monitoring: A Summary Report, Proceedings of the 2nd International Workshop on Structural Health Monitoring, Stanford, CA, 612-621.
- [2] Toso N., Alastair J., 2011, LIBCOS-Significance of Load upon Impact Behavior of Composite Structure, Research Project EASA 2009/3.
- [3] ASTM D3039/D3039M-08, 2008, Standard Test Method for Tensile Properties of Polymer Matrix Composite Materials.
- [4] ASTM D3518/D3518M-94, 2007, Standard Test Method for In-Plane Shear Response of Polymer Matrix Composite Materials by Tensile Test of a $\pm 45^\circ$ Laminate.
- [5] Bartoli I., Marzani A., Lanza di Scalea F., Viola E., 2006, Modeling wave propagation in dumped wave guides of arbitrary cross-section, Journal of Sound Vibration 285, 685-707.
- [6] PiCeramic, 2012, Piezo Material Data, www.piceramic.com, accessed 01.10.2012.
- [7] Gianneo A., 2012, Analysis and Experimental Design Applied to Structural Monitoring of CFRP plates by Lamb Waves, MSc. Thesis, Politecnico di Milano, Milano, Italy. [In Italian]
- [8] Mallick P. K., 2007, Fibre reinforced composites, 3rd Edition, Taylor & Francis, London.
- [9] Montgomery D. C., 2005, Design and Analysis of Experiment, McGraw-Hill [In Italian]
- [10] Su Z., Ye L., 2005, Selective Generation of Lamb Waves Modes and their Propagation Characteristics in Defective Composite Laminates, Journal of Materials: Design and Applications 218, 95-110.
- [11] Allen J. Fawcett, Gary D. Oakes (ATF), Boeing Composite Airframe Damage Tolerance and Service Experience Boeing Commercial Airplanes 787 Program
- [12] ASTM D7136/D7136M-12, 2007, Standard Test Method for Measuring the Damage Resistance of a Fiber-Reinforced Polymer Matrix Composite to a Drop-Weight Impact Event
- [13] Abrate S., Castanié B., Rajapakse Y. D. S., 2013, Dynamic Failure of Composite and Sandwich Structures Series: Solid Mechanics and Its Applications, Vol. 192 VIII, 643 p

FROM ACOUSTIC EMISSION TESTING (AT) TO ACOUSTIC MONITORING

Peter Tscheliesnig

TÜV AUSTRIA SERVICES GmbH
Deutschstrasse 10, A-1230 Wien, Austria, peter.tscheliesnig@tuv.at

ABSTRACT

Technical degradation processes like corrosion and fatigue cracks are the most frequent reasons for structural failures. To avoid the failure of those structures, maintenance and inspection have to be carried out adopting different strategies and using various methods. For the common methods (preventive maintenance, anticipatory maintenance) and the more modern Risk Based Inspection, AT would be an excellent tool to detect the main degradation processes during the shut down combined with an over-loading of the structure. In the last decades thousands of these tests were performed successfully. In any way, the results have been dependent on how good the normal service conditions were simulated by the different kinds of over-loading.

Nowadays an increasingly accepted strategy used to prevent structures from failing is "structural-health-monitoring (SHM)", which is an integration of sensorial and actuator elements to determine, analyse, locate and predict the load and damage situation with the aim, that the NDT becomes an integrative part of the structure. SHM integrates all the different sciences and analysis in terms of life time management of a structure and starting during its design. As long as we are not able to interfere in all stages of the life time management of a structure we have the opportunity to increase the availability and safety of the structure by using the gap between safe life and certain fail with a monitoring concept, which is able to detect, locate and determine crack during its sub-critical stage.

The only possible integrative method at the moment is Acoustic Emission, whit all its imponderability coming from its sensitivity against service and process noise.

Experience during the last years showed clearly, that AT is able to detect sub-critical crack growth but also different corrosion processes. The new modern AE equipments with the data acquisition, storage and data evaluation techniques open the field to discriminate the real useful AE signals from the service and process noise by frequency and/or logical filtering and also more complex pattern recognition techniques.

Every "monitoring" requires a permanent application of the AE sensors, cabling and data acquisition and evaluation equipment. By a harsh environment this can lead to extensive investigations before the application of the sensors. But also the normal service conditions have to be monitored and evaluated in advance. By the combination of all data in combination with a life time calculation the AE monitoring can determine if the structure can stay in-service or has to be stopped for a shut down and performance of a regular inspection, including an appropriate NDT.

Besides the comparison AE testing versus AE monitoring this paper shall present an example for the AT, preparations for monitoring, part time monitoring at different time spans or service time and permanent monitoring.

Key words: Acoustic Emission Testing, Acoustic Monitoring, Maintenance Strategies, Structural Health Monitoring

1. Introduction

It's well known, that the main technical degradation processes are corrosion and fatigue cracks. These two types of processes are most often the main reason for structural failures. To avoid these failure mechanisms, TÜV AUSTRIA performs since more than 35 years AE Tests during the normal required service inspections (repetition tests). In the first years the AT was mainly used for the first pressure test to exclude small irregularities, which later can be the reason for fatigue cracks. These first pressure tests were performed as hydro-tests with an over-pressurisation, like it was done since the 19th century. The information from the hydro-tests were weak, the vessel was good or it became leaky, would be deformed or explode and it had even the problem, that if a defect was introduced in the wall of the vessels, it wasn't detected normally. A further problem was that during the repetition tests the over-pressurisation was done with water, which led often to a residual humidity in the vessel, when it went back into service. This humidity led later on to corrosion within the metallic wall.

With the application of AT during these tests we got on-line information about irregularities, which can later lead to defects within the vessel. Because of the immediate information of defects occurring in the wall, we were able to make a further step forward. The over-pressurisation could be performed with gas, which could avoid introducing humidity into the vessel. Because of the pre-warning availability of AT during the pneumatic loading, these tests could be performed not only in bunkers, how it was done before. Due to the monitoring of the pressurisation with AE, the over-pressurisation could be performed often with the stock media themselves, which generated an economic advantage for the customer.

2. Example for Acoustic Emission Tests (AT)

An example was the testing of two natural gas storage spheres with a diameter of 32 meters and a pressure of 1,1 MPa. Before they were put in-service these spheres were tested as a first pressure test with water. These tests were done as well for a duplication of the NDT of the welds and to check if defects occur during the pressure test. For this unique loading of the spheres (pressure plus weight of the water), they have been supported by a ring, which was grounded 30 m deep, that hindered the sphere in their geometry. The repetition tests were done with natural gas, avoiding a costly shut-down, and we could demonstrate that the results are comparable (Fig.1).

The AT during such tests shall replace other NDT and detect also the defects, which occur during the pressure tests. The aim of the AT was also to justify the integrity during the next service period. For this reason, we have to be sure, that the kind of over-pressurisation is representative for the normal service loading, which sometimes has been difficult, especially when the pressure equipments are under cyclic and not static loading during service [1].

Nevertheless with all ambiguities of AE we performed tests on a lot of spheres and reactors during the following years for the first pressure tests but much more during the required periodic inspections of pressure equipments.

One very interesting test problem was the repetition tests of a steam drum, which for a normal pressure tests with water, has to be taken out of the paper mill production and has to be supported during the hydro-test, because of the weight of the water compared to steam during service [1]. By a pneumatic loading monitored with AE the steams can stay in the structure without harming the bears and/or the roundness of the drum (Fig. 2).

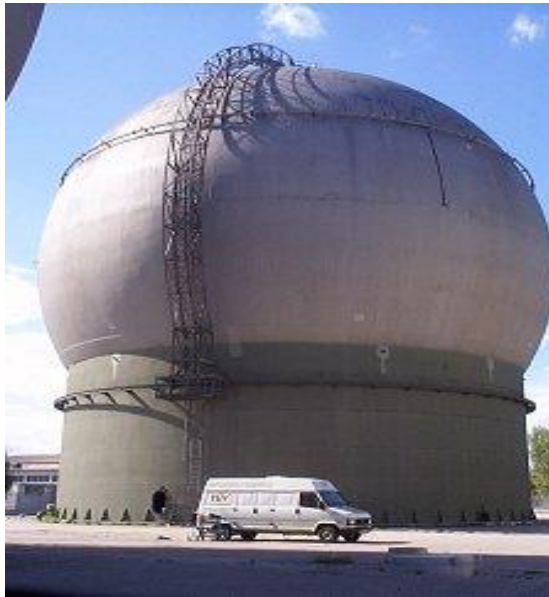


Fig. 1: Pressure tests with AT of a natural gas storage sphere with a diameter of 32 meters (first pressurisation and periodic inspection)



Fig. 2: Sensor application on a built-in steam drum for pneumatic loading

3. Discontinuous AE monitoring for in-service inspection

Compared to this time-span based inspection more modern and sophisticated inspection and maintenance methodologies were carried out, which shall help over the following years to avoid the failure of those structures within service. For all these concepts (preventive maintenance, anticipatory maintenance and the more modern Risk Based Inspection) AT was used. For the Risk Based Inspection, AT is an excellent tool to detect the most important degradation processes during any kind of over-loading. The draw back for this methodology was that the pressure equipment goes out of service. The advantage of AT is, that the over-pressurisation could often be performed with the gas (e.g. nitrogen) or even stock product itself.

The requirement to simulate the service loading during the AT can be fulfilled excellent by monitoring the pressure equipment during service. But AE is not only excellent for detecting defects, it is also sensitive for background noise coming from the process (pumps, temperature changes etc.). The developments in the data management of new AE system give us the opportunity to distinguish between useful AE and background, by application and use of analogue- and/or digital filtering or pattern recognition techniques.

4. Example for dissentious AE monitoring regarding in-service information on the integrity of the pressure equipment

An example in this direction are tests on pressure equipment (“Druckwechselabsorber”) of BASF SE at their plant in Ludwigshafen, where we performed a test programme to determine if the maintenance strategy, which at the moment is absolutely time driven, can use the Acoustic Monitoring for the detection of defects on time during the normal service [2].

To verify the AE monitoring different test steps became necessary: measurement of the background noise, measurement of the different wave propagation parameters, selection of the suitable sensor positions for localisation, monitoring during the normal service (cycling loading and de-loading within 15 min up to a pressure of 3 MPa) and at the end for comparison a “conventional” AT during a pressure test.

The results showed that the detection of a defect during a normal pressure test has had a higher probability than during the normal service, because of the speed of the service-loading and the influence of process noise. On the other hand we could demonstrate that the defect (crack) detection was possible during certain periods of the normal pressure cycles, emphasizing even more the advantages of an Acoustic Monitoring during the normal service (Fig. 3). Based on the results of 3 pressure equipments we could demonstrate that an Acoustic Monitoring for these specific pressure equipments and this specific process is possible and would be the safest, most cost-effective and time saving method for their maintenance strategy.

In this case we made a first step from an AT to a discontinuous Acoustic Monitoring and can change the maintenance strategy from a time driven preventive maintenance to a predictive maintenance driven by the momentous condition of the structure [3]. Clearly you can’t apply Acoustic Monitoring everywhere and without basis tests, like it was shown in this example.

5. Continuous Monitoring with AE (Basics and Examples)

Nowadays a more and more accepted strategy to prevent structures from failures is “structural-health-monitoring (SHM)”, which is an integration of sensors and actuators to determine, analyse, locate and predict the load and damage state with the aim, that NDT becomes an integrative part of the structure. SHM integrates different sciences and analysis regarding the life time management of a structure, starting during its design. As long as we are not able to interfere within all stages of the life time management of a structure we have the opportunity to increase the availability and safety of the structure by using the gap between safe life and certain failure with a monitoring concept, which is able to detect, locate and determine crack during its sub-critical stage [4].

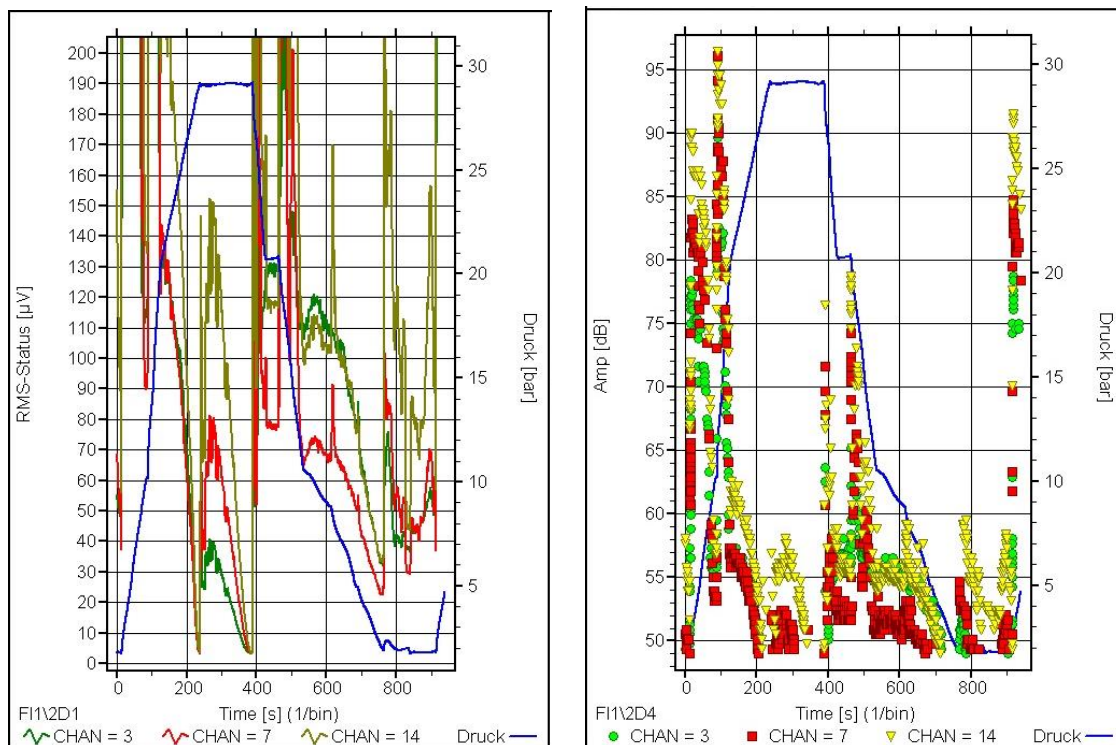


Figure 3: Load cycle of pressure swing absorber in service, pressurisation profile (blue with axis on the right) together with the corresponding acoustic emission noise level RMS (green, red and yellow with axis on the left) and acoustic emission signal peak amplitudes (green, red and yellow with axis on the left) for several sensors at different positions 3, 7, 14 at the shell of the pressure equipment

A first application for this Acoustic Monitoring was done during an EC funded project for detection of corrosion and fatigue cracks in transport products (ships, trucks and railway cars) [5]. The project showed a guideline, how this methodology could be inserted into the maintenance strategy of a structure. Although we tried to create a generic solution, each of these transport products has to be checked separately. As a basis for further work, we checked in the lab, that the material emits AE under the service condition and/or load (Fig. 4). Because we were sure that the structure will be harmed by corrosion and fatigue cracks we had to simulate the possible corrosive environment and also to put the material under cyclic load (type and frequency). The tests are also necessary to establish the evaluation methodology, digital filtering plus application of a frequency domain pattern recognition programme. Furthermore it has to be decided if you are able to monitor the complete structure or only some specific points. We decided, that we will monitor only hot spots, obvious decision in the case of a ship that can be 300 meter long or even more. But also transportation vessels/tanks of trucks and railway cars shall be checked on specific parts especially from an economic point of view. The hot spots could be defined on FE calculation or for very complex structures, like ships, based on experience with information gathered from the classification society. After the decision where these hot spots are the specific structures, without and with natural or artificial flaws, have to be tested under normal service conditions (Fig. 5 and 6). These tests define a milestone, where you have to check a sufficient signal to noise ratio and/or check also the specific evaluation methodology, which was developed during the lab tests. If the system works the most important task is to evaluate the borders for alarm and/or stop (go out of service). These values have to be ascertained and proven with other conventional NDT methods.

A further important task for any monitoring in practice and especially for transportation products is the AE equipment, which besides its feasibility to perform the AE detection and evaluation,

has to be certified according to the safety norms for the tested structure (intrinsically safe, explosion etc.).



Figure 4: Corroded sample of a lab tests, representing deck-plates with stiffeners



Figure 5: Oil tanker for AE monitoring (background and natural defects)

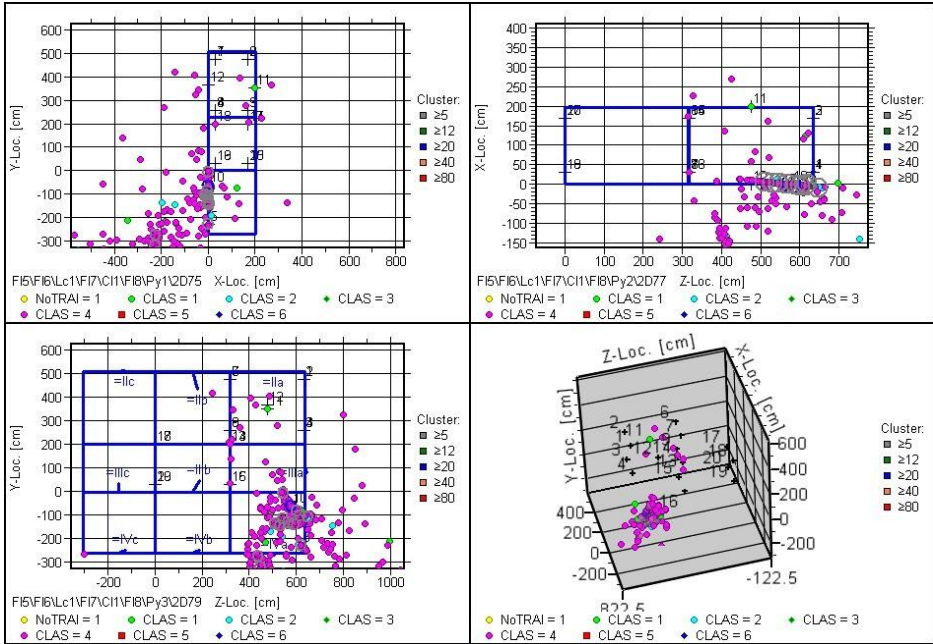


Figure 6: Corrosion in a water ballast tank

6. Conclusions

Acoustic Emission is a physical phenomenon whereby transient elastic waves are generated within material or by a process. The application of load or harsh environment in a material produces internal modifications such as local plastic deformation, crack growth, corrosion, erosion and phase transformations. AE sources also arise from impact, leakage (turbulent flow), cavitations, electric discharge and friction. All these mechanisms and processes are generally accompanied by the generation of elastic waves that propagate in materials or into ambient liquids. The waves therefore contain information on the internal behaviour of the material and/or structure.

AE is therefore an excellent tool to monitor initial proof or acceptance of pressure test equipment during the hydro-test or to perform requalification tests after defined service periods during loading of the structure with its storage products, mainly gas pressure tests. The AE could be a testing method for the health monitoring of structures during in-service conditions.

With the application of AE as a monitoring technique the following advantages and features of the method can be underlined:

- It is an integral, passive and non-invasive testing method;
- It allows the on-line monitoring during service independent from the storage medium;
- It allows detection of AE sources, coming from degradation and leakage under specific conditions;
- It offers the reduction of inside inspections and reduces the follow up NDT to areas of AE.

The main difference between AE and most NDT methods is that it is the material itself which releases the energy in consequence of structural degradation due to different source mechanism. This is different to detecting and measuring existing geometrical discontinuities in a static condition. These all together makes AE to an ideal tool for monitoring structures and verifying their integrity under normal service condition.

The biggest limitation for the method is its sensitivity to in-service or extraneous noise. Therefore it is necessary to check the presence of potential noise sources before performing any AE monitoring. Because it is normally not possible to remove the noise source, the applicability of AE has to be checked before any kind of application as a monitoring technique during in-service conditions.

7. References

- [1] Tscheliesnig P.: Thirty years experience of industrial applications of Acoustic Emission Testing (AT) at TÜV Austria, Proceedings of the 6th International Conference on Acoustic Emission, AEWG, Lake Tahoe (USA), 2007
- [2] Lackner G., Hecht A.: Prüfkonzept für Beschaffung und Betrieb von Druckwechseladsorber unter Einbeziehung der Schallemissionsprüfung, Proceedings of the DACH Jahrestagung, German Society for NDT, St. Gallen (CH), 2008
- [3] Tscheliesnig P., Lackner G.: Maintenance driven by Acoustic Emission Monitoring, Proceedings of the CM 2009, BINT, Dublin (Ireland), 2009
- [4] Christian Boller, "Structural Health Monitoring (SHM) als Werkzeug des Lebensdauermanagements", held at 11- Annual conference of the ÖGfZP; Linz (Austria), March 2009
- [5] Tscheliesnig P.: AE-monitoring for Surface Transport Products (Ships, Trucks and Railway Cars), Proceedings of the 6th European Workshop on Structural Health Monitoring, German Society for NDT, Dresden (D), 2012

THE NEW HIGHER ORDER SPECTRAL TECHNIQUES FOR NON-LINEARITY MONITORING OF STRUCTURES AND MACHINERY

L. Gelman

Cranfield University, UK

ABSTRACT

The new higher order spectral techniques, the normalized cross-covariances of complex spectral components, are proposed for monitoring structure and machinery non-linearity and signal non-Gaussianity and estimating the harmonic phase coupling of signals from structures and machines. Normalization of the proposed techniques is also developed. It is shown by simulation that the proposed techniques provide effectiveness gain for detection of non-linearity in comparison with the HOS.

1. Introduction

For monitoring of a structure and a machinery non-linearity and non-Gaussianity of signals from a structure and a machinery due to damage and estimating the harmonic phase coupling of signals from a structure and machinery, an input excitation (e. g. vibration excitation, acoustical excitation, etc.) excites the resonance oscillations of a structure or a machinery in question and resonance oscillations are processed by the higher order spectra (HOS) [1]. This approach has been widely investigated for stationary and non-stationary signals [1-13].

For diagnosing structure/machinery nonlinearity, we propose to use the normalised cross-covariances of order n between n complex spectral components. The physical sense of this proposition is that if complex spectral components have appeared due to nonlinearity (damage), these components have non-zero cross covariances.

It can be easily shown that the widely used normalized HOS: i.e. the bicoherence and the skewness for the HOS of order 3 and the kurtosis and the tricoherence for the HOS of order 4, do not present the exact normalized cross-covariances between three and four complex spectral components respectively. It also can be shown that in the general case, the normalised HOS of order n also do not present the exact normalized cross-covariances between n complex spectral components.

Therefore, the normalised cross-covariances between three, four and n complex spectral components cannot be estimated by these traditional normalized HOS.

Thus, the main novelty of this paper is the proposed new higher order spectral techniques that are the normalized cross-covariances between n complex spectral components.

The purposes of this paper are to:

- propose the new higher order spectral techniques for structure and machinery health monitoring: the normalized cross-covariances of n complex spectral components
- compare by simulation the proposed techniques with the normalized HOS

2. The new higher order spectral cross-covariances

The novel condition monitoring techniques are proposed here: the higher order spectral techniques, the normalized cross-covariance of n complex spectral components. For estimating the proposed techniques, the following steps should be undertaken: the time domain signal should be divided into overlapping segments by the internal time window, $m=1\dots M$, M defines the total number of overlapping segments in the signals.

The generic expression of the proposed cross-covariances of order n based on the Fourier transform is as follows:

$$ncov(f_1, f_2, \dots, f_{n-1}) = \frac{1}{M} \sum_{m=1}^M \{ [\prod_{j=1}^{n-1} X_m(f_j) - \bar{X}(f_j)] \cdot [X_m(f_{n\Sigma}) - \bar{X}(f_{n\Sigma})]^* \} \quad (1)$$

where $X_m(f_j)$ is the Fourier transform at frequency f_j at segment duration Δt_m of a signal, $j=1, n-1$, $f_{n\Sigma}$ is the accumulated frequency, $f_{n\Sigma} = \sum_{j=1}^{n-1} f_j$, $*$ is a symbol of the complex conjugate, $\bar{X}(f_j)$ is the mean value of variable $X(f_j)$.

The proposed cross-covariances (1) are complex valued, estimated by the Fourier transforms of a signal at n frequencies and depend on $(n-1)$ frequencies. Only in the particular case of the zero-mean complex spectral components, the functions (1) for order n , 3 and 4 are the classical unnormalized HOS of order n , the classical bispectrum and the classical trispectrum respectively. In the general case of the non-zero-mean complex spectral components, the proposed functions of order 3 and 4 are not the bispectrum and the trispectrum. The physical significance of the proposed functions is that they provide a measure of cross-covariances between n complex spectral components.

It is known from the classical statistical analysis that the cross-covariances should be normalised in order to avoid the misleading interpretation.

The standard normalization of the cross-covariances is employed here as follows for order n , 3 and 4 respectively:

$$C(f_1, f_2, \dots, f_{n-1}) = \frac{ncov(f_1, f_2, \dots, f_{n-1})}{\sqrt{[\prod_{j=1}^{n-1} var(X(f_j))] var(X(f_{n\Sigma}))}} \quad (2)$$

$$tcor(f_1, f_2) = \frac{\frac{1}{M} \sum_{m=1}^M \{ X_m(f_1) - \bar{X}(f_1) \} \cdot \{ X_m(f_2) - \bar{X}(f_2) \} \cdot \{ X_m(f_1+f_2) - \bar{X}(f_1+f_2) \}^*}{\sqrt{var[X(f_1)] var[X(f_2)] var[X(f_1+f_2)]}} \quad (3)$$

$$fcor(f_1, f_2, f_3) = \frac{\frac{1}{M} \sum_{m=1}^M \{ X_m(f_1) - \bar{X}(f_1) \} \cdot \{ X_m(f_2) - \bar{X}(f_2) \} \cdot \{ X_m(f_3) - \bar{X}(f_3) \} \cdot \{ X_m(f_1+f_2+f_3) - \bar{X}(f_1+f_2+f_3) \}^*}{\sqrt{var[X(f_1)] var[X(f_2)] var[X(f_3)] var[X(f_1+f_2+f_3)]}} \quad (4)$$

where var is the symbol of the variance.

In the general case of order n , the proposed normalised cross-covariances (2) differ from the traditional normalised HOS of order n . It can be also seen from expressions (3-4), that for orders 3 and 4, the normalised triple and fourth covariances differs from the traditional normalized HOS, the bicoherence and skewness and the tricoherence and kurtosis respectively. This difference remains even for the zero-mean spectral components.

The normalisations of the proposed cross-covariances allow avoidance of the misleading interpretation of the proposed techniques (1) due to variations of the power spectral density of a signal.

The proposed techniques can be also used for non-stationary signals by employing the appropriate time-frequency transforms (e. g. the chirp-Wigner transform [14], the short time chirp-Fourier transform [15] etc.). This can be done by substituting the appropriate time-frequency transforms for the Fourier transform in equations (1-4).

To demonstrate that the proposed techniques can effectively detect structure non-linearity due to damage and to compare them with the traditional HOS, a simulation test with linear and non-linear (bilinear) structures was performed.

An input random cosine excitation with constant amplitude, random initial phase and linearly changed instantaneous frequency in time (i. e. the chirp signal) has been passed via the following nonlinear (bilinear) system:

$$\begin{cases} \ddot{x} + 2h\dot{x} + \omega_s^2 x = A \cos \Omega(t), & x \geq 0, \\ \ddot{x} + 2h\dot{x} + \omega_c^2 x = A \cos \Omega(t), & x < 0, \end{cases} \quad (5)$$

where $x = \frac{X}{m}$, X is the displacement, $h = \frac{c}{2m}$, h is damping; $\omega_s = \sqrt{\frac{k_s}{m}}$, $\omega_c = \sqrt{\frac{k_c}{m}}$, m and

c are the mass and damping coefficient respectively, k_s and k_c are the stiffness for positive

displacement and stiffness for negative displacement respectively, $A = \frac{A_1}{m}$, A_1 is the constant

amplitude of the input signal, $\Omega(t) = \int \omega(t) dt$, $\Omega(t)$ is the instantaneous phase, $\omega(t)$ is the linearly changed angular frequency.

The initial phase of the each simulated signal has been taken randomly and is uniformly distributed in the range $[0; 2\pi]$.

The output signal of the bilinear structure is transient, with variable instantaneous frequency; therefore, the normalised spectral cross-covariance of order 3 based on the chirp-Fourier transform [15] is employed for non-linearity detection.

The non-stationary random cosine vibration excitation excited the resonance oscillations of a structure. 300 signals from the linear structure and 300 signals from the bilinear structure were tested for non-linearity detection. The resonance frequencies of the linear and bilinear structures are 14.1 Hz and 13.9 Hz respectively, the chirp rate is 0.15Hz/s, the stiffness ratio is 0.05.

The proposed normalised cross-covariances of order 3 and the bicoherence based on the chirp-Fourier transform of the structure resonance oscillations have been employed for detecting additional level of structure nonlinearity. The cross-covariances and the bicoherence at the fundamental and second harmonics have been employed.

The following parameters have been used for estimating the cross-covariances and the bicoherence: the frequency resolution is 3.7Hz (i.e. segment size is 0.27s), duration of signals is 5s, segment overlapping is 60%, the internal time domain window is the Hamming window, the sampling frequency is 3600Hz.

The Fisher criteria [16] for detection effectiveness are 373 and 260 for the proposed technique and the bicoherence. It is known [16] that features with higher values of the Fisher criterion provide better detection effectiveness.

Thus, the proposed technique provides effectiveness gain 1.43 times in comparison with the HOS and, therefore, is more effective for non-linearity detection.

3. Conclusions

1. The new higher order spectral techniques, the normalized cross-covariances of n complex spectral components, are proposed for monitoring structure and machinery non-linearity and signal non-Gaussianity and estimating the harmonic phase coupling of signals from structures and machines. Normalization of the proposed techniques is also developed.
2. The proposed techniques differ from the classical higher order spectral techniques. The proposed un-normalised spectral cross-covariances coincide with the classical un-normalised higher order spectra only for the particular case of the zero mean spectral components. The normalised spectral cross-covariances differ from the classical higher order spectral techniques even for the particular case of the zero mean spectral components.
3. It is shown by simulation that the proposed techniques provide effectiveness gain 1.43 times for detection of non-linearity in comparison with the HOS.
4. The proposed techniques could be extended for monitoring of structure and machinery non-linearity and signal non-Gaussianity due to damage and estimating the harmonic phase coupling of signals from structures and machines for non-stationary signals by employing the appropriate time-frequency transforms in equations (1-4).

The proposed techniques could be used in mechanical and electrical engineering, telecommunication, underwater acoustics, etc.

4. Acknowledgement

The author is very thankful to MSc student A. Stepien (Cranfield University) for carrying out a simulation and processing of the simulated data.

5. References

1. Fackrell J. W, White P. R, Hammond J. K, Pinnington R. J. The interpretation of the bispectra of vibration signals. *Mechanical Systems and Signal Processing* 1995; 9(3): 267-274.
2. Kim Y. C, Powers E. J. Digital bispectral analysis and its applications to non-linear wave interactions. *IEEE Transactions on Plasma Science* 1979; 7 (2): 120-131.
3. Collis W. B, White P. R, Hammond J. K. High order spectra: the bispectrum and trispectrum. *Mechanical Systems and Signal Processing* 1998; 12 (3): 375-394.
4. Schreier P. J, Scharf L. L. Higher-order spectral analysis of complex signals. *Signal Processing* 2006; 86 (11): 3321-3333.
5. Mendel J. M. Tutorial on higher-order statistics (spectra) in signal processing and system theory: theoretical results and some applications. *Proc. of the IEEE* 1991; 79 (3): 278-305.
6. Nikias C. L, Mendel J. M. Signal processing with higher-order spectra. *IEEE Signal Processing Magazine* 1993; 10 (3): 10-38.
7. McCormick A. C, Nandi A. K. Bispectral and trispectral features for machine condition diagnosis. *IEE Proc. of the Vision, Image and Signal Processing* 1999; 146 (5): 229-234.
8. Gelman L, Petrunin I. The new multidimensional time/multi-frequency transform for higher order spectral analysis. *Multidimensional Systems and Signal Processing* 2007; 18 (4): 317-325.

9. Hanssen A, Scharf L. A theory of polyspectra for nonstationary stochastic processes. *IEEE Transactions on Signal Processing* 2003; 51 (5): 1243-1252.
10. Rivola A., White P., Detecting system non-linearities by means of higher order statistics. *Proceedings of the 3rd International Conference on Acoustical and Vibratory Surveillance Methods and Diagnostic Techniques*, 13-15/10/1998, Senlis, France, vol. 1: 263-272.
11. Gelman L., White P., Hammond J., Fatigue crack diagnostics: A comparison of the use of the complex bicoherence and its magnitude. *Mechanical Systems and Signal Processing*, 19(4), 2005: 913–918.
12. Hillis A., Neild S, Drinkwater B, Wilcox P., Global crack detection using bispectral analysis, *Proc. Royal Soc. A* 8, 2006, 462 (2069): 1515-1530.
13. Hickey D., Worden, K., Platten M., Wright, J., Cooper, J. Higher-order spectra for identification of nonlinear modal coupling, *Mechanical Systems and Signal Processing*, 23 (4), 2009: 1037-1061.
14. Gelman L., Adaptive time-frequency transform for non-stationary signals with nonlinear polynomial frequency variation”, *Mechanical Systems and Signal Processing*, 21(6), 2007: 2684-2687.
15. Gelman L., Ottley M., (2006) New processing techniques for transient signals with nonlinear variation of the instantaneous frequency in time”, *Mechanical Systems and Signal Processing*, 20 (5), 2006, pp.1254-1262.
16. Young T, K.-S Fu K-S., *Handbook of pattern recognition and image processing*. New York, Academic, 1986.

ASSESSMENT OF INFRASTRUCTURES BY MEANS OF PASSIVE AND POSITIVE ELASTIC WAVES APPROACHES

Tomoki Shiotani¹, Yoshikazu Kobayashi² and Shohei Momoki³

¹Graduate School of Engineering/ Graduate School of Business, Kyoto University
C-Cluster, Katsura Campus, Nishikyo-Ku, Kyoto 615-8540, Japan
shiotani.tomoki.2v@kyoto-u.ac.jp

²College of Science and Technology, Department of Civil Engineering, Nihon University
1-8-14, Kanda-Surugadai, Chiyoda-ku, Tokyo 101-8308, Japan
kobayashi.yoshikazu@nihon-u.ac.jp

³Research Institute of Technology, Tobishima Corporation
5472 Kimagase, Noda, Chiba 270-0222, Japan
shouhei_momoki@tobishima.co.jp

ABSTRACT

In matured countries for infrastructures, the assessment of current condition of infrastructures is in urgent demand. As a whole of infrastructures are not always maintained in the same level, each inspection techniques corresponding to the damage scale of interest shall be established. Elastic waves' approaches such as ultrasonic wave and acoustic emission have great potential to assess those wide range of damage as to adjust the adapting frequencies; however, they are yet to be generalized as there is a discrepancy between the laboratory studies and on-site applications. For example, damage areas could be extracted based on the active part of acoustic emission, and an index to quantify the integrity of the infrastructure could be determined from an elastic wave feature. For the former, however, as the monitoring procedure as well as the method of load-application have not been systematically studied, ultrasonic tomography has been well conducted supplementarily. For the latter, although such elastic wave features as wave velocities and frequencies have been applied to define the damage, no decisive parameter has yet to been generalized. In the paper, conventional damage-associated elastic wave parameters have been reviewed and new index to assess the damage has been proposed. The index, namely Q-value has been experimentally studied with specimens including a variety of artificial damages. And as for the approach to extract the damage-prone areas, an ideal and effective method, AE tomography, combining AE monitoring with elastic wave tomography is detailed through the calculation algorithm, followed by in-situ applications.

Key words: Infrastructures, damage assessment, ultrasonic waves, acoustic emission (AE), AE tomography, Q-value.

1. Introduction

There can be no doubt that infrastructures shall be maintained properly through their service life. For the proper maintenance, however, the strategic procedure not only for the detection of damage but also the effective repair method has not been established. The conventional way to maintain the infrastructure is referred to as 'reactive maintenance,' where repair or replacement have been carried out when the damage becomes remarkable. This concept is effective when sufficient amount of investment can be secured, while for the current situation of the country where a lot of infra-structures have been constructed and there a limited budget expected due to shortage of taxation, the existent infrastructure shall be maintained from their initial tiny-damage expecting to minimal investment. This idea as to maintain the infrastructure from the initial damage with minimal investment is referred to as 'proactive maintenance,' assuming the potential to assess the damage from the initial level. At present, nevertheless, there are no decisive technique to evaluate the initial damage in especial where the damage evolves from internal area of the infrastructure. Acoustic emission has potential to detect internal damage in progress as it uses elastic waves, namely AE waves generated due to cracking. As for the existent damage, where no progressive damage was anticipated, ultrasonic techniques transmitting and receiving ultrasonic waves might be applicable. In these circumstances the authors have been studying both of passive acoustic emission (AE) and active ultrasonic (UT) tomography technique and proved the usefulness to combine the AE and UT tomography to qualify and following identification of the damage for the laboratory specimen [1] and in-situ concrete bridge deck [2]. In addition to these strategic monitoring procedures, the quantification of damage is other crucial issue to assess the infrastructure. Ultrasonic wave velocities have been studied to relate the quality as well as the strength of the concrete [e.g., 3, 4]; however, the velocities are not intrinsic values that do not only depend on the quality of concrete but highly influenced by the frequency excited and eventually propagated distances [5, 6, 7].

2. Conventional damage related elastic wave parameters

2.1 Velocities

To simulate several amount of damage, a vinyl inclusion of 15 x 15 x 0.5 mm was prepared, and the cubic specimen with side of 150 mm included in contents of 1%, 5% and 10% of inclusions were each made [8]. P-wave velocities through the specimens can be found in Fig. 1. The pulse velocity of material with 10% inclusions is decreased by only 3% compared to plain mortar, while the material with 1% inclusions exhibits practically the same velocity with plain mortar, namely 4,000 m/s. It is mentioned that the typical error associated with the digitization sampling rate is 10 m/s, while the values are the average of 10 different measurements on each specimen. As a result, the above velocity differences between different materials (within 120 m/s) would not reveal mentionable quality discrepancies.

A feature that takes into account the later arrivals of a waveform is ‘group’ velocity. In general, group velocity is a measure of the velocity with which the major part of energy propagates. The calculated values of group velocity are depicted again in Fig. 1 for different inclusion contents. This parameter is much more sensitive to damage since the group velocity of material with 10% vinyl is decreased by 70% compared to the sound material’s one, while even material with 1% inclusions exhibits group velocity slightly decreased compared to the plain mortar.

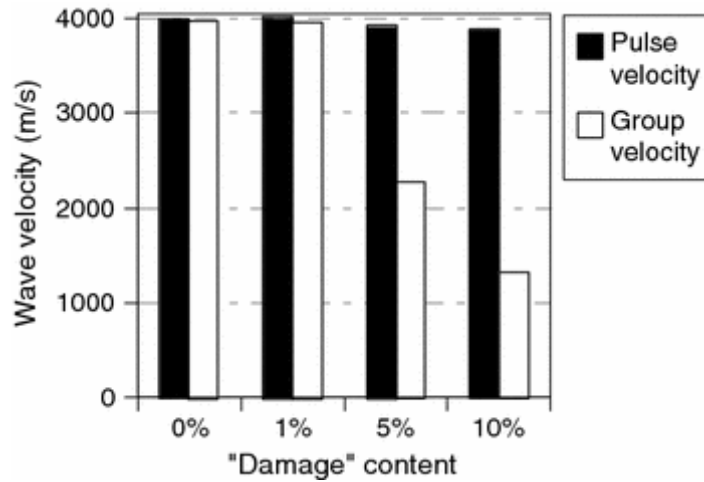


Fig. 1: Wave velocities with damage contents.

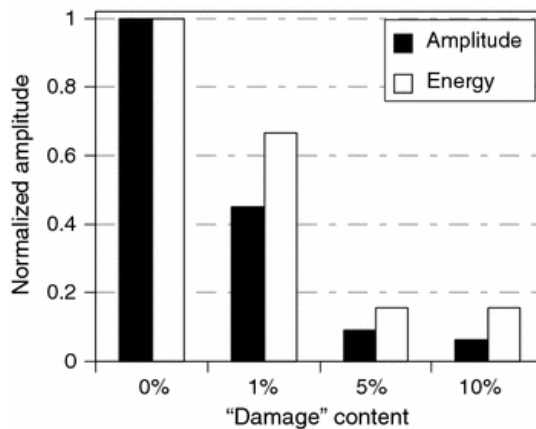


Fig. 2: Normalized amplitude with damage contents.

2.2 Energy

Energy parameters are more sensitive to damage than pulse velocity [9, 10]. To quantify the difference, the absolute amplitude of the waveform was used as well as the total energy, calculated by the area under the rectified signal envelope. The results are presented in Fig. 2. Both energy and amplitude decrease significantly with the inclusion content, even for the case of 1% inclusions. This loss of energy is mainly attributed to the combination of the following two reasons. One is the redirection of energy components that never reach the receiver and the other is the material damping that depends on the length of the wave path. Thus, its influence is

smaller for the shortest path (typical for propagation in homogeneous material) and higher for longer paths (in scattering media).

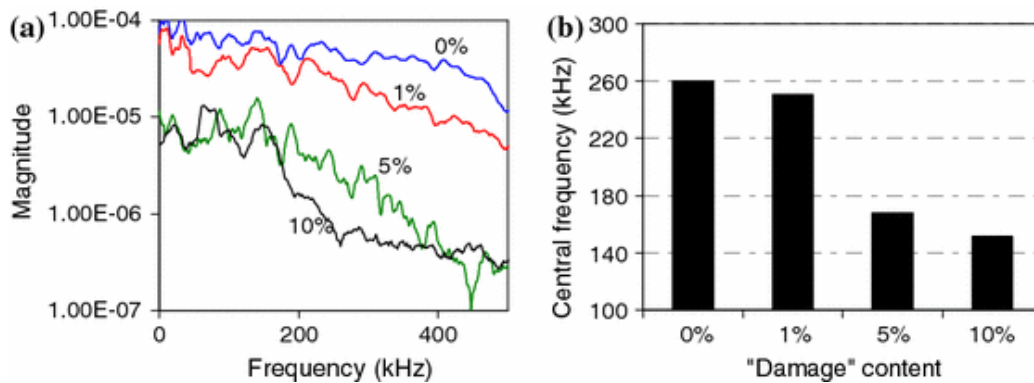


Fig. 3: Frequency features with damage contents.

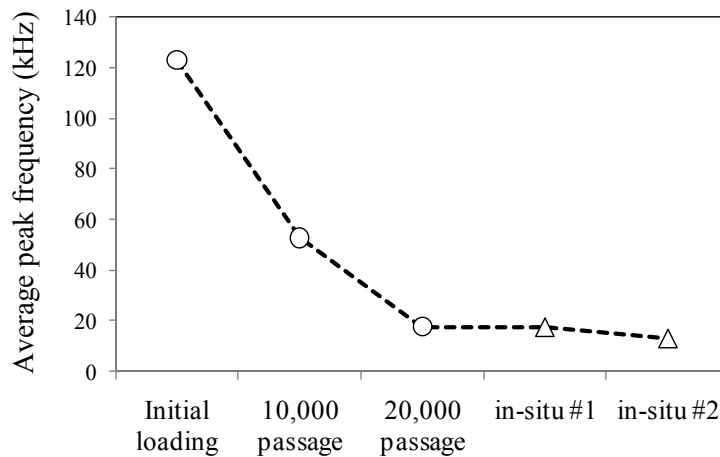


Fig. 4: AE peak frequency with progress of fatigue damage.

2.3 Frequencies

The inclusions could influence individual wavelengths in a different way. Therefore, except time domain, valuable information can be obtained by simple analysis in the frequency domain. In Fig. 3a, the fast Fourier transform (FFT) of typical signals from plain mortar and mortar with inclusions are depicted. The energy difference is evident. The other important feature is the downshift of the spectrum. The content at higher frequencies (e.g., above 200 kHz) is diminished more intensively than lower ones, as seen in Fig. 3a. The central frequency of 260 kHz for plain mortar decreases to 150 kHz for “damaged” mortar showing that this is another feature that can enhance the inhomogeneity characterization.

The frequency features of AE have also effective to assess the fatigue damage [11]. When dealing with the secondary AE activity obtained mainly from identical types of source, namely friction between existent crack interfaces, the frequency components of detected AE waveforms are worth studying. In this examination several levels of fatigue had been introduced by repetition of iron-wheel loads. Details can be found in the literature [11]. Figure 4 shows the

average of peak frequencies of detected AE waveforms in each case. Undoubtedly the peak frequency of AE events decreases with damage progress, and it was confirmed that the peak frequency of measured AE signals could be a clue to provide the degree of fatigue damage. In Fig. 4, the AE events obtained from in-situ specimens where serious lateral cracking had been confirmed are added as for the reference. Low average frequencies were obtained from both of the in-situ specimens. The average peak frequencies in the in-situ cases are equal to or even less than the value of 20,000, suggesting the in-situ specimens were damaged as equivalent or more to the case of 20,000 passage.

3. Q-value, new approach for assessing damage with transfer function of AE waveforms

As shown previously the frequency characteristics of AE waves could imply the damage condition of infrastructures. In this case, exact quantitative evaluation for the damage is only possible in case where every AE waves travelled in the compatible distance. As the frequency characteristics of AE waves are also known that they depend on the resultant propagation distance, obtained frequency does not always demonstrate the damage condition, providing the rough evaluation [12]. Thus transfer functions of propagation media are described here to quantify the damage with AE waveforms [13].

3.1 Conceptual configuration

AE waveforms are obtained as convolution of functions of source, propagation media, sensor and acquisition system in the time domain, and those frequency responses can be formulated by a simple multiple equation in the frequency domain:

$$X(f) = U(f)T(f)D(f)S(f) \quad (1)$$

Here $X(f)$, $S(f)$, $D(f)$, $T(f)$, $U(f)$ are Fourier transforms of detected AE waveforms, AE source, propagation media, sensor and acquisition system, respectively. $D(f)$ in Eq. 1 is the target to quantify the damage; however, as $S(f)$ is not readily obtained in AE technique, an approach to identify $D(f)$, being irrespective to source time function is crucial. In AE application, plural numbers of sensors are employed to locate the AE source, and therefore the comparison of waveforms detected among different sensors for an AE source could suffice this requirement as in Eq. 2 assuming the frequency responses of all the sensors employed are compatible.

$$\frac{X_2(f)}{X_1(f)} = \frac{T_2(f)}{T_1(f)} \cdot \frac{D_2(f)}{D_1(f)} \cong \frac{D_2(f)}{D_1(f)} \quad (2)$$

On the other hand, as $D(f)$ is dependent on propagation media attenuation, Eq. 3 can be defined as well, where f is a frequency (Hz), V is a P-wave velocity (m/s) and Q is a normalized value demonstrating attenuation rate.

$$D(f) = \exp\left(-\frac{\pi f}{VQ} d\right) \quad (3)$$

By combining Eq. 2 and Eq. 3, Eq. 4 is obtained.

$$\frac{X_i(f)}{X_1(f)} \cong \frac{D_i(f)}{D_1(f)} = \exp\left(-\frac{\pi f}{VQ} \Delta d_i\right) \quad (4)$$

$$\Delta d_i = d_i - d_1 \quad (d_i \geq d), \quad (i = 2, \dots, n)$$

Equation 4 shows that a function of frequency response can be expressed by an exponential function depending on the difference of distance Δd and frequency f .

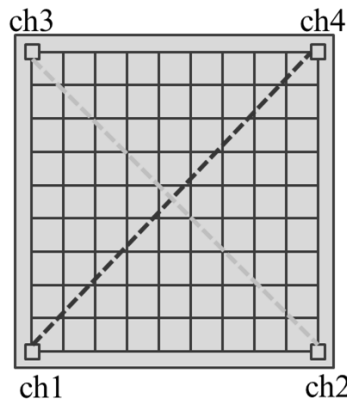


Fig. 5: Concrete specimen for ultrasonic measurements.

3.2 Preliminary examination

As shown in Fig. 5, concrete specimen of 500 x 500 x 100 mm was prepared placing four AE sensor of 60-kHz resonance at the four corners on the bottom surface. Ultrasonic wave excitation was made using the wideband AE sensor (1045S, Fuji Ceramics), where electric pulse was made by PUNDIT (-500 kHz, CNS Electronics).

To examine the potential influence of heterogeneity of the concrete specimen on the transfer function in the intact specimen, excitations at the intersectional points in the line between Ch1 and Ch4 sensors were conducted with Ch2 and Ch3 operated as receivers. Switching of sensor pairs was also used. Figure 6 shows the ratio of Ch1 to Ch4 in frequency response when the excitations were made along the line between Ch2 and Ch3. As many excitation points were employed, three lines for the mean value μ and $\mu \pm$ standard deviations σ were drawn. Two important facts can be found: even for intact condition the frequency response showed

difference from the point measured, and the frequency response needs to be discussed in the range of effective frequency response of the sensor employed, i.e., this case the range of 60 to 180 kHz.

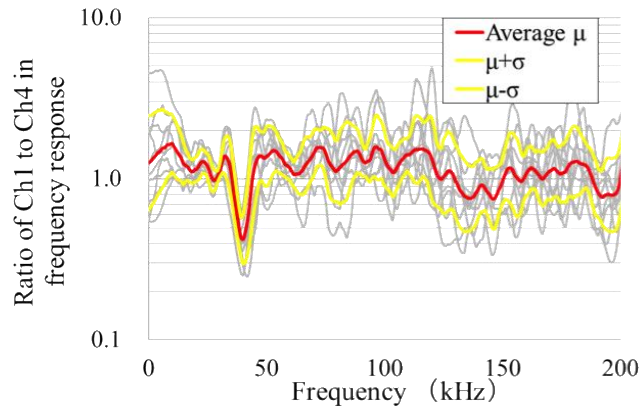


Fig. 6: Ratios of Ch1 to Ch4 in frequency response.

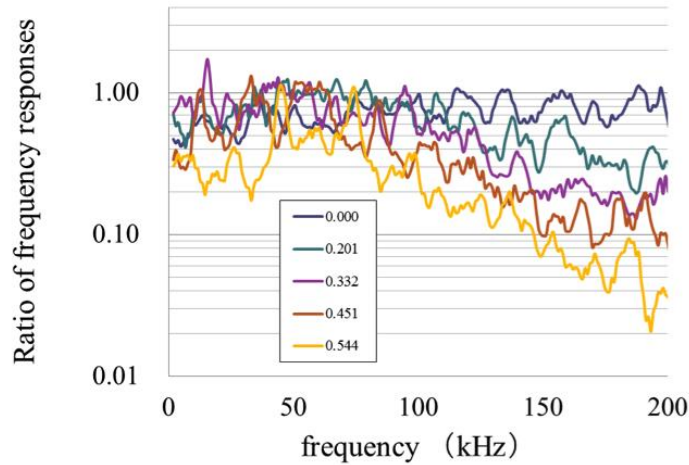


Fig. 7: Ratios of frequency responses for the differences of propagation distances.

To verify the frequency response corresponding to the propagation distance, other intersectional points than above were used to excite the signal. The ratios of frequency responses for the differences of propagation distances can be found in Fig. 7. The legends of the figure show the difference of propagation distances. The decrease rate for higher frequency above 100 kHz becomes more remarkable as the difference of propagation distances becomes larger. As this trend had a good accordance with Eq. 4, the slope of the ratios, α in Fig. 7 were calculated by the approximation, where the slope can be defined as Eq. 5.

$$\alpha = \frac{\pi \Delta d}{V Q} \quad (5)$$

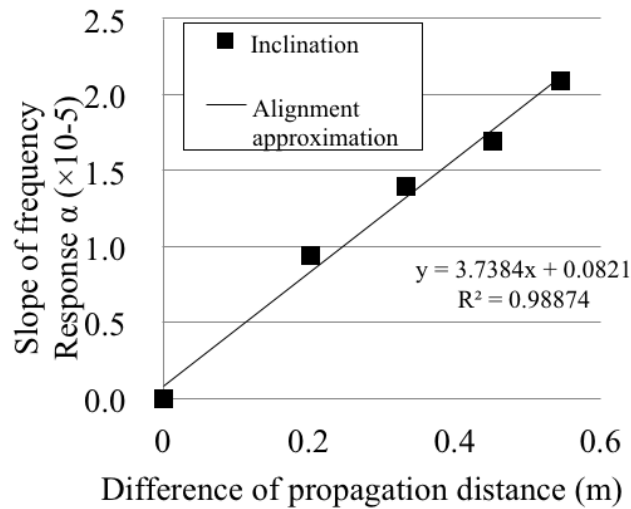


Fig. 8: Relation between the slope α and differences of propagation distances.

Figure 8 shows the relation between the slope α and differences of propagation distances. Surprisingly the relation can be well approximated by a linear equation, resulting in good agreement with Eq. 4. Of course this slope α correlates well to the difference of propagation distance, but more likely to demonstrate the properties of propagation media. This is the very concept to quantify the damage of the materials with transfer functions using AE waveforms.



Fig. 9: Prism mortar specimens with different height.

3.3 Application to the mortar specimens with several degrees of artificial damage

To verify whether the concept of the ratio of frequency responses is applicable to the damage assessment of concrete, homogeneous standard mortar with formed polystyrene spheres simulating damage was prepared as test specimens. As shown in Fig. 9, the prism mortar specimens have dimensions of 150 x 150 mm with different heights: about 100, 200, 300, 400 and 500 mm. In order to simulate the damage, spherical foamed styrene material (6 mm in diameter) was used as a false cavity, with four types of volumetric percentages as 0%, 1%, 5% and 10%. Two types of elastic wave excitation were made by pencil-lead break and electric pulser (PAC) with a wideband AE sensor (1045S, Fuji Ceramics). Piezoelectric sensors of 60 kHz resonant (R6, PAC) are employed for the receiver. The signals detected by the sensor were amplified by 40 dB at the amplifier, and processed and recorded by AE

monitoring system (SAMOS, PAC) with 1 MHz rate and 1k words samples. The elastic wave was excited at the center on the top surface of the specimen, and received by the sensor installed in the bottom surface.

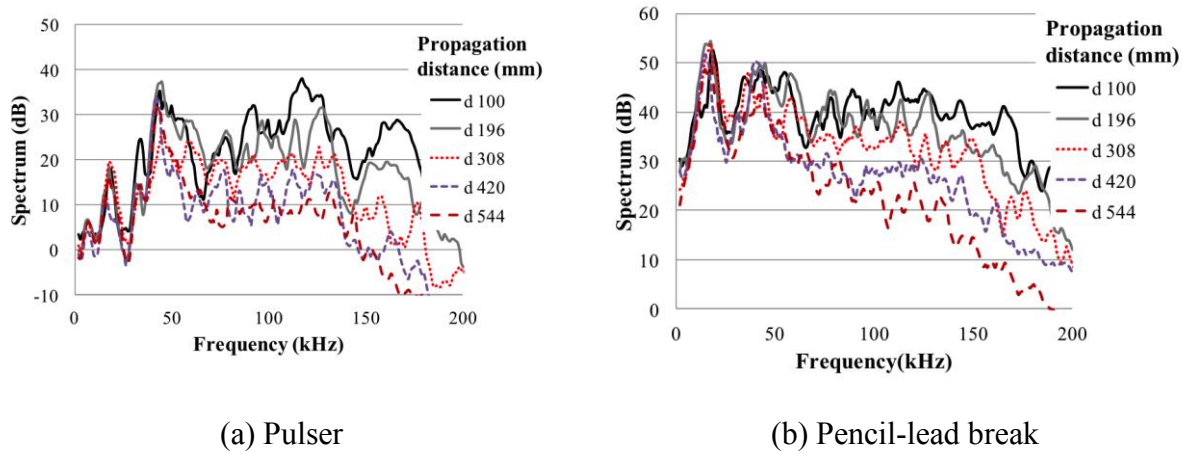
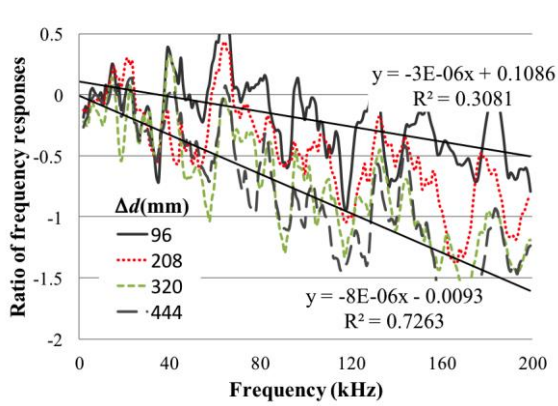
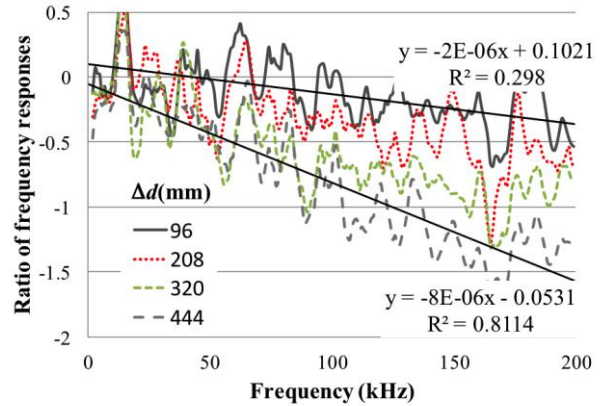


Fig. 10: Frequency distributions with different distances (damage content: 5%).

As a typical case, the result of damage content of 5% is shown as in Fig. 10. Figure 10a shows the frequency distribution for the case of elastic wave excitation by electric pulser, and b shows that by pencil-lead break. The frequency spectra decrease with the increase of propagation distance, and the decrease rate is large as the frequency becomes high. It can be thus obvious that this result accords well to the theoretical formula as shown in Eq. 3 demonstrating the decay with the propagation distance. As for the difference of propagation distances, the attenuation trend as a function of frequency becomes remarkable when the propagation distance becomes longer even in the case of the same degree of damage (5% in this case), suggesting that it is not easy to evaluate degradation only by the frequency related parameters as the frequency centroid and the peak-frequency which are well used to relate damage with elastic waves' parameter. The ratio of frequency spectrum response is determined based on the cases of at least 100-mm propagation distance. Specifically, the ratio of frequency response for the 96-mm propagation is obtained from the spectra of 196-mm and 100-mm propagation distances. Other ratios of the spectral difference of propagation distance for 208 mm, 320 mm and 444 mm are obtained in a similar manner from the frequency spectra of 200-500 mm in propagation distances (or the height of specimens). Calculated results (for 96 mm, 208 mm, 320 mm, and 444 mm) as a function of the frequency can be found in Fig. 26. Two straight lines in the figure show the linear approximation over the frequency between 0 to 200 kHz for the ratio of frequency responses of distance difference 96 mm and 444 mm. In this experiment, as the same type of receiving sensor were used for all the measurement, $T_2(f)/T_1(f)$ in Eq. 2 can be regarded as 1 in all the frequency bands. Because of the heterogeneity of the mortar specimen, the ratio of frequency responses does not form a straight line like a theoretical formula. Therefore, the regression line is used by carrying out linear approximation of the frequency response ratio.

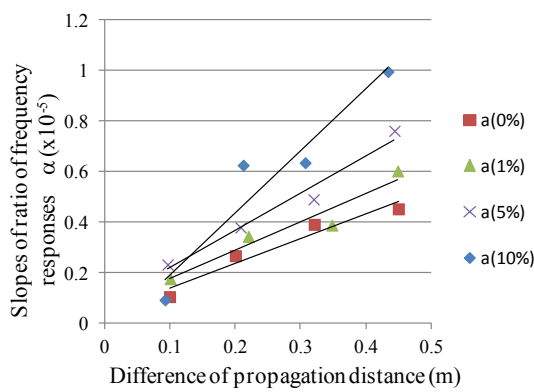


(a) Pulsar

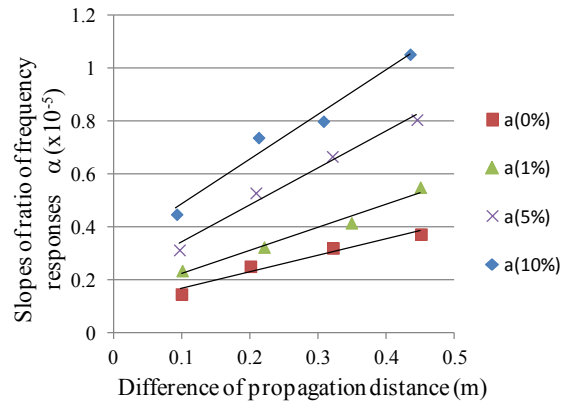


(b) Pencil-lead break

Fig. 11: Ratio of frequency responses with differences of propagations (damage content 5%).



(a) Pulsar



(b) Pencil-lead break

Fig. 12: Relation between slopes of the ratio of frequency responses and difference of propagation distances.

As shown in Fig. 11, the larger the difference of propagation distance, the larger the slopes of the ratio of frequency responses. Here, it was verified experimentally that the theoretical formula, Eq. 4, simulates the practical behavior well. By using the slopes obtained from Fig. 11, the ratio of frequency responses and the relation of a distance difference to each mix rate of damage simulation are shown in Fig. 12. It is found that correlations were uniquely acquired in all damage mixture rate and in both excitations. The frequency slope obviously becomes large with the increase of damage volume.

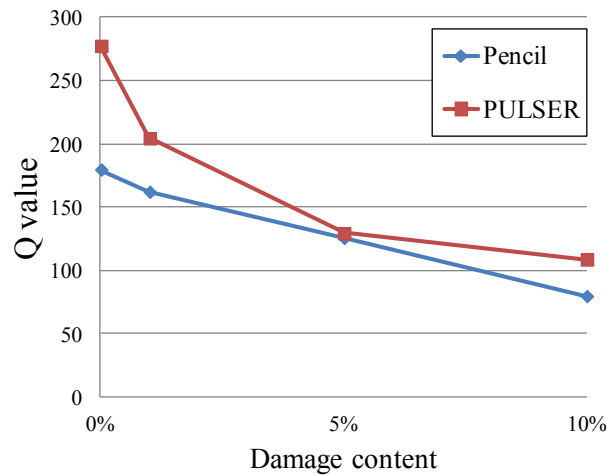


Fig. 13: Q-value with damage contents.

Q-value is also determined by using Eq. 4, substituting P-wave velocity, V , which was obtained by another measurement, and it is shown in Fig. 13. As mentioned previously, the velocity of P-wave shows the dispersion depending on the frequency, e.g., the velocity becomes large to a certain frequency then decreases, and this tendency appears more noticeable when more damage was included [14]. In addition, since Q-value also depends on the frequency, showing the dispersion [15], the value depends on frequency. Q values by two excitation methods (pencil-lead and pulser) were different as shown in Fig. 13; however, the damage could roughly be evaluated by Q-value, e.g., Q-value showing between 170-270 demonstrates intact condition of the material, 130 stands for 5%, and about 100 for 10% damage. The dependency of Q value on the frequency and allowable range of Q-value in regard to damage will be further studied in a subsequent paper.

4. AE tomography

Ultrasonic or seismic wave tomography has been carried out to evaluate integrity of infrastructures for past decades. The conventional ultrasonic wave tomography is a technique to reconstruct wave velocity distribution from travel times among each location of excitations and receivers. In this test, as the travel times must contain the information of source location and excitation time, the excitation shall be made at the designated point with an accurate time of excitation records. While for the AE measurement, AE sources could be identified by arrival time differences among AE sensors assuming a constant velocity in the material of interest. As one can be understood, AE source identification with AE monitoring and velocity reconstruction with tomography are each directly-opposed ideas in terms of the velocity. Pioneering works can be found in some literature [16, 17]. These studies have adopted an assumption that the wave ray-paths among sources and receivers are straight to simplify the computational procedure; however, this approach increases error of identified wave velocity

distribution due to its insufficient representation of the ray-paths. Therefore, the authors have been studying algorithm which can implement the both of wave ray-trace and AE source location. In this paper, newly proposed source location algorithms are demonstrated leaving tomographic procedure to the other literature [18].

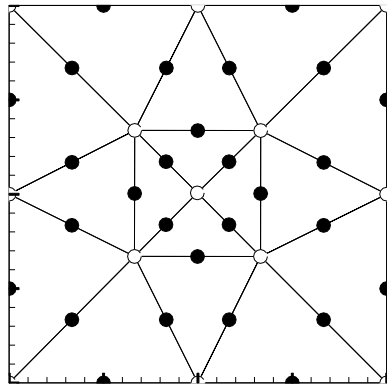


Fig. 14: Conventional set of the relay points.

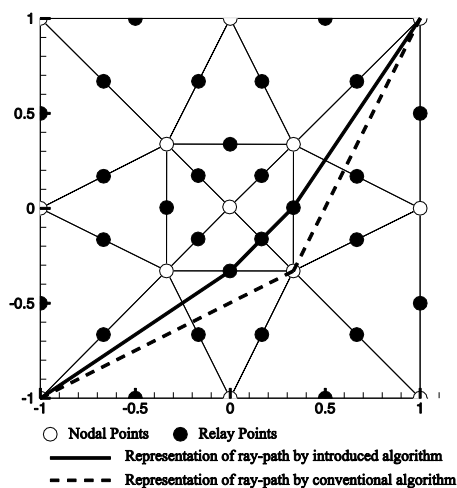


Fig. 15: Revised ray path in consideration of proposed relay points.

4.1 Source location technique

The source location technique is based on ray-trace algorithm [16]. This algorithm is characterized by installation of relay points in each cell as illustrated in Fig. 14. Since ray-paths are formed by segments among nodal points in conventional ray-trace algorithm, its resolution depends on the mesh, implying that high accuracy source location requires fine mesh. This leads to increment of the number of degrees of freedom since slowness, a reciprocal of velocity shall be defined in each cell, and consequently makes the identification procedure more complicated. In this ray-trace algorithm, the relay points between nodes are proposed and a ray-path is formed by segments among nodal and relay points as shown in Fig. 15. The resolution of ray-trace is increased without increment of the degrees of freedom by this approach. Besides as role of the relay points is relaying the signals, the relay points shall be distributed uniformly on the surface.

However, it is difficult due to the heterogeneous shape of cross section of concrete structures. To solve this problem, the relay points are installed by using isoparametric mapping that is used in the ray-trace algorithm. Since the each cell is mapped into isosceles right triangle, the relay points can be uniformly installed in the mapped cell as shown in Fig. 16. This algorithm does not give exactly uniform distribution of relay points if the shape of the cell is skewed; however, the distribution is improved by avoiding use of strongly skewed cells. The source location is estimated by using this ray-trace algorithm.

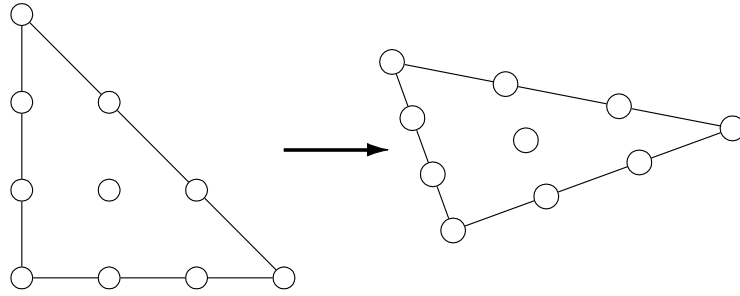


Fig. 16: Mapping to the global coordinate of set relay points.

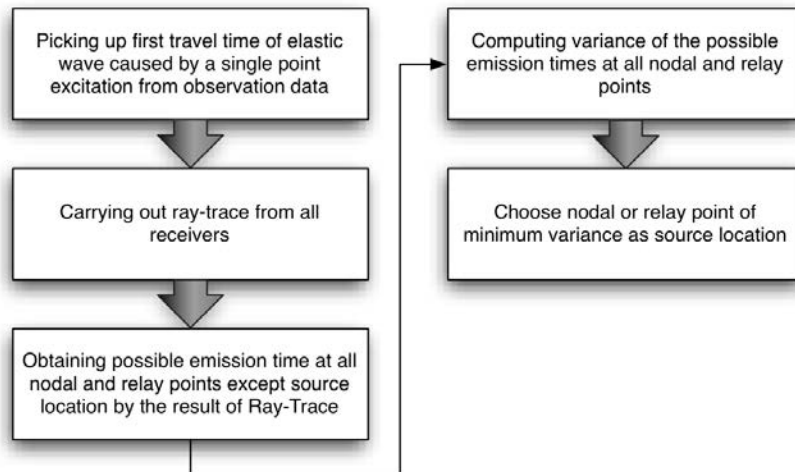


Fig. 17: Procedure to estimate the source locations.

The procedure of the estimation of source location is briefly described as in Fig. 17. As for the first step to estimate the source location, the ray-trace is carried out for a receiver as illustrated in Fig. 18. This procedure calculates travel times t_{ij} from a receiver i to all nodal and relay points that are numbered as j . Since first travel time T_i at receiver i is observed, the possible emission time of the signal E_{ij} is computed as follow at a nodal or relay point j .

$$E_{ij} = T_i - t_{ij} \quad (6)$$

The step is applied for all receivers, and then variance of the the E_{ij} is computed as follow.

$$\sigma_j = \frac{\sum_i (E_{ij} - m_j)^2}{N} \quad (7)$$

in which

$$m_j = \frac{\sum_i E_{ij}}{N} \quad (8)$$

where N is number of receivers. For the estimation of the source location, the variance σ_j is evaluated. If the slowness distribution is exactly identical to real slowness distribution, σ_j must be equal to zero at the source location and m_j must be the emission time. Due to the discretization error of slowness distribution and insufficient resolution of ray-trace, generally σ_j is not zero even at the source location while the identification procedure of seismic tomography. However, it is predicted that σ_j gets minimum at the source location. Hence, in this paper, the source location is determined as a nodal or relay point of minimum variance σ_{jmin} . Additionally m_j is used as possible emission time. It is noted that the accuracy of the estimation of source location is controlled by the density of nodal and relay points because the source location is assigned to a nodal or relay point in the proposed algorithm. Furthermore, by applying this technique to the iterative procedure of identification of wave velocity structure, the source locations are updated in every iterative step, improving the accuracy of the source location. This approach can be applied for not only AE signals, but also signals that are generated by any excitation point.

Fig. 18: Radiation of waveform from a receiver.

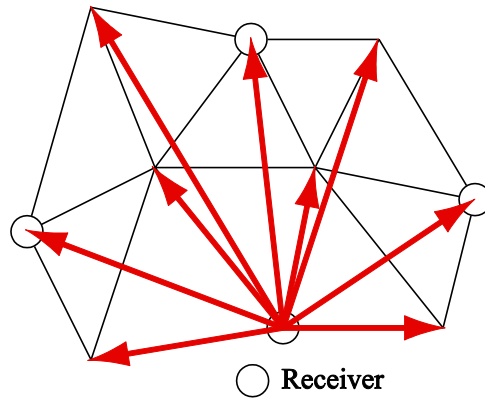
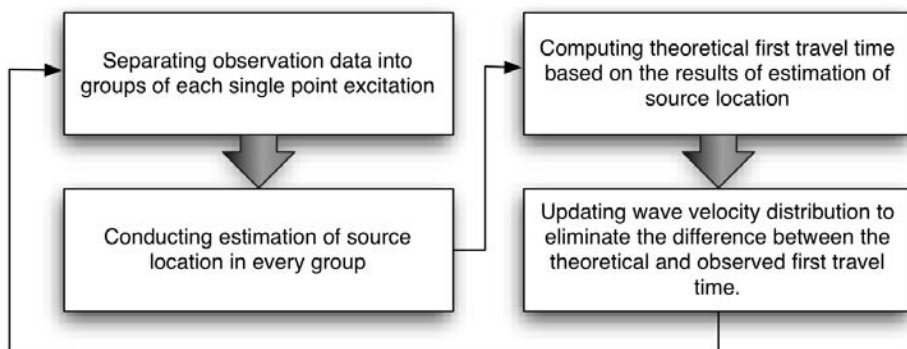


Fig. 19: Procedure of seismic tomography with estimation of source location.



4.2 Seismic tomography with estimation of source location

Seismic tomography requires source location, emission time and observed first travel time of signals. However, the signals having neither emission time nor source location can be used for seismic tomography if the source location and emission time are correctly identified. It is noteworthy that the source location and emission time are estimated from only observed first travel times and presumed wave velocity distribution by the method that was introduced in previous section. Based on these facts, a procedure of seismic tomography with estimation of source location is introduced. Figure 19 illustrates the procedure of seismic tomography with estimation of source location. In seismic tomography with estimation of source location, the first step is estimation of source location and emission time. If the observed first travel times can be separated into groups that are respectively associated with individual excitation points, the estimation of source location and emission time are carried out for each observed first travel time group. The second step is applying the ray-trace to all estimated source location. In this step, the ray-trace is carried out for the all of estimated source location, and travel time among the estimated source location to the other nodal or relay points are figured out. Finally by adding the computed travel time to the estimated emission time, the theoretical first travel times at receivers are given as follow.

$$T_i' = m_j + t_{ij} \quad (9)$$

In the third step, the slowness distribution is updated to eliminate the difference of the theoretical and observed first travel time by identification technique.

4.3 Application to RC bridge deck of bullet trains

As for one of the applications, AE tomography is applied to RC bridge deck of bullet trains. In the RC bridge deck, several internal lateral voids have been estimated by impact acoustics tests except for the area IV detailing in the later session. In the AE tomography, AE activity namely secondary AE sources form the defects induced by train passage will be utilized [19]. As AE data obtained includes mechanically induced noise as well as ambient noise which is irrelevant to the secondary AE activity, the extraction of this secondary AE activity which can also play as a source for tomography testing can be a clue to get a successful result. In addition to the AE monitoring, Rayleigh wave tomography with using accelerometer of 45 kHz-resonance was applied for the comparison.

The AE sensor array and estimated damage areas by the impact acoustics can be found as in Fig. 20, and the same manner of Fig. 20 but for the Rayleigh wave tomography can be confirmed by Fig. 21. The area of interest is 2.4 m x 2.4 m and 13 AE sensors of 60 kHz- resonance for AE tomography and 16 accelerometers for Rayleigh wave tomography are each arranged as in those figures. The estimated damage areas by impact acoustics is denoted by I, II and III, and IV is the area of which impact acoustics could not identify but estimated by other sophisticated techniques (no description for the name of the test could be recorded on site).

For the AE tomography, to set the threshold level ambient noise was first measured without any train passage and subsequently AE monitoring during train passage was repeated 10 times. While for the Rayleigh wave tomography, two types of the steel hammer with 11 and 15 mm in diameter for the impact surface have been employed to investigate the different depth of damage [20]. More details of the Rayleigh wave tomography can be found in the literature [20].

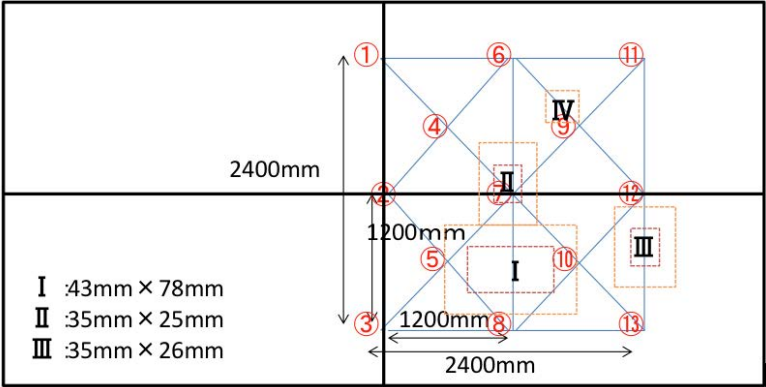


Fig. 20: AE sensor arrangement for AE tomography.

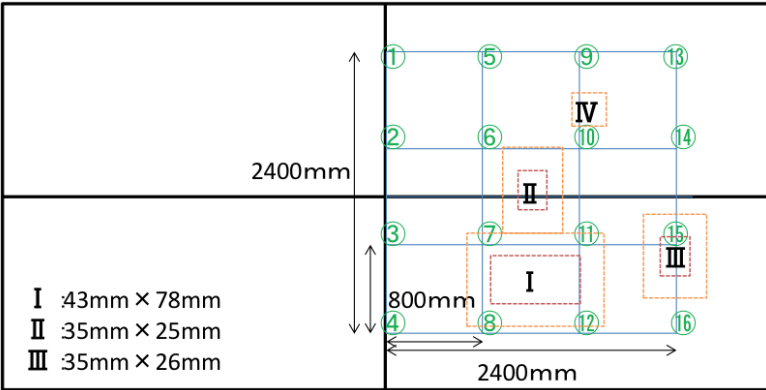
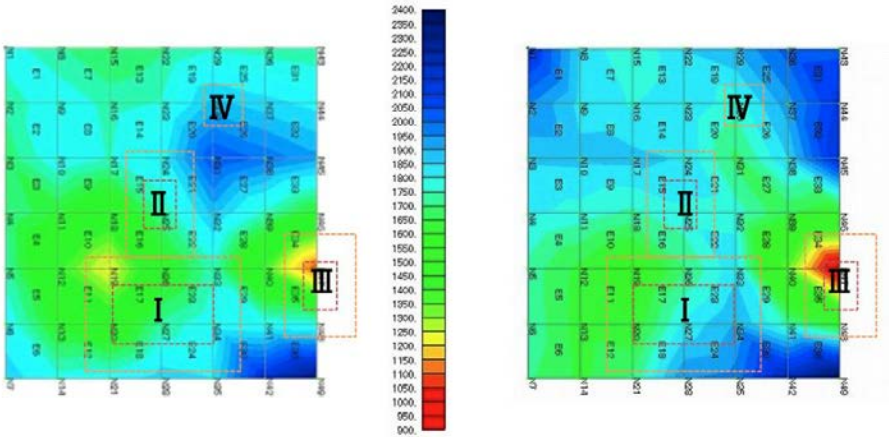


Fig. 21: Accelerometers arrangement for Rayleigh wave tomography.

Two types of Rayleigh wave velocity’s distributions can be seen as in Fig. 22. Figure 22a shows the result of 11mm dia. hammer, equivalent to the wavelength of 18 cm, while 20 cm in wavelength of 15mm dia. hammer as shown in Fig. 22b in the case. As considering both cases showing low velocity areas, damage area I, II and III could be identified with this Rayleigh wave tomography but damage area IV could not confirmed by this technique.

For the AE monitoring, in order to extract the secondary AE activity being different form other noise related AE activities, AE waveforms exhibiting higher peak frequency of 7 kHz were extracted. This criterion of peak frequency was successfully obtained when comparison was made between AE waveforms without train passage and those with train passage. The result of AE tomography with this high pass filter can be found as in Fig. 23. Surprisingly the damage area IV, which could not be evaluated by other inspections, could be revealed leaving slight incompatibility of I, II and III. As there still includes mechanical noises in the extracted AE activity, visual discrimination was further implemented. Figure 24 exhibits the AE tomography

result after both filters of high pass and this visual check. Although the damage area III could not well visualized, the damage area I and II can be successfully emerged. Two-dimensional AE tomography algorithm developed and employed in this analysis might be introduced the above discrepancy to the estimations of impact acoustics. The limitation of the Rayleigh wave tomography shall be also mentioned. As it has already reported that the maximum depth of which the Rayleigh wave tomography can be applied is the half depth/ thickness of the plate, e.g., in the case of 50 cm thick plate, more than the deeper area of 25 cm could not be investigated, while AE tomography has no restriction for the depth of measurement event for the thinner plate. Anyhow as three-dimensional algorithm of AE tomography has been already established awaiting the application to in-situ structures, this fact will be elucidated later and more reliable applications shall be shown up for the follow up paper.



(a) $\phi 11 \text{ mm}$

(b) $\phi 15 \text{ mm}$

Fig. 22: Velocity distributions by Rayleigh wave tomography.

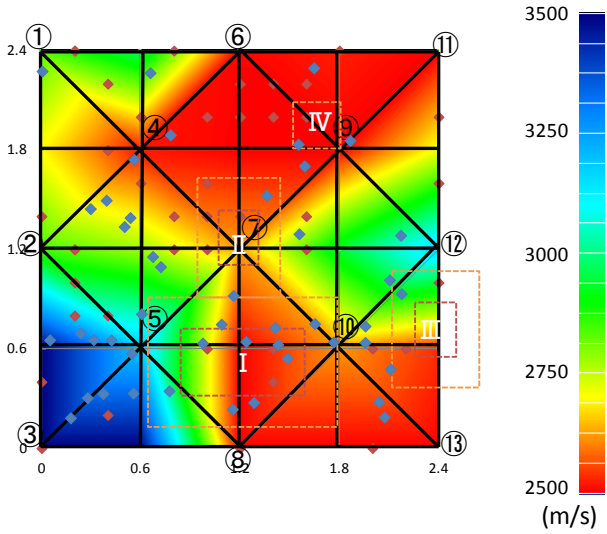


Fig. 23: AET result with using high pass filter of 7 kHz.

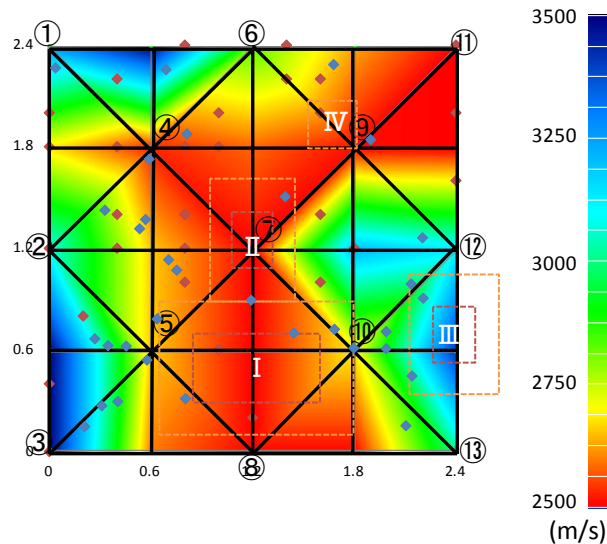


Fig. 24: AE tomography with both HP filter and visual filter.

5. Conclusions

In the paper, conventional damage-associated elastic wave parameters had been reviewed and new index, namely Q-values to assess the damage has been proposed. And as for the approach to extract the damage-prone areas, an ideal and effective method, AE tomography, combining AE monitoring with elastic wave tomography was detailed through the calculation algorithm, followed by in-situ applications. As a result, it was clarified that the Q-value could be an index to quantify the damage of concrete materials. As the frequency dependency of Q-value was still obtained, it will be further confirmed from a viewpoint of engineering by additional experimental studies using actual concrete mixture. Two-dimensional AE tomography was successfully applied to the RC bridge deck as almost damage areas that were estimated laterally developed revealed with low velocity's zones. Three-dimensional algorithm of AE tomography will be further elucidated and more reliable applications shall be shown up for the follow up paper.

6. References

- [1] Momoki, S., Aggelis, D.G., Hirama, A., Shiotani, T.: Combined stress wave techniques for monitoring of fracture in concrete slabs, Engineering Technics Press, Structural Faults and Repair 2008, 12th International Conference and Exhibition, 2008, CD-ROM.
- [2] Shiotani, T., Aggelis, D.G., Makishima, O.: Global monitoring of large concrete structures using acoustic emission and ultrasonic techniques: case study, ASCE Journal of Bridge Engineering Vol. 14, No. 3, 2009, 188-192.
- [3] Popovics, S.: Analysis of the Concrete Strength versus Ultrasonic Pulse Velocity Relationship. Mater Eval 59(2), 2001, 123–130.

- [4] Popovics, S., Popovics J.S.: Effect of stresses on the ultrasonic pulse velocity in concrete. *Mater Struct*, 24, 1991, 15–23.
- [5] Philippidis, T.P., Aggelis D.G.: Experimental study of wave dispersion and attenuation in concrete. *Ultrasonics* 43, 2005, 584–595.
- [6] Chaix J.F., Garnier, V., Corneloup, G.: Ultrasonic wave propagation in heterogeneous solid media: Theoretical analysis and experimental validation. *Ultrasonics* 44, 2006, 200-210.
- [7] Aggelis D.G, Philippidis, T.P.:Ultrasonic wave dispersion and attenuation in fresh mortar. *NDT & E Int* 37(8), 2004, 617–631.
- [8] Shiotani, T., Aggelis, D.G.: Wave propagation in cementitious material containing artificial distributed damage, *Materials and Structures* 42, 2009, 377-384.
- [9] Selleck, S.F., Landis, E.N., Peterson, M.L., Shah, S.P., Achenbach, J.D.: Ultrasonic investigation of concrete with distributed damage. *ACI Mater J* 95(1), 1998, 27–36.
- [10] Shah, S.P., Popovics, J.S., Subramanian, K.V., Aldea, C.M.: New directions in concrete health monitoring technology. *J Eng Mech-ASCE* 12126(7), 2000, 754–760.
- [11] Shiotani, T., Ohtsu, H., Momoki, S., H.K. Chai, Onishi, H., Kamada, T.: Damage evaluation for concrete bridge deck by means of stress wave techniques, *ASCE, Journal of Bridge Engineering*, Vol. 17 (6), 2012, 847-856.
- [12] Polyzos, D., Papacharalampopoulos, A., Shiotani, T., Aggelis, D.G.: Dependence of AE pa-rameters on the propagation distance, *JSNDI, Progress in Acoustic Emission XV*, 2010, 43-48.
- [13] Shiotani, T., Takada, Y., Watanabe, T., Ohtsu, H.; Damage evaluation of heterogeneous materials by Q-value analysis of AE waveforms, *JSNDI, Progress in Acoustic Emission XV*, 2012, 1- 6.
- [14] Aggelis D.G., Shiotani, T.: Stress wave scattering: Friend or enemy of non destructive testing of concrete?, *Journal of Solid Mechanics and Materials Engineering*, 2008, Vol. 2, No. 4.
- [15] Yoshimura, K., Andou, S., Sakashita, S., Bruines, P., Okumura, H., Nishiyama, S., Ohnishi, Y.: Experimental study on imaging hydraulic conductivity of rock masses based on elastic wave velocity dispersion,” *BUTSURI-TANSA*, Vol. 62, No. 3, 2009, 307-318 (in Japanese).
- [16] Schubert, F.: Basic principles of acoustic emission tomography, *Journal of Acoustic Emission*, Vol. 22, 2004, 147-158.
- [17] Schubert, F.: Tomography techniques of acoustic emission monitoring, *ECNDT 2006*, We. 3.6.2.
- [18] Kobayashi, Y.: Mesh-independent ray-trace algorithm for concrete structures, *Emerging Technologies in Non-Destructive Testing V*, Taylor & Francis Group, 2012, 103-109.
- [19] Luo, X., Haya, H., Inaba, T., Shiotani, T.: Seismic diagnosis of railway substructures by using secondary acoustic emission, *Elsevier Science, Soil Dynamics and Earthquake Engineering*, Vol. 26, 2006, 1101-1110.
- [20] Chai, H.K., Aggelis, D.G., Momoki, S., Kobayashi, Y., Shiotani, T.: Single-side access tomography for evaluating interior defect of concrete, *Elsevier Science, Construction and Building Materials*, 24, 2010, 2411-2418.

ACTUAL POSSIBILITIES OF DAMAGE EVALUATION OF MACHINES WITH ROTATING PARTS BY ACOUSTIC EMISSION

Pavel Mazal, Libor Nohál, Filip Hort

Institute of Machine and Industrial Design, Faculty of Mechanical Engineering,
Brno University of Technology
Technická 2, CZ 616 69 Brno, Czech Republic, mazal@fme.vutbr.cz

ABSTRACT

Authors present an overview of the contemporary applications of acoustic emission method for the diagnosis of non-standard operating conditions of machines with rotating parts. The main attention is focused on operational diagnostics of axial and radial bearings. In part are reviewed also options of supplementary use of the AE method for the diagnosis of damage of gears and real gearboxes. This overview of published results is confronted with the practical experiences gained during the implementation of several projects at Laboratory of Acoustic Emission of the Institute of Machine and Industrial Design in Brno University of Technology.

Key words: acoustic emission, diagnostics, bearings, gears, gearbox, damage.

1. Introduction

Condition monitoring of technical devices with rotating parts forms a very important area of evaluating of the operational reliability of machinery. Bearings and gearboxes are significant parts of every means of transport or rotating machinery and the detection of their incipient fault is very important for the evaluation of a service life time and for safety operation of the whole device. Quality monitoring is a crucial element of the reliable and safe operation. In the spinning elements typically uses vibration measurements of the whole system, temperature, noise, etc. NDT methods, especially acoustic emission (AE), are applied very significantly in condition monitoring too.

The acoustic emission as a phenomenon can be defined as transient elastic waves resulting from local internal micro-displacements in materials of the tested structures. AE method has become a common NDT method used mainly for testing of the stationary equipments - tanks, pressure vessels, reactors, pipelines, bridges, etc. In these applications, the AE method is fully accepted and standardized. The advantage of AE method is the ability of testing of the entire structure, locating of potential defects and assessment of their risk for the integrity of the structure. AE application brings significant economic benefit to all users. The partial disadvantage is the limited ability of precise identification of the defect type and it is necessary to use other NDT methods for their identification.

2. Application of AE testing for bearings

An application of AE method in condition monitoring of rolling bearings has been the subject of interest of many authors since the beginning of this method application in engineering. Compared to monitoring of stationary equipments the monitoring of devices with rotating parts is much more complex. Rolling bearings consist of many parts which are in mutual contact during function. This leads to a gradual degradation of the contact surfaces. Very important issue in this area is the quality of lubrication. An important role is played by temperature changes during bearing operation. In such devices, there are many sources of AE signal. Nevertheless, the possibility of continuous monitoring of bearing health is extremely appealing.

Information regarding the use of acoustic emission in this area can be found already in the 70s and 80s [1], [2], [3]. A significant development of AE applications appeared in the late 20th Century and continues to the present. Extensive works arise in a number of workplaces. Very significant results are mainly associated with the works of staff at the University in Telford [4], [5].

Some work studied the possibility of the detection of artificial defects created on the raceway [6]. Elforjani et al. [4] proved the possibility to detect and localised the natural damage initiation and propagation. The AE method is more sensitivity to detection of this mechanism than the vibration based methods. The incipient damage detection in slow speed bearings using acoustic emission was studied by Elforjani et al. [7]. This study shows that low-energy transient bursts generated from incipient fatigue damage are not detectible using vibration monitoring. Nélias et al. [8] described the new methodology of rolling contact fatigue evaluation and studied the influence of dents on the endurance limit. In a review study about rolling bearing fault detection, it is suggested that out of the time domain statistical parameters, the Kurtosis value is the most effective one for defect identification [9]. At the initial stage of bearing failure, high-frequency techniques such as the vibration acceleration envelope analysis, the AE measurements, and the shock pulse method (SPM) have been successfully applied.

AE application for the identification of contact involved damage started in our workplace (BUT FME) approximately from 2004 [10]. Unlike most of the other work our laboratory deals with real axial and radial bearings of small size at relatively high speeds. Diagnostics of creation of the damage in rolling bearings is already quite well developed and this methodology could be used for evaluation of the durability of bearings. Of course there are still a number of problems, particularly in the identification of the type of damage, localization of defect and potential automation of damage diagnostic.

Example of a very promising application of this diagnostic method may be can the energy sector - monitoring the bearings of large steam turbines. When we talk about use in the production of electricity, one possible application is the monitoring of wind turbines, which uses non-invasive diagnostics and transmission of the information to the recording of the evaluation centre is provided by telecommunication technology [11]. One of the non-traditional usages can be the use for diagnosis of turbines of jet aircraft...

Currently, monitoring and examination of various conditions of loading of bearings and bearing materials devotes a number of authors, e.g. Tandon et al. [12]. He gave a comparison of several diagnostic methods for condition monitoring of rolling bearings of induction motor. The authors used these monitoring techniques: vibration monitoring, stator harmonic currents, acoustic emission and shock pulse method (SPM). Manifestations of techniques have been observed on the defect of the outer ring of radial bearings.

AE monitoring was carried out in conjunction with other techniques of measurement from zero loads to full load. Comparison of different monitoring techniques damage used in the experiment for different degrees of damage, and load is shown in Fig. 1, where the percentage increase in response is damaged bearings with respect to the average value of healthy bearings. As shown in these graphs, the highest share is always the AE method followed by SPM. Velocity measurement and stator currents are on the third, fourth, respectively. Although the method of

measuring of the stator currents appeared to be the least effective, this method has minimal equipment requirements and it is sometimes also referred to as non-sensor method.

AE has for its higher sensitivity (in the time domain shooting) better placed to detect emerging damage sooner and easier than vibrating procedures, which is an important consideration identification of damage frequency analysis. However, either as a supplement or basis for monitoring of the device status is desirable the vibration monitoring for example, if the fault source generates low-frequency waves (e.g. unbalance of rotating components).

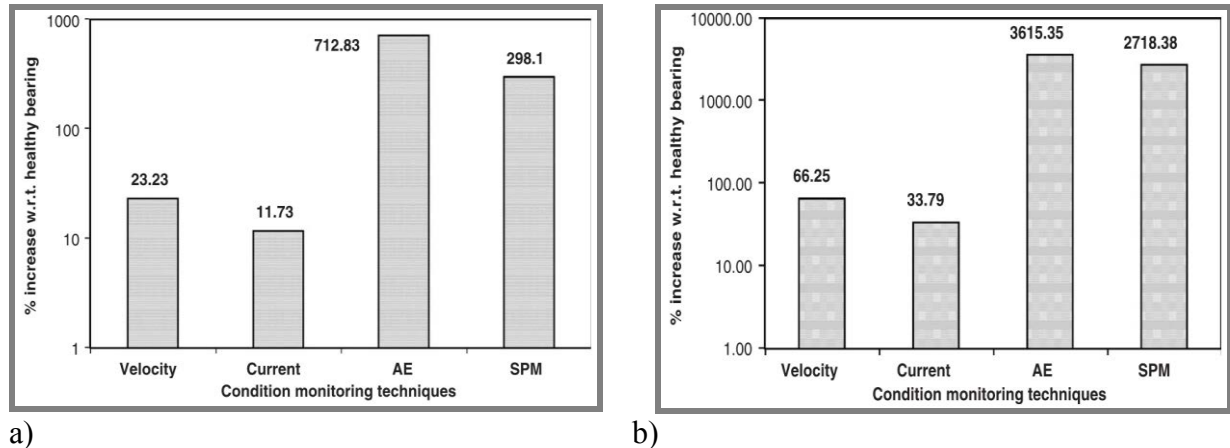


Fig. 1: Comparison of monitoring techniques for the minimum size of the defect) and the maximum size of the defect b) [12].

One of the most active in this area at present is D. Mba and his research group. This team published numerous articles dealing with the detection and localization of damage, especially for the axial bearings [4], [7], and [9]. In the published works authors deal with the application of AE as a tool to detect the emergence and development of contact damage on samples of bearings and bearing materials, such as complementary and comparative measurement is used vibration accelerometers.

An example of standard results of the damage identification which has been obtained in our laboratory is shown in Fig. 2, 3 and 4 [13]. The axial bearing was tested in Axmat stand, the applied load in this test was 2660 N. During the first fifteen minutes of the test, an increase in AE activity was detected, see figure 2. This corresponds to running-in phase of test, after this period (15 min) count rate levels, RMS, and vibration parameters were constant. It was observed that after 180 minutes into the test count rate levels began to increase steadily and the vibration acceleration or temperature do not response. On the termination of the test (500 min) the count rate, RMS and vibration increased to the significant activity. After 180th minute of test AE counts levels and RMS were slowly rising. This is caused by the initiation and propagation of pitting in the track on the upper ring (material specimen). Next stage after 420th minute correlate with the vibration level monitoring shown in Fig. 3. A step-level change is caused by tearing of the material from the surface and followed by a development of spalling.

The vibration observation and temperature monitoring during the test is presented in Fig. 3. After the running-in stage of specimen N1, the temperature remains steady at 42 °C. The temperature drop of 1 or 2 °C in the final phase of testing is caused by lowering the temperature of the air around the test-rig. In this case, the test was terminated after the creation of small pitting and therefore was recorded only a slight increase in temperature as a response on final damage. The vibration level was during running-in stage and steady-state constant. The increase in level of vibration after 420th minute corresponds to spalling propagation. This was observed also in AE monitoring.

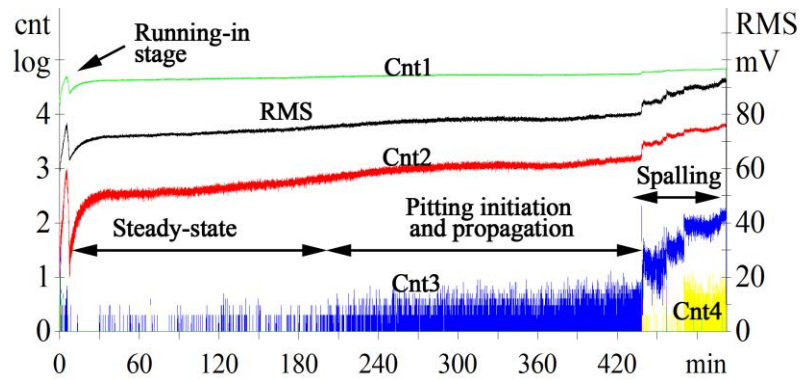


Fig. 2: Observation of N1 test – AE count rate (4 levels), RMS [13].

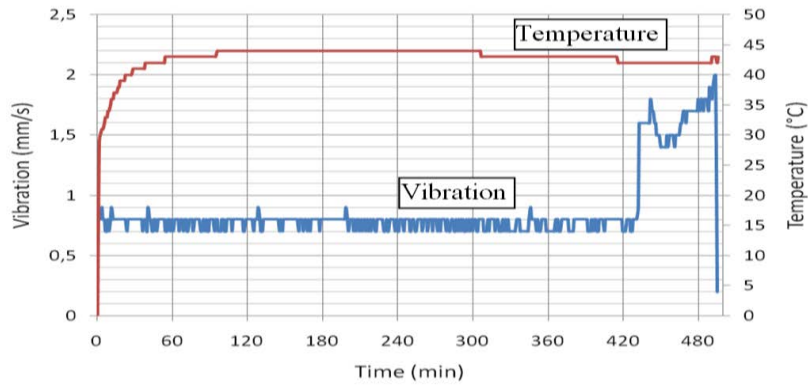


Fig. 3: Vibration level and temperature during test N1 [13].

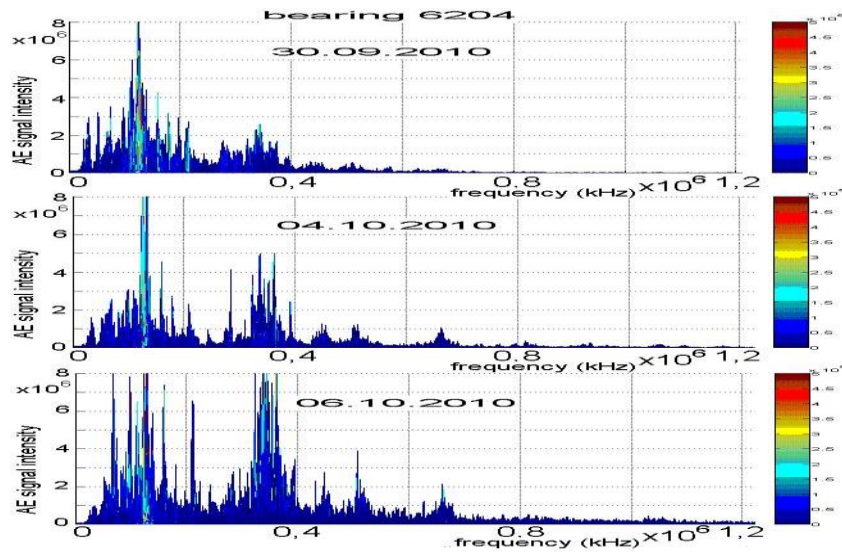


Fig.4: Comparison of AE signal intensity in different frequencies in the starting stage of test (upper plot) and in the final stage of test (bottom) - test of radial bearing 6204 [14].

Currently is available already a considerable amount of experimental data and research teams consideration is focused on finding of suitable parameters of AE signals to distinguish the different types of damage. Example of changes in AE signal intensity in different frequencies (the frequency spectrum) is plotted in Fig. 4. - Higher frequencies were identified in the final stage of the test [14].

A separate but very important, area of problems forms a question of an effective filtering of interfering signals.

3. Application of AE method for testing of gearboxes

Much more complicated is the situation in the application of AE method for diagnostics of the status and possible damage of gears and gearboxes. Standard gearbox consists of many rotating parts and evaluation of the obtained data is very difficult due to complex structure.

Many authors dealt with the simple single-stage spur gearbox [15] or single-stage helical gearbox [16]. Transducers were in these cases placed close to the tested gear or directly on the wheel. The various methods were used for damage detection, for example noise emission, vibration levels, and AE technique and temperature measurement. Albers et al. [17] dealt with comparison of the AE with laser vibrometer. The results of this work indicate that the obtained data can be correlated only in frequency range from 20 to 60 kHz. The other authors dealt with experiment on the spur gear and for evaluation used parameters such as vibration levels, temperature and AE parameters – RMS, ring down counts, energy.

Authors of the paper *Identification of the acoustic emission source during a comparative study on diagnosis of a spur gearbox* [18] tried to ascertain and validate the applicability of AE to seeded gear defect identification. As a direct consequence of the experimental programme, the relationship between temperature, oil film thickness and AE activity were investigated.

Lixin Gao et al [19] made a basic analysis of the AE data from the faults of on-spot low-speed heavy-duty gears. The application of redundant second generation wavelet and AE testing in gear fault diagnosis was investigated in this study. Through the analysis of on-spot cases, the following conclusions were obtained: a) AE testing diagnosis could be applied to the fault diagnosis of on-spot low-speed heavy-duty gears and was a crucial supplement to the vibration testing diagnosis. b) The length of the approximation signals and detail signals obtained after the decomposition of redundant second generation wavelet was the same as that of original ones, so the amount of information was twice that of the original. Such a characteristic of redundant second generation wavelet guaranteed that it could achieve an effect better than conventional wavelet and second generation one. With the denoising technique based on redundant second generation wavelet, all fault shock information could be preserved, which was unmatched for other denoising techniques. c) The validity of the algorithm of the redundant second generation wavelet transform during the processing and denoising of acoustic emission signals was verified.

Chee Keong Tan and David Mba published the study *Limitation of Acoustic Emission for Identifying Seeded Defects in Gearboxes* [20]. This paper reviews recent developments in application of AE to gear defect diagnosis. Furthermore, experimental results examine and explore the effectiveness of AE for gear defect diagnosis. It is concluded that application of AE to artificially seeded gear defect detection is fraught with difficulties, particularly for fault identification. In addition, the viability of the AE technique for gear defect detection by making observations from non-rotating components of a machine is called into question. Nevertheless, guidance is offered on applying the technique for monitoring the natural wear of gears.

While vibration analysis on gear fault diagnosis is well established, the application of AE to this field is still in its infancy. In addition, there are limited publications on application of AE to gear fault diagnosis. Siores et al. [21] explored several AE analysis techniques in an attempt to correlate all possible failure modes of a gearbox during its useful life. Failures such as excessive backlash, shaft misalignment, tooth breakage, scuffing, and a worn tooth were seeded during tests. Siores correlated the various seeded failure modes of the gearbox with the AE amplitude, RMS, standard deviation and duration. It was concluded that the AE results could be correlated to various defect conditions. Sentoku [22] correlated tooth surface damage such as pitting to AE activity. An AE sensor was mounted on the gear wheel and the AE signature was transmitted from the sensor to data acquisition card across a mercury slip ring. It was concluded that AE amplitude and energy increased with increased pitting.

This paper has demonstrated that artificially seeded gear defect detection with AE is fraught with difficulties. Experiments to identify seeded defect identification with AE RMS and energy were not satisfactory. The influence of oil temperature on AE activity has been presented.

Some examples of our results are plotted on Fig. 5 and Fig. 6 [23], [24]. In collaboration with the Laboratory of gearboxes testing (BUT FME) we carried out several experiments focused on the possibility of AE signal sensing from automotive gearbox. The experiments were carried out on the automobile gearbox used by the Volkswagen Group. It was a gearbox bearing MQ 200 used in vehicles with engine torque to 200 Nm (e.g. Skoda Fabia). On this transmission was artificially created damage to the driven wheel (helical wheel) of the fifth gear. For experiments was used the test station consisting of drive flange for mounting gear, eddy dynamometer with maximum torque of 500 Nm load simulating. During all tests was used as filling mineral gear oil. We have obtained many interesting results, but due to the complexity of real gearboxes it is still very difficult to prepare a unified methodology for these parts testing. Examples of AE signal recording during the load change of gearbox is shown in Fig. 6.

We can say that in general, that the most significant source of AE is the inequality in contact. This is usually caused by either dents of foreign bodies into the surface of the tooth flank or by erosion of the material during pitting. The most sensitive AE parameter in damage detecting is the effective value of the signal (RMS). To extract suitable parameters from the raw signal is therefore necessary to use an advanced signal processing. An example might be an application of wavelet transform, which improved the ability to detect damage acoustic emissions.

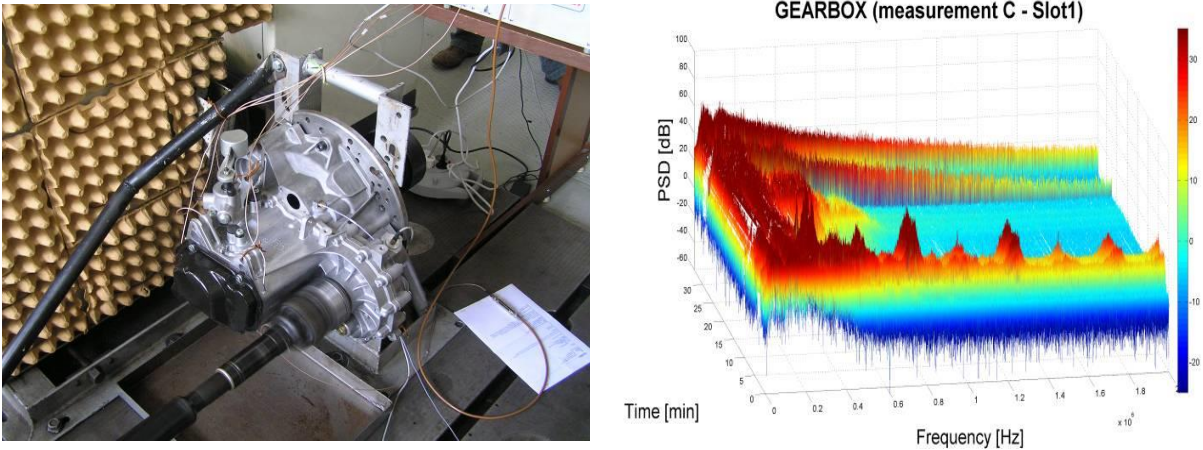


Fig. 5: Gearbox Skoda Fabia and the 3D plot of changes in frequency domain of AE signal during the load change [23].

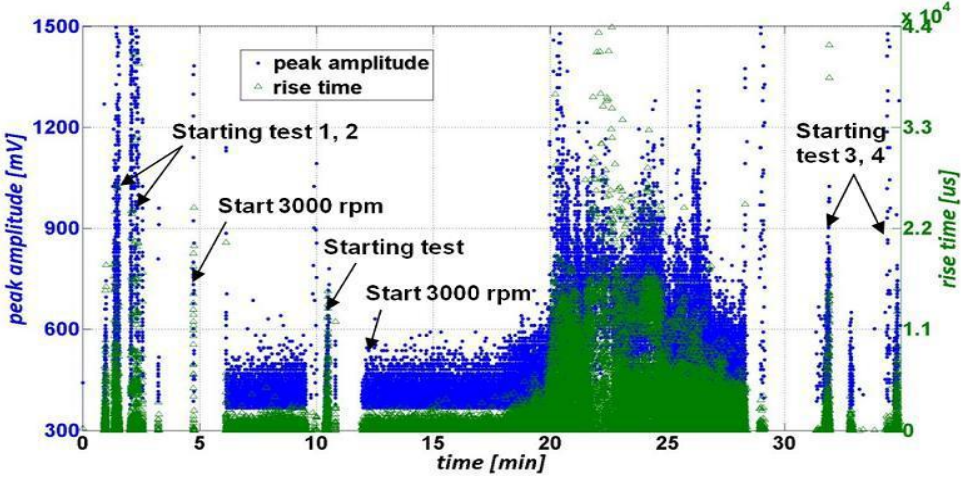


Fig. 6 Changes of peak amplitude and rise time of AE events during the different load regimes of the tested gearbox [24].

The way of transmission of AE signal in this case is too complicated and is subject to significant or inhibits the occurrence of unwanted noise signal. However, despite these complications AE method could detect the damage at a level comparable with vibrodiagnostics. Detection

capability is dependent on the degree of smoothing unevenness in contact obliterated damage was not possible, as mentioned above, to identify the acoustic emission signal. Examples of changes in the frequency of AE signals that occur during changes in load transmission are shown in Fig. 5.

4. Conclusions

The presented results show the extensive possibilities application of acoustic emission method in this field. Most of the work is still performed in laboratory conditions. Is relatively well mastered methodology sensing signal, especially in the area of thrust bearings and partially also radial bearings. The situation in the diagnosis of gearboxes is still very complicated. It is necessary to focus on the area of signal processing, the identification of suitable parameters of the AE signal, which can be used for repeated measurements in real conditions. Very important is the development of methods for the elimination of interferences. Already now, however, acoustic emission can be used as a very useful complementary method for vibration diagnostics (AE method can signalize the damage creation). However, the potential of AE is large, and certainly in the near future this method will be among the basic diagnostic procedures in the field of rotating machinery.

Acknowledgements

Results were created in the framework of the research project NETME Centre under the Operational Programme Research and Development for Innovation (reg. No. CZ. 1.05/2.1.00/01.0002) supported by European Regional Development Fund and project MPO CR TIP FR TI4/602 "Diagnostics complex for detection of leaks and material defects.

5. References

- [1] Balerston H.L.: The detection of incipient failure in bearings. *Mater. Evaluation*, 1969; 27; p. 121–8.
- [2] Roger, L.M.: The application of vibration analysis and acoustic emission source location to on-line condition monitoring of anti-friction bearings. *Tribology Internat.*, 1979; p. 51-59.
- [3] Yoshioka T, Fujiwara T.: Application of acoustic emission technique to detection of rolling bearing failure. American Society of Mechanical Engineers, Production Engineering Division publication PED, 1984, 14, 55-76.
- [4] Elforjani M., Mba D.: Detecting the onset, propagation and location of nonartificial defects in a slow rotating thrust bearing with Acoustic Emission, *Insight*, Vol. 50 No 5, p. 264 – 268, May 2008
- [5] Mba D.: The use of AE for estimation of bearing defect size, *Journal of Failure Analysis and Prevention*, American Society for Metals (ASM), Vol. 8, No. 2, April, 2008, 188-192.
- [6] Bhadeshia H.K.D.H.: Steels for bearings, *Progress in Materials Science*, Vol. 57, No. 2, pp. 268-435, February 2012.
- [7] Elforjani M., Mba D.: Accelerated natural fault diagnosis in slow speed bearings with AE, *Engineering Fracture Mechanics*, Vol. 77, No. 1, pp. 112-127, Januar 2010.
- [8] Nélias D., Jacq C., Lormand G., Dudragne G., Vincent A.: New Metodology to Evaluate the Rolling Contact Fatigue Performance of Bearing Steels With Surface Dents: Application to 32CrMoV13 (Nitrided) and M50 Steels, *ASME Journal of Tribology*, 2005, Vol. 127, pp. 611-622.

- [9] Al-Dossary, Hamzah R.I.R., Mba D.: Observations of changes in acoustic emission waveform for varying seeded defect sizes in a rolling element bearing. *Applied Acoustics*, Jan 2009, vol. 70, no. 1, p. 58-81.
- [10] Mazal P., Zykova L., Pazdera L.: Identification of Contact Fatigue Stages with Acoustic Emission Method. In 9th ECNDT 2006, Berlin, DGZfP, 2006, p. P4 (8 p.). ISBN 3-931381-86-2.
- [11] Timmerman H.: Monitoring the Winds of Change. *Evolution Business and technology magazine from SKF* [online]. 2006, Vol. 3, no. 3/06, [cit. 2011-03-12]. <<http://evolution.skf.com/zino.aspx?articleID=14982>>
- [12] Tandon N., Yadava G.S., Ramakrishna K.M.: A Comparison of Some Condition Monitoring Techniques for the Detection of Defect in Induction Motor Ball Bearings. *Mechanical systems and signal processing*. Vol. 21, No. 1, INDE: ITMME Centre. New Delhi, 2005, pp. 244-256, ISSN 0888-3270.
- [13] Nohal L., Hort F., Mazal P.: An Experimental Study on Damage Monitoring of Rolling Bearings Using Acoustic Emission Method, The Tenth International Conference on Condition Monitoring and Machinery Failure Prevention Technologies, Krakov 2013, p. 133 -140.
- [14] Mazal P., Hort F., Drab, M., Slunecko T.: Some Possibilities of AE Signal Treatment at Contact Damage Tests of Materials and Bearings. In: *Jour. of AE* 2008, vol. 26, p. 189-198, AE Group, CA, USA, 2009, ISSN 0730-0050.O2 – 50.
- [15] Toutountzakis T. et al.: Application of acoustic emission to seeded gear fault detection. In *NDT & E International*, Vol. 38, Issue 1, January 2005, Pages 27-36, ISSN 0963-8695
- [16] Eftekharijad B., Mba D.: Seeded fault detection on helical gears with Acoustic Emission, *Applied Acoustics*, 70 Issue: 4, p. 547-555, 2009.
- [17] Albers A. et al.: Validation of AE - signals recorded with conventional equipment using 3D Scanning-Laser-Vibrometer. In: 29th Europ. Conf. on AE Testing 2010, Vienna, Austria, 8 pages, CD edition, NDT.net - The Open Access NDT Database, Germany, ISBN 978-3-200-01956-0.
- [18] Tan Ch.K, Mba D.: Identification of the acoustic emission source during a comparative study on diagnosis of a spur gearbox. In: *Tribology Int.*, Vol. 38, Issue 5, May 2005, p. 469-480.
- [19] Lixin Gao, Fenlou Zai, Shanbin Su, Huaqing Wang, Peng Chen and Limei Liu: Study and Application of Acoustic Emission Testing in Fault Diagnosis of Low-Speed Heavy-Duty Gears *Sensors* 2011, 11, 599-611; ISSN 1424-8220
- [20] Tan Ch.K. and Mba D.: Limitation of Acoustic Emission for Identifying Seeded Defects in Gearboxes *Journal of Nondestructive Evaluation*, Vol. 24, No. 1, March 2005, Springer Science+Business Media
- [21] Siores E. and Negro A. A.: Condition monitoring of a gear box using acoustic emission testing, *Material Evaluation* pp. 183–187, 1997.
- [22] Sentoku H.: AE in tooth surface failure process of spur gears, *J. Acoust. Emiss.* 16 (1–4), pp. S19–S24 (1998).
- [23] MAZAL P., NOHAL L., HORT F., KOULA: Possibilities of the damage diagnostics of gearboxes and bearings with acoustic emissions method, 18th World Conference on Nondestructive Testing, 16-20 April 2012, Durban, South Africa
- [24] Nohal L., Mazal P.: Identifikace poškození součástí automobilové převodovky metodou AE. In: *NDE for Safety 2011*. Brno, ČNDT, 2011. p. 107 - 114. ISBN 978-80-214-4358-7 (in Czech).

A STUDY ON THE PERFORMANCE OF ACOUSTIC EMISSION AND LOW FREQUENCY VIBRATION METHODS TO THE REAL-TIME CONDITION MONITORING OF RAILWAY AXLES

M. Carboni¹, S. Bruni¹, D. Crivelli¹, M. Guagliano¹, P. Rolek¹

¹Department of Mechanical Engineering – Politecnico di Milano

Via La Masa 1, 20156 Milano, Italy

michele.carboni@polimi.it, stefano.bruni@polimi.it, davide.crivelli@mecc.polimi.it,
mario.guagliano@polimi.it, pawel.rolek@polimi.it

ABSTRACT

Railway axles are safety-critical components whose failure could result in large additional costs for the infrastructure manager and the railway operator and, in most serious cases, even lead to unacceptable human losses. For this reason, they are periodically inspected by means of non-destructive techniques usually requiring expensive service interruptions. Considering the special case of solid axles for freight cars, this paper investigates the feasibility to apply two structural health monitoring techniques to increase vehicle safety and reliability and, at the same time, to decrease the cost of damage inspection. In particular, the considered structural health monitoring techniques are Acoustic Emission and the measurement of low frequency vibrations. In the present paper, a study about the application of both these techniques to freight railway axles is introduced and discussed.

Key words: structural health monitoring, freight railway axle, acoustic emission, low frequency vibrations, full-scale crack propagation test

1. Introduction

Railway axles are safety-critical components designed against fatigue limit, as defined in relevant standards like EN13261 [1], EN13103 [2] and EN13104 [3]. Actually, due to their very long service life, they are prone to service damages, like impacts due to the ballast or corrosive aggression. These events are able to initiate fatigue cracks leading to service failures, whose effects entail large additional costs for the infrastructure manager and the railway operator and, in the most serious cases, may be cause of serious accidents and even lead to unacceptable human losses. Besides, while laboratory tests to assess the fatigue limit of materials and components usually assume 10 million cycles as the run-out condition, it is true that fatigue failures can happen for longer durations and with applied stress lower than the fatigue limit; that is to say that to consider the fatigue limit determined on the base of 10^7 cycles for infinite life fatigue design is not always a safe criterion, especially for critical parts, like railway axles are.

For all these reasons, in the framework of a damage tolerant approach for maintaining structural integrity, as generally defined by Grandt [4] or specifically for axles by Carboni and Beretta [5], railway axles are periodically inspected by means of well-established non-destructive techniques (typically ultrasonic and magnetic particle inspections) usually requiring expensive service interruptions. Considering the special case of solid axles made of A4T steel grade [1], this paper investigates the feasibility to apply structural health monitoring (SHM) techniques, which, in the aeronautical field, have shown, according to Chang [6], the possibility to decrease the costs of damage preventive inspection up to 30 % without losing accuracy.

The number of SHM techniques available in the literature and likely applicable to the detection of fatigue cracks in railway axles is rather large: acoustic emission, low frequency vibrations (nxRev periodicity), high frequency vibrations (changes in natural frequencies), microwave testing, alternating current field measurements, induced current focusing potential drop, AC thermography and laser-air coupled hybrid ultrasonic technique. Among all of them, the present study focuses on acoustic emission (AE) and low frequency vibrations (LFV), as they are the ones whose equipment seems to be the less invasive and bulky, a very important and critical characteristic considering the configuration of real axles mounted on running trains.

The chosen techniques were judged, by their application, during a crack propagation full-scale test carried out on freight solid axles made of A4T steel, one of the standardised European grades for production of axles [1]. Before proceeding to the description of the research, a short remind of the basic ideas and concepts lying at the base of the chosen SHM techniques is given in the following.

1.1 Acoustic emission (AE)

AE SHM is based on the observation that damage developing in a material releases energy in form of ultrasonic elastic waves, which could be fruitfully detected [7]. These waves (so-called “hits”) are typically short and transient (“burst events”) with bandwidth in the 100-1000 kHz range, which makes AE quite robust against audible noise and structural vibrations. Traditionally, the so-called “parametric AE” is used, in which the transient waveforms are used for the calculation of some traditionally well-established parameters (like peak amplitude, duration, energy). These parameters are then stored and used for further processing, while the waveforms are generally discarded to avoid the need of undesirably large storage systems.

AE is traditionally used and standardized as a non-destructive technique to assess the structural integrity of metallic components (e.g. pressure vessels and pipelines) under static and fatigue loadings [8], with very few applications to the railway field [9], which usually focus on fixed parts, such as rails and bogies.

1.2 Analysis of low frequency vibrations (LFV)

LFV is based on the measure of harmonic components in the axle bending vibration having periodicity which is an integer sub-multiple of the revolution period. These vibrations are induced by the “crack-breathing” mechanism and by asymmetry in the bending inertia of the axle, as produced by a propagating crack. The advantage of this second method consists in the possibility to use low-frequency vibration, hence using simple, robust and inexpensive transducers. This method was initially proposed for crack detection in the shaft of turbo-machinery [10], and was demonstrated to provide reliable results for this kind of application based on experiments performed on a laboratory test rig. Crack detection and localisation is performed by representing the crack as an equivalent excitation, produced by a bending moment having nxRev periodicity applied on a short section of the shaft. Then, an inverse problem is solved in the frequency domain to derive the most probable location and amplitude of the equivalent excitation. The latter is then translated into a guess of the crack amplitude based on look-up tables defined using a finite element model of the cracked axle. Aim of this research is to assess the possibility to extend this method to crack detection in railway axles. Some additional difficulties, posed by this specific application, must be kept into account:

- i) effect of disturbance produced by wheel-rail contact (in particular, wheel out of roundness is also cause of $n \times Rev$ vibration of the axle, so this effect needs to be depurated);
- ii) limited number of measuring sections available in the railway axle;
- iii) in the railway application, the angular speed of the axle is changing according to a more complicate profile, whereas in a turbo-machine run-up and run-down measurements can be applied for identification purposes;
- iv) in turbo-machines, the method is typically applied to rotors running at high speed, above the first critical, whereas the railway axle is running at speeds much lower than the first critical.

2. Experimental set-up and plan

The experimental full-scale test was carried out by means of the “Dynamic Test Bench for Railway Axles” (BDA) available at the labs of Politecnico di Milano – Department of Mechanical Engineering. The BDA is fully compliant with the relevant standards about the qualification of axles (EN13261 [1], EN13103 [2] and EN13104 [3]) and the test procedure and results are Quality Certified ISO9001 since 2003. Figure 1 shows the static scheme and a view of the BDA. In particular, a three point rotating bending is applied to the full-scale specimen via an actuator group and an electric motor: in this way, both constant amplitude and block loading fatigue or crack propagation tests can be carried out as explained in [11].

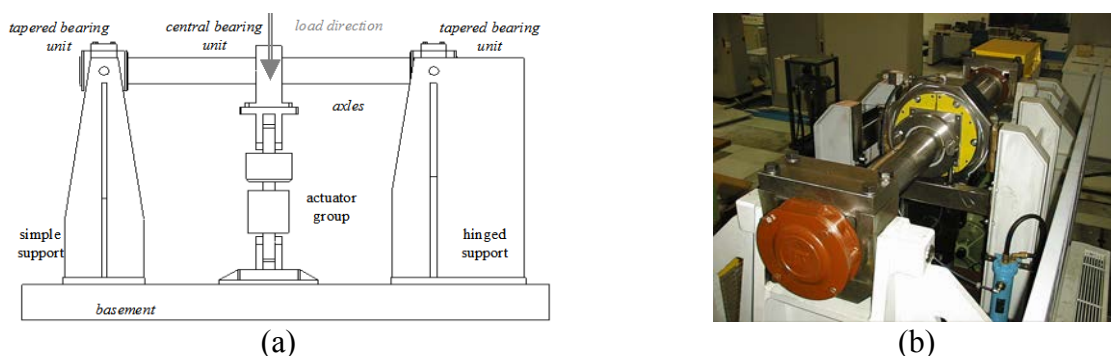


Fig. 1: Dynamic Test Bench for Railway Axles: a) static scheme; b) view of the test bench.

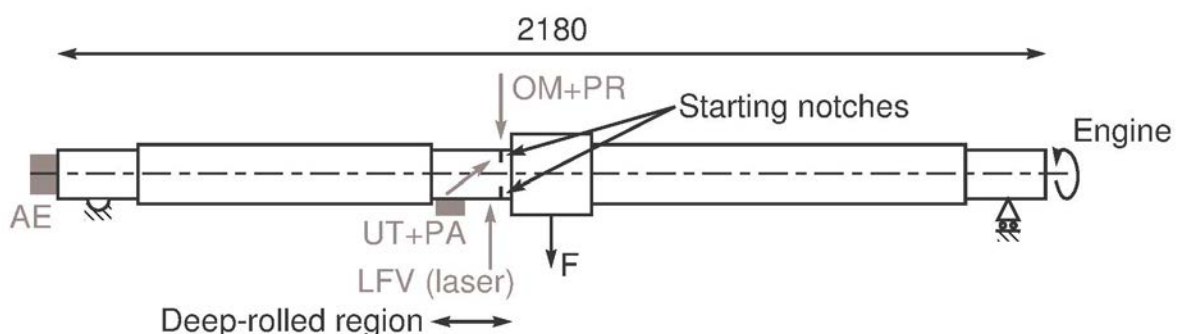


Fig. 2: Scheme of the full-scale axle adopted for the crack propagation test and applied SHM and NDT techniques.

The test was carried out considering the special case of a deep-rolled axle and consisted in a crack propagation test. The scheme of the full-scale specimen is shown in Figure 2. Two starting notches, located at 180° one from the other and useful for initiating two independent fatigue cracks in the section of interest of the axle, were introduced by electro-discharge machining (EDM) in the deep-rolled cylindrical part of the axle. These starting notches had a semi-circular shape with radius $R = 4$ mm. The full-scale specimen was subjected to a block loading sequence

experimentally derived from the typical service spectra of a tilting train on European lines. More details about the experimental set-up for the full-scale crack propagation test are reported in [12]. AE and LFV signals were acquired to monitor damage development during the application of multiple repetitions of the block loading sequence. In particular, the AE probe was applied at one free end of the axle (Figure 2) using a custom made carter (Figure 3) designed to hold in position the sensor and its pre-amplifier. The rotating group was then connected to a sliding contact to bring the signals to the AE acquisition system (Vallen AMSY-5, [13]). The custom carter allows the positioning of the sensor without removing the whole assembly, with the aid of a thin sheet metal part. It has to be underlined that the choice of leaving the preamplifier on the axle was due to noise issues, which arose during preliminary tests, mainly due to the low sensor output (which is in the mV range). The sensor was then coupled to the axle with grease, to avoid the formation of air bubbles and to reduce signal attenuation. The assembly was regularly checked to ensure the grease was not deteriorated or moved away during the test. The use of a single AE sensor, due to the particular layout of the test bench, did not allow the use of localization algorithms, though in a real application this would be easily feasible. A calibration of the AE system was performed according to the standard pencil lead break test [14]: the signal attenuation along the axle was found to be negligible. The acquisition was run throughout the entire test. After one minute of rotation without any load application to assess the noise levels, the noise threshold was set at 55 dB.



Fig. 3: Custom made carter to hold the AE sensor and its pre-amplifier: a) CAD model; b) application at the axle end.

LFV was applied via a laser pointing to the central region of the axle, close to the starting notches (Figure 2), so to get the highest displacements produced by the applied loads. With the aim to have a feedback on crack propagation to evaluate the efficiency of the applied SHM techniques, other NDT methodologies were applied at test interruptions between the repetitions of the block loading sequence. In particular, the surface region around the starting notches was inspected (Figure 2) by an optical microscope (OM) and through the application of plastic replicas (PR). The possible under-skin crack growing was, instead, monitored (Figure 2) by traditional ultrasonic testing (UT by a probe having 45° refraction in steel and 4 MHz working frequency) and by ultrasonic phased array testing (PA by a probe having 32 active crystals working at 5 MHz and in S-Scan configuration). It is, finally, worth noticing that another test is now running considering crack propagation in a second deep-rolled axle containing two starting semi-circular notches with $R = 3$ mm. All the SHM and NDT techniques shown in Figure 2 are again being applied.

3. Results

The test lasted for 66 repetitions of the block load sequence, corresponding to about 3.5 million kilometres of service. Figure 4 shows two examples of OM pictures taken at the deepest point of one of the starting notches after 14 repetitions of the block loading (Figure 4a) and at the surface of one of the surface edges after 14 repetitions of the block loading (Figure 4b). In the latter case, the observation was also supported by PR.

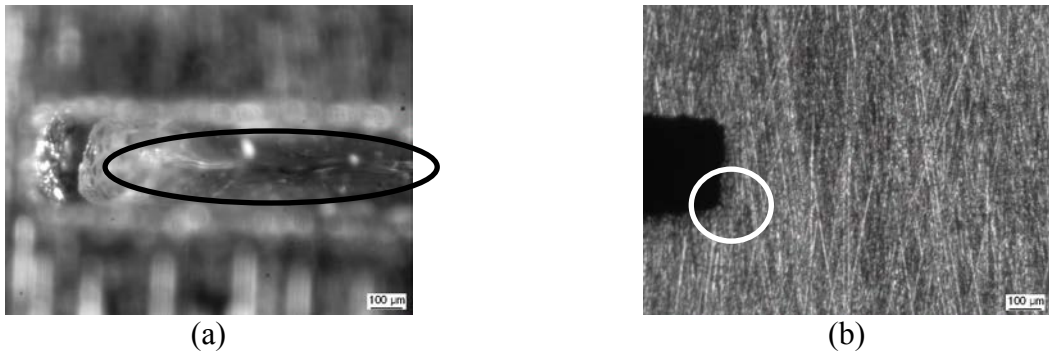


Fig. 4: Optical microscopy of fatigue cracks: a) deep region; b) surface.

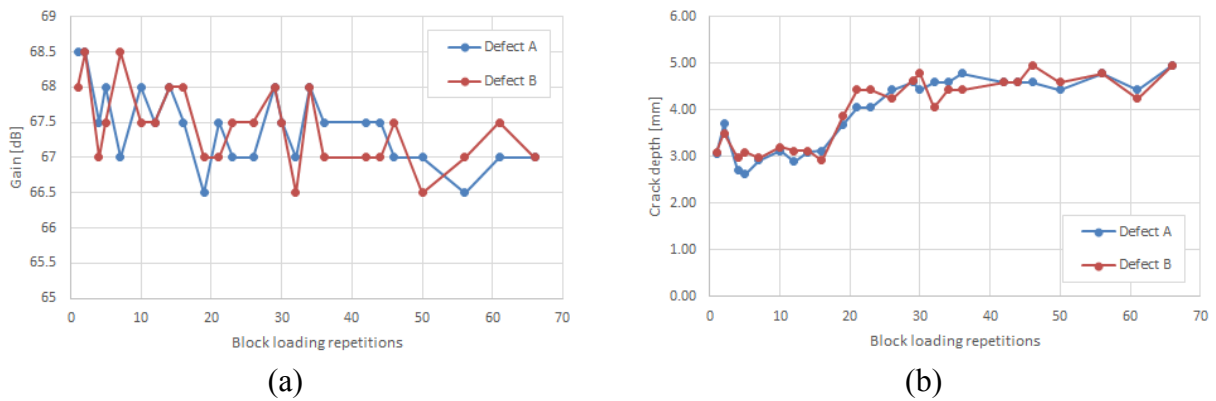


Fig. 5: Ultrasonic measurements of the growing crack: a) traditional UT; b) phased array UT.

The application of UT and PA allowed estimating the cracks dimensions along the whole test. In particular, Figure 5a shows the response of UT in terms of the acoustic energy reflected by the growing cracks: the trend is slightly decreasing, suggesting a very small increase of cracks dimensions during the whole test. Figure 5b shows, instead, the estimation of crack depth obtained using PA and the crack tip diffraction method: total crack growth resulted to be about 1 mm.

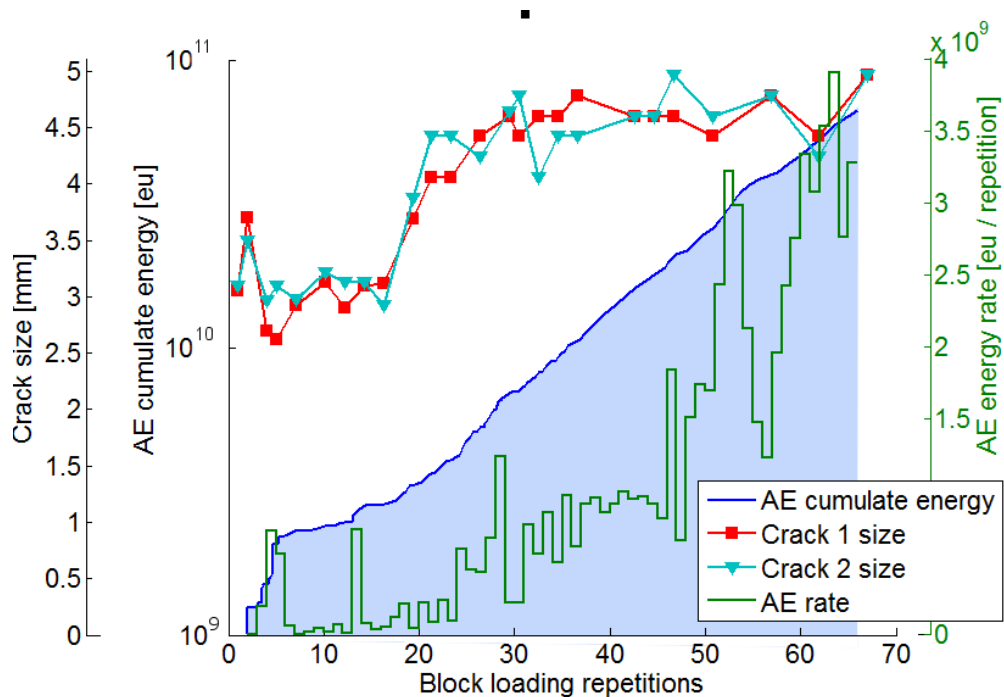


Fig. 6: Acoustic Emission energy released compared with measured crack sizes.

AE data from this test are shown in Figure 6. It can be seen that, during crack propagation and as measured by UT, the amount of AE energy released increases. In particular, the slope of the AE curve shows different phases: a first run-in phase, then some high-slope moments (which correspond to the crack propagation seen between repetitions 15 and 20) and a stable slope phase, coincident with stable crack propagation. AE cumulate energy is shown here, but AE activity (i.e. events per unit of time) carries almost the same information.

Some results showing the application of the LFV technique to the crack propagation test are reported in Figures 7 and 8. Figure 7 shows the spectral components of the axle bending vibration measured in the starting phase (Fig. 7a) and in the final stage of the test (Fig. 7b): a number of n xRev harmonics appear in the measured signal, and the increase in the level of vibration is evident for some of these harmonics, namely the 1xRev, 2xRev and 7xRev. This confirms, as expected, that a rotating cracked axle produces an increased level of bending vibration at some integer multiples of the revolution frequency.

Figure 8 compares the trend of the amplitude of the first four harmonics (1xRev to 4xRev) with the number of cumulated loading blocks in the crack propagation experiment. The 2xRev component shows the largest increase in amplitude with the progress of the tests (and hence with the size of the crack) and a nearly monotonically increasing trend. The amplitude of the 1xRev component is also quite sensitive to the number of cumulated loading blocks, but the trend is less clear, probably on account of disturbances such as thermal effects that may produce a bow of the rotating axle. The 3xRev component shows a lower sensitivity to the number of block loading repetitions and a non-monotone trend. Finally the amplitude of the 4xRev component remained very low during the whole crack propagation test. In conclusion, the 2xRev vibration component appears to be the one best suited to be set in relationship with the presence (and possibly with the size) of a propagating crack in the axle.

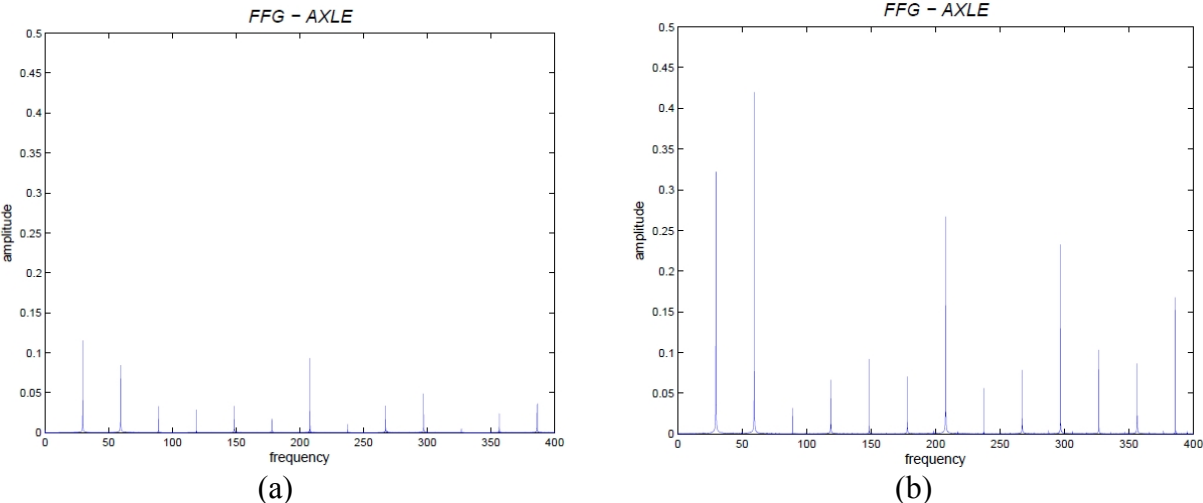


Fig. 7: Change in n xRev components amplitude during crack propagation test: a) initial stage; b) at the end of the test.

4. Concluding remarks

This paper proposes the possible application of two different SHM methods, acoustic emission (AE) and the variation of low frequency vibrations (LFV), to detect the presence of propagating cracks in deep-rolled freight railway axles made of A4T grade and subjected to service load spectra.

A full-scale crack propagation test, performed on a railway axle, was used to assess the effectiveness of the two proposed SHM approaches. The obtained results are encouraging and

show the potential of both methods to represent viable approaches to real-time crack monitoring in railway axles.

In more detail, the amplitude of AE hits is well correlated with the load applied to the axle. More research work is ongoing to further investigate how AE events correlate to crack propagation.

As far as the LFV monitoring technique is concerned, measurements of the bending vibration of a specimen axle taken across a whole crack propagation test show that the level of vibration associated with the 1xRev, 2xRev and 7xRev harmonic components is increasing with the progress of the test, and hence with the size of the crack. Among these components, the 2xRev is the one showing the better correlation with the number of cumulated block loading repetitions. Comparisons with the measured size of the crack are in progress.

Future developments of this work will be aimed firstly to derive a more comprehensive set of conclusions based on more tests carried out on other pre-cracked axles. In case the applicability of one or both methods to crack detection will be confirmed, the research will then aim at solving problems related with transferring the crack detection SHM system from the laboratory to in-service applications.

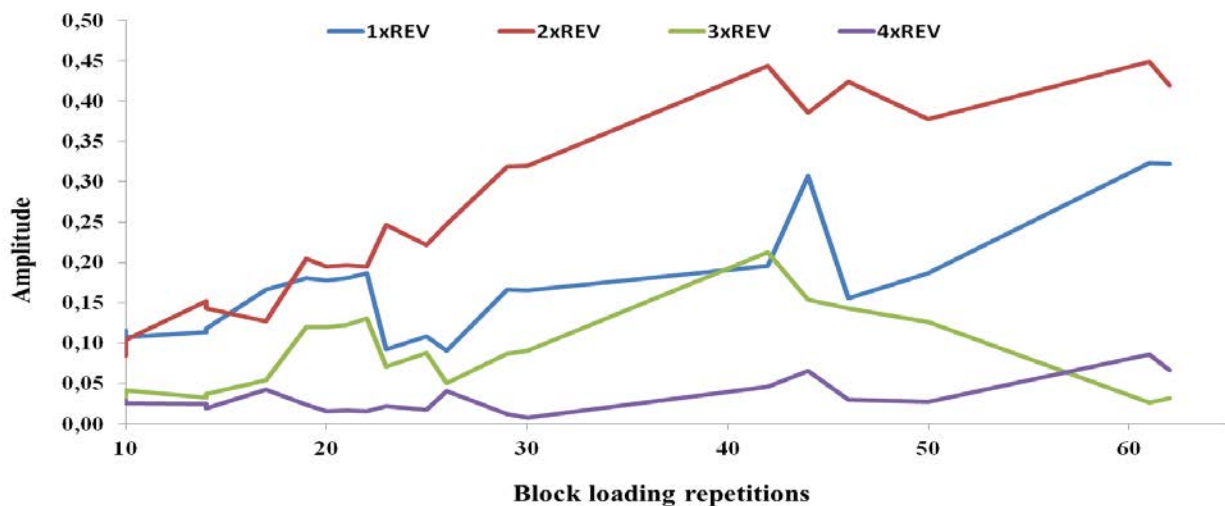


Fig. 8: nxRev components amplitude during crack propagation test.

5. Acknowledgements

The SHM results shown in the present research were obtained in the frame of the SUSTRAIL Collaborative European Project (Grant Agreement #265740). The full-scale crack propagation test is carried out in the frame of the MARAXIL Project co-funded by Regione Lombardia (ID 16973, Rif. n° MAN-15). The authors would like to thank Prof. S. Beretta and Mr. D. Regazzi (Dept. Mechanical Engineering, Politecnico di Milano) for the useful help and discussions.

6. References

- [1] EN 13261, 2011, Railway applications - Wheelsets and bogies - Axles - Product requirements, CEN.
- [2] EN 13103, 2012, Railway applications - Wheelsets and bogies - Non powered axles - Design method, CEN.
- [3] EN 13104, 2011, Railway applications - Wheelsets and bogies - Powered axles - Design method, CEN.

- [4] Grandt A. F. Jr.: *Fundamentals of Structural Integrity*, John Wiley & Sons, Hoboken, New Jersey, 2004.
- [5] Carboni M., Beretta S.: Effect of probability of detection upon the definition of inspection intervals of railway axles, *Proc. Instn Mech. Engrs Part F: J. Rail and Rapid Transit*, Vol. 221, 2007, 409-417.
- [6] Chang F. K.: *Structural Health Monitoring: A Summary Report*, Proceedings of the 2nd International Workshop on Structural Health Monitoring, Stanford, California, 1999.
- [7] Grosse C., Ohtsu M.: *Acoustic Emission Testing*, Springer-Verlag, Berlin Heidelberg, 2008.
- [8] Huang M. et al.: Using acoustic emission in fatigue and fracture materials research, *JOM*, Vol. 50, 1998, 1–12.
- [9] Jiang C., Wen Y., Wang L., Chu M., Zhai N.: Real-time monitoring of axle fracture of railway vehicles by translation invariant wavelet, 2005 International Conference on Machine Learning & Cybernetics, Guangzhou, China, 2005, 2409-2413.
- [10] Pennacchi P., Bachschmid N., Vania A.: A model-based identification method of transverse cracks in rotating shafts suitable for industrial machines, *Mechanical Systems and Signal Processing*, Vol. 20, 2006, 2112-2147.
- [11] Beretta S., Carboni M.: Variable amplitude fatigue crack growth in a mild steel for railway axles: experiments and predictive models, *Eng. Fract. Mech.*, Vol. 78, 2011, 848-862.
- [12] Regazzi D., Beretta S., Carboni M.: The effect of roll-forming onto fatigue life of railway axles, *Proc. 19th European Conference on Fracture*, Kazan, Russia, 2012.
- [13] Vallen AMSY-5 product brochure (archive.org September 2011 version) goo.gl/FLkUL accessed 14/03/2013.
- [14] ASTM E976: *Standard Guide for Determining the Reproducibility of Acoustic Emission Sensor Response*, ASTM International, West Conshohocken, PA, 2010.

NEW PROSPECTS TO USE ACOUSTIC EMISSION DURING SCRATCH TESTING FOR PROBING FUNDAMENTAL MECHANISMS OF PLASTIC DEFORMATION

A. Danyuk, D. Merson, A. Vinogradov

Laboratory of Physics of Strength of Materials and Intelligent Diagnostic Systems, Togliatti
State University, Togliatti, Russia, alexey.danyuk@gmail.com

ABSTRACT

The acoustic emission technique has been widely used during indentation or scratch testing. A common problem is that, when the elementary modes of deformation are of concern, the testing has to be performed locally. Such a testing model implies inevitably in a very small (microscopic) volume involved into plastic deformation under the indenter tip. Therefore, the AE generated during the test has a quite small amplitude hardly distinguishable on a background of the electric noise if the traditional threshold-based acquisition is utilized. With the specific aim at identifying and characterizing fundamental mechanisms of plastic deformation through analysis of AE signals, the present work seeks to offer new strategies in AE acquisition and processing during scratch testing of material to get a better insight on the elementary processes of local plastic deformation. The experiments have been performed on the model pure copper which has been well characterized microstructurally in the local area along the indented path using a scanning electron microscopy. The AE technique appears a viable and powerful tool for investigations of local deformation mechanisms in situ.

Key words: scratch test, deformation mechanisms, acoustic emission, microscopy.

1. Introduction

A broad variety of local destructive or non-destructive methods is applied for routine nondestructive testing as well as for innovative academic research, which benefit strongly from development of modern nano-indentation and kinetic/dynamic micro-indentation and scratching techniques enabling precise characterization of the mechanical behavior of materials and coatings. These techniques have been enjoying booming popularity due to excellent reproducibility of results, high accuracy and capacity to measure the properties of geometrically small objects or local properties in large samples otherwise not assessable in conventional mechanical testing in the laboratory. Overall, these features of local loading techniques has ensured their outstanding reputation and reliability in NDT applications where a rapid and cost-effective evaluation of mechanical properties is required in small objects such as individual grains, grain or phase boundaries. Plenty of valuable information pertinent to the analysis of deformation processes is offered by the post-factum analysis of the morphology of the footprint of the indenter. The real-time information concerning the local behavior of the materials during testing is provided by the kinetic indentation diagram or by the measurements of the friction

coefficient during a scratch-test. However, the temporal resolution of these measurements is not very high to resolve elementary processes of plastic deformation and fracture. To compensate the obvious deficit of the real-time data and provide a new means for characterization of local plastic deformation and fracture, the acoustic emission (AE) technique opens a wide avenue for deriving real time information from a locally deforming object during non-destructive materials evaluation and quantitative characterization of materials properties. The thorough AE analysis enables discrimination between different types of deformation mechanisms and estimation the intensity of AE sources in dependence on the microstructural features and loading conditions. In this way, to turn a modern AE technique to a real quantitative tool for characterization of deformation mechanisms and local properties, it is essential to establish robust relationships between the AE signal and elementary deformation processes. To accomplish this fundamental goal we have chosen a well annealed copper polycrystal with the initial microstructure characterized by orientation image microscopy (OIM) and scanning electron microscopy (SEM). The obvious problem which most researchers have faced while applying the AE measurements to the scratch (indentation) test, is that due to a small deforming volume the cumulative AE signal is small and hardly distinguishable from a background noise if elementary dislocation reactions are of concern. The appealing opportunity is however that local loading allows us to follow the deformation process in its finest details with less interference between different of sources in the AE signal. It is therefore a challenging task for the present work to discriminate the features of dislocation behavior under indenter from a low amplitude AE.

2. Experimental procedure and AE methodology during scratch testing

The samples of technical purity 99.9% polycrystalline copper with dimensions 20x20x2 mm were cut by spark erosion. They were mechanically polished by emery paper to the grade of #2000 and then annealed in vacuum at 1170K for 1 h and furnace cooled. Finally, the front surface of the samples was electrolytically polished for microscopic observations prior to and after the test.

The microstructure was investigated by electron backscattered diffraction (EBSD) measurements in high-resolution FE-SEM ZEISS SIGMA microscope with field emission gun and EDAX/TSL Hikari-5 OIM detector.

To correlate the AE signal with the deformation structure along the scratch path, the crystallographic orientation of grains was determined before test by the EBSD technique, Fig. 1 where the orientation of the grains is inked according to the standard inverse pole figure coding showed in the inset. Depending on the crystallographic orientation of grains, the slip systems with the highest Schmidt factor are activated, i.e. the local texture controls the anisotropy of mechanical properties of the crystallites and the appearance of different slip systems on the surface.

Scratch tests were performed under controlled conditions on the Nanovea Scratch Tester with a Berkovich diamond indenter moving linearly along the sample at constant speed of 12 mm/min. For better quantification of the AE signal during indentation/scratch testing one needs to ensure as high signal-to-noise ratio (SNR) as high as possible. However, as mentioned in the Introduction, scribing of ductile materials such as well-annealed pure fcc metals results typically in low level AE. The measures have to be taken to increase the SNR by proper tuning of the testing rig. The tester was adjusted to minimize the mechanical and electrical noise in the AE recording channels so that the feedback parameters of the mechanical actuator were tuned precisely to a monotonic smooth scratch test. The normal load during the test was chosen below 1 N to minimize the mechanical friction in the vicinity of the indenter tip according to recommendations given in ref. [1]. The final length of the groove was about 2 mm.

The record the AE from dislocation sources operating in a small deforming volume the following conditions imposed onto the sensor and amplifier have to be met:

- minimum internal electrical noise to provide an acceptable SNR;
- maximum sensitivity in the reasonably wide frequency band to enable spectral analysis for source recognition. Assuming that the AE sources during scratching of pure copper would be dislocation segments emerging with a high velocity on a free surface under action of the image force, this type source can be represented simply as a delta-type force function with a wide power spectral density.

The 10 mm diameter piezoelectric sensor AE-9000-S-WB (NF Electronics, Japan), with a frequency band of 100–1000 kHz, was attached with coupling oil on the side of the samples. The signals were passed through low-noise 2/4/6/ pre-amplifier with 60 dB gain and were finally acquired by means of the PIC-2 board (Physical Acoustics Corporation, USA) operated in a continuous threshold-less mode at the sampling rate of 5MSPS. The on-board filters were set in the widest possible range of 20kHz to 2MHz and the additional +6 dB gain was pre-set. The AE waveforms were continuously recorded and synchronized with with the scratch path.

3. Experimental results

The inverse pole figure colored OIM of the surface of copper polycrystal and the view of the scratch across the grain structure is shown in Fig. 1. One can clearly see that during testing the scratch passes through several grains with different orientations, overcomes grain boundaries and triple junctions which well suites the goals of the present work.



Fig. 1: The inverse pole figure colored OIM of the surface of the annealed copper polycrystal and the view of the scratch across the grain structure .

A typical example of the AE signal recorded during scratching is shown in Figure 2. Although the SNR of this signal is quite low for conventional AE testing assuming a threshold based acquisition, it can be considered “reasonably high” for typical scratch testing of a ductile copper sample. In what follows, we shall demonstrate that using appropriate filtering helps to improve the SNR and to reveal some important fine futures of AE sources in the rectified signal.

The AE signal processing workflow includes the following steps:

- 1 A continuous raw stream was divided into frames of 8192 readings.
- 2 For each frame two parameters were calculated in a time domain - the peak U_{peak} and root-mean-square voltage U_{rms} , respectively.
- 3 For each frame the FFT denoising procedure involving forward and inverses FFT was applied, and two parameters were calculated in the frequency domain - Energy (power), E , as the integral over the power spectral density and the Median frequency, F_{median} , as the frequency which separates the low and high frequency spectral domains with equal Energy (power).
- 4 The obtained time series of respective variables (U_{peak} , U_{rms} , Energy or F_{median}) were smoothed by a low-pass Butterworth filtering procedure with the cut-off frequency of 19 Hz.

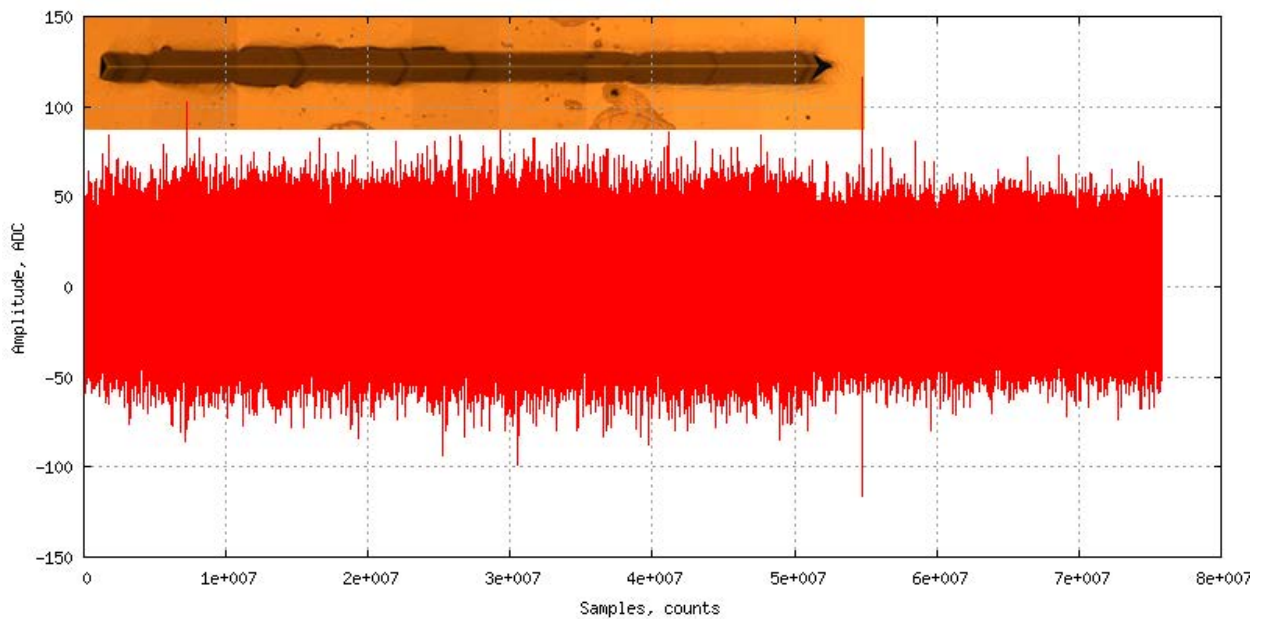


Fig. 2: Continuously recorded raw AE data stream acquired during the scratch test with the view of the scratch groove on the surface superimposed. The indenter moved from left to right under 1 N applied force.

Figure 3 (left hand side) shows the behavior of the AE spectral parameters - Median frequency and Energy as well as Upeak and Urms as defined from the original stream. The low-pass filtering applied to these time-series filters out the high frequency components and reveals the trends, which are shown in Fig 3 (right hand side). The use of this filtering with the cut-off frequency as low as 19 Hz is justified because the grain structure of the annealed specimen is coarse and the indenter propagates a reasonably long time within a homogeneous area within the same grain with the mean size around 0.2 - 0.8 mm. Importantly is that the AE signal reflects well the alternations in the microstructure encountered by the indenter tip when it crosses the grain boundaries. When the transition from one grain to the other occurs, the new slip systems are activated resulting in different hardening, the rate of which depends primarily on the dislocation interaction in the intersecting slip systems. The most pronounced changes in the AE signal are seen in the Energy behavior.

The non-surprising anisotropy of mechanical properties during the scratch test of a copper single crystal has long been recognized [2]. Several early studies highlighted a strong AE dependence on the crystallographic orientation of single crystals [3, 4] and the relation of the AE spectral parameters to the activation of different slip systems [5]. The strong dependence of AE parameters on the crystallographic orientation of the grains during the scratch test can be vividly expressed in a scatter-plot showing the distribution of AE descriptive variables such as Energy and Median frequency, Fig. 4. The clustered pattern corresponding to AE, which is observed in several selected grains (see the inset OIM image), is evident. In this diagram, one can see a set of compact well separated clusters with higher or lower energy and/or median frequency. The position of centroids and the shapes of the clusters depend on the crystallographic orientation, i.e. on the specific dislocation behavior and hardening in different grains. The blue points correspond to AE observed during the indenter propagation through the rest of the specimen.

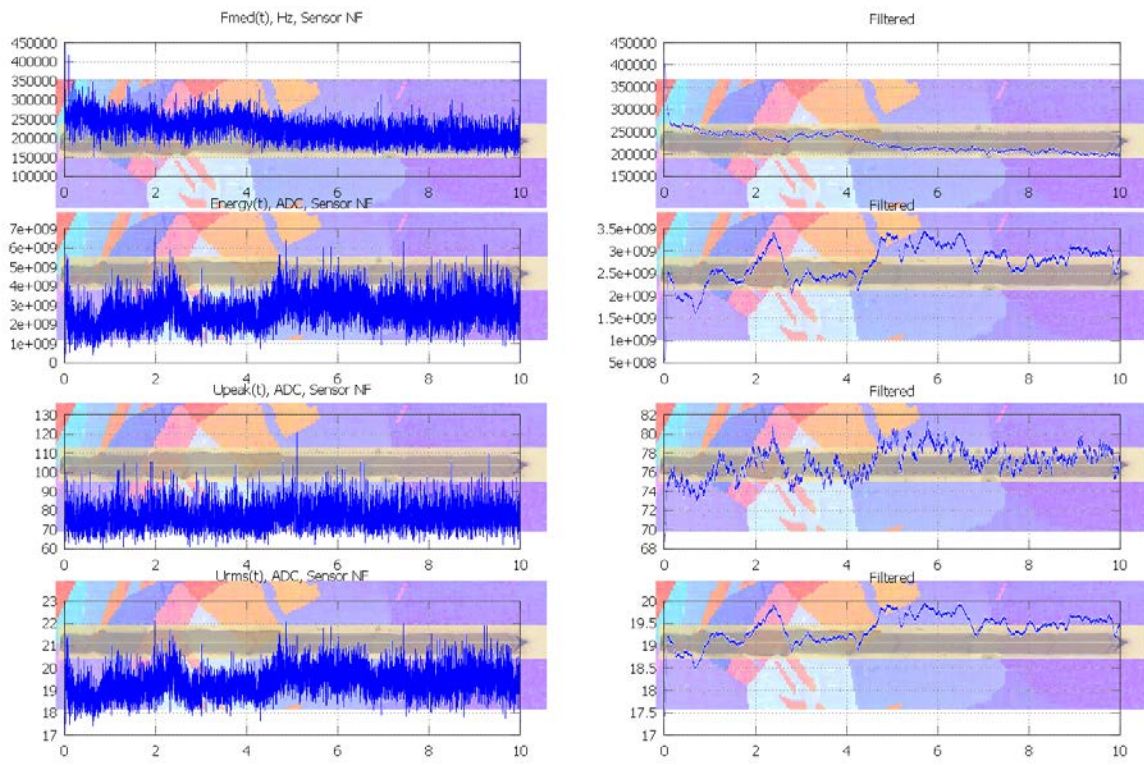


Fig. 3: Evolution AE parameters during scratching: unfiltered data on the left and low-pass filtered data on the right

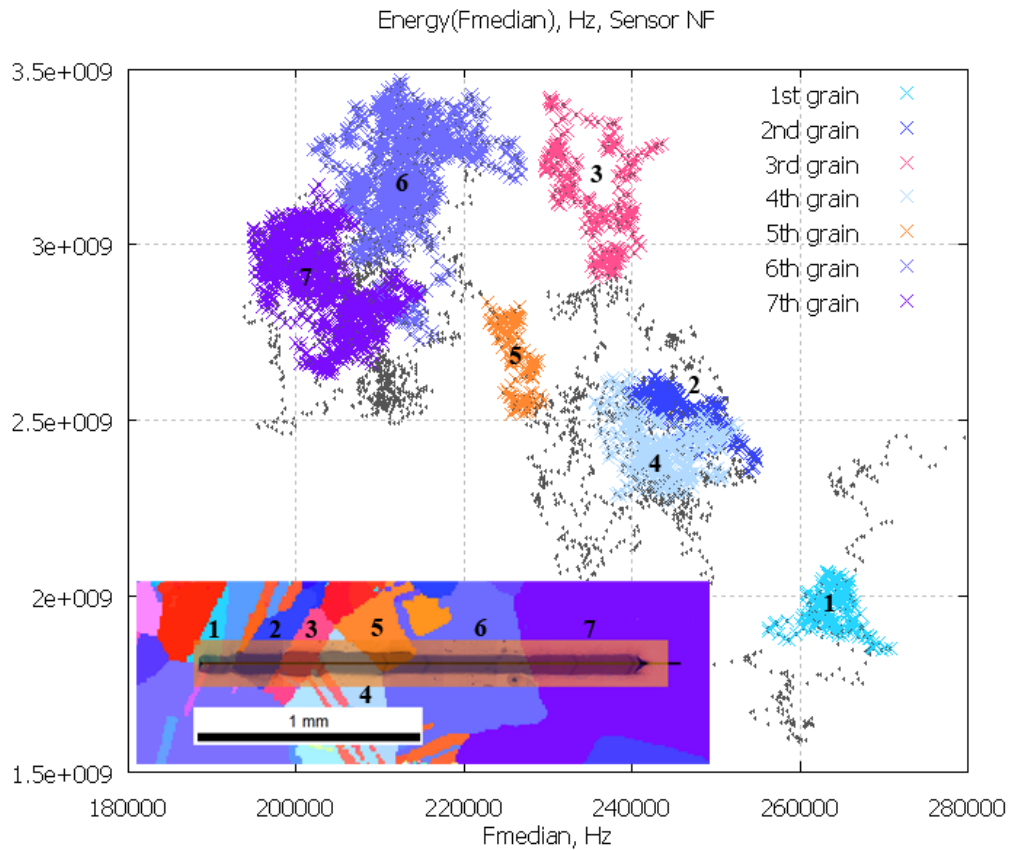


Fig. 4: AE Energy - F_{median} bi-variate distributions highlighting the changes in the AE properties with indenter transition from one grain to the other. The grains are numerically labeled on the OIM map and the corresponding Energy- F_{median} distributions are colored as shown in legend.

The important feature of the AE waveforms, which are recorded typically during plastic deformation mediated by dislocation slip in pure metals, is that they commonly manifest themselves as a continuous noise-like signal, Fig.2. The continuous signal, such as that shown in Fig. 2, is associated with a huge number of dislocation segments generated here and there within the loaded solid and moving nearly concurrently across the grains. However, on a microscopic scale plastic deformation of metals is spatially heterogeneous and temporally intermittent by nature due to discrete origin of carriers of plasticity - lattice dislocations [6-8] creating clearly separated fine slip lines on the surface during deformation, cf. Fig.5. This discrete character of dislocations is the root cause of local fluctuations in stress and strain giving rise to measurable AE. The detectability of AE is commonly supposed to be quite limited [9]. The detectability threshold is of course dependent strongly on the noise level and the capacity of the AE system to discriminate the signals on a background of the electric noise. The latter in turn is temperature dependent. The modern signal processing techniques can substantially improve the SNR making use the key property of the electric noise – its stationarity. The AE signal and noise are additive. Therefore, the stationary spectral characteristics of the noise can be judiciously subtracted from the signal by a variety of methods called commonly “denoising”. Perhaps, the simplest workflow aimed at noise subtraction is based on a Fourier analysis and can be implemented for the continuously streaming AE record as follows:

- 1 The signal is digitally amplified by +14 to +20 dB.
- 2 The noise is identified on the AE stream (usually at the beginning of the end of the stream when the testing rig is off).
- 3 The noise Fourier spectral density is calculated, averaged and used as a baseline for subtraction from the entire data stream.
- 4 Repeat step 1: the denoised signal is amplified again by +40 to +50 dB.
- 4 Repeat steps 2 and 3: evaluation of noise average spectrum and use at again subtract the noise from data.

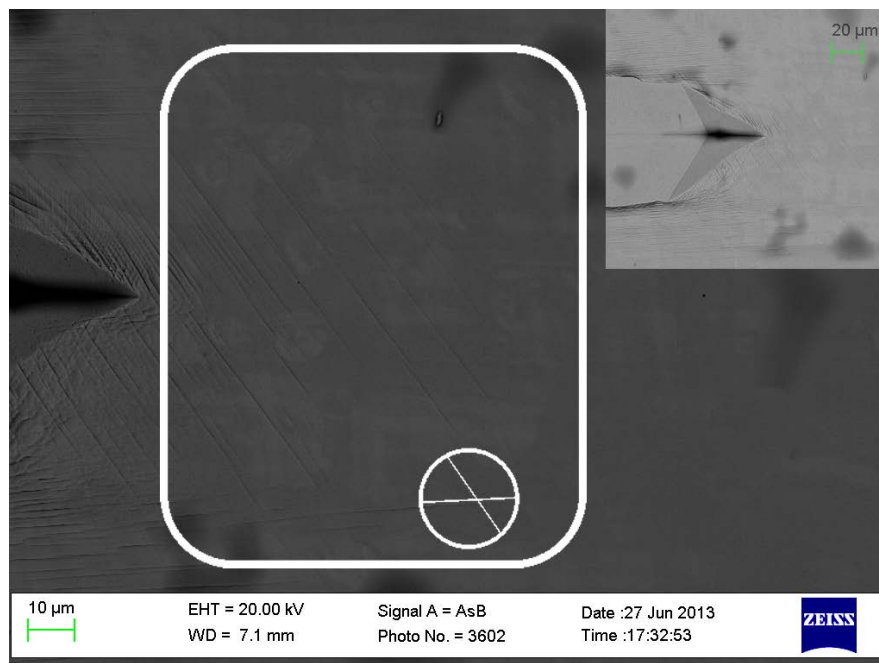


Fig. 5: SEM micrograph showing the dislocation slip pattern ahead of indenter tip. The rectangle indicates approximately the plastic zone where the active sources of AE are seen as individual slip lines in two highlighted slip systems – primary and secondary.

This kind of rectification procedure was applied to the noise-like continuously looking signal shown in Fig. 2. The shape the “denoised” waveform is shown in Fig. 6. We should note that

even a superficial juxtaposition of the raw and filtered signals shown in Figs. 2 and 6, respectively, reveals an obvious differences between these two: (i) the SNR increased spectacularly, revealing fine temporal features in AE, which correspond well to the position of the tip of the indenter during motion, and (ii) the magnified outlook of the waveform (cf. the inset) reveals a discrete nature of the AE time-series at a smaller time scale. The latter observation is particularly important in view of the above discussion on the intermittency of the dislocation glide. The observed small-scale frequent AE bursts. This poses a new challenge for quantification of a real detectability threshold in terms of the number and properties of dislocation segments which can be detected by the AE technique. We do believe that the commonly accepted estimates of the number of cooperatively moving dislocation segments needed for detection of AE signals, which amount to several thousand, are significantly overestimated. The relevant experimental studies are currently in progress and the results will be reported elsewhere.

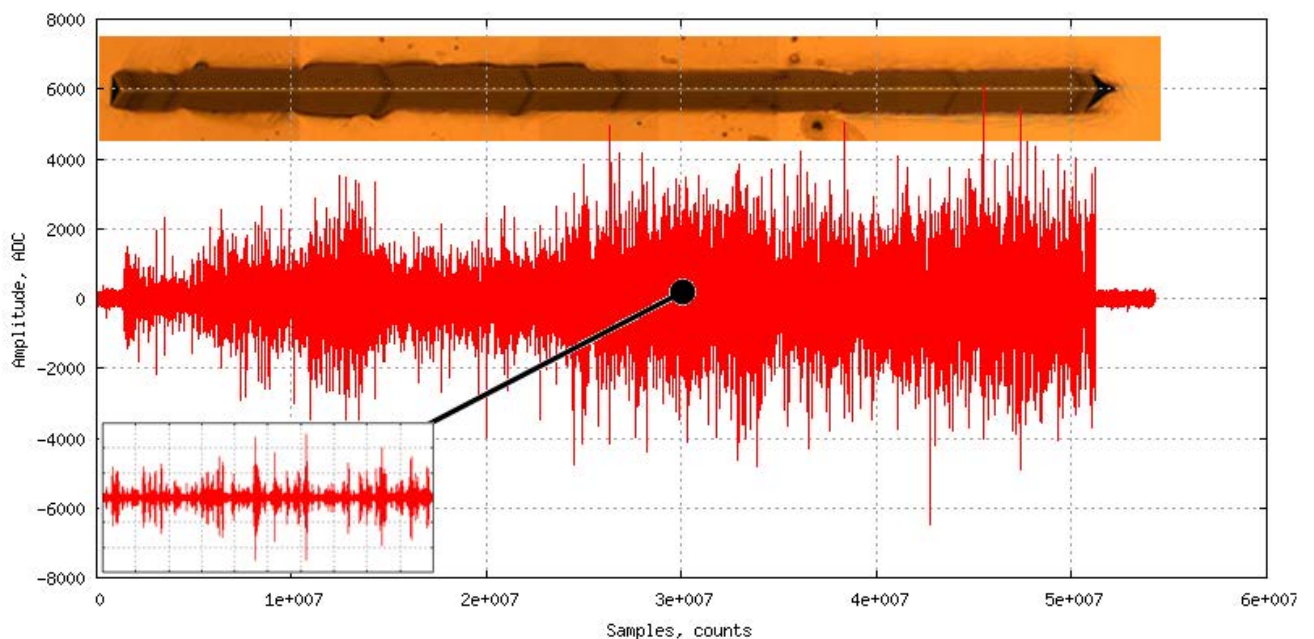


Fig. 6: Stream of AE signal after FT denoising.

The dislocations emerging at a free surface have long been recognized as a very powerful source of AE [10]. The slip lines ahead of the indenter tip form a clear plastic zone. The size of the plastic zone and the elastic stress distribution in the material under the indenter has been evaluated by many authors is reviewed [11, 12]. Regardless of details of models and calculations, most of them merge at a point that in the first order approximation the plastic zone can be considered semi-spherical with tensile stresses ahead the indenter tip. The radius of the plastic zone is evaluated roughly to be 1.5 – 2 of the width of the scratch. The size of the plastic area was estimated in the SEM as shown in Figure 5. The white rectangle encompasses approximately the elastic-plastic area with easy slip lines it is area of "strongest" sources of acoustic emission signal. In circles shown exit direction of shear bands of different slip systems.

Finally, the analysis of the data shown in Figs. 3 and 4 allows us to conclude that most powerful AE (in terms of Urms or Energy) corresponds to the motion of the indenter through the grains with the crystallographic ordinations favoring multiple slip and highest strain hardening rate in fair agreement with former observations performed during tensile deformation of conventional massive single crystals [5]. To summarize this part observing, the sources of AE signal move ahead relative indenter tip at a distance like stress field.

4. Conclusions

Using the annealed model copper specimens with carefully characterized microstructure and post-mortem observations of the dislocation slip traces in the local area along the path of the indenter during the scratch test we demonstrate that the modern AE technique appears as a viable and powerful tool for investigations of local deformation mechanisms *in situ*. The capacity of the AE technique to detect low amplitude events from elementary dislocation slip can be substantially improved if a threshold-less continuous data acquisition and appropriate filtering is utilized. The optimal “denoising” strategy has yet to be found to quantify the real detectability limit of the AE technique.

Acknowledgements

Financial support from the Russian Ministry of Education and Science through the grants-in-aid 11.G34.31.0031 and from the Russian Foundation for Basic Research (RFBR) under project No. 13-08-00259 is gratefully appreciated.

5. References

- [1] Williams J.A., Analytical hardness models of scratch hardness. *Tribology International*, Vol. 29, No. 8, 1996, 675–694.
- [2] Brookes C.A., Green P., Anisotropy in the Scratch Hardness of Cubic Crystals. *Proceedings of the Royal Society London. Series A, Mathematical and Physical Sciences* Vol. 368, 1979, 37–57.
- [3] Bibik ZI. Acoustic-Emission during Deformation of Pure Aluminum Single-Crystals. *Fizika Metallov I Metallovedenie* 1987;63:811.
- [4] Sedgwick RT. Acoustic Emission from Single Crystals of LiF and KCl. *JOURNAL OF APPLIED PHYSICS* 1968;39:1728.
- [5] Vinogradov A, Nadtochiy M, Hashimoto S, Miura S. Acoustic-Emission Spectrum and Its Orientation Dependence in Copper Single-Crystals. *Materials Transactions Jim* 1995;36:496.
- [6] Zaiser M, Seeger A. Chapter 56 Long-range internal stresses, dislocation patterning and work-hardening in crystal plasticity. In: Duesbery FRNNaMS, editor. *Dislocations in Solids*, vol. Volume 11. Elsevier, 2002. p.1.
- [7] Miguel MC, Vespignani A, Zapperi S, Weiss J, Grasso JR. Intermittent dislocation flow in viscoplastic deformation. *Nature* 2001;410:667.
- [8] Richeton T, Weiss J, Louchet F. Breakdown of avalanche critical behaviour in polycrystalline plasticity. *Nature Materials* 2005;4:465.
- [9] Wadley HNG, Mehrabian R. Acoustic emission for materials processing: a review. *Materials Science and Engineering* 1984;65:245.
- [10] Merson D, Nadtochiy M, Patlan V, Vinogradov A, Kitagawa K. On the role of free surface in acoustic emission. *Materials Science and Engineering a-Structural Materials Properties Microstructure and Processing* 1997;234:587.
- [11] Kolesnikov Yu.V., Morozov E.M.: *Contact fracture mechanics*, Nauka, Moscow, 1989.
- [12] Johnson K.L.: *Contact mechanics*, Cambridge University Press, Cambridge, 1985.

MONITORING OF AUTONOMOUS HEALING PROCESS OF CONCRETE BY ACOUSTIC EMISSION AND DIGITAL IMAGE CORRELATION

E. Tsangouri^{1*}, K. Van Tittelboom², N. De Belie², D. G. Aggelis¹ and D. Van Hemelrijck¹

¹Department Mechanics of Materials of Constructions (MeMC), Vrije Universiteit Brussel (VUB), Belgium & SIM program SHE vzw, Technologiepark 935, etsangou@vub.ac.be

²Magnel Laboratory for Concrete Research, Ghent University, Belgium & SIM program SHE vzw, Technologiepark 935

ABSTRACT

In this study, cracking formation and repair due to autonomous healing of concrete beams, tested in two stages of bending (loading-reloading) are reviewed. Encapsulated PU-based healing agent is embedded into concrete beams and is released when crack formation triggers and actuates the chemical repair process. The released agent fills the open crack and seals the fractured area. The potential mechanical recovery of the damage is investigated. Advanced optical and acoustic experimental methods evaluate the mechanical response of the composite material. Acoustic Emission monitors breakage of the capsules embedded into the specimens and locates and quantifies the damage occurred. In parallel, Digital Image Correlation visualizes the controlled crack opening/closure and reopening due to bending. Correlation of the experimental results obtained by both techniques gives a full view of the healing efficiency of the proposed system. Monitoring of potential differentiations at the formation of the fracture process due to capsule breakage phenomena is the main aim of this research.

Key words: cracking of concrete, healing response, capsule breakage, digital image correlation, acoustic emission

1. Introduction

Nowadays, the damage evaluation of concrete elements in which an embedded healing mechanism actuates the fracture recovery is a hot topic in engineering material science. The detection of test conditions under which the healing system is activated is the main topic of this study. Monitoring the experimental activity during concrete bending tests by the use of advanced optical and acoustic methods was done in this study and is a very innovative technique is the key manner and innovation of our research.

2. Autonomous healing of concrete samples monitored by Acoustic Emission and Digital Image Correlation

2.1 Mode-I fracture testing

Crack formation and propagation in normal concrete is frequently studied in literature. The last few decades, different fracture models provide plethora of theories to characterize the damage mechanisms in concrete. Focusing on the simplest case in which cracking forms under pure bending load (Mode-I) the experimental approach to the problem is comprehensively described by RILEM 50-FMC Technical Committee [1]. Concrete beams with a central notch are loaded under three- point bending and the energy and general fracture process is estimated. Application of loading damages the beam by crack formation, initiating from the pre-cracked notch. Unloading of the sample finalizes the testing procedure. Subsequent loading of the sample, re-opens the existing crack and propagates further the damage centrally across the height of the beam.

2.2 Encapsulation of healing agent

Encapsulation healing agent is the most promising autonomous self-healing approach. Van Tittelboom et al. embedded a two- component PU- based healing agent in concrete beams using tubular glass capsules. Damage occur, ruptures the glass tubes, releasing the healing agent. Triggering of material polymerization leads to crack filling and finally sealing and/or healing of the damaged area in short term. Detection of healing actuation during cracking is experimentally investigated by three- point bending tests. A repetition of loading 48 hours after initial crack formation can validate the healing performance [2].

2.3 Monitoring healing actuation and material recovery

In practice, identifying the damage level at which capsule breakage occurs is a challenging task. In this research, monitoring of capsule activation is done by Acoustic Emission (i.e. AE) and Digital Image Correlation (i.e. DIC). Both methods are well-established in experimental mechanics field and are not presented in detail in this paper.

Particularly, in the current experimental configuration, elastic waves released due to capsule breakage during fracture and crack propagation are captured by AE sensors placed at the concrete surface. The signal waveform features give a clear indication of damage characteristics. Furthermore, the location of cracking and capsule rupture is accurately done by using a 3-D location algorithm application [3]. In parallel, DIC full- field overview of cracking provides all the information about the fracture process and the volume of damage. Displacement profiles of the central region of the beam calculate the crack opening and propagation during bending. Strain concentration initially located at the notched pre-crack and distributed across the height of the sample till the end of testing visualize the crack opening-closure (loading stage) and reopening (reloading stage) of the crack [4].

3. Experimental configuration

3.1 Materials

The concrete mix composition is shown in the following table [4]:

Table 1: Concrete beams mixture

MATERIAL	VOLUME (kg/ m3)
<i>Sand 0/4</i>	<i>805</i>
<i>Aggregates 4/8</i>	<i>150</i>
<i>Aggregates 6.3/14</i>	<i>850</i>
<i>Cement CEM I 52.5 N</i>	<i>390</i>
<i>Water</i>	<i>188</i>

A series of concrete samples are casted into wooden molds for 24 hours. After demolding, the specimens are cured under water for 14 days before testing. A notch was created in the samples with dimensions of 840x 100x 100 mm, are pre-cracked by means of a Teflon- slice (dimensions: 10 x 5 mm) standing in the middle of the mold's bottom [1].

The glass tubes are 50 mm long; their inner diameter is 3 mm. Several capsules are filled by injection with the PU- prepolymer and another with catalyzing agent which hardens and expands the prepolymer when the two components come into contact. Pairs of glass capsules are positioned at different locations into the beam. The capsules are attached to thin, poor in stiffness metallic wires crossing the length of the beam in order to insure that during mixing their place is accurately fixed.

The encapsulation system is shown at Fig.1.

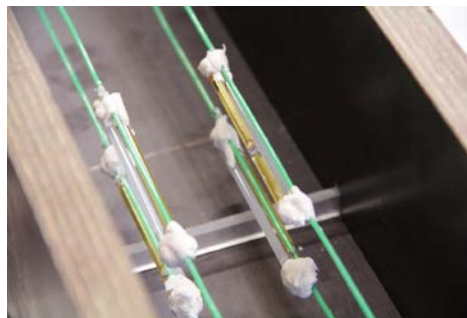


Fig. 1: Capsule placement during casting

3.2 Bending test set-up

An Instron bending machine applies displacement controlled loading by means of pin at the middle of the sample. The beam is placed on supports fixing a bending span of 800 mm. The displacement rate is 0.04 mm/min [1]. A crack mouth opening device (i.e. CMOD) is attached over the pre-crack notch at the bottom of the sample. Guided by EN 14651, CMOD gage mounted to the specimen can provide a precise display of the pre-crack opening.

3.3 Digital Image Correlation test set-up

A DIC speckle pattern is applied by airbrush at one of the white painted sides of the beam. The region at the middle of the beam above the pre-crack notch is chosen as the DIC Area of Interest. Two CCD cameras are placed facing the side of the beam, focused and successfully calibrated at the Area of Interest- AOI. The DIC trigger box synchronizes the images captured every 3 seconds during testing and the data acquisition system stores the images and the load cell values received by the Instron device. Artificial light is used to increase the light contrast and is positioned next to the DIC cameras facing the sample.

3.4 Acoustic Emission test set-up

Eight sensors are placed at the sides and the bottom of the concrete sample. R15 resonant frequency transducers are taped at the surface and mounted by vaseline sealant. During testing, the signals are transferred through pre-amplifiers at the AE computer board and the full configuration of waveform signals is stored. 3D location of AE events and several AE waveform calculated by AEwin software and Noesis post-processing program provides the cracking and capsule breakage damage mode. The location of sensors is shown at Table 2.

The test set-up is presented in Fig. 2 and the AE and DIC technical set-up characteristics are shown in Table 2.



Fig. 2: Test set- up

Table 2: AE and DIC set-up.

channel	X (mm)	Y (mm)	Z (mm)	AE set- up		DIC set-up	
				Threshold	Pre-amplifier	CCD Camera type	Lenses
1	345	25	0	45 dB	40dB	AVT Stingray	23 mm
2	335	75	0	3-D	4.000 m/sec	2456 x 2058	100x100 mm
3	455	50	0	hits/event	min: 4 max: 8	Subset	27x 27
4	445	0	25			Subset spacing	5
5	355	0	75			Strain field size	15
6	335	50	100				
7	465	25	100				
8	475	75	100				

4. Experimental results

4.1 Digital Image Correlation and Acoustic Emission analysis

The loading response indicates regain in strength and stiffness due to healing process. As it is shown in Fig. 3, the maximum load reached during reloading is 55% of the maximum loading case. The response of the healed samples is compared to concrete beams which do not contain healing agent (namely reference beams). Significant recovery of the mechanical properties needs to be correlated further to fracture of the capsules.

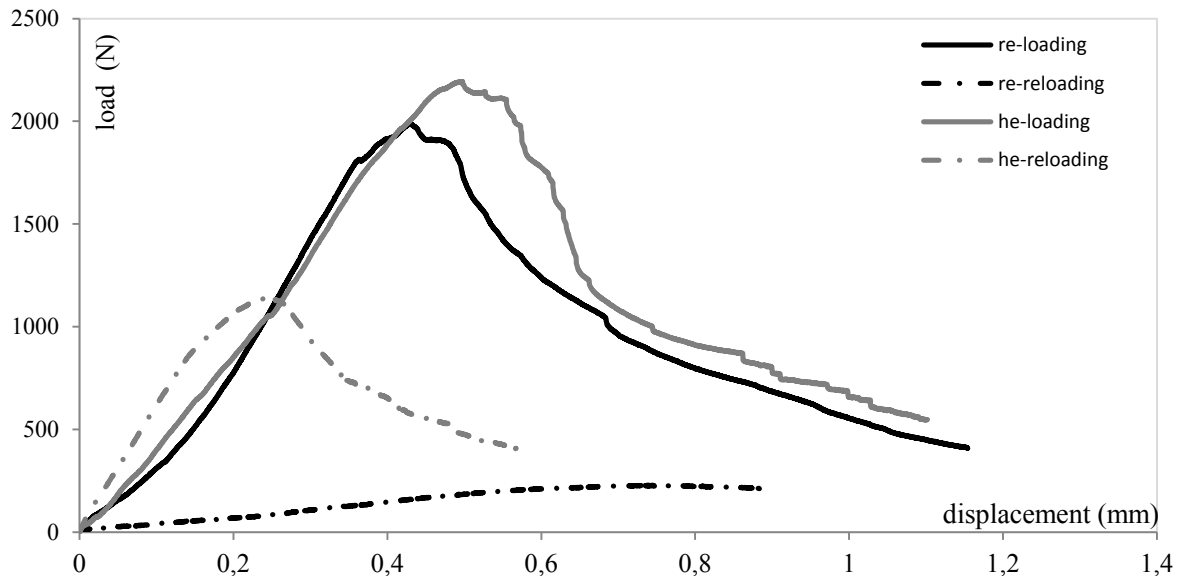


Fig. 3: Loading response comparison between reference (re-) and healed (he-) beams

Acoustic Emission energy activity provides the criterion to classify capsule breakage. It is shown that the hits energy released during capsule breakage is higher than 2000. On the other hand, bending fracture releases energy lower than 1000 in most of the cases (crack opening energy is less than 500). The clustering of cracking and capsule breakage is presented in Fig. 4.

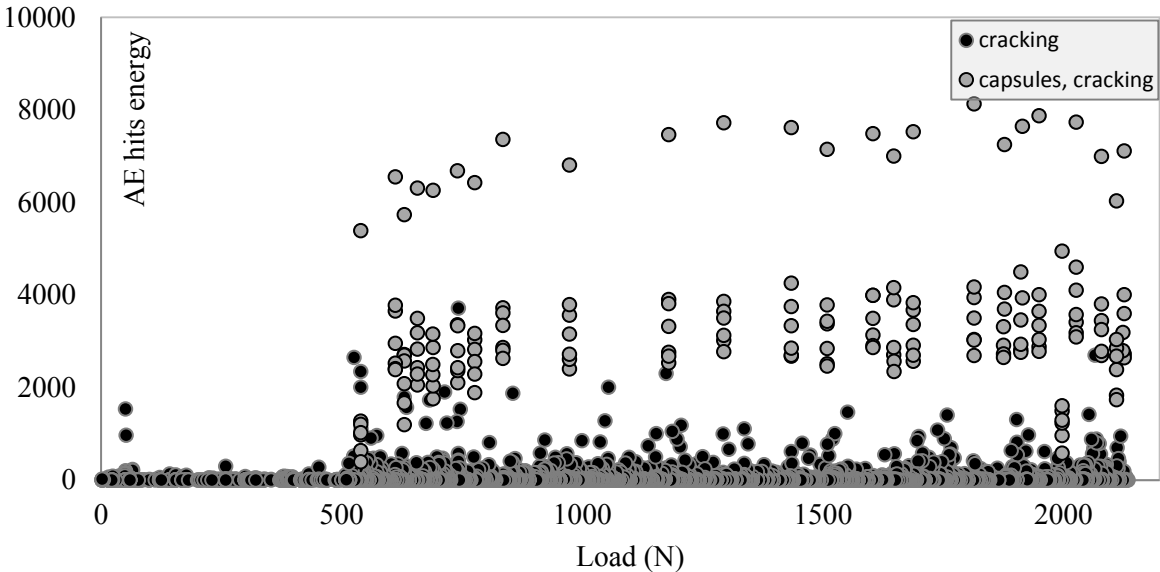


Fig. 4: AE hits energy clustering of capsule breakage and cracking fracture

As it known from fracture mechanics models, the crack propagates further from the notch when the maximum load is reached. In this study, AE energy-based analysis proves that capsules break at the post-peak stage of loading. Rupture of capsules is monitored at the moment crack formation is initiated. Further, as crack propagates capsule breakage events appear in different levels of crack opening. The well- distributed location of AE capsule breakage events can be related to the fact capsules are placed at several beam's heights. The aforementioned observation is graphically shown at the graph of Fig. 5 in which the load and crack opening (CMOD measurements) at the bottom of the sample correspond to moments AE capsule breakage events are detected.

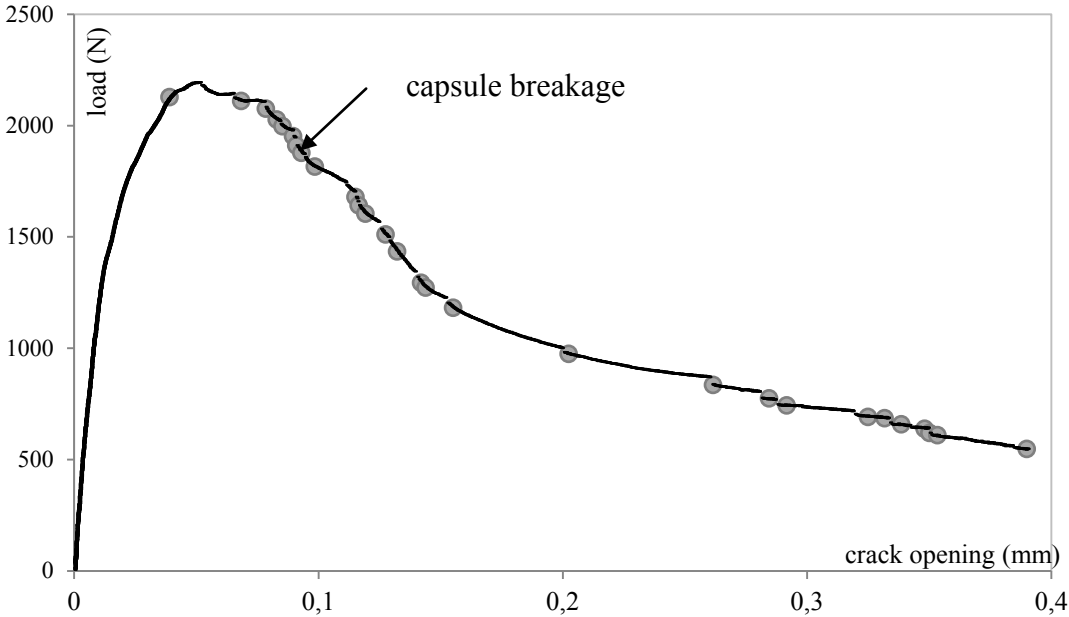


Fig. 5: Capsule breakage location as crack opening occurs

Projecting in 2-D the AE capsule breakage events across the length of the beam and distribution of events across the height of the sample are results in Fig. 6. An AE location algorithm can provide the location of capsule rupture events with an accuracy of 5 mm and indicates the region in which the healing agent is released. The damaged area at the vicinity of AE capsule events may recover. Focusing at the fracture process in that region, further information about the healing mechanism can be derived.

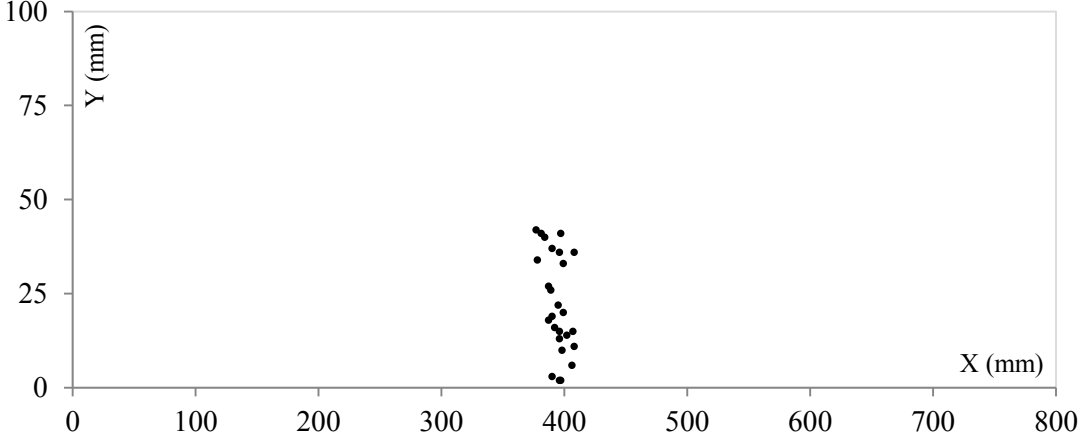


Fig. 6: AE hits energy clustering of capsule breakage and cracking fracture

Observing the location graph above, it is noticed that the crack opening measured at the bottom of the sample by CMOD does not correspond accurately to the crack opening at the place where capsule breakage occurs. Consequently, DIC displacement profiles at the cracked region of the sample contribute to this research. DIC provides information about the crack opening in the full-field of the sample’s side. Measuring the crack opening displacement in time at the bottom and at the top of capsule breakage region located by AE, the following (Fig.7) curves are calculated.

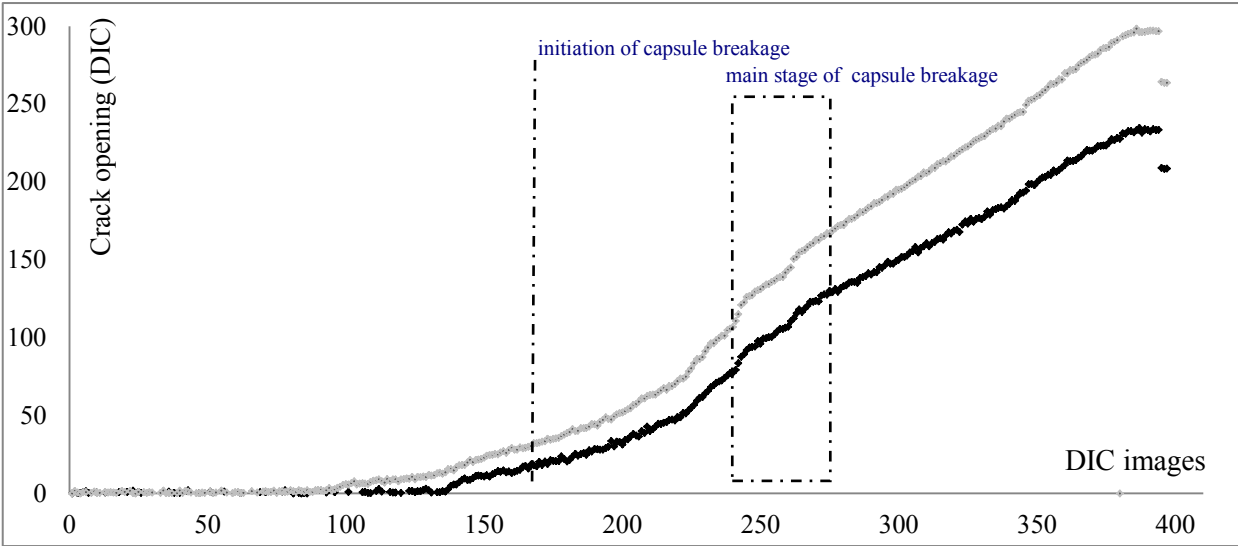


Fig. 7: AE hits energy clustering of capsule breakage and cracking fracture

As it is indicated at the graph above, initial crack fracture appears when the crack is only 25 μm wide. Finally, the stage of loading in which most of the capsule breakage occurs corresponds to a crack range of 80-110 μm and 130-160 μm at the bottom and top of the capsule breakage region respectively.

5. Conclusions

It is concluded that advanced optical and acoustic experimental techniques applied on concrete beams with autonomous healing properties create a promising and full-field view set-up to monitor the fracture and recovery of healing mechanisms. Focusing at the capsule rupture phenomena occurring during testing, AE and DIC combination provides the information required to locate and characterize the fracture phenomena.

6. Acknowledgements

We acknowledge the SIM-SHE program for the financial support and Dr. ing. Kim Van Tittelboom for preparing and providing encapsulated healing agent.

7. References

- [1] RILEM Technical Committee 50-FMC (1985). Determination of the fracture energy of mortar and concrete by means of three-point bend tests of notched beams, proposed RILEM draft recommendations. RILEM, Materials and Structures 18(106), 285–296
- [2] Van Tittelboom K., De Belie N., Van Loo D., Jacobs P., 2011. Self-healing efficiency of cementitious materials containing tubular capsules filled with healing agent, Cement and Concrete Composites, Volume 33, Issue 4, 497–505
- [3] Aggelis D. G., 2011. Classification of cracking mode in concrete by acoustic emission parameters, Mechanics Research Communications 38, 153–157
- [4] Sutton M., Orteu J., H Schreier H., 2009. Image correlation for shape, motion and deformation measurements: Basic Concepts, Theory and Applications

CLUSTERING OF AE SIGNAL AMPLITUDES BY MEANS OF FUZZY C-MEANS ALGORITHM

Rajko Svečko¹, Aleš Hančič², Dragan Kusić² and Janez Grum³

¹ University of Maribor, Faculty of Electrical Engineering and Computer Science
Smetanova 17, 2000 Maribor, Slovenia, rajko.svecko@uni-mb.si

² TECOS Slovenian Tool and Die Development Centre
Kidričeva 25, 3000 Celje, Slovenia, dragan.kusic@tecos.si, ales.hancic@tecos.si

³ University of Ljubljana, Faculty of Mechanical Engineering
Aškerčeva 6, 1000 Ljubljana, Slovenia, janez.grum@fs.uni-lj.si

ABSTRACT

Clustering of numerical measurement data into clusters offers a great potential to find similar objects, which are normally neglected when observing a production process. In this paper, the clustering results obtained with the use of basic fuzzy c-means algorithm on acoustic emission (AE) signal amplitudes are presented. AE signal amplitudes were captured during total of six production cycles of standard polypropylene test specimens under two processing conditions. The final results revealed that the objective function minimization during iterations is very dependent on the number of selected clusters. In case of higher number of clusters the fuzzy c-means algorithm clearly needs more iteration runs to cluster the input dataset.

Key words: Clustering analysis, fuzzy, c-means, centroids, dataset.

1. Introduction

Clustering analysis is a task in which data is grouped into a set of similar objects. Objects in the same group are called cluster and are more similar to each other than to those in other groups (or clusters). Similar objects for example can represent a collection of patterns that are normally formed as a vector of measurements in a multidimensional space. By representing the data with fewer clusters we normally lose certain fine details, but can achieve simplification. Clustering analysis can be divided into:

- hard clustering, where each object can belong to a cluster but not necessarily,
- soft clustering (better known as fuzzy clustering), where each object belongs to each cluster to a certain degree.

From a practical point of view the clustering analysis plays an important role in data mining applications such as medical diagnostics, information retrieval, industrial data exploration, pattern classifications, and many others. Typical cluster analysis activity of patterns involves only a few easy steps, such as: pattern representation, definition of a distance measure (function

like for example Euclidean distance) that is appropriate for the given data, grouping (clustering), abstraction of data (not always needed) and output assessment (if its needed).

The ordinary c-means algorithm is one of the most popular clustering algorithms and is still used in scientific and industrial applications. Each of k clusters $C_{j=1..k}$ is represented by the mean (or weighted average) c_j of its points known as centroid. The sum of differences between a data point and its centroid, which is expressed through appropriate distance, is used as the objective function. During each iteration the objective function is then minimized until the predefined stopping criteria is reached.

In fuzzy clustering the data points can belong to more than one cluster. Membership levels are associated with each data point and are later used for assigning these data points to one or more clusters. Among many fuzzy clustering algorithms the Fuzzy C-Means (FCM) algorithm, which was introduced by Bezdek, is most widely used [1-16]. A short description of the fuzzy c-means algorithm is shown in the next subchapter.

2. Experimental procedure

2.1 Description of the Fuzzy C-means clustering algorithm

Majority of known fuzzy clustering algorithms are based on optimization of ordinary (basic) c-means objective function or by its modification. As already previously stated the majority of today's fuzzy clustering algorithms is usually based on minimization of the fuzzy c-means objective function, which is formulated as

$$J(Z;U,V) = \sum_{i=1}^c \sum_{k=1}^N (\mu_{ik})^m \|z_k - v_i\|_A^2 \quad (1)$$

where

$$U = [\mu_{ik}] \in M_{fc} \quad (2)$$

is a fuzzy partition matrix of data $Z = \{z_1, z_2, \dots, z_N\}$,

$$V = [v_1, v_2, \dots, v_c], \quad v_i \in \mathbf{R}^n \quad (3)$$

is a vector of cluster center that have to be determined,

$$D_{ikA}^2 = \|z_k - v_i\|_A^2 = (z_k - v_i)^T A (z_k - v_i) \quad (4)$$

is a squared distance norm A from point z_k to center of cluster i , and

$$m \in [1, \infty) \quad (5)$$

is a parameter that determines the fuzziness of the resulting clusters. The minimization of the objective function represents a nonlinear optimization problem that can be solved during iterative minimization or for example, with genetic algorithms. It can be shown that if $D_{ikA}^2 > 0$, for all i, k and $m > 1$, then $(U, V) \in M_{fc}$ may minimize the objective function only if

$$\mu_{ik} = \frac{1}{\sum_{j=1}^c (D_{ikA} / D_{jkA})^{2/(m-1)}}, \quad 1 \leq i \leq c, \quad 1 \leq k \leq N, \quad (6)$$

and

$$v_i = \frac{\sum_{k=1}^N (\mu_{ik})^m z_k}{\sum_{k=1}^N (\mu_{ik})^m}, \quad 1 \leq i \leq c. \quad (7)$$

The fuzzy c-means algorithm iterates through the last two Equations 6 and 7. The last equation gives v_i as a weighted mean of the data items that belong to a cluster and the weights are the membership degrees.

A short summary of the fuzzy c-means algorithm can be expressed in a few simple steps: For a given dataset Z , we first choose the number of clusters $1 < c < N$, termination tolerance $\varepsilon > 0$, norm matrix A and the weighting exponent $m > 1$. The fuzzy partition matrix is randomly initialized in such form that $U \in M_{fc}$.

For $l = 1, 2 \dots \max$. repeat

- step 1: compute the cluster means with $v_i^{(l)} = \frac{\sum_{k=1}^N (\mu_{ik}^{(l-1)})^m z_k}{\sum_{k=1}^N (\mu_{ik}^{(l-1)})^m}, \quad 1 \leq i \leq c.$
- step 2: distance computation $D_{ikA}^2 = (z_k - v_i^{(l)})^T A (z_k - v_i^{(l)}), \quad 1 \leq i \leq c, \quad 1 \leq k \leq N.$
- step 3: Update the partition matrix for $k=1:N$, and if $D_{ikA} > 0$, and $i=1:c$ then $\mu_{ik}^{(l)} = \frac{1}{\sum_{j=1}^c (D_{ikA} / D_{jkA})^{2/(m-1)}},$ otherwise $\mu_{ik}^{(l)} = 0$ if $D_{ikA} > 0$, and $\mu_{ik}^{(l)} \in [0,1]$ with $\sum_{i=1}^c \mu_{ik}^{(l)} = 1.$

until $\|U^{(l)} - U^{(l-1)}\| < \varepsilon.$

As can be seen from the above description the clustering process stops when the maximum number of iterations is reached or when the objective function improvement between two consecutive iterations is less than the minimum amount of specified improvement.

2.2 Dataset preparation

For testing the fuzzy c-means algorithm we used the acoustic emission measurement results that were obtained during injection molding of standard test specimens. Acoustic emission measurement system AMSY-5 from Vallen-Systeme GmbH was used for capturing and analyzing the AE signals. Amplitudes of the acoustic emission signals can be given in the form of a voltage, but it is usually converted into decibels by the following equation

$$A_{AE} = 20 \log \left(\frac{|V(t)|}{V_r} \right) \quad (8)$$

whereas $V(t)$ is the maximal measured voltage of AE signal and V_r is the reference input voltage on preamplifier, which was in our case equal to 0.001 mV [17-18].

We closely focused just on the AE signal amplitudes dataset (expressed in dB) that were obtained in two different production runs. Here we used two different set of processing parameters and each test was repeated 3 times. The melt temperature was set in both test runs to 240 °C same as filling pressure (1100 bar), holding pressure (300 bar). We varied the injection speed from 40 mm/s to 50 mm/s, the holding time from 3 s to 5 s and cooling time from 10 s to 6 s. In this way during test specimens production the captured AE signal amplitudes dataset was prepared for clustering analysis, as can be seen in Fig. 1.

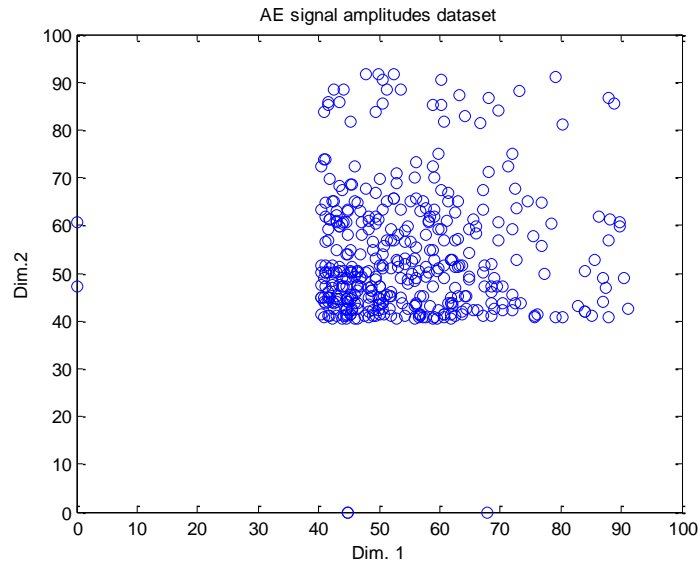


Fig. 1: Preparation of AE signal amplitudes dataset for clustering.

3. Experimental results

On the given experimental dataset we tested the fuzzy c-means algorithm by specifying two different cluster numbers. In the first part, we defined 3 clusters and calculated the final centroids position and surface of the membership function. We set the weighting exponent to 2, termination tolerance was set to 0.00001 and the maximal iteration number was set to 100. In the second part, we defined 6 clusters and tested the algorithm under same predefined values. Before the start only the fuzzy partition matrix is randomly initialized. The weighting exponent is an important parameter since it has a large influence on fuzziness of the resulting partition. On Fig. 2 the final results are presented which were obtained for 3 clusters. The final position of each cluster centroid is shown in Table 1.

Table 1: Final centroid positions for 3 clusters.

Cluster centroid number	Dim.1	Dim.2
1	47.077	47.027
2	53.095	70.161
3	68.252	48.731

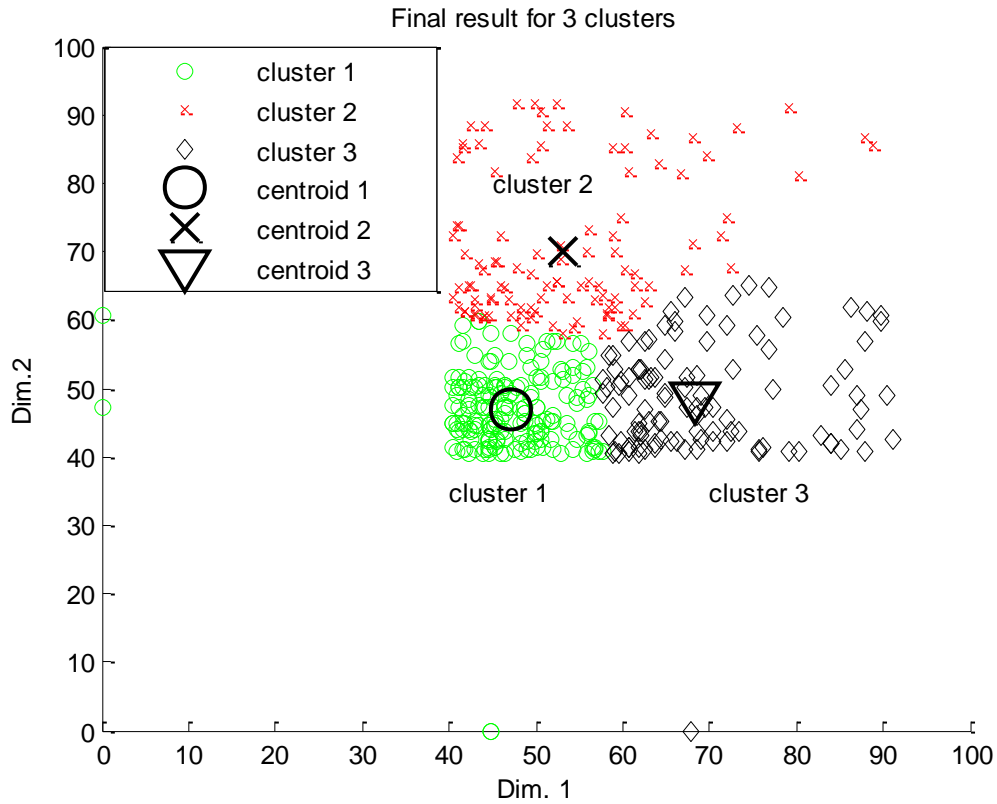


Fig. 2: Final clustering analysis result obtained for 3 clusters.

From Fig. 3 we can see that the objective function was successfully minimized during iterations and that fuzzy c-means algorithm grouped the clusters finally after 16 iterations. In Fig. 4 the membership function surface obtained at cluster 1 is presented and confirms that objective function represents in fact a nonlinear optimization problem.

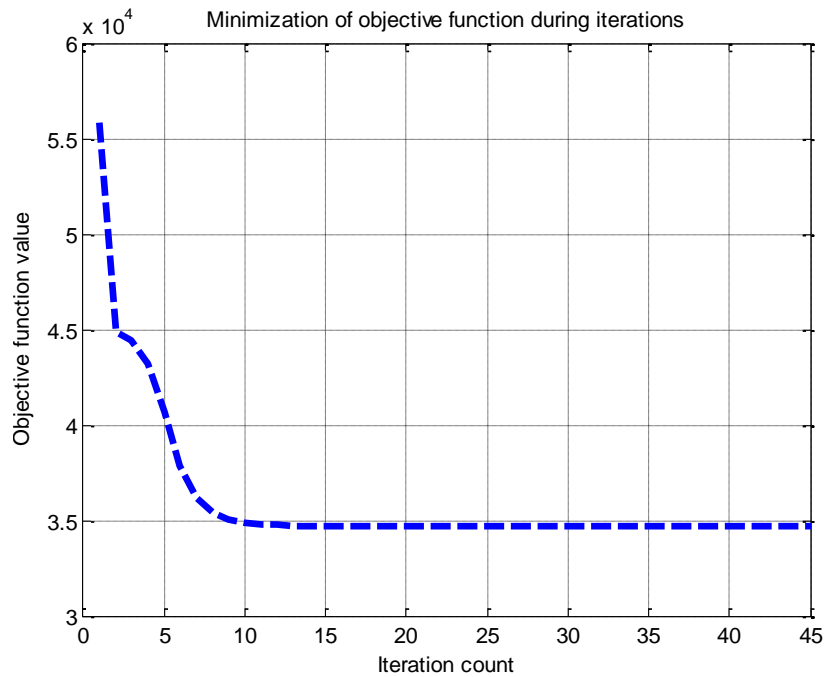


Fig. 3: Objective function minimization during iterations (3 clusters).

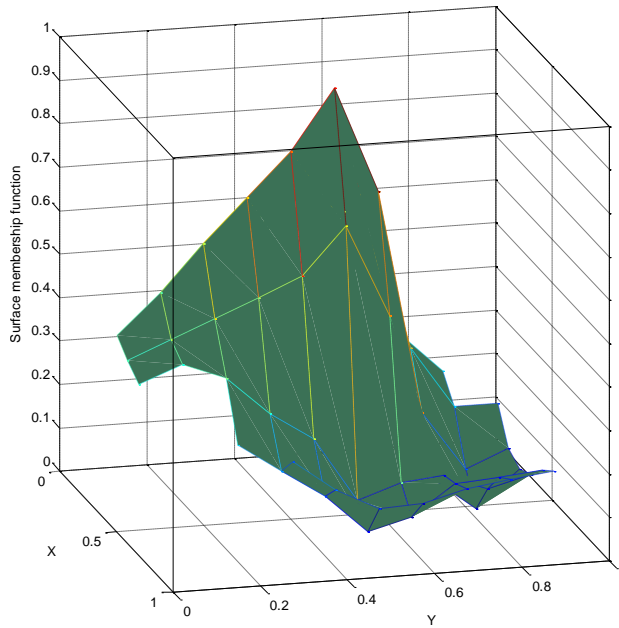


Fig. 4: Example of surface membership function obtained for cluster centroid 1.

In the second phase we selected 6 clusters and the final position of each cluster centroid is shown in Table 2.

Table 2: Final centroid positions for 6 clusters.

Cluster centroid number	Dim.1	Dim.2
1	45.441	45.519
2	45.888	61.848
3	82.167	47.468
4	53.499	85.877
5	60.699	44.636
6	61.166	61.027

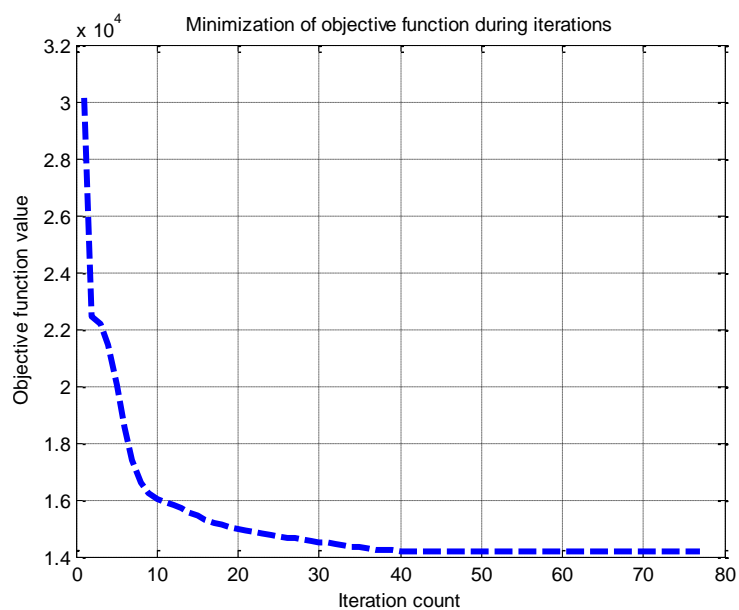


Fig. 5: Objective function minimization during iterations (6 clusters).

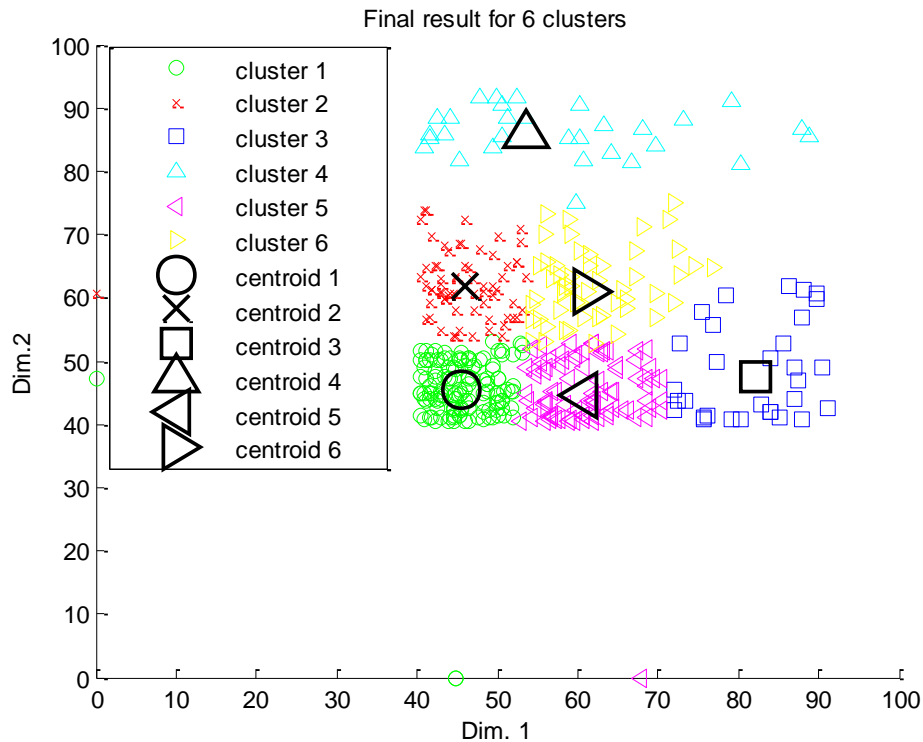


Fig. 6: Final clustering analysis result obtained for 6 clusters.

In Fig. 5 we can notice that the objective function was successfully minimized during iterations and that fuzzy c-means algorithm grouped the clusters finally after 45 iterations. From Fig. 6 the final results for 6 clusters with their centroids are shown. By comparing the results in Fig. 2 and Fig. 6 we can state that the defined number of cluster has a strong influence on the fuzzy c-means performance during iterations. As can be seen in Fig. 3 and Fig. 5 the number of iterations necessary to achieve the local minimum of the objective function in case of 6 clusters is 3-times higher.

4. Conclusions

In this work the results of clustering analysis conducted on AE signal amplitudes with fuzzy c-means algorithm are presented. Our results confirmed the fact that the preselected number of clusters has a large impact on the fuzzy c-means algorithm efficiency in case when the rest of parameters are fixed and not varied, such as fuzziness exponent, termination tolerance and norm matrix $A=I$. Overall performance of such clustering algorithms is influenced also by the density of individual clusters, their spatial relations and their distances. A lack of this algorithm is the fact that it converges to local minimum of the functional. So in cases when a different initialization is used we obtain often different results. Additional improvements of this algorithm are possible mainly in the direction of changing the objective function, distance measure and by varying the above mentioned parameters of this algorithm.

Acknowledgement

The research work was partly financed by the European Union, European Social Fund, and by the Slovenian Ministry for Higher Education, Science and Technology.

5. References

- [1] Bezdek J.C., Ehrlich R., Full W.: FCM: The fuzzy c-means clustering algorithm, *Computers & Geosciences*, Vol. 10, 1984, 191-203.
- [2] Bezdek J.C., Chuah S.K., Leep D.: Generalized k-nearest neighbor rules, *Fuzzy Sets and Systems*, Vol. 18, 1986, 237-256.
- [3] Pal N.R., Bezdek J.C., Hathaway R.J.: Sequential Competitive Learning and the Fuzzy c-Means Clustering Algorithms, *Neural Networks*, Vol. 9, 1996, 787-796.
- [4] Flores-Sintas A., Cadenas J., Martin F.: Membership functions in the fuzzy C-means algorithm, *Fuzzy Sets and Systems*, Vol. 101, 1999, 49-58.
- [5] Liu J., Xu M.: Kernelized fuzzy attribute C-means clustering algorithm, *Fuzzy Sets and Systems*, Vol. 159, 2008, 2428-2445.
- [6] Ji Z., Sun Q., Xia Y., Chen Q., Xia D., Feng D.: Generalized rough fuzzy c-means algorithm for brain MR image segmentation, *Computer Methods and Programs in Biomedicine*, Vol. 108, 2012, 644-655.
- [7] Kannan S.R., Ramathilagam S., Devi R., Hines E.: Strong fuzzy c-means in medical image data analysis, *Journal of Systems and Software*, Vol. 85, 2012, 2425-2438.
- [8] Chuang K.S., Tzeng H.L., Chen S., Wu J., Chen T.J.: Fuzzy c-means clustering with spatial information for image segmentation, *Computerized Medical Imaging and Graphics*, Vol. 30, 2006, 9-15.
- [9] Wang H., Fei B.: A modified fuzzy C-means classification method using a multiscale diffusion filtering scheme, *Medical Image Analysis*, Vol. 13, 2009, 193-202.
- [10] Huang P., Zhang D.: Locality sensitive C-means clustering algorithms, *Neurocomputing*, Vol. 73, 2010, 2935-2943.
- [11] Yang J.F., Hao S.S., Chung P.S.: Color image segmentation using fuzzy C-means and eigenspace projections, *Signal Processing*, Vol. 82, 2002, 461-472.
- [12] Tsekouras G.E.: On the use of the weighted fuzzy c-means in fuzzy modeling, *Advances in Engineering Software*, Vol. 36, 2005, 287-300.
- [13] Zhang D.Q., Chen S.C.: A novel kernelized fuzzy C-means algorithm with application in medical image segmentation, *Artificial Intelligence in Medicine*, Vol. 32, 2004, 37-50.
- [14] Goktepe A.B., Altun S., Sezer A.: Soil clustering by fuzzy c-means algorithm, *Advances in Engineering Software*, Vol. 36, 2005, 691-698.
- [15] Mukherjee D.P., Pal P., Das J.: Sodar image segmentation by fuzzy c-means, *Signal Processing*, Vol. 54, 1996, 295-301.
- [16] Chtioui Y., Bertrand D., Barba D., Dattee Y.: Application of fuzzy C-Means clustering for seed discrimination by artificial vision, *Chemometrics and Intelligent Laboratory Systems*, Vol. 38, 1997, 75-87.
- [17] Vallen H.: *Acoustic Emission Testing: Fundamentals, Equipment, Applications*, Vol. 6, Castell Publication Inc., Wuppertal, 2006.
- [18] Miller R. K., Hill E.v.K., Moore P. O.: *Nondestructive Testing Handbook*, Third edition, Vol. 6, *Acoustic Emission Testing*, American Society for Nondestructive Testing, Inc., 2005.

ENHANCEMENT OF EFFICIENCY OF TRIBOLOGICAL TESTING BY USING ACOUSTIC EMISSION MEASUREMENTS

I. Rastegaev, D. Merson, A. Vinogradov

Laboratory for the Physics of Strength of Materials and Intelligent Diagnostic Systems,
Togliatti State University, Belorusskaya str., 14, Togliatti, 445667, Russia,
E-mail: RastlgAev@yandex.ru, D.Merson@tltsu.ru, alexei.vino@gmail.com
www.intelligent-lab.ru

ABSTRACT

The last two decades saw an explosive growth of research activities in the non-destructive testing and quality control of a board variety of tribological materials and units. The substantial amount of data has been accumulated to date, proving the efficiency of the modern acoustic emission (AE) technique for tribological examinations of materials and coatings using a single-contact tribometer. In the present work we review the available knowledge and align it with our original investigations using standard linear reciprocating tribometers (ball-on-disk, ball-on-cylinder, ball-on-plate) and the rotary tribometers (ball-on-disk, ball-on-plate, cylinder-on-cylinder and four-ball friction machines).

Key words: friction and wear, deformation mechanisms, health monitoring, real-time analysis.

1. Introduction

The use of standardized types of contact friction machines and methods, e.g. [1-5] allows for reasonably interpretable, reproducible and comparable results obtained by different researchers. A strong demand still exists in accelerated tribological testing routines without compromising the ability of restoration of the history of contact surfaces damage during the test. One effective way to solve this problem is to replace the "post mortem" microscopic investigations and weighting studies by the "in-situ" acoustic emission (AE) monitoring.

Several threshold-based AE techniques aimed at reaching this goal are known [6]. However, the AE analysis of AE therein is limited to few most common parameters such as the number of oscillations in the signal N , total count N_{Σ} , count rate \dot{N} , signal amplitudes A and their distribution $n(A)$, and "pseudo" energy / power loosely defined as combinations of the above parameters as $A \cdot N$, $A \cdot N_{\Sigma}$, $A \cdot \dot{N}$ or $A^2 \cdot \dot{N}$. These parameters have historically gained their popularity due to simplicity in their hardware implementation. On the other hand, the use of some of them, e.g. A , N and their derivatives, has been physically justified [6] as follows. Under normal conditions of friction (linear wear law) and permanent influencing factors (load P , sliding speed v), area of the damaged layer / lubricant layer S_0 appears to be proportional to N , the number of wear particles formed is proportional to the AE amplitude $n_{\Sigma} \sim A$, the volume rate of wear $\Delta \dot{m}$ is proportional to $\bar{A} \cdot \dot{N}$, and the identification of the source type of AE control the

running, the transition between the different mechanisms of wear and performance of lubricants is determined by the ΔA , $\Delta \dot{N}$ and $\Delta n(A)$. Identification of the AE source, control of wear-in, transition between different wear mechanisms and lubricant efficiency is related to variations in respective parameters ΔA , $\Delta \dot{N}$ and $\Delta n(A)$.

From definitions given in ref. [7] it follows that N_{Σ} , N и \dot{N} are only indirectly related to the source power (through the number of counts exceeding the discrimination threshold A_{th}). To the contrast, the amplitude A does not deliver any information of the source activity. Parameters $\bar{A} \cdot \dot{N}$ and $A^2 \cdot \dot{N}$ are strongly threshold dependent. They are hardly to be well calibrated due to lower bond limits threshold limits by the threshold and the upper bond limits by the throughput rate limits. Besides, due to these limitations of the conventional AE apparatus, the $\bar{A} \cdot \dot{N}$ and $A^2 \cdot \dot{N}$ values are crudely evaluated either for the pulses of amplitudes which are significantly higher than the threshold or for the large averaging time (typically of 1 s) [6].

2. Experimental

From the above preceding section it follows that, the threshold-less strategy of AE data recording can be most beneficial for maximum efficiency of the integral evaluation of AE during sliding wear. Thus, in the present work we employed continuous recording of the AE Envelope Y and the root-mean-square, RMS, obtained in the analogue circuits as:

$$Y(T) = \frac{1}{T} \int_0^T |A(t)| dt \quad (1)$$

$$RMS(T) = \sqrt{\frac{1}{T} \int_0^T A(t)^2 dt} \quad (2)$$

where T is the integration time and $A(t)$ is the instant voltage at the sensor output as a function of time. The time $T = 0.1$ s was empirically chosen to smooth out the electric noise yet to follow the details of AE bursts. To characterize the AE waveforms, they were digitally recorded. Each frame of 1.3 ms duration contained 8192 readings. Frames were triggered periodically by timer with 19 ms period. Hence, during the time interval T of 6 AE frames were captured. AE recording was carried out in a frequency range 50÷1000 кГц with total gain 40 dB using a home-built system having ADC boards La-1.5PCI-14 and La-N20-12PCI at the core. The maximum irregularity of the sensor frequency response in this band did not exceed +- 5 dB. The sampling rate for parametric data and AE envelope and RMS was 1 kHz, while the AE waveform were samples at 6.25 MHz.

The tribological tests were performed on (i) a four-ball friction tribometer, (ii) universal tribometer with a rotating and reciprocating stage Nanovea and (ii) an original valve-roller friction machine designed at AutoVAZ Ltd., Togliatti, Russia. The test schematics for turning, rotation, circular and spiral movement and reciprocal sliding is shown in Fig. 1, where P is the load, w and v are the cyclic and linear velocities, respectively, e is the axis offset. implement: spinning, rotation, circular and spiral movement and reciprocal sliding. The AE sensor was securely mounted on a housing in the intimate vicinity to the friction pair.

The following contact materials were used as typical friction pairs: the balls of the bearing steel ShH-15 of 12.7 (Fig.1a) and 6.0 mm (Fig.1b), the plates of steels 20 and 45 of 30×40×5 mm (Fig.1b), cylinder of 40HGNM steel or Aluminum alloy AMG3 of \varnothing 8 mm and rollers made of cast Iron Gh190 of 50 mm diameter and 5 mm width (Fig.1c). Both dry and lubricated friction conditions were used with the following lubricants: water, SHRUS-4M, Renolit IP 1619, LITOL-24, Unirex-3, FIOL-1, SAE 10W-40 «Lukoil-Standard».

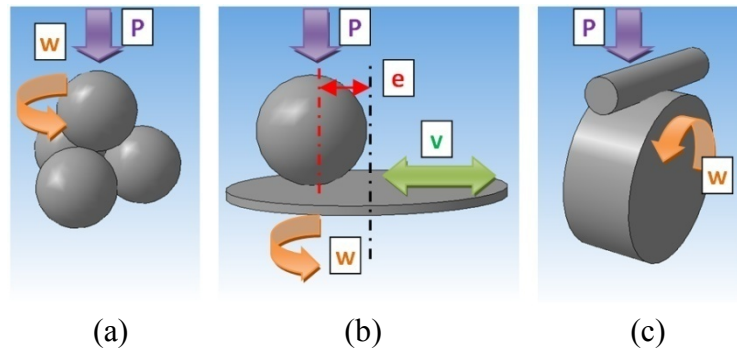


Fig. 1. Schematics of friction units: (a) four-ball friction tribometer, (b) universal tribometer and (c) valve-roller friction machine.

The standard tribological techniques, which were used in the present work, are mainly summarized as:

1. Comparative analysis of wear (Δm) at constant influencing factors ($P = \text{const}$, $v = \text{const}$) for a given constant period of testing time ($t[\text{s}] = \text{const}$);
2. Comparative analysis of time $t[\text{s}]$ to the appearance of the signatures of critical wear at $P = \text{const}$ and $v = \text{const}$;
3. Step-wise increasing loading ($\uparrow P$) at constant linear velocity of the reciprocating motion $v = \text{const}$) and identification of the load P_k or P_c when scoring or edging sets in, respectively.

Microscopic investigations and the calculation the volume of the edged metal and the area of the frictional seizure were performed by means of the 3D surface profilometry of the wear spots. The Olympus LEXT OLS4000 laser confocal microscope was used for this purpose.

3. Results of AE analysis

Despite the differences in test procedures, schedules and types of friction all observed patterns of the AE Envelope and RMS can be reduced to the two types presented in Fig. 2.

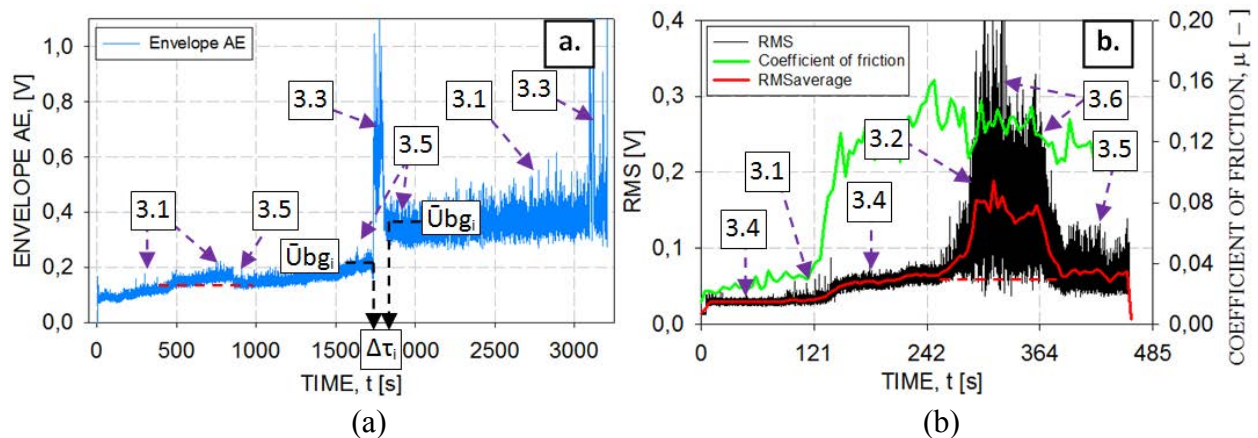


Fig. 2. AE patterns during friction testing using (a) four ball tribometer and (b) universal tribometer with a reciprocating motion.

It was observed that the behavior of the AE envelope Y and RMS does not differ significantly under similar conditions. In what follows we shall label them by the same symbol \bar{U} . Main experimental findings are summarized as follows.

- 3.1. The presence of the groups of AE bursts with amplitudes $\bar{U}_{peak_i} = (1.1 \div 3) \cdot \bar{U}_{bg_i}$ (where \bar{U}_{bg_i} is the background voltage) and $\Delta\tau = 0.1 \div 0.5$ s or longer (where $\Delta\tau$ is the time interval where $\bar{U} > \bar{U}_{bg_i}$) is accompanied by the appearance of *individual points of bonding* on the wear spot with the total area of 20 ÷ 30 % (Fig. 2a and 3a).
- 3.2. Intensive bursts with $\bar{U}_{peak_i} = (\geq 3) \cdot \bar{U}_{bg_i}$ and $\Delta\tau \approx 0.3 \div 0.5$ s give rise to a large variance in \bar{U} compared to the background. These intensive bursts in all cases signified scoring caused by bonding-debonding mechanism with the total area greater than 50% (Fig. 2b и 3b).
- 3.3. The steep increase of \bar{U} to the magnitudes $\bar{U}_{peak_i} = (\geq 3) \cdot \bar{U}_{bg_i}$ with high variance and duration as long as $\Delta\tau \approx 1 \div 5$ s at $P \approx P_k$ or $\Delta\tau = 10 \div 80$ s at $P < 0.6 \cdot P_k$ in all cases accompanied scoring caused by plastic edging (Fig. 3c). The characteristic AE feature of this process is that the lower bond level of \bar{U} is always higher than \bar{U}_{bg_i} (Fig. 2a);
- 3.4. Increasing \bar{U}_{bg_i} value without clearly pronounced peaks such as those outlined in 3.1 ÷ 3.3 is related to the progressive increase of the area of the wear spot. The average \bar{U}_{bg_i} level in this case is by a factor of 1.1 ÷ 1.5 less than the minimal level of AE accompanying scoring. The wear type is mainly the abrasive-fatigue resulting in the total area of individual disparate points of localized bonding between contacting solid surfaces and their breaks of 15 ÷ 20 % of the total damaged area (Fig. 2b and 3a);
- 3.5. The running-in process during the beginning of friction is accompanied by the background level \bar{U}_{bg_i} reduction, which levels out during the steady normal wear. During scoring the high AE level \bar{U} is also associated with the increase in the wear spot area though this occurs in a more complex way than that in 3.4. After scoring has become evident on the AE diagram, the following running-in levels out the AE signal although the background level \bar{U}_{bg_i} is 1,1 ÷ 3 times higher than that before scoring. (Fig. 2);
- 3.6. Scoring can be accompanied by a gradual increase/reduction of the AE level \bar{U} according to 3.2 и 3.3, which indicates that scoring occurs nearly uniformly over the whole contact area (Fig. 2a). Several stages can be observed during the increase/reduction of the AE level \bar{U} resulting in several peaks/valleys of \bar{U} , which reflect the respective stages in the wear spot growth or in the alternating scoring in the case of the multipoint contact between the friction surfaces (Fig. 2b);

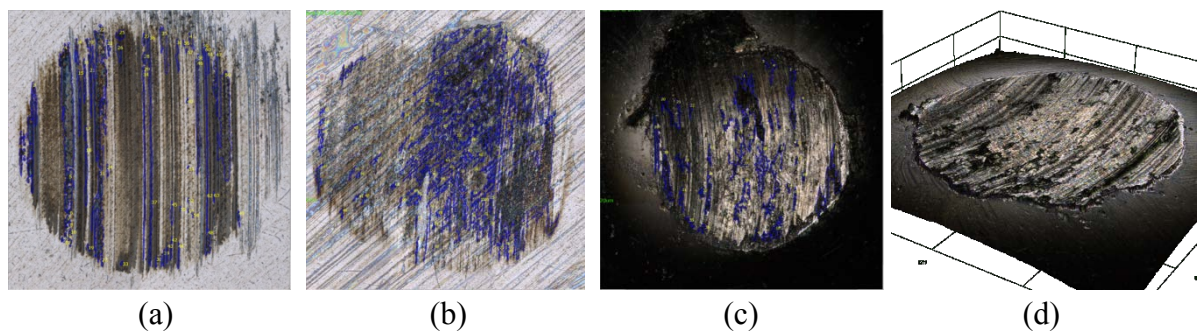


Fig. 3. The typical morphology of the wear spots: (a) abrasive-fatigue wear, (b) scoring and разрывом областей контакта, (c) plastic edging, (d) example of 3-D surface map of the wear spot. Blue color highlights the area of scoring.

The analysis of a bulk volume of experimental data allows us to conclude that the features of major wear mechanisms can be reliably identified by the AE technique. Once the AE system is trained in such a way that a characteristic for a given mechanism AE pattern is recognized (see the next section), the use of the AE technique enables substantial shortening of the testing time due eliminating microscopic observations. Moreover, it may help to calculate the mass wear and to establish the moments of transition between dominating mechanisms of damage. In what follows we shall illustrate this conclusion in the case studies below.

Case 1. Figure 5a shows experimental AE data obtained during standard testing using the four-balls tribometer aimed at determination of the loads corresponding to the onset of scoring Pk and bonding Pc at constant applied loads with different lubricants and friction pairs. Figure 4 shows that the systematic use of the integral AE parameters is quite useful for identification of scoring and bonding without microscopic investigations. Importantly is that if one compares the results of determination of Pk and Pc by measuring the limiting wear and by the AE peaks denoted as Pk^{AE} and Pc^{AE} , respectively, the results of both methods appear identical, i.e. $Pk = Pk^{AE}$ and $Pc = Pc^{AE}$. Therefore one can propose to shorten the testing time by measurements of Pk^{AE} and Pc^{AE} during a stepwise increase of the applied load on one and the same set of balls and lubricant with the time elapsed between subsequent steps not longer than 2÷5 s. Let the obtained in this express AE method loads be labeled as AE_{Pk} and AE_{Pc} . In this case, due to the formation of the contact area and partial heating during the previous load steps, the values of the load and AE_{Pk} and AE_{Pc} are obtained slightly higher (by 10 ÷ 20 MPa) above Pk and Pc, respectively, obtained in independent tests. In this regard, one can clarify actual loads Pk and Pc by standard methods, but only within AE_{Pk} minus 30 MPa and AE_{Pc} minus 30 MPa. The use of the AE technique has shortened the testing time by a factor of 50 if compared to the standard method, Fig. 4.

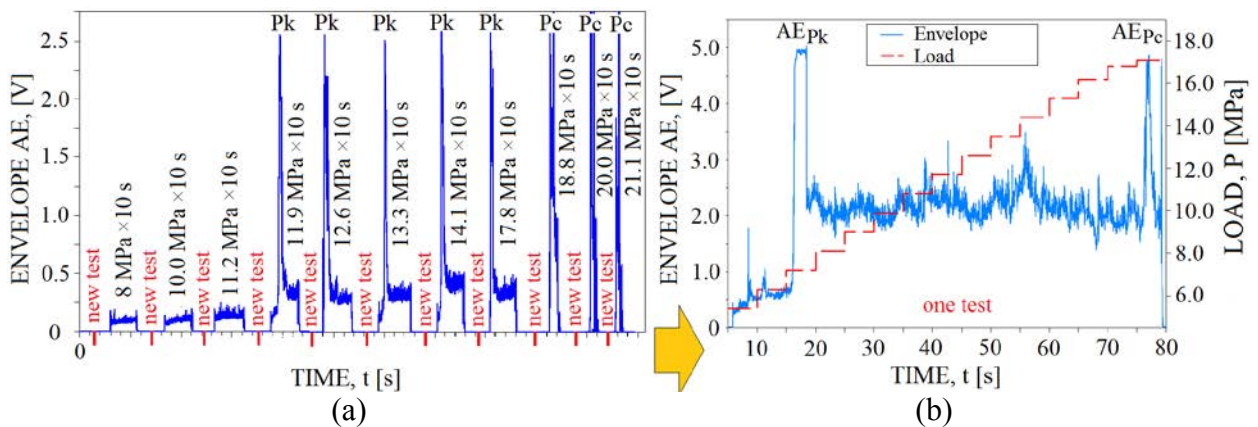


Fig. 4. Results of AE measurements during tests performed on the four-ball tribometer: (a) standard loading schedule and (b) the proposed step-wise “continuous” loading scheme.

Case 2. Different tribological testing (especially long-term tests which are accompanied by scoring) results often in pretty much the same wear spots because the surface artifacts signifying a certain damage process have been overridden by the routine wear process during long-term testing. The ambiguity always arises if the questions are asked when a catastrophic wear sets in and which mechanisms govern the damage? The measurements of integral AE characteristics and conclusions 3.1-3.6 allow us to answer these questions quite reliably. Figure 6 shows the AE record disclosing the history of damage evolution on the friction surfaces, which demonstrate that the contact materials in different thermal conditions do not equally respond to the load. However, the AE record indicates the start of scoring (Tsc), running-in after scoring (Trun) and points when changes occur in wear mechanisms (Ti).

Case 3. During long term tribology testing it is plausible to record AE periodically by timer. However, the exact moment of scoring can be missed on the AE diagram in this case. Notwithstanding, the occurrence of scoring can be reliably recognized with a reasonable accuracy by increasing \bar{U} level in comparison with normal wear conditions (cf. 3.5 and Fig. 6a).

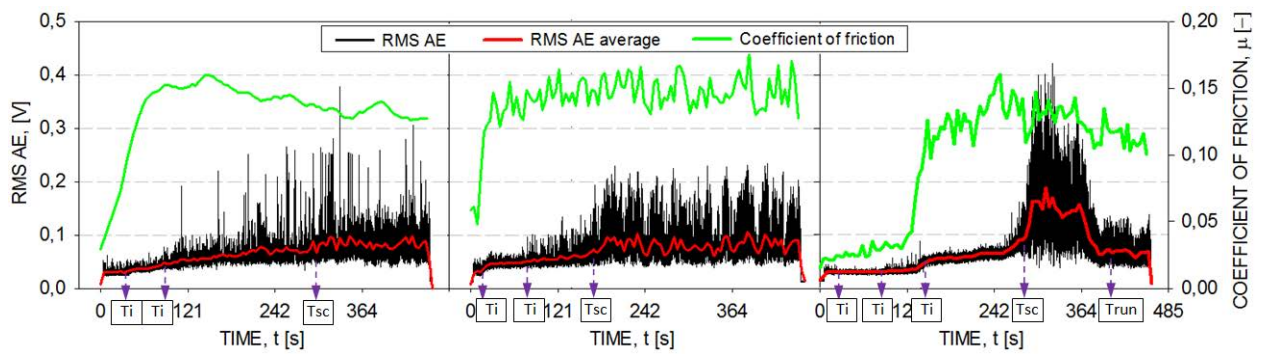


Fig. 5. Typical example of the AE records corresponding to three tests during reciprocating motion of the friction pair ShH-15-steel 45, разной поверхностной термообработки (the depth of the damaged layer corresponding to the wear is less than the depth of the hardened layer)

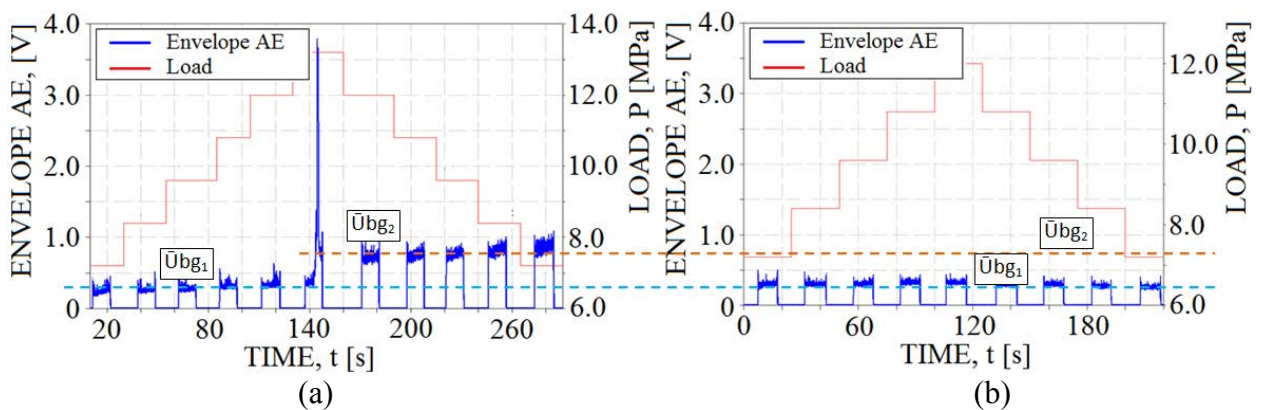


Fig. 6. Typical example of AE during a step-wise loading and scoring formation.

As a summary, let us notice that all observations of AE during a broad variety of wear processes investigated using standard tribological procedures overviewed in this section can be used quite straightforwardly for a training of a simple automated system aimed at identification of damage mechanisms and at a cost effective express wear testing under different lubrication conditions.

4. Conclusions

It is shown that real-time AE monitoring and analysis delivers valuable information which can be crucial for understanding of wear processes and improving the quantitative outcome of tribological testing. In particular, the following common issues can be addressed with an aid from the AE technique:

1. Determination of the critical regime of friction;
2. Time and area of roughness burnishing; and wear of protective coatings or a hardened layer;
3. Comparison of wear of various lubricants on the basis of the dominant mechanisms, the timing and sequence of their actions;
4. Acceleration of the tribological tests and reduction of their cost without loss of quality and reliability of the results.

Financial support from the Russian Ministry of Education and Science under grant-in-aid 11.G34.31.0031 is gratefully appreciated

6. References

- [1] ASTM G99 - 05(2010) Standard Test Method for Wear Testing with a Pin-on-Disk Apparatus (standard)
- [2] ASTM G133 - 05(2010) Standard Test Method for Linearly Reciprocating Ball-on-Flat Sliding Wear (standard)
- [3] ASTM D2266 - 01(2008) Standard Test Method for Wear Preventive Characteristics of Lubricating Grease (Four-Ball Method) (standard)
- [4] ISO 20808 Fine ceramics (advanced ceramics, advanced technical ceramics) - Determination of friction and wear characteristics of monolithic ceramics by ball-on-disc method (standard)
- [5] DIN 50324 Tribology; testing of friction and wear model test for sliding friction of solids (ball-on-disc system) (standard)
- [6] Baranov V., Kudryavtsev E., Sarychev G., Schavelin V.: Acoustic emission in friction, Tribology and interface engineering series 53, Editor: Briscoe B.J., Elsevier, Great Britain, 2007
- [7] ISO 12716:2001 Non-destructive testing, Acoustic emission inspection, Vocabulary (standard)
- [8] Belyi V., Kholodilov O., Sviridyonok A., Acoustic spectrometry as used for the evaluation of tribological systems, *Wear*, 1981, V.69, №3, P. 309-319
- [9] Filatov S. Acoustic emission under the abrasive wear of metals, *Journal of Friction and wear*, 1982, V. 3, № 3, P. 559-562
- [10] RU 979958 Sviridyonok A., Kalmykova T., Kholodilov O., Smurugov V., Method of study of wear resistance of solids, 1981 (patent of Russian Federation)

Wavelet Based Approach to Acoustic Emission Phase Picking

E. Pomponi, A. Vinogradov

Laboratory for the Physics of Strength and Intelligent Diagnostic Systems, Togliatti State University, 445667 Togliatti, Russia, eraldo.pomponi@gmail.com – alexei.vino@gmail.com

ABSTRACT

One of the most appealing features of Acoustic Emission (AE) NDT technique is its ability to spatially locate the sources, using times of arrival of elastic waves emitted by the same source, at the antenna of the sensors. The most commonly adopted triangulation procedure for source location relies on the accuracy in the time-localization of the picked phases at each different sensor. To the authors' best knowledge, all presently available commercial AE systems adopt a threshold based phase detection. Although this process is the most simple, choosing the threshold adds another source of uncertainty and it suffers from several major drawbacks, particularly when the testing environment is noisy. This results in false detections, missed events or incorrect time-location detection. The aim of this paper is to propose a novel algorithm for phase detection based on the Wavelet transform. Specifically, we exploit the neighboring concepts that have been found capable of considerably improve the de-noise performance of the wavelet shrinkage method, to construct an Acoustic Emission Activity Detector. Among other beneficial characteristics of the proposed method, preliminary tests conducted in different working conditions have shown a better accuracy in the time-localization of the picked phases.

Key words: Acoustic Emission, Phase Picking, Wavelet, De-Noising, Neighboring Concepts.

1. Motivation

One of the key points in the success of AE as an NDT inspection technique is its capability to locate the source of an event so that becomes clear where a certain amount of energy has been released. At the base of this capability plays a fundamental role the ability to exactly locate in time the first arrival of the AE wavefield at each sensor, i.e. phase picking. The uncertainty proper of this procedure fixes a lower bound for the source location accuracy. It is clear that the aim of a phase picker algorithm is to discover when what is acquired by the sensor is no more noise but a proper signal. In the threshold based approach, the most largely adopted phase picker in commercial systems, this distinction is done just looking at the AE amplitude considering noise everything do not overcome the fixed threshold level. Although this method is effective in many application where the S/N ratio is consistently high (e.g. > 10 dB), its false detection rate and time accuracy lowers down soon when this ratio tends to diminish. Another consistent drawback of a threshold based phase picker is its completely arbitrary setup: there exist "good practice" recommendations that experienced practitioners apply when choosing the threshold level but it still remains an arbitrary choice that will affect the entire acquisition process. Those facts motivated us to look for a "data-driven" procedure that could overcome the limitations

stated above attending mostly to the impact on the time location accuracy for low S/N ratio. The proposed solution exploits:

- Time coherence of AE signal
- Resonant nature of AE sensors
- Wavelet block-thresholding [1] de-noise properties

In what follows, we will be focusing on the description of the basis concepts of our approach leaving the details to a successive in-depth publication.

2. Wavelet transform, De-Noise and Neighboring concepts

Wavelet transform (WT), in both continuous (CWT) and discrete (DWT) form, is a popular and powerful tool for analyzing non-stationary data and has been extensively adopted for AE characterization/de-noise [2–6] and source location [7–11]. What makes it so appealing is not only the time-localization property but also the opportunity to do a multi-scale analysis that opens new and sometimes easier paths, to difficult tasks like modal analysis, source characterization etc. [4,5,12]. Before describing the algorithm, it is necessary to remind few important reference works about WT properties and how its de-noise capabilities have evolved from the “classic” wavelet shrinkage [13] to the block-thresholding based shrinkage [1].

In their first seminal paper, Donoho and Johnstone [13] introduced the concept of wavelet shrinkage as the process of shrinking WT coefficients depending on their amplitude compared to a fixed threshold directly estimated from the data (i.e. proportional to the estimated noise power). They called this method VisuShrink with two possible variant: Hard and Soft thresholding. For instance, since that time, the same authors and many others have extensively proved [14–19] that the wavelet based approach to function approximation/de-noising is optimal in many sense and outperforms the Fourier transform based one. Another significant step ahead has been done with the introduction of “neighboring concepts” in the shrinking process, following a simple intuition: A coefficient in the wavelet transform is expected to describe the noise or the signal not just depending on its value but also on the values of a certain number of neighboring coefficients (i.e. time coherence). Here's the introduction of blocks of coefficients in the approximation/de-noise process as first proposed by Hall et al. [20] and successively refined in [1,19,21,22]. Although there exist theoretical justified rules for an optimal choice of the block-size for a large class of signals/functions and affecting noise [1,19], we aim to extend them with something that is specific for AE signals and their acquisition chain. On the other hand, it is straightforward to envision our approach applied to signals of different “nature” (e.g. Voice) but this kind of investigation is outside the scopes of the present work.

For our purpose, we will focus on the “NeighBlock” method (i.e. Cai and Silverman [1]), because it is one of major success between the many that have been developed since [13], even if, potentially, other WT block-based de-noise methods could be adopted as well.

3. Algorithm description

The algorithm is here described in some details however we want to clearly state that it is not in the scope of this paper to report an in-depth analysis of all the steps that are involved in the proposed new method. Indeed, we want to give the reader a precise perception of what have been the ideas behind this work and their basic assumptions.

Let define minimum time-coherent span the duration of the shortest AE signal that we can acquire (i.e. with a certain acquisition chain). It depends on many factors that, unfortunately, we cannot control neither measure in most cases (e.g. source properties and medium properties). However, there exist an upper bound for its “dual” (i.e. in frequency domain) that we can easily

find: the maximum frequency band where we can expect useful information is dictated by the sensor response.

Assuming for simplicity a single resonance sensor and adopting a Gaussian model to describe its response, it is easy to show that the “rise time” (t_r) for that system is related to the bandwidth ($BW \simeq 0.009\sigma$) by the approximate relation $t_r \simeq 0.35/BW$. Applying this formula we have immediately an estimation of the “minimum” rise time that we can expect for the system under inspection. It is then straightforward to adopt this value to fix a lower bond in the time-coherency (*block size*) that we impose on the WT transform when applying the block-thresholding. The resulting mask (i.e. equal to 1 for those blocks retained by the block-thresholding rule and equal to 0 for those blocks shrunk) obtained for each decomposition level m will be called “*Probability of Presence*” at level m (m -PoP). To get a one-dimensional “*Probability of Presence*” (PoP) we recombine point-by-point (in time), all m -PoP probability curves according to the “cone of influence” definition [23] (i.e. defines the time localization of each coefficient at different decomposition levels) plus this simple assumption: m -PoP are independent for every m and every time t .

This is the simplest form of the proposed algorithm and we will show an example of application in the next section. It must be noticed that, for real problems, the simple Gaussian model doesn't fit really well with most of the response curves of common AE sensor so it has usually been adopted a multi-resonance model plus a second order approximation for the rise-time calculation respect to each resonant point. Moreover, instead of a (0,1) binary mask (i.e. Hard thresholding) in the block-thresholding algorithm we adopted a continuous mask (i.e. Soft thresholding) that admits all the values in the interval [0,1]. About the choice of the mother wavelet we took the Haar wavelet for its (theoretical) arbitrary time-localization accuracy. All the implication of those choices are discussed elsewhere.

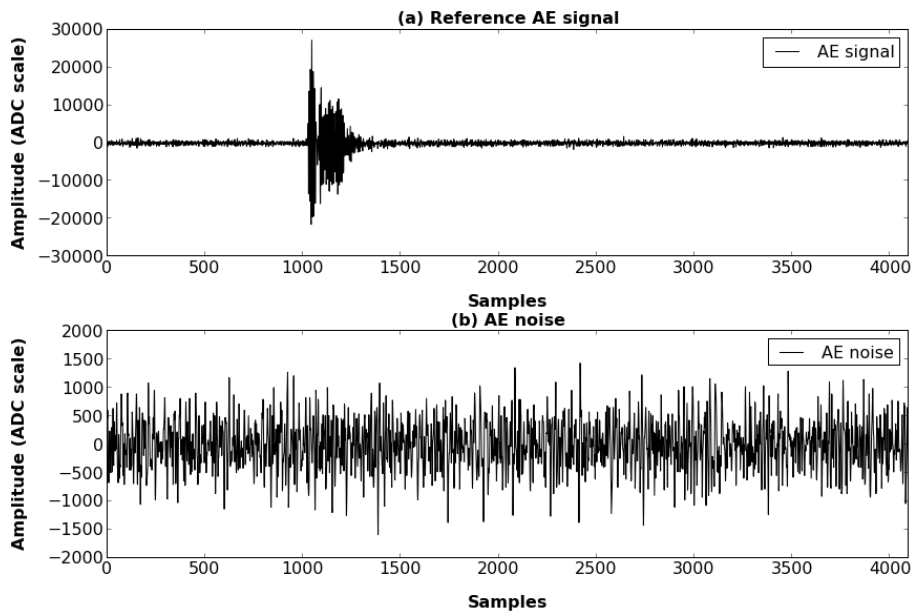


Figure 1: (a) Reference AE signal and (b) AE noise.

4. Application

To prove that the proposed method is effective in the detection of the Time of Arrival (TOA) (a.k.a. Time of Flight) and that it is much less sensible to the S/N ratio respect to other methods, we constructed a set of testing signals taking one frame (4K samples) of a “real” AE signal, reported in Figure 1(a), and summing “real” AE noise, Figure 1(b), (i.e. real colored noise acquire during an AE inspection before starting the loading of the specimen but with the sensors

already attached to its surface) controlling the resulting S/N ratio, calculated respect to the entire frame length. We will consider two examples respectively for $5dB$ and $-5dB$ S/N ratio. We will also report the result obtained with the proposed method for $-10dB$, to confirm its low sensibility to the S/N ratio. The sample frequency is $f_s=3.125$ Ms/s and we will compare our performance (i.e. the obtained TOAs) respect to a threshold based method with the threshold fixed to $30dB_{\mu}$, assuming a pre-amplifier gain of $20dB$ and a “dead-time” of $32 \mu s$ (100 samples).

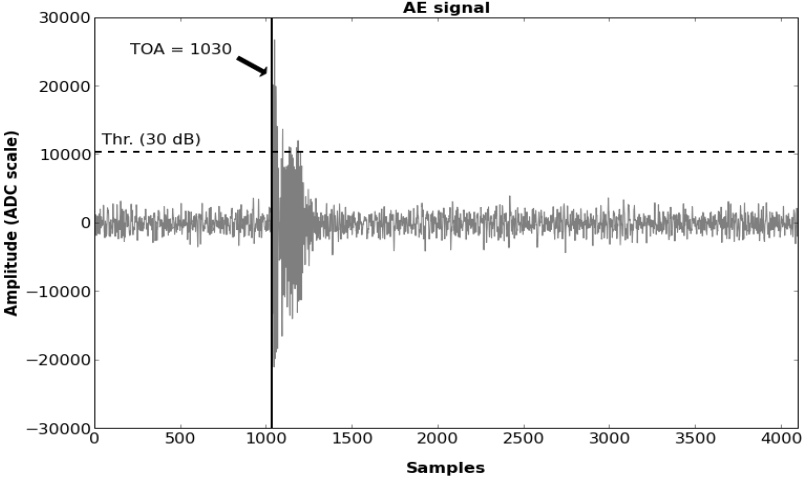


Figure 2: Threshold method S/N 5 dB

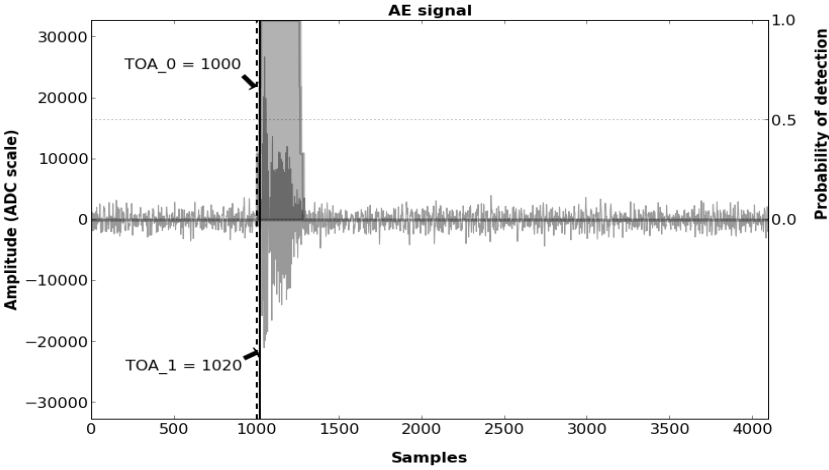


Figure 3: Proposed method S/N 5 dB

5. Remarks & Conclusions

As clearly shown in Figure 2, 3, 4, 5 and 6 mostly, the proposed method outperform the threshold based phase picker and returns almost the same single TOA (i.e. when chosen between TOA_0 that indicates the first sample where $PoP \neq 0$ and TOA_1 that indicates the first sample where $PoP = 1$) even for low S/N ratios. Being the computational complexity of a standard DWT $O(n)$ so less than that one of the FFT $O(n \log n)$ and being all the other operations in the algorithm linear in n , the proposed method is potentially capable to work in real-time moreover, without any additional cost, it produces already the de-noised AE signal.

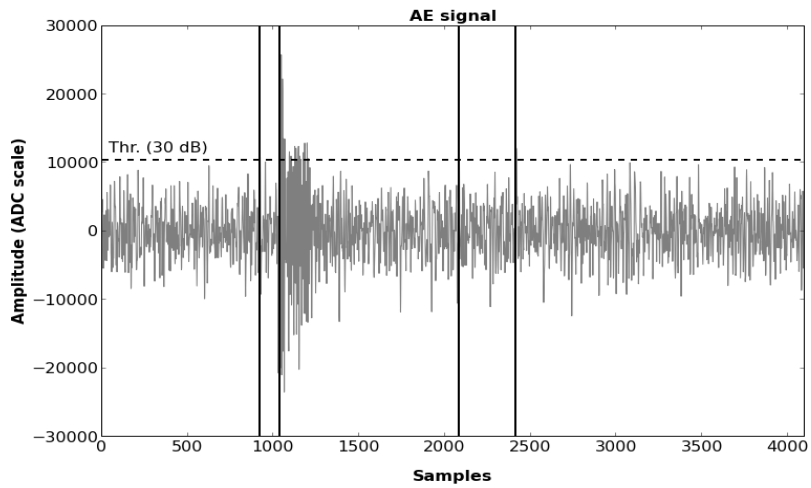


Figure 4: Threshold method S/N -5 dB

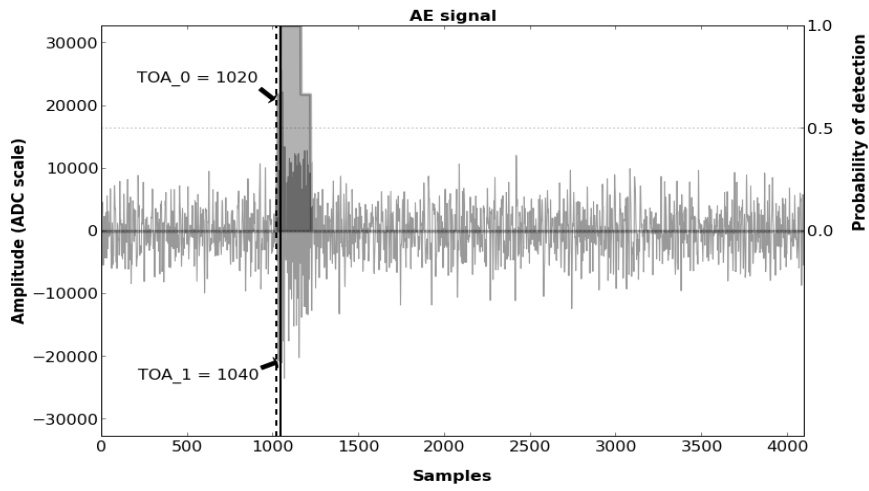


Figure 5: Proposed method S/N -5 dB

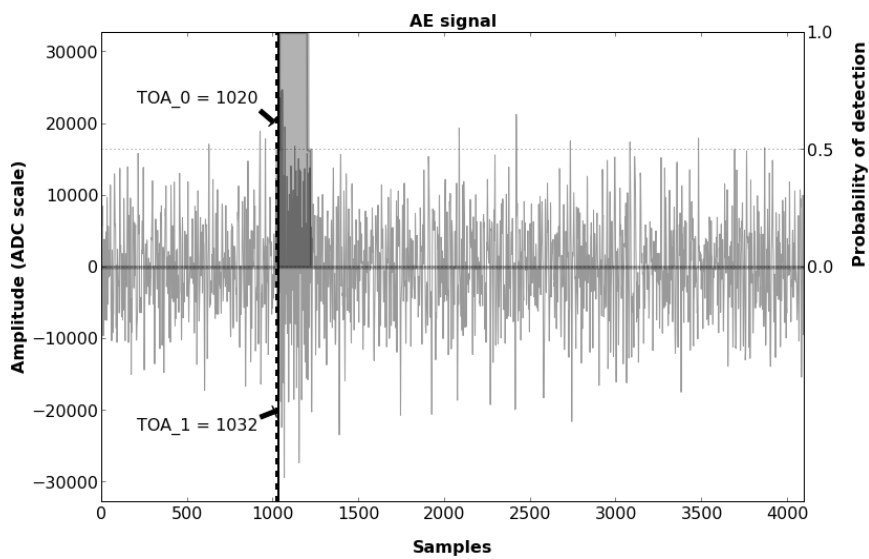


Figure 6: Proposed method S/N -10 dB

References

- [1] T.T. Cai, B.W. Silverman, Incorporating information on neighbouring coefficients into wavelet estimation, *Sankhyā: The Indian Journal of Statistics, Series B.* 63 (2001) 127 – 148.
- [2] H. Suzuki, T. Kinjo, Y. Hayashi, M. Takemoto, K. Ono, Wavelet transform of acoustic emission signals, *Journal of Acoustic Emission.* 14 (n.d.) 69–84.
- [3] E.P. Serrano, M.A. Fabio, Application of the wavelet transform to acoustic emission signals processing, *Signal Processing, IEEE Transactions On.* 44 (1996) 1270–1275.
- [4] G. Qi, Wavelet-based {AE} characterization of composite materials, *{NDT} & E International.* 33 (2000) 133–144.
- [5] M.A. Hamstad, A. O’Gallagher, J. Gary, A wavelet transform applied to acoustic emission signals: part 1: source identification, 20 (2002) 39–61.
- [6] C.U. Grosse, F. Finck, J.H. Kurz, H.W. Reinhardt, Improvements of AE technique using wavelet algorithms, coherence functions and automatic data analysis, *Construction and Building Materials.* 18 (2004) 203–213.
- [7] M.A. Hamstad, A. O’Gallagher, J. Gary, A wavelet transform applied to acoustic emission signals: Part 2: Source location, *Journal of Acoustic Emission.* 20 (2002) 62–82.
- [8] J. Jiao, C. He, B. Wu, R. Fei, X. Wang, Application of wavelet transform on modal acoustic emission source location in thin plates with one sensor, *International Journal of Pressure Vessels and Piping.* 81 (2004) 427 – 431.
- [9] F. Ciampa, M. Meo, Acoustic emission localization in complex dissipative anisotropic structures using a one-channel reciprocal time reversal method, *The Journal of the Acoustical Society of America.* 130 (2011) 168.
- [10] E.M. Lympertos, E.S. Dermatas, Acoustic emission source location in dispersive media, *Signal Processing.* 87 (2007) 3218–3225.
- [11] N.F. Ince, C.S. Kao, M. Kaveh, A. Tewfik, J.F. Labuz, Averaged acoustic emission events for accurate damage localization, *IEEE International Conference on Acoustics Speech and Signal Processing.* 9 (2009) 2201–2204.
- [12] a. R. Oskouei, Wavelet-based acoustic emission characterization of damage mechanism in composite materials under mode I delamination at different interfaces, *eXPRESS Polymer Letters.* 3 (2009) 804–813.
- [13] D.L. Donoho, I.M. Johnstone, Ideal spatial adaptation by wavelet shrinkage, *Journal Of Comparative Education.* 81 (1992) 425–455.
- [14] D.L. Donoho, On minimum entropy segmentation, *Wavelets: Theory, Algorithms, and Applications.* (1994) 1–43.
- [15] D.L. Donoho, I.M. Johnstone, G. Kerkyacharian, D. Picard, Wavelet shrinkage: asymptopia?, *Journal of the Royal Statistical Society Series B Methodological.* 57 (1995) 301–369.
- [16] D.L. Donoho, I.M. Johnstone, Adapting to unknown smoothness via wavelet shrinkage, *Journal of the American Statistical Association.* 90 (1995) 1200 – 1224.
- [17] R.R. Coifman, D.L. Donoho, Translation-invariant de-noising, *Time.* 103 (1995) 125 – 150.
- [18] D.L. Donoho, I.M. Johnstone, Asymptotic minimaxity of wavelet estimators with sampled data, *Statistica Sinica.* 9 (1999) 1–30.

- [19] T.T. Cai, Adaptive wavelet estimation: a block thresholding and oracle inequality approach, *The Annals of Statistics*. 27 (1999) 898–924.
- [20] P. Hall, S. Penev, G. Kerkyacharian, D. Picard, Numerical performance of block thresholded wavelet estimators, *Statistics and Computing*. 7 (1997) 115 – 124.
- [21] P. Hall, G. Kerkyacharian, D. Picard, On the minimax optimality of block thresholded wavelet estimators, *Statistica Sinica*. 9 (1999) 33 – 49.
- [22] T.T. Cai, On block thresholding in wavelet regression: Adaptivity, block size, and threshold level, *Statistica Sinica*. 12 (2002) 1241–1273.
- [23] M. Vetterli, J. Kovačević, *Wavelets and subband coding*, Prentice Hall PTR, Englewood Cliffs, New Jersey, 1995.

ARC WELDING PROCESS MONITORING BY AUDIBLE SOUND

Ivan Polajnar¹, Zoran Bergant², Janez Grum³

¹Welding Institute, Ptujška 19, 1000 Ljubljana, Slovenia

ivan.polajnar@fs.uni-lj.si

²Faculty of mechanical engineering, Aškerčeva 6, SI-1000 Ljubljana, Slovenia

zoran.bergant@fs.uni-lj.si

³Faculty of mechanical engineering, Aškerčeva 6, SI-1000 Ljubljana, Slovenia

janez.grum@fs.uni-lj.si

ABSTRACT

The paper presents the results of experimental gas metal arc welding. Namely, this welding process is commonly used in the automation and robotization of fusion welding, where adaptive regulation is indispensable.

In addition to variable welding voltage and current, a distinctive characteristic of arc welding processes are also the pressure of audible sound phenomena which reflect the variable conditions in the arc to the highest extent. It follows that it is reasonable to monitor these phenomena and that the results can be used for the implementation of adaptive welding process control.

Key words: Fusion welding, arc, material transfer, mild steel, welding parameters, audible sound.

1. Introduction

A constant increase in the demand for automation and robotization of arc welding and the requirements with regard to the desired quality of welds have led to a logical demand for a reliable on-line monitoring and control of welding processes. The prevailing control systems among the well-established variants are based on continuous measurement of arc voltage and welding current intensity. These control systems may provide reliable information about the material transfer in the arc, but they are considerably less informative with respect to the integral course of the welding process. For a given type and thickness of base material, joined to form a product by using a weld joint of some sort, the quality of welding is not determined only by the material transfer mode. Instead, the quality depends on the size and shape of the welding pool, the level of splashing, and the shape and magnitude of remelting of base material. However, it is impossible to extract all this information only from the recorded signals of welding current and welding voltage. It follows that a comprehensive evaluation of the welding quality must also incorporate some other process parameters, absolutely including the audible sound pressure level [1,2].

Several papers have been published on the topic of using the sound in monitoring the welding process, all of them having something in common – the measurement of sound pressure during the welding and the frequency analysis after the welding [3,4]. The results of frequency analysis are commonly bound with time windows related to various physical phenomena [5, 6]. These

include the arc ignition and burning, which is especially easy detectable when welding with short-circuit filler material transfer. Furthermore, the accessible literature does not deal with the relations between the results of measurement of audible sound and the results of measurement of light intensity and welding current intensity [6, 7].

A mathematical model relating the sound pressure to the welding current would provide a new dimension and added value in identifying various modes of material transfer, and could serve as a foundation for a system using the measured sound pressure for a controlled supply of electrical energy to the arc. In this way, it would be possible to implement reliable control of welding process stability for the GMAW processes, and consequentially to control the quality of such welds.

2. Sound generation during metal transfer

In gas metal arc welding process (GMAW) an electric arc is established between the consumable wire electrode and the melted zone on the welding part. Both are shielded by different gases (inert Ar, active CO₂ or gas mixtures containing Ar, CO₂, etc).

Generally, for all arc welding processes, there are many different modes of metal transfer which are, according to International Institute of Welding (IIW), classified into eight basic groups. In GMAW, there are only three characteristic modes of metal transfer, short circuit, globular and spray mode, figure 1.

The differences in the way the filler material melts are reflected in the shape of the melt pool, and also in the generation of several different sound phenomena [8, 9, 10]. The prevailing mode of filler material melting depends on the current type and intensity, voltage and the shielding atmosphere.

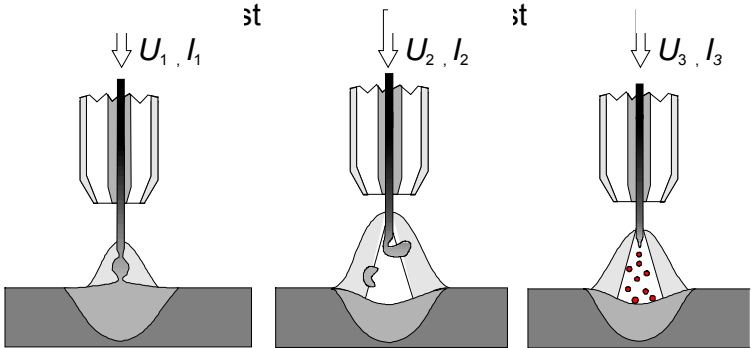


Fig. 1: Characteristic modes of metal transfer in GMAW, w=const., U₁<U₂<U₃, I₁<I₂<I₃, (a) short circuit, (b) globular mode, (c) spray mode

The filler material transfer is reflected to a great extent in the temporal variability of welding voltage, welding current intensity, light intensity and sound pressure generation [11, 12]. The temporal variation of current intensity in short-circuit transfer of filler material is both very illustrative and well defined, figure 2.

The short circuit metal transfer can be established at lower welding current and lower voltage which is a convenient mode to study the sound phenomena. At lower energy input the shape and the length of arc is unstable and lead to significant variations in sound pressure.

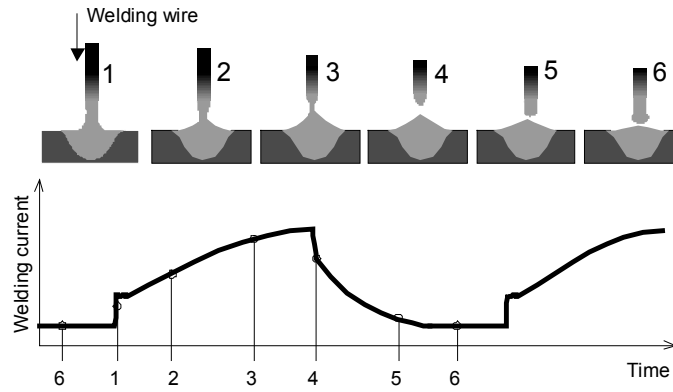


Fig. 2: Description of six different phases of material transfer during GMAW in the short-circuit mode

The electrical circuit of the welding system (power supply, cable, consumable wire, arc and welding material) consists only of the basic elements: resistance R in ohm (Ω), inductance L in Henry (H) and capacitance C in Farad (F). A suitable equation describing the electrical scheme can be obtained by using the second Kirchhoff's law:

$$U = RI + L \frac{dI}{dt} + \frac{R_a I}{1 + j\omega C_a R_a} \quad (1),$$

where I is the electric current in Amperes (A), U is the equivalent open-circuit voltage supply in volts (V), R_a is resistance (Ω), C_a capacitance of the arc in farad (F), and ω is the angular frequency. The capacitance of the arc C_a in Eq. (1) assumes a very small value and may be neglected, and since the arc is responsible for noise generation, we expressed the arc voltage U_a explicitly as

$$U_a = R_a I = U - RI - L \dot{I} = U - U_R + U_L \quad (2).$$

It follows from the interpretation that a fast enough capture of data on the changing electrical quantities during welding makes it possible to identify the type of filler material transfer. The presented research aims to identify the possibilities of making an analytical description of filler material transfer based on the variation of sound pressure.

3. Welding process as a cybernetic system

GMAW can be treated as an electro-thermo-mechanical system with multiple input and output quantities – signals. There are input signals that can be controlled and those that cannot be influenced, but can be measured. The latter may also be termed as the noise signals. A complete description of GMAW therefore requires a system of differential equations, some of them non-linear, such as the equation describing the sound generation based on the welding current signal [13]. Systems of non-linear differential equations are sensitive with respect to the accuracy of their coefficients. If the coefficients are not determined to a certain precision, they do not describe the welding process well, and the results may even happen to diverge. The mathematical model is therefore complex and not absolutely stable, which means that it is not practical for on-line welding process control.

In real operating conditions, it is therefore only reasonable to treat the GMAW process as a simple system with one input, one output, and one common noise factor, figure 3. To be able to select the most appropriate input and output quantities, it is reasonable to measure the welding

current, welding voltage and sound intensity at different welding conditions, and to analyze the results separately [14,15].

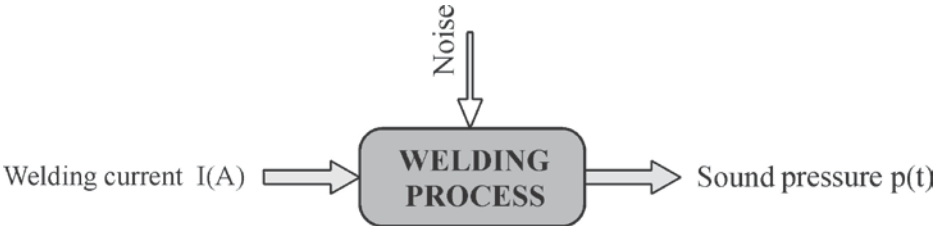


Fig. 3: The block diagram of the welding process with input and output variables

4. Experiment and results

Experiments were conducted using St36 mild steel (0.1% C, 0.48% Mn), which is often used in the metalworking industry and is suitable for welding. The geometry of the work piece was selected so that the welds were suitable for the preparation of specimens for the strength tests and metallographic examination of welds. The dimensions of work piece halves were: 10 x 60 x 250 mm.

The experiments were conducted using the experimental setup shown in Fig. 4. Standard industrial welding equipment was used. The Iskra E-450 power source has a horizontal static characteristic. The VAC 60 consumable wire electrode with $\phi = 0.8$ mm was used and the shielding gas was pure CO₂ [16].

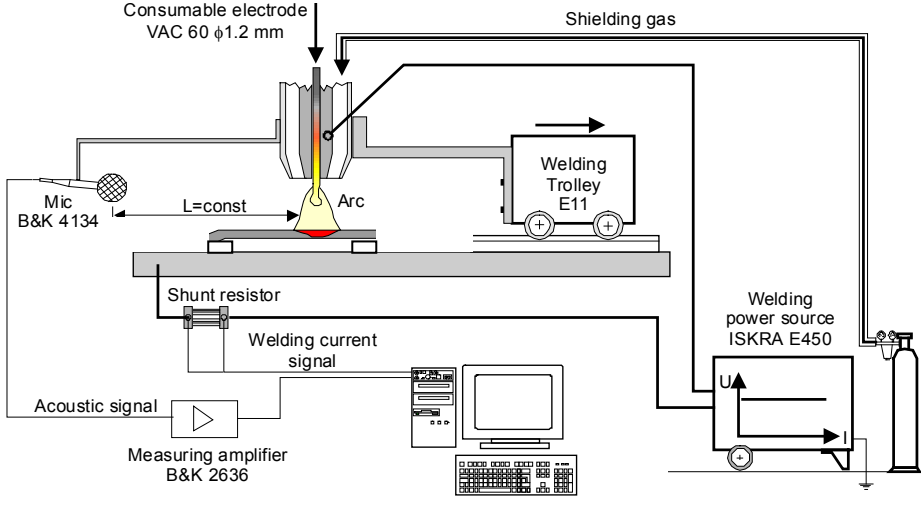


Fig. 4: Experimental setup

4.1 Measurement results

The settings on the welding rectifier and the control unit were chosen so that one of the two boundary modes of filler material transfer was obtained: short-circuit or spray. Table 1 presents the rectifier and control unit settings for both materials transfer modes, as well as the mean measured values of welding voltage and current intensity.

Table 1: Welding parameter settings and the measured values

Settings/measured values	Short-circuit transfer	Spray transfer
Rectifier	1-4	1-6
Control unit	5.5	13
Wire feed rate [m/min]	6.3	13.8
Welding voltage [V, rms]	23	38
Welding current [A, rms]	98	178

The data acquisition was performed with an A/D converter, with a sampling rate of 50 kHz per channel and with 8-bit data resolution. 2 sec of welding process was recorded for each setting and stored on the hard drive. The welding current was measured via a shunt resistor. The Bruel&Kjær type 4134 condenser microphone was fixed to the welding head to maintain a constant distance. Since the noise spectra appear in the frequency range above 4 kHz, the microphone could be attached at a shorter distance. All measurements were conducted using the same 0.35 m distance of the microphone from the arc. During the welding, the temporal variations of current intensity $I_w = I(t)$, light intensity $i_w = i(t)$ and sound pressure $p_s = p(t)$ were recorded simultaneously. The recorded data for typical short-circuit filler material transfer in the time 10 ms is shown in Figure 5.

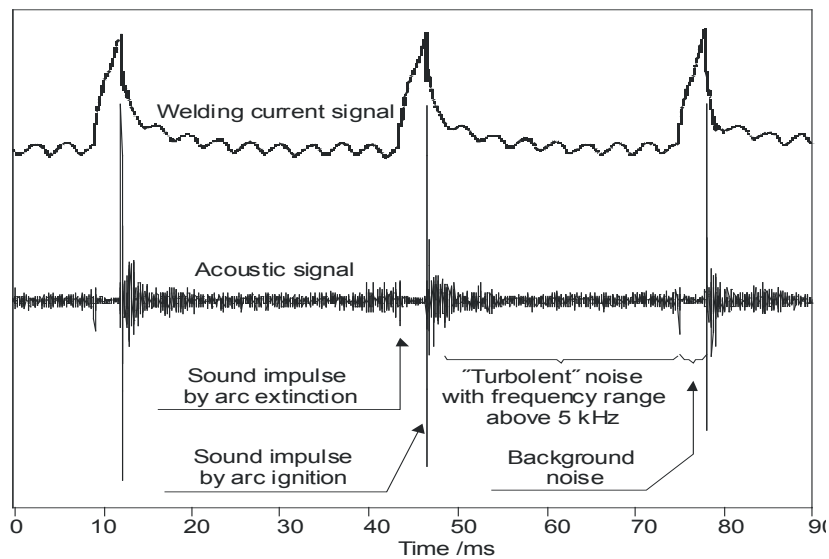
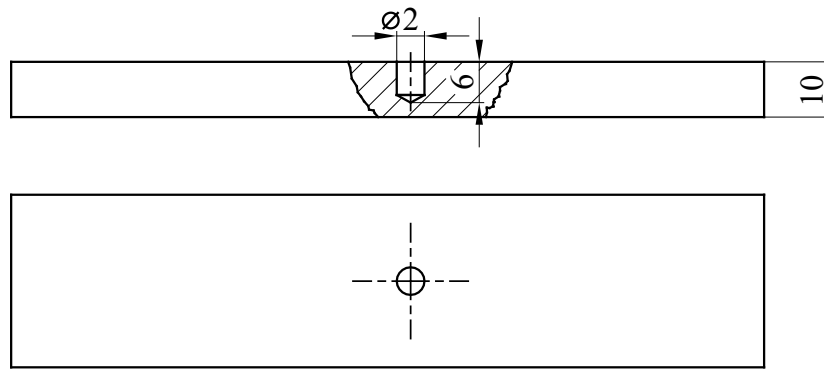
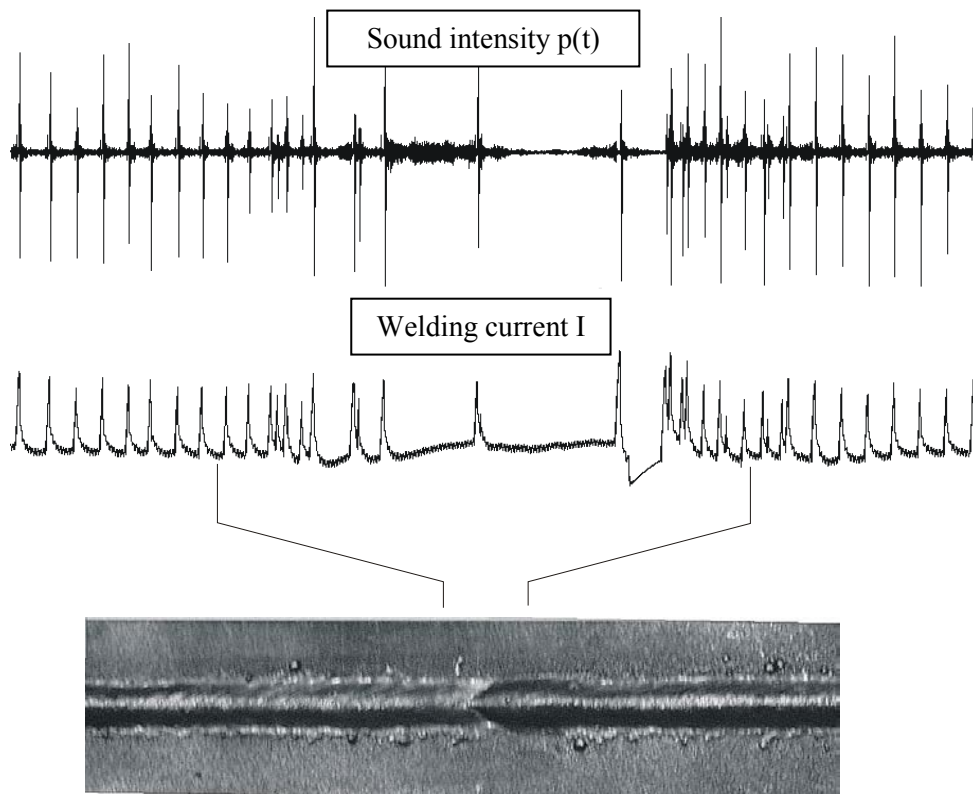


Fig. 5: Waveform of welding current and sound pressure

Figure 6 shows a comprehensive overview of measured temporal variation of welding current intensity, light intensity and sound pressure for both boundary filler material modes, recorded in 0.2 and 2 s time intervals.



(a) Specimen preparation



(b) Waveform of welding current and sound and photos of weld bead

Fig. 6: Welded overlay with constant parameters on the weldpiece with geometrical defect

4.2 Findings

After reviewing and comparing the results of the conducted measurements, the main findings can be summed up as follows:

The current signals are useful especially for discerning the stability of conditions in the arc. In short-circuit filler material transfer, the current signal also provides information about the number of short circuits and the mean size of molten droplets. These cannot be established with certainty in the case of spray transfer mode.

The sound signal is considerably more sensitive to variable conditions in the arc, the material transfer mode and the disturbances in the welding process. For example: the sound signal indicates high-frequency arc oscillations which may lead to process instability, which cannot be identified from the light signals. The sound signals therefore appear to be considerably more noisy, and a thorough analysis can extract more useful information from them. It follows that the sound pressure technique is suitable for monitoring the welding process.

5. Conclusions

The quality of arc welding can be evaluated by detecting the pressure of audible sound, especially the fact that the welders monitor and adaptively control the welding process by using their sight, hearing and sensing the forces in their hands. The research revealed that the sound pressure measurement during the welding is directly connected with the arc changes and quality of weld. Modern systems of on-line monitoring and control are generally based on measuring the welding current and voltage. The information about the process obtained in this way may be adequate, but it is often too inaccurate to ensure a first-class repeatability and quality of welds.

In our research it was found that the sound measurement data represents a valuable contribution for monitoring of the welding process. The online sound pressure monitoring and signal processing is proposed as a new approach of quality control of weldments.

The sound signal is extremely sensitive to the disturbances in the stability of welding process. Objectives of the further investigation of sound pressure signals is to detect other instabilities of the arc behavior connected to the weld quality, as well as small deviations during material transfer. The applicability thereof for the online welding process control has not been made known and researched enough. For this reason, we will attempt to upgrade research in the future with further evaluation of weld quality.

6. References

- [1] Saini D. Floyd S.: An Investigation of Gas Metal Arc Welding Sound Signature for On-line Quality Control, *Welding Journal*, pp. 172-179, April 1998
- [2] Arata Y. Inoue K. Futamata M.: Investigation on welding arc sound – report 1, IIW/IIS doc. VIII-1340-86, 1986
- [3] Polajnar I, Bergant Z., Grum J.: Spremljanje MIG/MAG varjenja z detekcijo zvočnega tlaka. V: GRUM, Janez (ur.), BERGANT, Zoran (ur.). 11. slovenska konferenca z mednarodno udeležbo z naslovom Uporaba sodobnih neporušvenih metod v tehniki, Ljubljana, 14. februar 2013. *Zbornik referatov*. Ljubljana: Slovensko društvo za neporušitvene preiskave: Fakulteta za strojništvo, 2013, pp 114-122
- [4] Jesnitzer et.al.: Apparatus for controlling electric welding process, U.S. Patent No. 3.679.865, 1972
- [5] Choi J.H., Lee C.D., Yoo C.D.: Simulation of dynamic behaviour in a GMAW system, *Welding Journal*, Vol. 80, pp. 293-245, 2001
- [6] Mansoor A.M., Huissoon J.P.: Acoustic identification of the GMAW process, 9th International conference on computer technology in welding, NIST special publication, Detroit 1999
- [7] Magori V. Monitoring sensor for the production of welds, U.S. Patent No.: 4,650,958, 1987
- [8] Rostek W.: Investigation on the connection between welding process sound emission and electric short circuit in GMA welding, IIW/IIS doc. 212-725-89, 1989
- [9] Grad L., Prezelj J., Polajnar I., Grum J.: Weld quality assessment by analysing on line measured acoustic signals, In: Grum, Janez (ed). 6th International Conference of the Slovenian Society for Non-Destructive Testing, Portorož, Slovenia, September 13-15, 2001. pp. 185-189, 2001.
- [10] A. Fasana and B. A. D. Piombo: Identification of linear mechanical system by deconvolution techniques, *Mechanical Systems and Signal Processing*, Volume 11, Issue 3, 3 May 1997, pp. 351-373
- [11] Prezelj J., Polajnar I.: Slišni zvok kratkostičnega MAG varjenja, *Varilna Tehnika*, 51(3), pp. 80-85, 2003

- [12] S. M. Kuo: Active Noise Control Systems - Algorithms and DSP implementation, Wiley interscience, New York, 1996
- [13] Kovacevic R., Zhang Y.M. and Li L.: Monitoring of weld joint penetration based on weld pool geometrical appearance. *Welding journal* pp 317-329s, vol. 75, No. 10, 1996.
- [14] Polajnar I., Prezelj J., Grad L., Grum J.: Ocena kakovosti obločnega varjenja z detekcijo slišnega zvoka in svetlobnega sevanja, In: Grum, Janez (ed). 7th International Conference of the Slovenian Society for Non-Destructive Testing, Brnik, Slovenia, November 18, 2004. Conference proceedings. pp. 139-147, 2004.
- [15] Langus, Danijel, Kralj, Viljem, Grum, Janez. Optimisation of welding parameters in pulsed MIG/MAG welding width-controlled sine-wave current pulses. Part 1: Determination of a general synergetic equation and a normalised parametric diagram with a defined parametric welding range. *Int. j. mater. prod. technol.*, 2007, letn. 29, št. 1/2/3/4, pp 244-254
- [16] Grum J., Bergant Z., Polajnar I., Monitoring the GMAW process by detection of welding current, light intensity and sound pressure. V: PAZDERA, Luboš (ur.), MAZAL, Pavel (ur.). *NDE for Safety 2012 : proceedings : sborník příspěvků*. Brno: Brno University of Technology, 2012, pp. 291-299

THE SYSTEM OF AE CONTROL AND DIAGNOSTICS OF TECHNICAL STATUS OF ELECTRIC SWITCH MECHANISM

S.V. Altynbaev^{1*}, V.S. Fadeev², N.A. Semashko²

¹ «STC Information Technologies» Perevedenovskiy str. 13/7, 105082, Moscow, Russia, s.altynbaev@tmaster.ru

² «STC Information Technologies» Perevedenovskiy str. 13/7, 105082, Moscow, Russia, infotech.mos@gmail.com

ABSTRACT

Increasing of the speed and passenger traffic intensity on the railways require the comprehensive approach in organization of the control of the technical status of rolling stock in order to ensure the safety of trains. In connection with it, it is very relevant to create intelligent diagnostic systems for technological processes of repair and operation of rolling stock.

The AE method is designed for technical inspection of motor and electric switch components. The acoustic emission method based on the parameter analysis of the acoustic radiation from various working nodes of different devices. The value of acoustic emission energy is uniquely connected with the state of interacting nodes of the mechanism. The acoustic system allows to control the technical status of main electric switch components in real working mode and gives a possibility to determine the residual resource without disassembling and inspecting the electric switch.

Keywords: nondestructive control, railway, ground equipment, point.

1. Introduction

Increasing of the speed and passenger traffic intensity on the railways require the comprehensive approach in organization of the control of the technical status of rolling stock in order to ensure the safety of trains. Losses from passenger trains delays and derailment amount to hundred million rubles annually. In addition, passenger trains derailment may result in human casualties. In connection with it, it is very relevant to create intelligent diagnostic systems for technological processes of repair and operation of rolling stock. These intelligent diagnostic systems have to be united into a single information space. Today, the main method of controlling the technical status of the ground equipment elements (nodes), including the electric switches, is the method of visual inspection by service regulations.

2. Application of AE method in condition monitoring of point machines (electric switches)

2.1 Description of the diagnostic method

The AE method is designed for technical inspection of motor and electric switch components. The acoustic emission method based on the parameter analysis of the acoustic radiation from various working nodes of different devices. The value of acoustic emission energy is uniquely connected with the state of interacting nodes of the mechanism. The method is successfully used for diagnosing oil and gas facilities, power plants, in aviation industry and other areas of engineering.

2.2 System of acoustic control of point machines (SACP)

The acoustic system allows to control the technical status of main electric switch components in real working mode and gives a possibility to determine the residual resource without disassembling and inspecting the electric switch. There is no need in scheduled repair of electrical switch mechanism. Replacement and repairs are performed depending on the actual state of its elements. The extent of controlled node degradation and its residual life is estimated by the analysis of the main parameters of the AE radiation from electric switch elements in the real work. Output information can be implemented in a version with three lights of different colors, that would allow to use the low-skilled technicians and eliminate the human factor in the process of diagnostics.

2.3 Structure of SACP

The AE control system includes two separate blocks, as illustrated in Figure 1 and 2.



Fig. 1: General view of SACP.

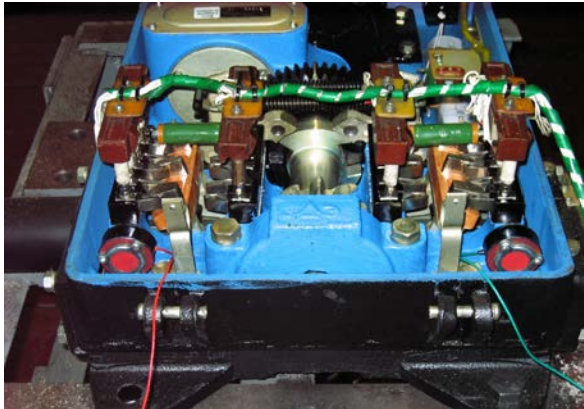


Fig. 2: Positions of the sensors on the electric switch.

The first unit includes sensors, connected to the preliminary AE amplifiers. The sensors are located directly on the controlled elements of the electric switch (motor, gear, friction clutch, gate, switches). Preliminary amplifiers are mounted on the inside of the case with an output to the multi-connector mounted on the outside of the case.

The second block includes a multi-channel system like SACP, which processes the AE information, analyses and graphically displays all incoming information on controlled objects with the help of special cables connected to the terminals of the first unit and a personal computer (PC) with Maestro software.

SACP system is built on the principle of parallel multi-channel digital recording parameters of AE signals. The system software can display SACP complex parameters of AE test in real time, as well as provide wide opportunities for processing the obtained information in afteranalysis mode. Comparing the acoustic image of reference elements of a new electric switch with the that of the real element (Figure 5 a, b) in comparison mode allows to assess the degree of degradation of the controlled element and its remaining life.

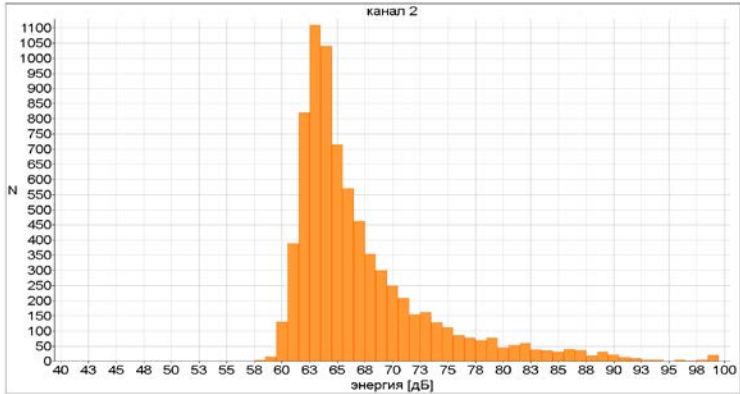


Fig. 3 (a): The energy spectrum of the gearbox in the optimum technical condition.

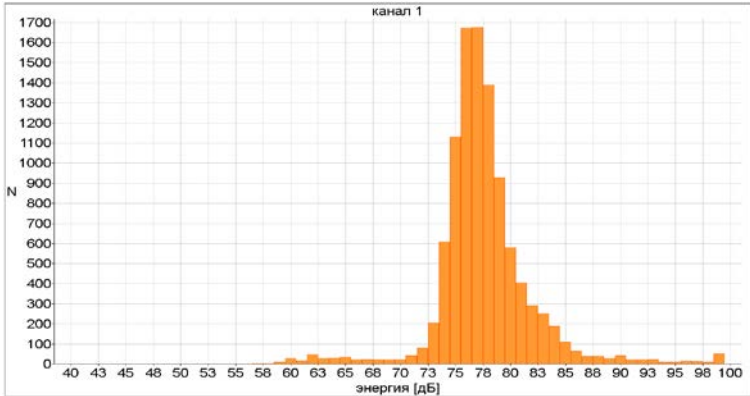


Fig. 3 (b): The energy spectrum of the gearbox after 10 years of operation.

3. Application of SACP in repair factories

The diagnostics of electric switch has been held on repair factories in Pskov, Armavir and Barnaul, Russia. The position of an electric switch on a testing stand is shown in Figure 4.



Fig. 4: The position of an electric switch on a testing stand.

More than 100 electric switches in different technical condition were diagnosed during the time of work. The ranges of critical values of acoustic parameters were defined allowing to diagnose the remaining life of the electric switch nodes and the whole mechanism in general. The SAACP usage methodology for repair factories has been developed for the input quality control of supplied electric switch nodes and output quality control of the repaired products.

The remote dispatch control system of active acoustic monitoring of point machines (electric switches, further referred to as SAACP) has been developed. The structural scheme is shown in Figure 5.

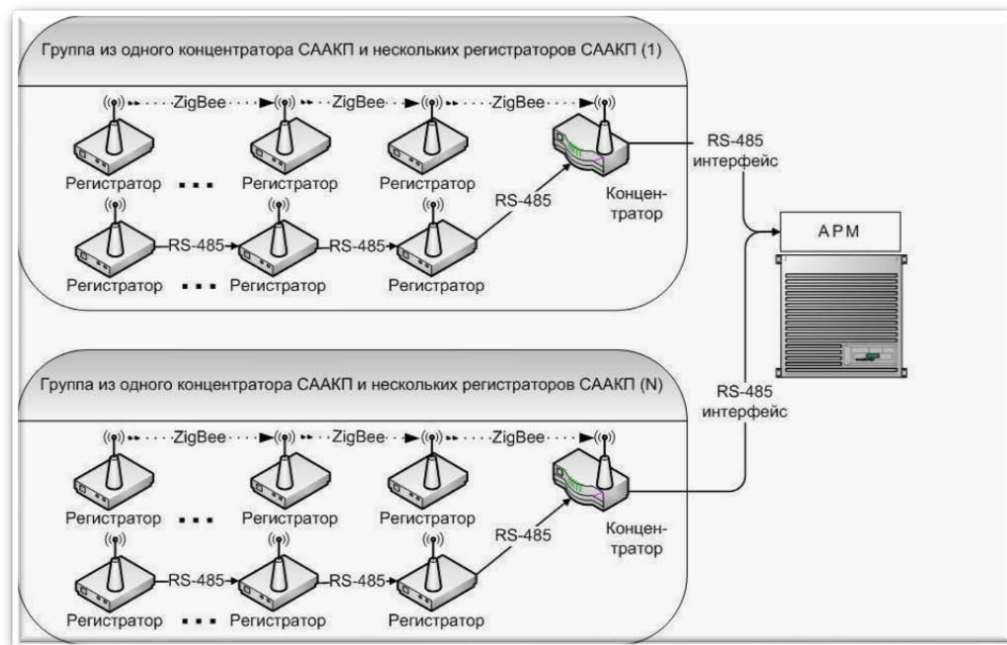


Fig. 5: The structural scheme of SAACP.

Constant monitoring of electric switch technical condition is necessary for high-speed tracks. It is crucial to forecast the durability and the remaining life of electrical switch nodes on these tracks. An electric switch node breakdown can lead to disastrous accidents. At the moment the

system is undergoing factory tests and is going to have trial operation on the Russian Railways objects.

SAACP aroused interest of the Russian Railways train department. The research works connected with diagnosing locomotive gear boxes are being held at the moment.

4. References

- [1] Акустическая эмиссия в экспериментальном материаловедении /Н.А.Семашко,В.И.Шпорт,Б.Н.Марьин и др:М.: Машиностроение, 2002. — С. 8-55.
- [2] Волович_Схемотехника аналоговых и аналого-цифровых электронных устройств, Мсква, Наука, 2005, 110-125

STATISTICAL EVALUATION OF INJECTION MOLDING PROCESS PARAMETERS IMPACT ON THE DETECTED ACOUSTIC EMISSION EVENTS

Dragan Kusić¹, Rajko Svečko², Aleš Hančič¹, Tomaž Kek³ and Janez Grum³

¹ TECOS Slovenian Tool and Die Development Centre
Kidričeva 25, 3000 Celje, Slovenia, dragan.kusic@tecos.si, ales.hancic@tecos.si

² University of Maribor, Faculty of Electrical Engineering and Computer Science
Smetanova 17, 2000 Maribor, Slovenia, rajko.svecko@uni-mb.si

³ University of Ljubljana, Faculty of Mechanical Engineering
Aškerčeva 6, 1000 Ljubljana, Slovenia, tomaz.kek@fs.uni-lj.si, janez.grum@fs.uni-lj.si

ABSTRACT

The main objective of this article was to statistically evaluate the impact of process parameters on the detected AE events during production of test specimens. The worst and the best test specimens were scanned using an optical 3D scanner for accurate measurement of test specimen dimensions in width and length. The optimal set of parameters that provided minimal number of detected AE events during specimens' production was determined by the Taguchi method. The most influential parameter was statistically obtained through an analysis of the variance method. With the help of response surface methodology we explored the relationships between the influential parameters on the detected AE events, which were captured with two 150 kHz piezoelectric acoustic emission sensors. As expected the final statistical results from response surface methodology confirmed that the most influential parameter (holding pressure) from analysis of variance has the largest influence on the detected AE events.

Key words: Acoustic emission, Taguchi, analysis of variance, test specimens, PZT sensors.

1. Introduction

Acoustic Emission (AE) is a popular non-destructive testing (NDT) method used for monitoring structures or components to detect actively propagating flaws. By applying stresses to a test specimen, an active flaw releases acoustic energy as an elastic waveform, which is detected, located and characterized by the AE measurement system. Acoustic emission is different compared to other non-destructive testing methods. The reason lies in the fact that AE signal originates within material and that it can detect movement while most other testing methods detect existing geometric discontinuities. AE's most important advantage as an NDT method is the capability of providing complete flaw site information on the entire volume of the structure. Therefore it can be used for locating structural discontinuities and flaws without losing time with point-to-point search method over the entire structures surface. Sources of AE in case of tool

steel may be different for example, from crack advance, corrosion reactions to deformation during production etc.

Injection molding is one of the most important polymer manufacturing processes where heated molten polymer material is injected into a mold cavity under high pressure. Polymer material solidifies into a shape inside the mold. This manufacturing process is very popular because of simple operation steps. An ordinary production cycle starts when the mold closes. After that the polymer material is injected into the mold cavity. Once the cavity is filled, additional pressure compensates the material shrinkage. Then the screw turns and feeds the next shot to the front screw tip. This causes the screw to retract as the next cycle is almost prepared. Once the injected part is sufficiently cooled, the mold opens and the produced part is ejected. An example of different polymer granules (types of polypropylene) is shown in Fig. 1.



Fig. 1: Example of different plastic polymer granules.

2. Experimental procedure

The polymer material used in the experiments was polypropylene (Isofil H 40 C2 F NAT) from manufacturer Sirmax SpA. This type of material is widely used because its price is relatively low and due to its suitability for use in various applications, for instance in automotive industry usually for dashboard components, fans, ductwork etc. Practical experiments have been carried out on a KraussMaffei (KM80SP380CX) injection molding machine, which has a 40 mm screw diameter and maximal clamping force of 800 kN. Acoustic emission signals were captured during the production cycle of standard test specimens that are used for material shrinkage evaluation. Acoustic emission measurement system AMSY-5 from Vallen-Systeme GmbH was used for capturing AE signals and analyzing the AE events. Two piezoelectric AE sensors VS150-M (resonant at 150 kHz) were mounted with silicone grease with two sensor holders on the tool steel insert from both sides. Both PZT sensors were connected via two preamplifiers AEP4 with a fixed gain of 40dB on the first and second channel of AMSY-5 measurement system. In the evaluation stage of acquired AE signals we focused closely on the number of detected AE events on both measurement channels. The main aim was to statistically evaluate the influence of processing parameters on the measured AE hits (events).

To lower the number of experiments we used the Taguchi method. An ordinary L_{18} orthogonal array was chosen in the experimental study as shown in Table 1. Therefore six process parameters (factors) have been analyzed to determine their influence on the detected AE events. These factors are melt temperature (A in two levels 230 °C and 240 °C), injection speed (B in three levels 40 mm/s, 45 mm/s and 50 mm/s), injection pressure (C in three levels 1000 bar,

1100 bar and 1200 bar), holding pressure (D in three levels 300 bar, 400 bar and 500 bar), holding time (E in three levels 3 s, 4s and 5s) and cooling time (F in three levels 6 s, 8s and 10 s). After conduction of all experiments we proceeded with the statistical evaluation of the obtained measurement results (AE events).

Table 1: The layout of the L_{18} Orthogonal Array with obtained AE events.

Trial No.	A	B	C	D	E	F	Number of hits at CH 1	Number of hits at CH 2	Total hits
1	1	1	1	1	1	1	103	126	229
2	1	1	2	2	2	2	56	64	120
3	1	1	3	3	3	3	44	50	94
4	1	2	1	1	2	2	102	104	206
5	1	2	2	2	3	3	84	99	183
6	1	2	3	3	1	1	53	70	123
7	1	3	1	2	1	3	123	144	267
8	1	3	2	3	2	1	40	48	88
9	1	3	3	1	3	2	50	58	108
10	2	1	1	3	3	2	71	85	156
11	2	1	2	1	1	3	96	126	222
12	2	1	3	2	2	1	62	71	133
13	2	2	1	2	3	1	56	57	113
14	2	2	2	3	1	2	45	55	100
15	2	2	3	1	2	3	85	103	188
16	2	3	1	3	2	3	77	70	147
17	2	3	2	1	3	1	70	101	171
18	2	3	3	2	1	2	89	56	145

3. Experimental results

We varied the processing parameters in 18 experimental runs according to L_{18} orthogonal array. Analysis of variance (ANOVA) was then used for evaluating the effect of process parameters on the total number of detected hits (AE events). In Table 2 the ANOVA results are presented.

Table 2: ANOVA results for total number of detected AE events

Source	df	S	V	F	p-value	Significance
A	1	102.72	102.72	0.0828	0.7832	no
B	2	146.33	73.17	0.0589	0.9433	no
C	2	9463	4731.5	3.8138	0.0853	no
D	2	14646.33	7323.17	5.9028	0.0383	yes
E	2	6277	3138.5	2.5298	0.1597	no
F	2	7265.33	3632.67	2.9281	0.1296	no
Residual	6	7443.78	1240.63			
Total	17	45344.5				

As can be seen only the factor D (holding pressure) is the most influential factor that affects greatly the total number of detected AE events. According to this result we used the response

surface methodology to explore further the relationships between the influential parameters on the detected AE events. As can be seen from Table 1 during production of test specimen in 7th experimental run the highest number of total hits was 267. On the other side the test specimen produced in the 8th experimental run had the smallest number of detected hits only 88. These two test specimens were scanned with an optical 3D digitizer ATOS II SO. Both scanned specimens are shown in Fig. 2.

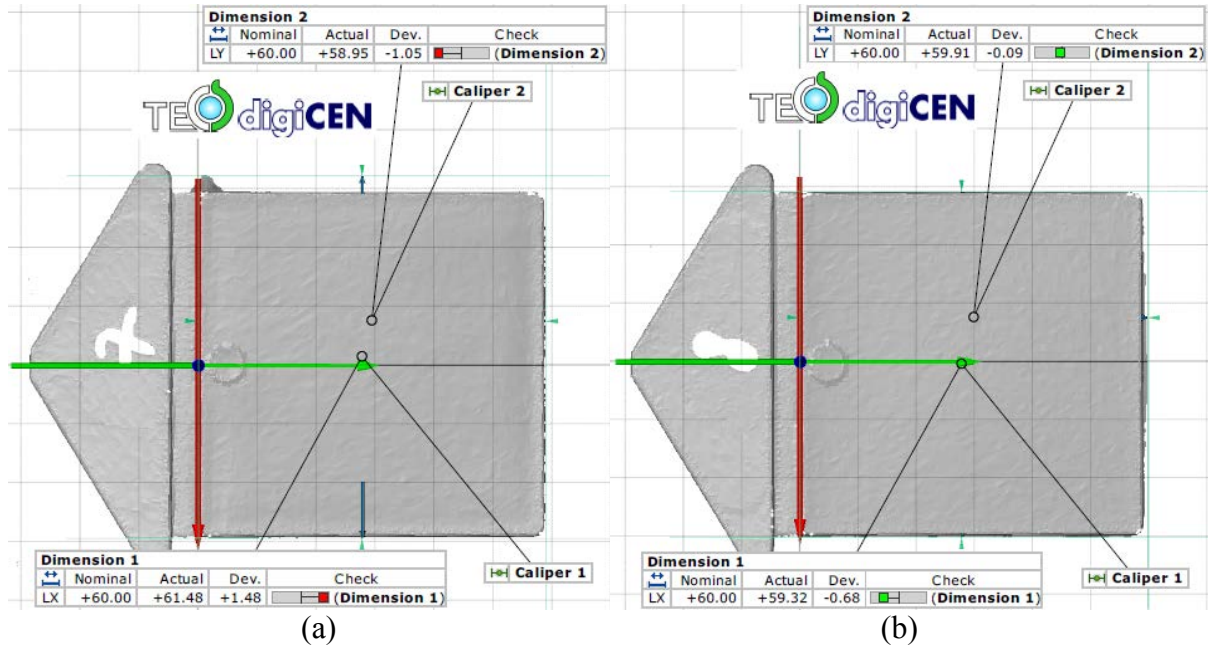


Fig. 2: Scanned test specimens (a) specimen 7 and (b) specimen 8.

Optical 3D Digitizer is based on the principle of capturing images through the camera, which then through an appropriate program prepares a computer model. The accuracy that can be achieved with these digitizers depends largely on the quality of the camera, which records the desired object. Of course, in a very small precision scale the accuracy itself also depends on the wavelength of the light. The biggest advantage of 3D digitizer lies in extremely rapid procedure of digitizing and excellent precision (precision declared for very small objects are up to 2 microns). As can be seen from Table 1 and Fig. 2 the number of detected AE events during production of test specimens 7 and 8, is largely affected by the used set of the process parameters in which the most influential is factor D (holding pressure).

The acoustic emission signal intensity is proportional to signal energy [6-7] and defined by an integral of signal square

$$E_{AE} = \int_0^{\infty} |V(t)|^2 dt \quad (1)$$

Amplitudes of the acoustic emission signals can be given in the form of a voltage, but it is usually converted into decibels by the following equation

$$A_{AE} = 20 \log \left(\frac{|V(t)|}{V_r} \right) \quad (2)$$

whereas $V(t)$ is the maximal measured voltage of AE signal and V_r is the reference input voltage on preamplifier, which was in our case equal to 0.001 mV. Fig. 3 shows the amplitudes and AE signal energy during the production of test specimens 7 and 8.

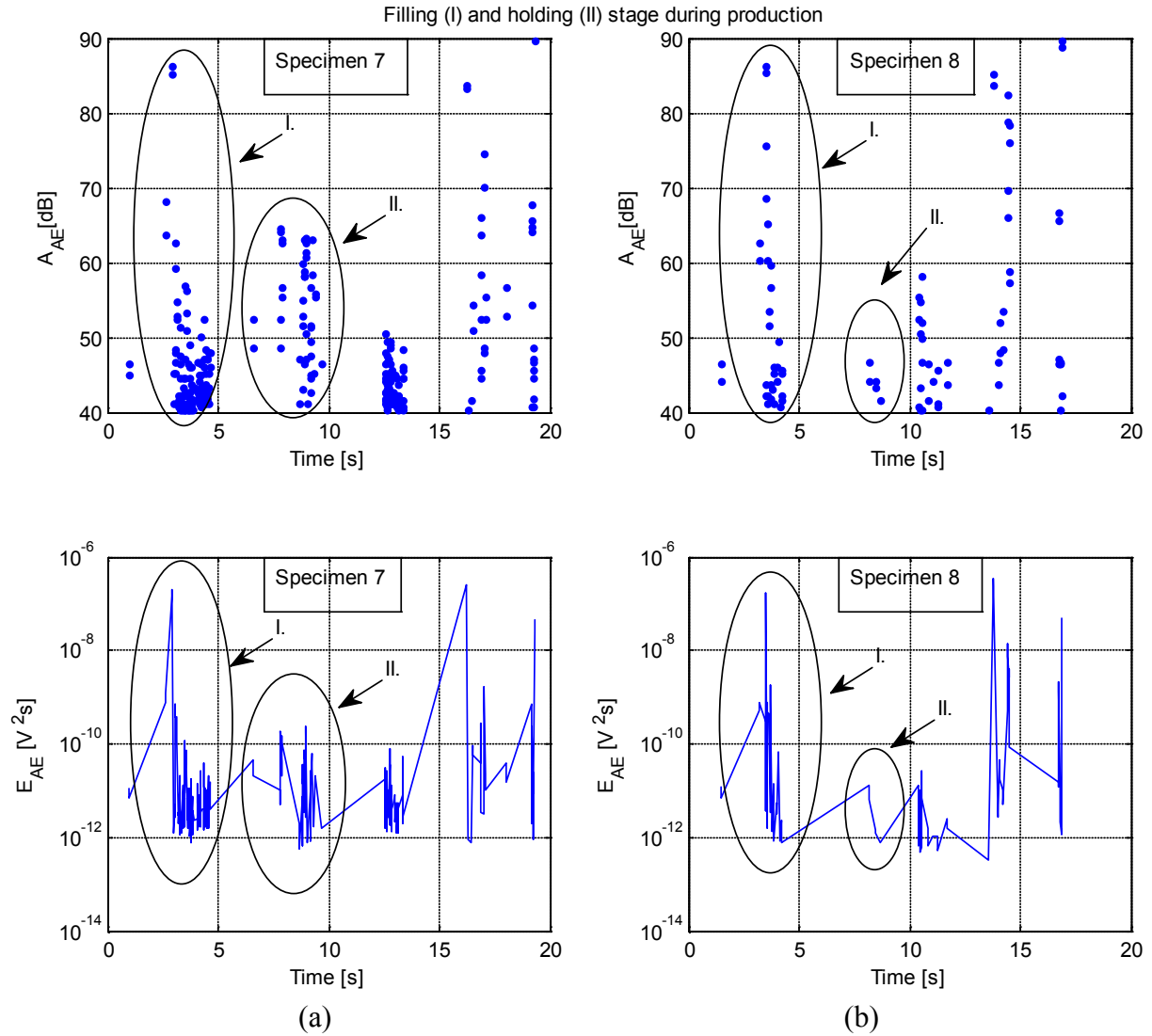


Fig. 3: Amplitude and energy values of AE signals during production of (a) test specimen 7, (b) test specimen 8.

As can be seen from Fig. 3 the obvious difference in total number of detected AE hits is both in filling as well as in holding stage during both test specimens production.

Response surface methodology (RSM) is a collection of mathematical and statistical techniques for empirical model building. In most RSM problems, the form of the relationship between the response and the independent variable is unknown. Normally, a low-order polynomial in a region of the independent variables is employed. We modeled the response by a linear function of two independent variables, so the approximation function is the first order model defined as

$$y = \beta_0 + \beta_1 x_1 + \beta_2 x_2 + \dots + \beta_k x_k + \varepsilon \quad (3)$$

where y is the response, β 's are parameters to be determined, x_k are variables that represents the factors. In our case we investigated the relationships between two parameters on the output response (total hits). The most influential parameter D (holding pressure) was investigated first to parameter E (holding time) and later also to parameter F (cooling time). Normally it is unlikely that a polynomial model will be a good approximation of the parameters relationship over the entire 2-D space. Therefore our goal was to cover only a small region of parameter values inside which the model gives good results.

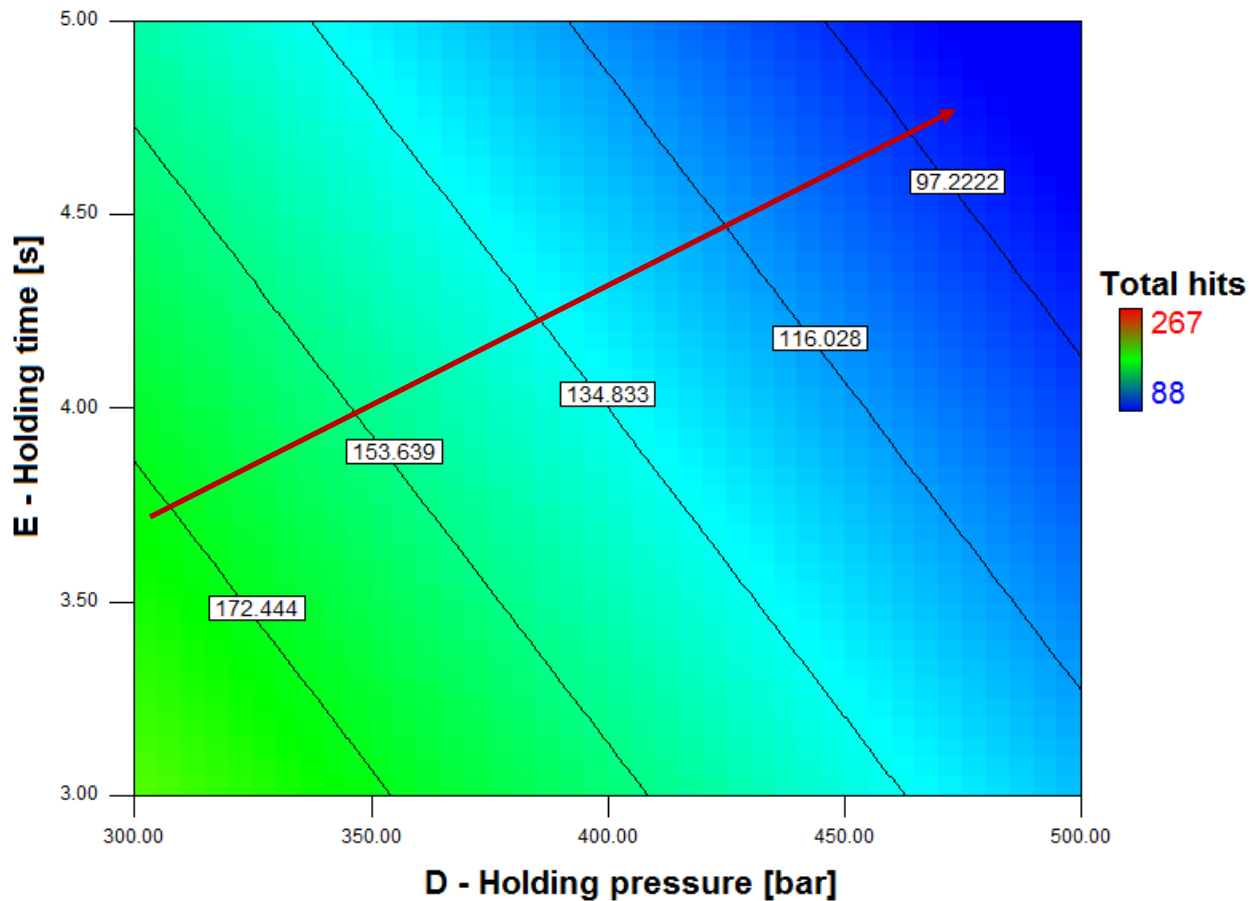


Fig. 4: Contour plot of a total hits response with factors D and E.

Fig. 4 shows the contour plot of a total hits response in regards to the holding pressure and holding time. The contour was plotted by taking into account (beside levels of factors D and E) also the following actual factor values:

- A-Melt temperature = 235°C
- B-Injection speed = 45 mm/s
- C-Injection pressure = 1100 bar
- F-Cooling time = 6 s

From Fig. 4 we can state that by increasing the amount of holding pressure to the maximal level of 500 bars and by prolonging the holding time to 5 seconds then the number of total hits can be minimized (method of steepest descent) to the region of 88 detected AE events. This is in accordance with the obtained measurement results and theoretical assumptions. The aim of the contour plot is to lead the experimenter efficiently and quickly to the desired goal, which in our case is the minimum of detected AE events at which the test specimens are produced with acceptable quality. Inside the contour plot the lines between two factors represent the constant response (number of detected AE events in our case).

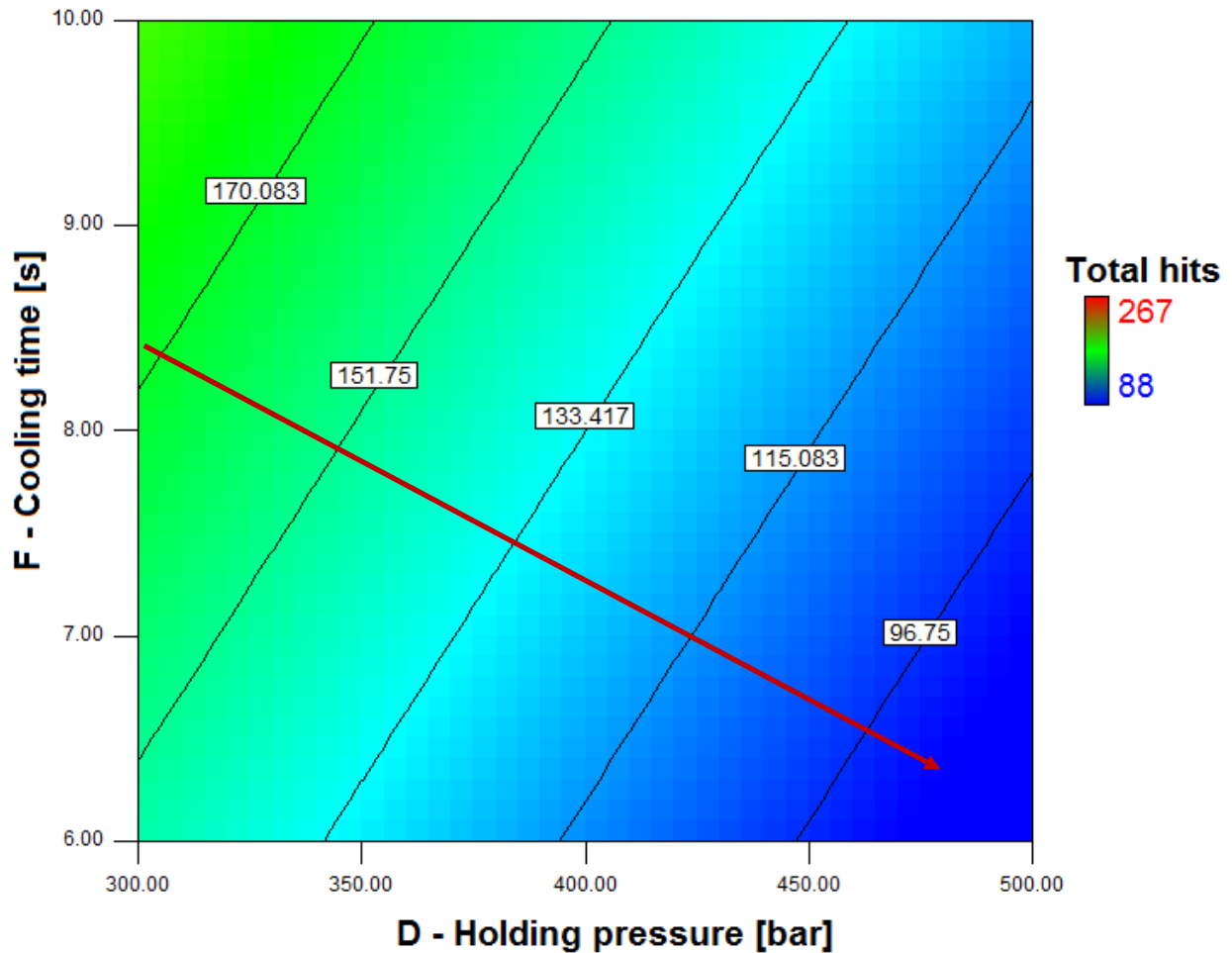


Fig. 5: Contour plot of a total hits response with factors D and F.

Fig. 5 shows similar like previously the contour plot of a total hits response in regards to the holding pressure and holding time. The contour was plotted by taking into account (beside levels of factors D and F) also the following actual factor values:

Contour for total hits response regarding the holding pressure and cooling time

The actual factors:

A-Melt temperature = 235°C

B-Injection speed = 45 mm/s

C-Injection pressure = 1100 bar

E-Holding time = 5 s

From Fig. 5 we can state that by increasing the amount of holding pressure to the maximal level of 500 bars and by decreasing the holding time to 6 seconds then the number of total hits can be minimized to the region of 88 detected AE events by taking into account also the above values of actual factors. In this way the experimenter is capable to obtain the desired number of AE events in the future AE tests. According to his process knowledge obtained from practical situations during production he can quickly adjust the factors levels or simply keep the factor values at the optimal level value.

4. Conclusions

In this research work we statistically evaluated the measurement results obtained during 18 experimental runs. The goal was to minimize the number of AE hits (events) and to investigate the impact of different process parameters on the detected AE hits. We found that test specimens with good quality were produced at lower number of AE hits, which were captured by AMSY-5 measurement system from Vallen-Systeme GmbH. Among 18 produced test specimens we scanned the worst and best test specimen according to the number of detected AE hits during production cycle. With the help of ANOVA method the most influential parameter (holding pressure) was found which significantly affects the total number of AE hits. With response surface methodology we closely explored the relationships between the holding pressure and two other factors on the total number of detected AE hits. In case of holding time we saw that this factor needs to be increased if we want to reach minimal number of AE events. In opposite to this, the cooling time needs to be decreased for the same goal, which is in accordance with theoretical assumptions. The RSM results confirmed all our expectations from practical experiments. Still an improvement in the final RSM result would be possible to achieve by using a higher degree of polynomial, for example second order model where optimal point can be precisely reached.

Acknowledgement

The research work was partly financed by the European Union, European Social Fund, and by the Slovenian Ministry for Higher Education, Science and Technology.

5. References

- [1] Taguchi G., Chowdhury S., Wu Y.: Taguchi's Quality Engineering Handbook, Wiley and Sons, New Jersey, 2005.
- [2] Montgomery D.C.: Design and analysis of experiments, Wiley, New York, 2001.
- [3] Khuri A.I.: Response Surface Methodology And Related Topics, World Scientific, Singapore, 2006.
- [4] Khuri A.I., Cornell J.A.: Response Surfaces - Designs and Analyses, Marcel Dekker Inc., New York, 1996.
- [5] Pukelsheim F.: Optimal Design of Experiments, Wiley and Sons, New York, 1993.
- [6] Vallen H.: Acoustic Emission Testing: Fundamentals, Equipment, Applications, Vol. 6, Castell Publication Inc., Wuppertal, 2006.
- [7] Miller R. K., Hill E.v.K., Moore P. O.: Nondestructive Testing Handbook, Third edition, Vol. 6, Acoustic Emission Testing, American Society for Nondestructive Testing, Inc., 2005.

TESTING PRESSURE VESSEL WITH ACOUSTIC EMISSION

Goran GAVRANIĆ², Tomaž KEK¹ and Janez GRUM¹

¹University of Ljubljana, Faculty of Mechanical Engineering, Aškerčeva 6, 1000 Ljubljana, Slovenia, tomaz.kek@fs.uni-lj.si , janez.grum@fs.uni-lj.si

²Ecoplin Zadel d.o.o., Inspection body for pressure vessels, Žabjek 15, 1294 Višnja Gora, Slovenia, goran@ecoplin-zadel.si

ABSTRACT

The article presents the results of testing pressure vessels for liquefied petroleum gas (LPG) with acoustic emission. The main objective is to show the most significant impacts which have influence on measured AE-signals, like human error, bad weather conditions and also corrosion on the pressure. An integral part of the test is pressurization, which is necessary for emergence of acoustic waves, which are later detected as AE signals. We record this signals with two resonant 150 kHz piezoelectric sensors, which are mounted directly on the coat of the pressure vessel. From these measurements we gained valuable information, which help us evaluate the pressure vessel and determine the class of it.

Key words: acoustic emission, pressure vessel, pressurization, AE monitoring

1. Introduction

Acoustic emission is elastic energy, which is spontaneously released from material, when it is under stress. In our case we achieve stress in material with pressurization. Bigger the stress is and faster is pressurization, more AE-signals we sense (also depend from characteristic of sensor). The sound waves produced by the stress (pressurization) in an isotropic material propagates in concentric circles. When wave propagates, also attenuate [1]. Wave attenuation is important when we decide how many sensors we shall put on pressure vessel. Sensor must sense waves which are generated anywhere on pressure vessel. Today is testing with AE applied for periodic inspection of pressure vessel. For evaluation of test we used only burst signals and not continuous signals [2]. Burst signal is result of formation or propagation of crack. But also this signal in some cases doesn't show us the real state of material as we shall see later in this article. The big advantage of AE compared to other NDT methods is that we can check all volume of material. AE allow us to check very large surface. Larger the surface is more sensors we need. We can predict failure of material before it happened. That's why this method is appropriate for testing pressure vessel when it's talk about safety. If we estimate on base of measured signals, that pressure vessel contain specific defect, which can cause failure of material, we are allowed to prohibit it further use.

Important effect which can appear during test are Kaiser and Felicity effect. For Kaiser effect it is typical that AE-signals appears when we reach higher pressure as it was at previous loading. This effect is normal phenomena when testing with AE. Felicity effect is more dangerous,

because AE-activity appear before reaching previous load. This show that material have difficulties to reach stable condition [3].

It is important to know that fluid, which is used for pressurization is the same as it is used for storage. That prevent any additionally corrosion and contribute to longer life of pressure vessel.

2. Procedure for testing pressure vessel

We have tested small pressure vessel (5m^3). Before testing we have to gather information about pressure vessel. Different constructions demands different procedure for testing, also different sensor location. Following information must be known about pressure vessel:

- characteristic of geometry,
- characteristic of material,
- location of welds, legs, valve, identification table
- already known defects or repairs,
- extreme conditions during operation
- results from previous tests

In table we can see description of measuring equipment which is used for gathering AE-signals and evaluating them.

Table 1: Description of measuring equipment

System	MISTRAS - SAMOS - PCI8
Type of sensors	R15I (40 dB integriran predojačevalnik)
Peak sensitivity	-65 dB/ R15I
Resonant frequency	150 kHz / R15I
Operating frequency range	80-200 kHz / R15I
Evaluation threshold	40 dB

Pressure which we have to reach during test is minimal 12 bars. For 5m^3 pressure vessel we use only two sensors, because we have to satisfy conditions from standards EN 15495:2007, EN 14584:2005 and EN 12817:2010. On fig. 1 we can see location of sensors for two different types of pressure vessels [5].

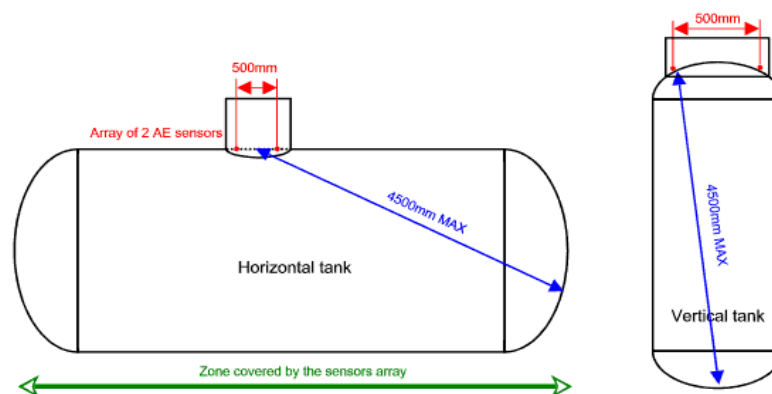


Fig. 1: Location of sensors

The surface below the sensors shall be cleaned to ensure the maximum coupling efficiency. Bad coupling efficiency can prevent credible evaluation of material. The characteristics of the type of the acoustic couplant used shall not affect the structure adversely. The sensors are directly attached to the pressure vessel with magnetic holders [4, 6].

3. Results of the tests where errors

3.1 Raining during the test

On fig. 2, we can see part of the test of the pressure vessels with volume 2,8m³ and length of 1,8m, during which started to rain. Raining started at time 1100s, which is shown as increased activity of hits. During 1100s and 1300s we tried to hold down the pressure, to get the most reliable data, how rain affects on measured signals. As we can see on Fig. 2 measured signals mostly have low amplitudes (< 60 dB). Around 1250s we can see hits with bigger amplitudes. That we could attribute to bigger drops which have fallen from the nearest tree.

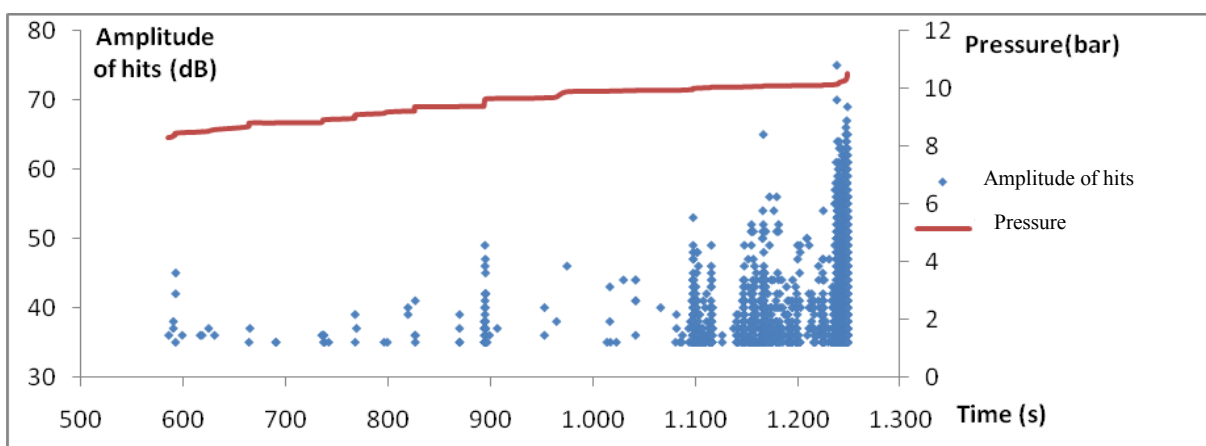


Fig. 2: AE activity versus time and pressure

Fig. 3 show amplitude of the measured AE-event versus clusters (area between two sensors divided on 9 parts) during the test of pressure vessel. During the test the biggest activity was measured in cluster 9 and the smallest in cluster 4. The biggest amplitude in cluster 9 was 70 dB.

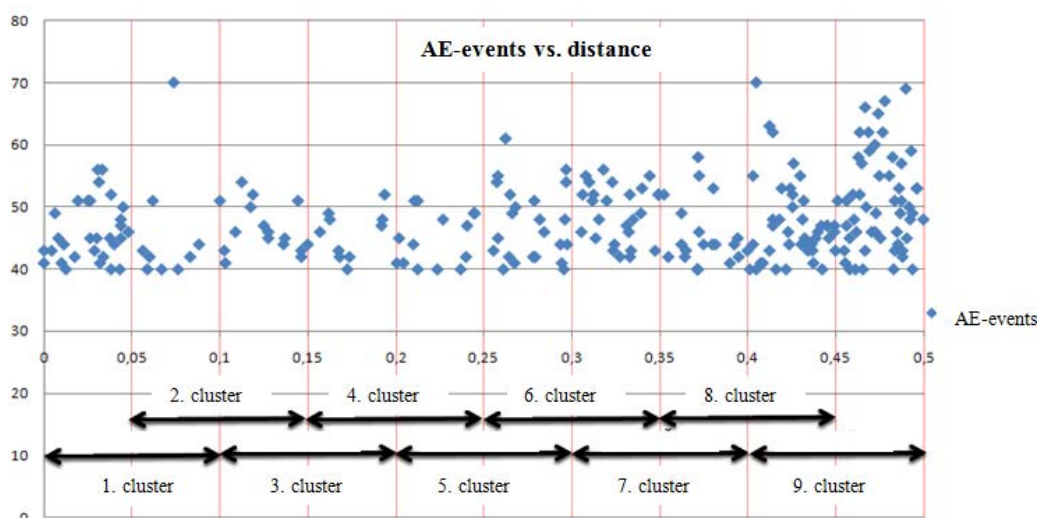


Fig 3: Measured AE-events versus clusters

On Fig. 4 are shown amplitudes of measured signals versus time and pressure. It was slowly raining during whole test. As we can see from Fig. 4 we have a lot of hits with low amplitude, lower than 40 dB if we are precise. We used filter, which we are using in such a cases to delete signals which were caused by rain drops. Blue squares show hits before using filter, while red squares present hits after using filter. We can see that during holds of the pressure AE-activity didn't decreased significantly. In case of not raining during the test, that would show possible danger. Amplitudes are quite high for this time interval and achieve also 50 dB. AE-activity is the biggest at the end of the test cause pressure there achieves maximum limit and rain only contribute to increased AE-activity.

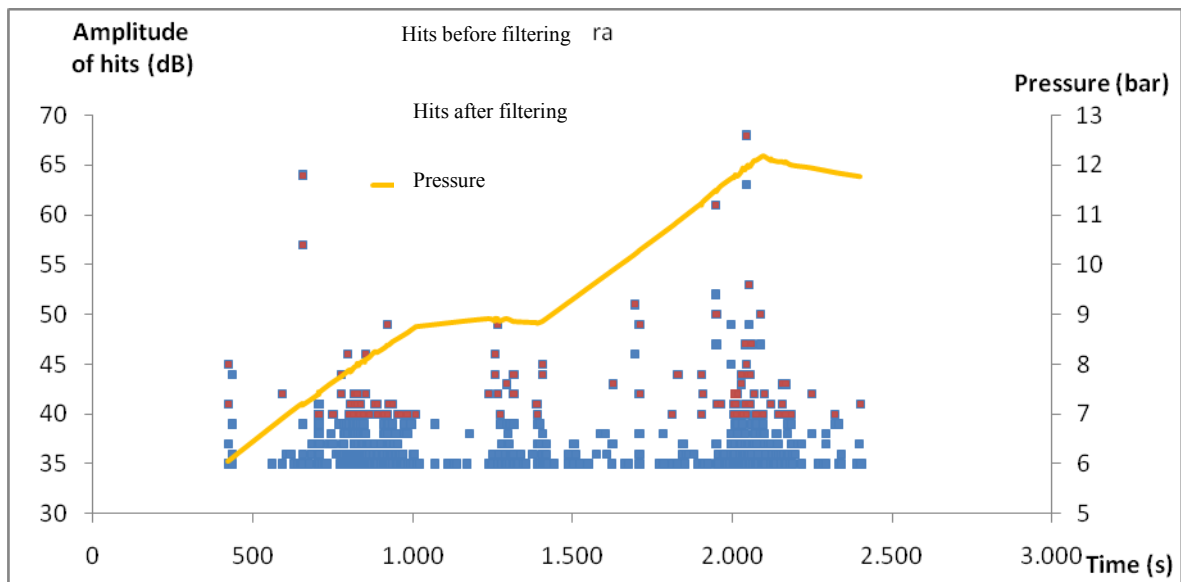


Fig. 4: AE activity versus time and pressure

On Fig. 5 we can see one of the transient AE-signal caused by rain drop. Amplitude of signal quickly exceeds the acquisition threshold. Signal is short with typical exponential amplitude decreasing.

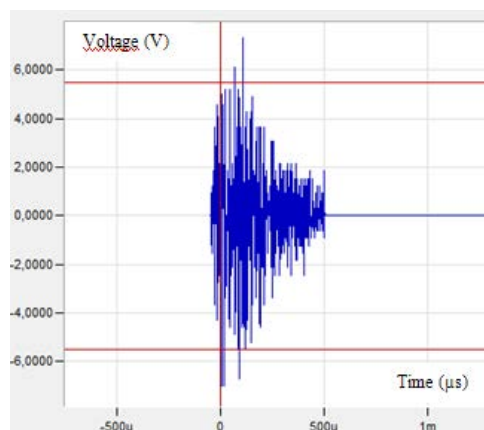


Fig. 5: AE-signal caused by rain

3.2 Touch of the pressure vessel during the test

We were testing pressure vessel for LPG with volume 1,8m³ and length of 2m.

With ellipse on Fig. 6 we can see hits which were caused by touch of the hand during the test. As we can see AE-activity significantly increase, mostly with low amplitudes but in so large number. Number of hits during this touch was increased from 111 to 786 hits.

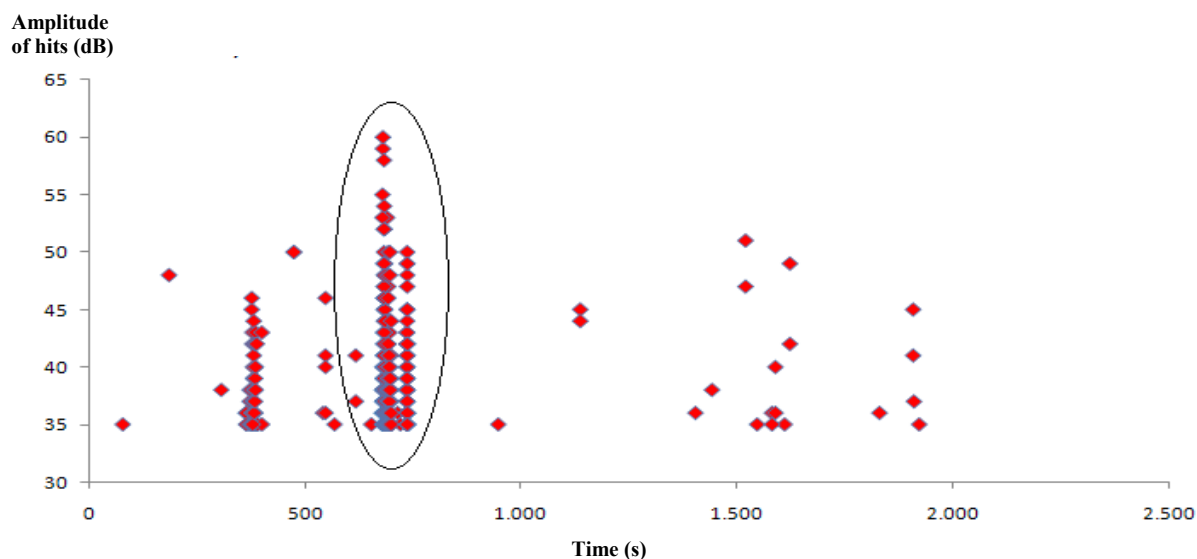


Fig. 6: AE-activity versus time during the touch of the pressure vessel

On Fig. 7 we can see one of the transient AE-signal caused by touch. Amplitude is extremely high already at the beginning. It raises high but also drop very quickly and fall under acquisition threshold.

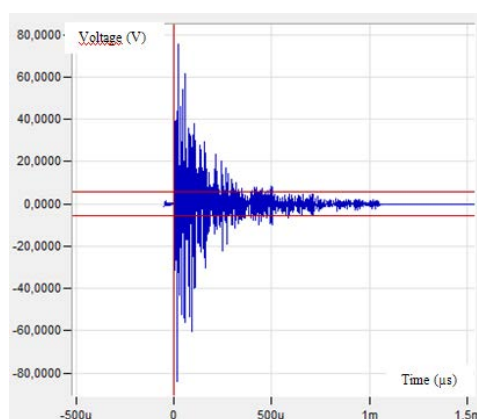


Fig. 7: AE signal caused by touch

3.3 Močno korodirana tlačna posoda

One goal of acoustic emission testing on the pressure equipment is to diagnose the propagation of localized corrosion or to verify the integrity of the corrosion protective layer on the coat. Corrosion damage propagate very fast in some cases, if coat of pressure vessel is damaged for example. AE has been applied, not only to detect or confirm corrosion but also to validate repairs and evaluate efficiency of corrosion protection. Corrosion cracking is important damage phenomenon when we talk about pressure vessels. Unpredicted failures can occur in service, with safety, health, economic and environmental consequences. Pressure vessel is often corroded on external coat, because of weather influence (rain, ice, sun,...). It's hard to separate signals generated from corrosion, from others like particle impacts, crystallization, [3].

We were testing pressure vessel for LPG with volume 5m^3 and length of 2,3m.

On Fig. 8 we can see AE-activity during test heavily corroded pressure vessel. We raised up acquisition threshold from 35 to 40dB because we exceed criteria for beginning of pressurization. The amplitude range is up to 65dB. Number of hits goes over 1000 and AE-events stop at number 159. We classify pressure vessel in class 2, cause AE-events don't have high amplitudes. From this results we can come to conclusion that corrosion have big influence on increased AE-activity, with low amplitudes, during the test. That kind of pressure vessel must be restored and painted with corrosion resistant paint. AE-activity starts increasing during second pressurization, higher pressure. On Fig. 9 we can see number of hits on each channel through whole test. Number of hits is bigger on second channel, from which we can conclude there was more corrosion near second sensor.

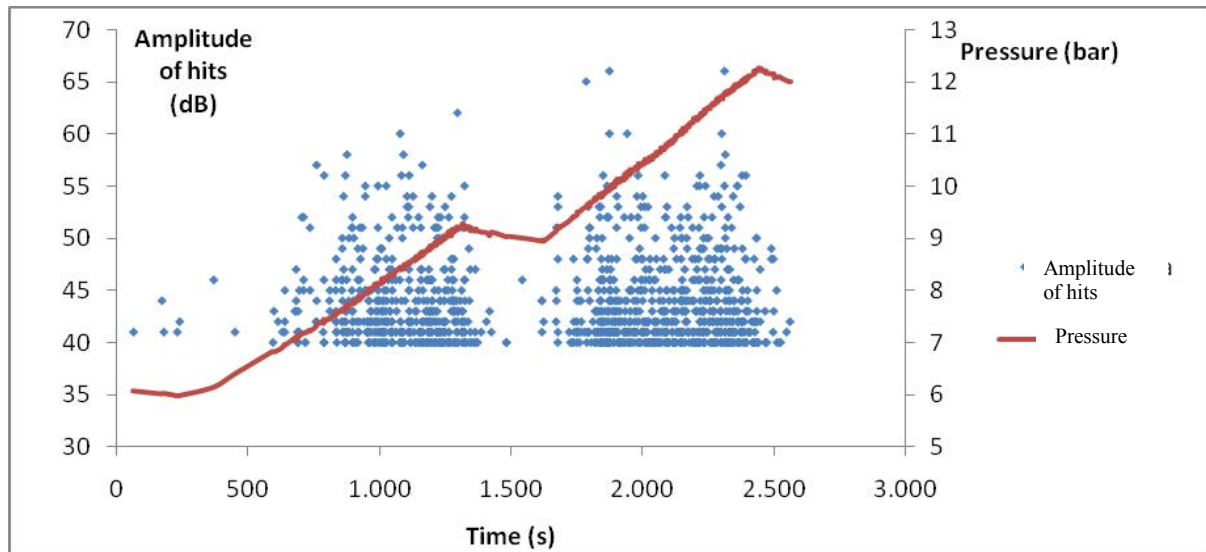


Fig. 8: AE activity versus time and pressure

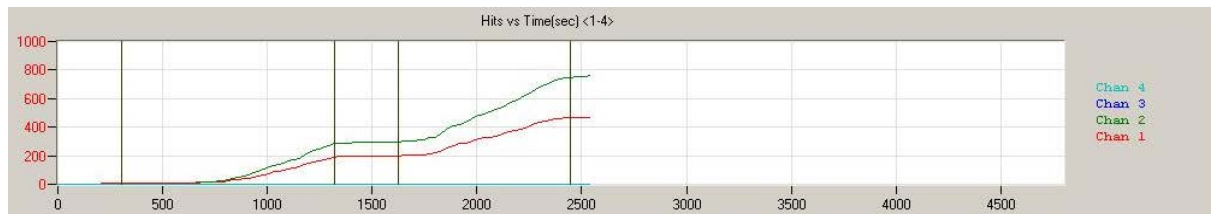


Fig. 9: Hits increasing on both channels

3.4 Leakage on probe for measuring pressure

We were testing pressure vessel for LPG with volume $2,5\text{m}^3$ and length of 1,5m.

In some cases leakage appear during the test even though we checked for leakage before starting the test. On Fig. 10 we can see increased ASL (average signal level), marked with red ellipse, which can tell us that somewhere on pressure equipment leakage is presented. We found that that probe for measuring pressure wasn't tighten well. We tighten it and continued with test.

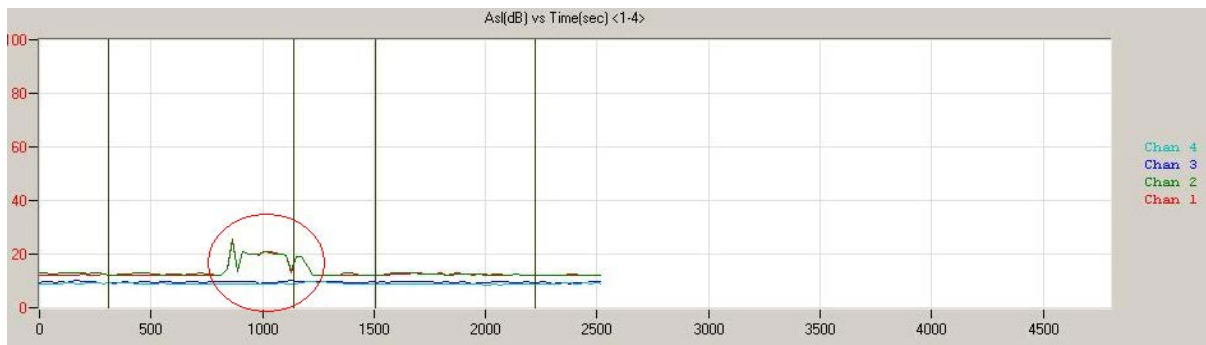


Fig. 10: Increased ASL caused by leaking

3.5 Wrong valve opened

Here we have some similar results as in previous paragraph where we talk about leakage. Fig. 11 shows us what happened if we open wrong valve, with which we control pressurization speed. Instead of opening gas valve we opened liquid valve. System detected different fluid flow as this time there was liquid phase in pipe and not gas as usually and this was shown as increased ASL, from 13 to 22dB. Similar thing happened if we open gas valve to fast.

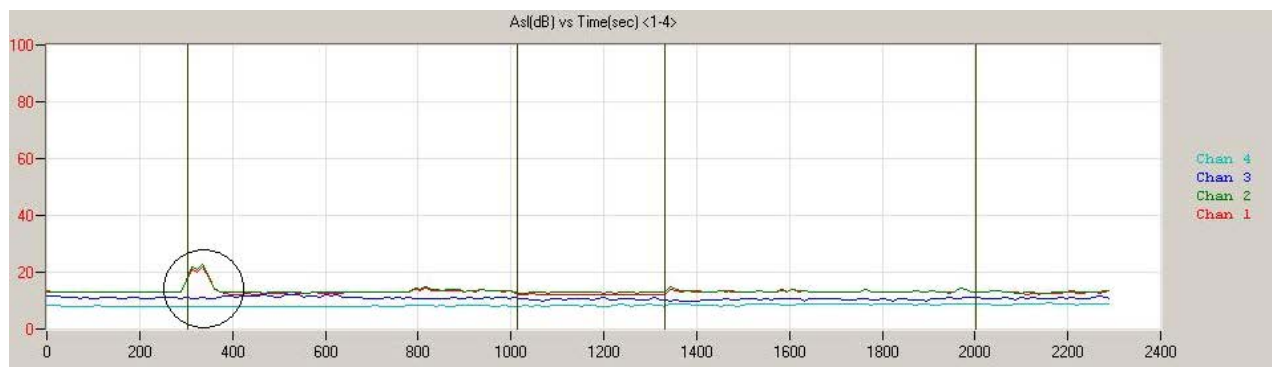


Fig. 11: Increased ASL caused by opening wrong valve

4. Conclusion

In this article are shown are represented results which were made by some interruptions during the tests with AE. Based on the results, we can come to the conclusion that rain affects on results of the test as it increases the AE-activity. Amplitudes of hits are mostly low (<60dB), but in some cases there are also some higher amplitudes. At the touch of a hand also come to increased AE-activity, but when we put hand down from pressure vessel AE-activity dropped rapidly. One of AE-signal has in that case typical shape, with high amplitude at the beginning, which get lower with time. Leakage during the test of pressure vessels or any sudden change in the gas flow (to quick pressurization) is detected as an increase of the ASL. With ASL values we can check leakage on any other pressure equipments. At corroded pressure vessel we detect an increased AE-activity already at the beginning of pressurization. The amplitude range is up to 65 dB. During the pressure hold AE-activity decreases, which is quite a normal phenomenon, because at some time during the pressure hold movements in material stops.

5. References

- [1] Hartmut Vallen: German Society for NDT, Vallen systeme: Acoustic emission testing, Fundamentals, Equipment, Applications, Volume 6, 2006, 6-48
- [2] SIST EN 1330-9 Non-destructive testing –Terminology – Part 9: Terms used in acoustic emission testing
- [3] Ronnie K. Miller, Eric v. K. Hill, Patrick O. Moore: Nondestructive testing handbook, Acoustic emission testing, Volume 6, American Society for Nondestructive Testing, 2005, 13, 38, 415-422
- [4] SIST EN 15495:2008 Non-destructive testing – Acoustic emission – Examination of metallic pressure equipment during proof testing – Zone location of AE sources
- [5] SIST EN 12817:2010 LPG equipment and accessories- Inspection and requalification of LPG tanks up to and including 13 m³
- [6] SIST EN 14584:2005 Non-destructive testing- Acoustic emission- Examination of metallic pressure equipment during proof testing- Planar location of AE sources

ACOUSTIC EMISSION MONITORING OF FRACTURE PROCESS STAGES IN HYDROGEN EMBRITTLED HIGH- CARBON STEEL

E. Merson, D. Merson, A. Vinogradov

Laboratory for the Physics of Strength of Materials and Intelligent Diagnostic Systems,
Togliatti State University, Togliatti, 455667, Togliatti, Russia
mersoned@gmail.com

ABSTRACT

The acoustic emission (AE) technique was used for monitoring of the fracture process during slow three-point bending of smooth Zn-plated high-carbon steel specimens. It was shown that electrolytic Zn-plating results in hydrogen charging of specimens, which exerted a strong effect on the ductility of steel. The primary AE sources during slow monotonic loading of the hydrogen embrittled specimens, which were revealed with an aid of SEM, were associated with brittle cracking along austenitic grain boundaries or sulphides. The concurrent AE analysis allowed distinguishing between five stages of the fracture process: (I) microcracks nucleation during the incubation period showing a low AE activity; (II) the stage of the increasing rate of AE signals accumulation and increasing RMS level caused by accelerated damage accumulation; (III) the overall stable crack growth, followed by damage rate reduction, (IV) the stage preceding the critical regime corresponding to formation and propagation of a catastrophic crack (V).

Key words: hydrogen embrittlement, fracture, acoustic emission, high-carbon steel

1. Introduction

Hydrogen embrittlement (HE) of metals and alloys is a well-known scientific and engineering problem. Dissolved hydrogen can cause a serious deleterious effect on service properties of metallic articles. A degree and form of HE manifestation is dependent on many factors such as the microstructure, chemical, physical and mechanical properties of metal, concentration and state of hydrogen, temperature and strain rate, etc. HE of steels usually results in crucial downgrade of their ductility and strength [1], particularly for high-strength steels [2] where even a little concentration of hydrogen (<1ppm) can cause a substantial drop in ductility [3]. One of the most common sources of hydrogen for such steels is electrolytic plating which is often used as a final technological operation during manufacturing. Hydrogen dissolves predominantly in the coating and the surface layers of the steel substrate during this process [4]. In addition, the distribution of hydrogen can easily change under the influence of elastic stress, temperature, electric field, etc., because of high mobility of hydrogen atoms inside the metal. Therefore, any elastic distortion inside the metal matrix caused by structural irregularities such as dislocations, grain and interphase boundaries etc. can serve as potential traps for hydrogen [2].

The increased concentration of atomic or molecular hydrogen in a local volume of metal can lead to microcrack nucleation and propagation near this region.

Several mechanisms have been proposed to explain the effect of hydrogen on mechanical properties of materials. The most commonly cited mechanisms include (i) the hydrogen pressure buildup mechanism, in which the pressure of hydrogen bubbles provides the stress for the formation and propagation of a crack, (ii) hydrogen adsorption at the crack tip or surface imperfections, which reduces the surface energy for crack propagation, (iii) hydrogen-induced reduction of the cohesive strength of the lattice, (iv) hydrogen accumulation at precipitates and second-phase particles, which can lead to dislocation generation or nucleation and growth of a crack, (v) formation and fracture of brittle hydrides, (vi) hydrogen-induced reduction in stacking-fault energy and (vii) hydrogen-induced enhancement of dislocation mobility, which promotes dislocation motion at a lower applied stress [5]. However before any mechanism sets in, local enrichment of metal with hydrogen has to occur up to levels at least 10 times higher than normal mean volume concentration. Thus the most pronounced effect of HE near room temperature appears at slow strain rates or at static load due to a large enough time for hydrogen diffusion [6]. Unfortunately, such service conditions are most frequently encountered for a wide range of steel parts and constructions. That is the reason for many failures caused by hydrogen.

Hence, to prevent crucial consequences of HE the effective non-destructive technique capable of monitoring for equipment exposed to HE is required along with the deepened insight into the processes which occur within a material under the influence of hydrogen. One of the most promising instrument for solving both problems is the acoustic emission (AE) technique which is known to be highly sensitive to HE [7–14]. In case of the HE of a high-strength steels the intergranular cracking proposed as a main AE source [8,10,15]. Therefore, the amplitude of the AE events is higher for the high strength steel after hydrogen charging and amount of the AE events correlates with the number of intergranular cracks [8]. Troiano [16] has shown that under static load of the high strength steel the crack growth occurs involves three stages: (i) incubation period interpreted as the time required for a critical amount of hydrogen to diffuse to the point of crack initiation; (ii) nucleation and slow discontinuous crack growth under macroscopic diffusion of hydrogen; (iii) unstable rapid crack growth through the material free of hydrogen. However, because of its low sensitivity, electrical resistance technique cannot measure the resistance change for a very small crack and also it does not give a detailed insight into the process of crack initiation and propagation [17]. Therefore the same staging was revealed in [17] with the help of the AE technique.

Despite a significant progress in the field of AE application to the HE phenomena it should be noted that most of investigations were conducted with notched specimens under static load. Such conditions allow discovering the kinetics of a single crack growth when the most part of specimen material is in a state of elastic deformation. However for the successful non-destructive testing of the steel parts in service it is important to conduct the AE experiments under conditions close to reality. Thus, the objective of this investigation is to reveal the hydrogen-assisted fracture kinetics in the smooth high-carbon steel specimens under slow active loading.

2. Experimental

High carbon steel 70 in Russian designation (AISI 1070 is a close analogue) was chosen for the present study because it is wide-spread industrial use as spring steel, which is known to be prone to premature failure due to HE [12]. The chemical composition of this steel is shown in Table 1. The samples were machined to have a rectangular shape of 120 mm length, 20 mm width and 1.8 mm thickness. They were thermally treated using a schedule that is commonly used for this type steels: 1) quenching from 850 ± 10 °C in oil; 2) low tempering at temperature of 240 ± 10 °C for 1 h; 3) primary tempering at 450 ± 10 °C for 2 h followed by cooling in air. The hardness after this treatment was of 49 ± 2 HRC.

Table 1. Chemical composition of steel 70.

C	Si	Mn	Cr	S	P	Cu	Ni	Fe
0.70	0.29	0.72	0.03	0.006	0.013	0.06	0.02	balance

For hydrogen charging a part of the specimen was electrologically plated with a Zn layer of 15 mm thick from an alkaline solution containing of 110-120 g/l NaOH and 12-14 g/l ZnO. The plating was performed at electric current density of 8 A/dm² during 20 min. Reference specimens were left unplated for comparison.

Using a Bruker AXS G8 gas analyzer with a nominal accuracy $\pm 0,05$ ppm the hydrogen content [H] was measured in a reference and Zn-plated specimens and also in a specimens with removed Zn coating. The samples of 5×5×1.8 mm dimensions were used for the gas analysis. Surface layer of ~50 μ m depth was mechanically removed with the grinding paper for a part of Zn-plated specimens in order to reveal a hydrogen distribution along the specimen thickness.

Three points bending mechanical testing was performed at room temperature using a screw driven Instron-type frame. The load was applied at a constant cross head velocity of 0.07 mm/min. The ductility was characterized by the maximum deflection at failure Δ_{max} .

Acoustic emission was recorded using a home-made PC-controlled system with a 12 bits ADC at the core. A broadband (50-500 kHz) piezoelectric transducer MSAE-L2 (Microsensors AE Ltd., Russia) with a low noise built-in 27 dB preamplifier was securely mounted on the specimen using vacuum oil as a couplant. The signal from the sensor's preamp output was transferred through a main filter-amplifier MSAE-FA010 with the gain set at 40 dB and the frequency band set between 50 and 1200 kHz. The laboratory noise did not exceed 30 μ V (peak-to-peak). The burst AE signals having relatively high amplitude above 1 mV (of 30dB threshold) were recorded and counted synchronously with the load signal. The waveforms of 4096 readings were stored for the post-mortem analysis: the energy per realization was calculated from the power spectral density function as described in detail in [18]. The MSAE-FA010 amplifier contains a built-in circuit allowing precise measurement of the true root-mean-square voltage U_{RMS} with 100 ms integration time. The U_{RMS} signal was fed to a 14 bit ADC for continuous acquisition at 1 kHz sampling rate.

The fracture surface was observed by a scanning electron microscope LEO1455VP.

3. Results and discussion

The gas-analysis has shown that electrolytic Zn-plating results in the substantial increase in the hydrogen concentration [H] in the steel specimens (c.f. Table 2). It is accompanied by the loss of specimens ductility (Δ_{max}) and the dramatic increase of the number of AE events (N_{Σ}). For the all specimens AE events have a burst type waveforms (c.f. Fig. 1a) which are usually relates to the crack growth process including hydrogen-assisted crack growth [19]. In case of Zn-plated specimens with high hydrogen content a part of recorded AE events is performed as a sequence of burst waveforms which goes successive with a high frequency (c.f. Fig. 1b).

Table 2: Hydrogen content [H], maximum deflection at failure Δ_{max} and number of AE events N_{Σ} for tested specimens

Specimen type	[H], ppm	Δ_{max} , mm	N_{Σ}
Reference	2,5±0,3	16,9	317
Zn-plated	32,9±0,6	6,5	5172

After removing a surface layer from the Zn-plated specimens the hydrogen content drops to the initial value of 2.3 ± 0.5 ppm corresponding to the reference samples. Thus the most part of hydrogen introduced into the steel during Zn-plating is preserved within the surface layer of the specimens and Zn coating. This observation appears to be in agreement with the early works [4].

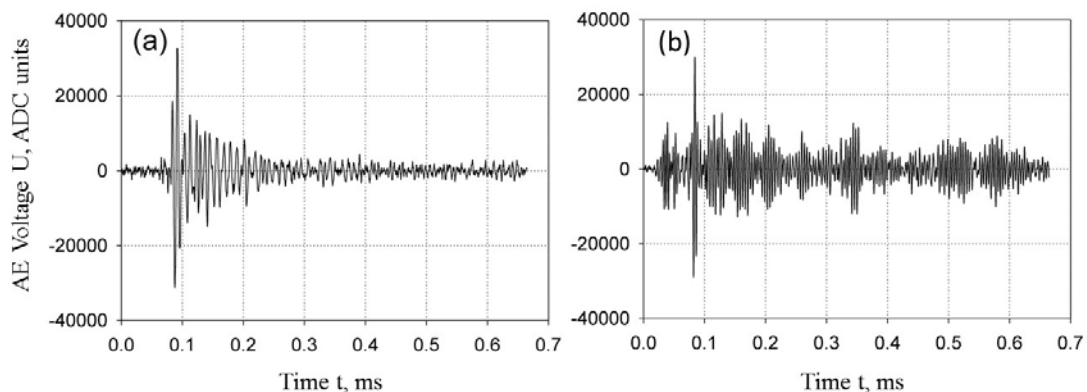


Fig. 1: Typical AE waveforms in tested specimens: (a) discrete AE “burst”-type signal, (b) a short time series of overlapping burst-type signals.

The fracture surface of the reference samples exhibits mainly ductile features, Fig. 2a, with separate brittle facets in a central part, which are presumably caused by the initially dissolved hydrogen, Fig. 2b. The ductile transcrystalline microcracks can also be seen in a central part of the fracture surface as characteristic “steps” between the MnS sulfides, Fig. 2c. The X-ray energy-dispersive analysis, Fig. 2c, revealed an excess amount of S and Mn atoms in the local area corresponding to the steps clearly visible at the fracture relief. Inclusions, such as MnS, can act as stress raisers attracting diffused hydrogen to the site so that hydrogen-assisted microcracks usually initiate along the interphase boundaries at inclusions [20]. Decohesion of sulfide inclusions has long been recognized as a powerful AE source in high strength steels [21,22].

The fracture surface appearance of Zn-plated specimens is distinctly different. Figure 3a reveals a brittle zone having an approximately elliptic shape in the central part of fracture surface. Intergranular cracking is the main fracture mechanism in this zone as can be seeing at higher magnification, Fig. 3b. The small sites of transgranular relief separate intergranular facets, Fig. 3c. The brittle zone evidently appears due to electrolytic hydrogen diffused from the surface toward center part of the specimen during the test.

A macroscopic crack aligned with the major ellipse axis in the middle part of the brittle zone can be commonly noticed. This intercrystalline crack extends in the direction normal to the fracture surface, Fig. 3d, across the whole brittle zone, although the signatures of sulfides decohesion, such as those seen in Figs.2, are rare, Fig.3b, c. Since the macrocrack exists on the fracture surfaces of the both reference and Zn-plated specimens it is not due to hydrogen and possibly it forms due to features of the stress-strain state. However the mechanisms of it forming can be significantly changed under action of hydrogen as shown above.

Thus the electrochemical Zn-plating results in substantial increase of the hydrogen content and ductility reduction in steel 70. The reduced ductility gives rise to the increasing area fraction of brittle intergranular fracture surface, Figs.2 and 3, and, simultaneously, to the increasing amount of discrete type AE, Table 2. It is therefore plausible to suppose that these AE transient signals are originated from microscopic brittle fracture processes such as intergranular cracking along the boundaries separating austenitic grains. However, the AE count reflects only the fact of AE arrival, i.e. it says only that a certain local structural transformation, e.g. crack, has occurred within the sample, but it does not say anything about the scale of damage. In the contrast, the AE amplitude (or rms voltage, or energy) can be related to the size of the defect and its velocity [23]. Therefore, the concurrent analysis of the AE_{RMS} behavior and the AE signals accumulation with

regard to the loading curve can be useful for distinguishing of the fracture kinetics.

At the initial stage of loading before load P_{II} (table 3, stage I) the “silent” zone is observed without evident AE, Fig. 4. The incubation period is a well-known feature of the hydrogen-assisted cracking during static load testing of the notched specimens [1,16,17]. A start of the loading activates the redistribution process of the diffusible hydrogen in the specimen. The high hydrogen concentration appears in the zone of the maximum triaxial stress ahead of the notch and microcracking process begins. Because of the low scale and velocity of this process the AE activity is negligible during that period [17].

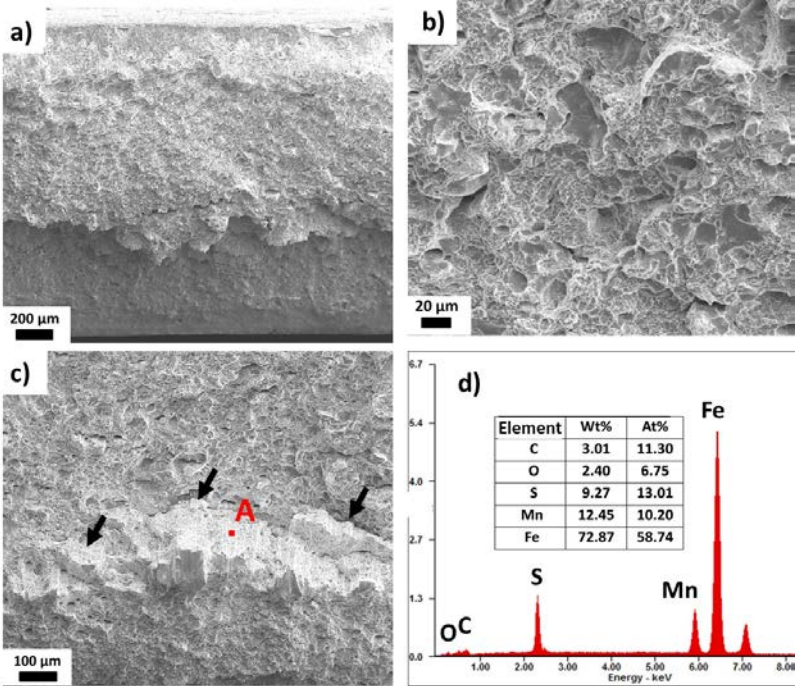


Fig. 2: Fracture surface of the reference specimens: a) – central part, b) – brittle facets, c) – cracking along sulfides, d) – EDS spectrum taken from one of inclusions marked by A on c).

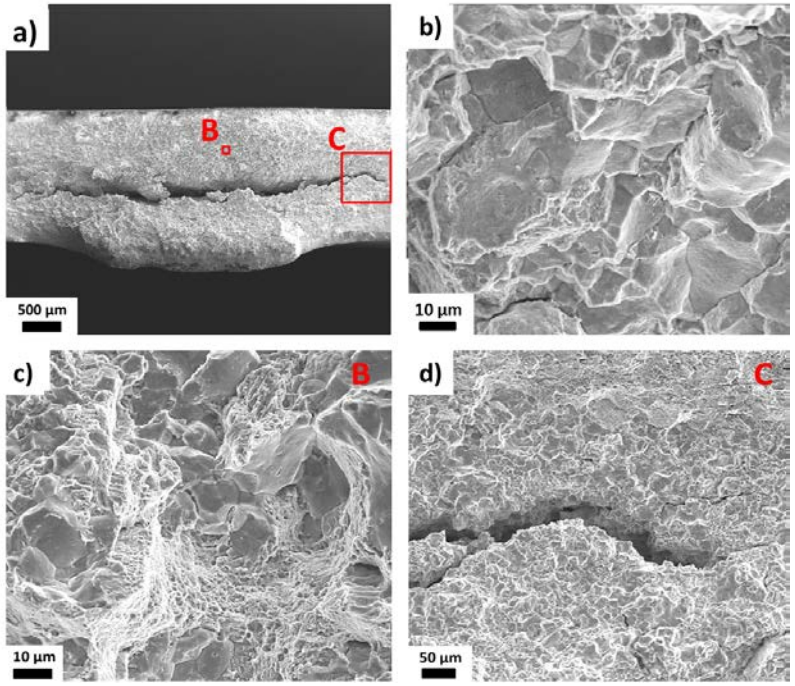


Fig. 3: Fracture surface of the Zn-plated specimens: a) – central part, b) – , c) – cracking along sulfides, d) - EDS spectrum taken from one of inclusions marked by A on c).

Table 3: AE parameters for the different stages of fracture of Zn-plated specimen

Stage	Mean rate of event accumulation, event/s	Mean rate of event energy accumulation, arb.units/s	Mean rate of U_{RMS} accumulation, mV/s
I	0.05	0.65	0.01
II	3.01	624.10	15.03
III	8.30	1716.85	72.49
IV	3.53	79.43	22.32
V	1.29	143.16	44.07

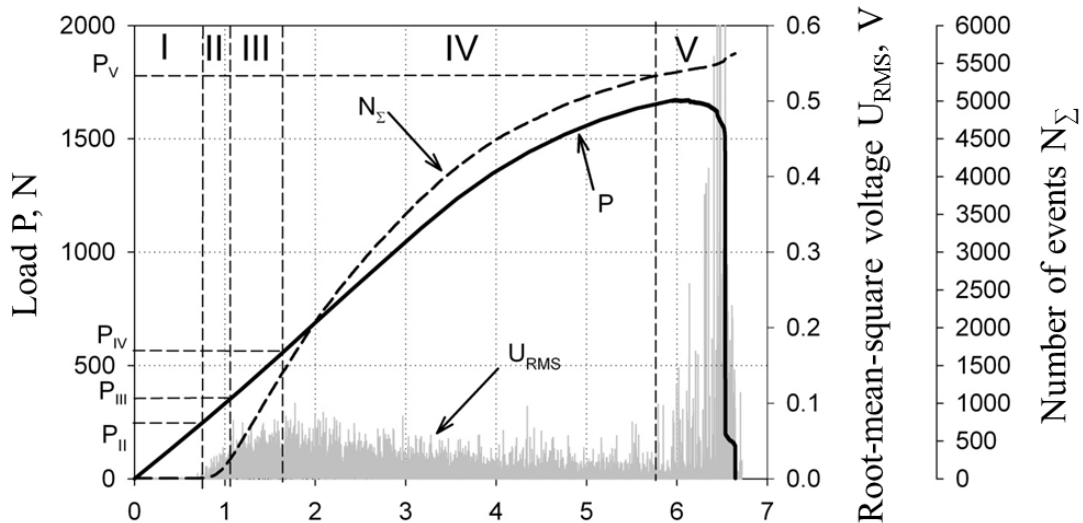


Fig. 4: Stages of Zn-plated specimen fracture.

The “silent” zone, which is observed in the present work, has similar features as the incubation period in [16]. However, in the present case of active loading of the smooth specimen having no notch, the multiple microcracks initiates near the natural stress concentrators and hydrogen traps such as grain boundaries or sulfides. Thus, the formation of the main crack occurs by the coalescence of numerous microcracks. Indeed, the intensive AE appears when a certain critical load P_{II} (stage III) is reached, Fig. 4. As the first signal appeared, the rate of AE events accumulation increased steeply until the maximum value is attained at P_{III} , Fig. 4. The increase in U_{RMS} is also observed during this stage, Table 3.

Presumably, the stage II ($P_{II} < P < P_{III}$) begins when the stress in a hydrogen enriched zone becomes high enough to trigger multiple cracking. This process should start near the specimen surface because of the high hydrogen concentration and the maximum stress in this region. The big amount of stress risers surrounded by hydrogen can lead to fracture initiation in multiple places over the specimen surface. The stress growth down to the specimen thickness during the loading should result in an increase of both the number of microcracks and the number of AE events. Therefore, this can probably explain the dependence of the AE events accumulation rate on the load on the stage II. As a certain time after the load P_{III} is elapsed (stage III), the cracking process occurs with a high constant rate independently of the load magnitude. One can suppose that, in this stage the cracks growth is controlled by diffusible hydrogen in a way similar to the metastable crack growth during a delayed failure observed in [16]. The microcracking events follow each other with a high frequency as reflected by both the AE events accumulation curve, Fig. 4, Table 3, and the AE waveforms, Fig.1b.

At the load P_{IV} the decline of AE activity occurs (stage IV). The accumulation rate of number and energy of the AE events decrease (fig. 4).

In fact from the beginning of the loading the deformation of the specimen controlled by two competing mechanisms – the plastic deformation and destruction (microcracks initiation and growth). Apparently accumulation rate of the AE events controlled by the rate of the microcracks initiation and growth. In this case the uniform plastic deformation does not contribute to AE because no continues type AE waveforms are found. Steady reduction of the cross-section area due to destruction result in activation of the plastic deformation between the appeared defects. Thus the forming of the main crack is junction of the brittle microcracks by the plastic deformation. This is evidenced by the areas of the ductile relief between the brittle intergranular facets in the Fig.3c. Simultaneous junction of the microcracks and AE activity reduction was observed in [14] for the low-carbon steel.

A final fracture stage V corresponding to the unstable main crack growth, Fig.4, sets in at the load P_V . This stage is featured by the increase of the AE event energy and U_{RMS} accumulation rate, Table 3, Fig. 4. This fact is explained by the formation of the main crack of critical size and its fairly rapid growth by a ductile mechanism through the rest of the sample. It should be noticed that the accumulation rate of the number of AE events still reduces during this stage but their energy increases, Table 3. Thus the U_{RMS} and the energy of AE signals are the appropriate parameters for the identification of the stage V.

It is shown that fracture kinetics of the smooth hydrogen charged specimens during monotonic loading has a difference compared with a case of static loading of the notched specimens in [7]. Due to the notch, the main crack forms immediately after the incubation period (stage I). So stages II and III of the multiple microcracking exist only at loading of the smooth specimen, Fig. 4. Moreover, if there is no notch on a sample the forming of the main crack and its propagation during stage IV presumably occurs by the ductile junction of the brittle microcracks of critical size. Because of slight contribution in AE of plastic deformation process the activity of AE reduces in this stage. But in the case of static load the main crack growth is controlled by the diffusion of hydrogen so fracture occurs in a brittle manner. It is accompanied by the intensive AE as showed in [7] for the stage of metastable crack growth.

4. Conclusions

1. The primary AE source in the high-carbon steel during monotonic three-point bending is associated with microfracture events such as cracking along the austenitic grain boundaries or nonmetallic inclusions. Thus, the number of the discrete AE events correlates with the deflection of the samples and brittle area on their fracture surface.

2. Simultaneous analysis of the AE RMS behaviour, the AE signals accumulation kinetics and the loading curves allowed distinguishing between five stages of the fracture process: (I) microcracks nucleation during the incubation period having a low AE activity; (II) the stage featured by the increasing rate of AE signals accumulation and increasing RMS level caused by accelerated damage accumulation; (III) the overall stable crack growth, followed by damage rate reduction, (IV) the stage preceding the critical regime corresponding to formation and propagation of a catastrophic crack (V).

Financial support from the Russian Ministry of Education and Science under grant-in-aid 11.G34.31.0031 is gratefully appreciated.

5. References

- [1] Bernstein I.M.: The role of hydrogen in the embrittlement of iron and steel, *Materials Science and Engineering*. 1970, Vol. 6, No 1, 1–19.
- [2] Hirth J.: Effects of hydrogen on the properties of iron and steel, *Metallurgical and Materials Transactions A*, 1980, Vol. 11, No 6, 861–890.

- [3] Wang M., Akiyama E., Tsuzaki K.: Determination of the critical hydrogen concentration for delayed fracture of high strength steel by constant load test and numerical calculation, *Corrosion Science*, 2006, Vol. 48, No 8, 2189–2202.
- [4] Beloglazov S.: Surface layer absorption of hydrogen and embrittlement of high-strength and low-carbon steels during electrochemical processes, *Met. Sci. Heat Treat.*, 2008, Vol. 50, No 5, 273–277.
- [5] Robertson I.M.: The effect of hydrogen on dislocation dynamics, *Engineering Fracture Mechanics*. 2001, Vol. 68, No 6, 671–692.
- [6] Brown J.T., Baldwin W.M.J.: Hydrogen embrittlement of steels, Jr., *Trans AIME*, 1954, Vol. 203, 298–304.
- [7] Bhattacharya A.K., Parida N., Gope P.C.: Monitoring hydrogen embrittlement cracking using acoustic emission technique, *J. Mat. Sci.*, 1992, Vol. 27, No 6, 421–427.
- [8] Carpenter S., Smith D.: The effects of cathodic charging on the acoustic emission generated by intergranular cracking in sensitized 304 stainless steel, *Metallurgical and Materials Transactions A*, 1990, Vol. 21, No 7, 1933–1939.
- [9] Caskey G.R.J.: Acoustic emission from hydrogen saturated Type 304L stainless steel, *Scr. Metall*, 1979, Vol. 13, No 7, Pages: 583–587.
- [10] Padmanabhan R., Suriyayothin N., Wood W.: Grain size-acoustic emission relationships in hydrogen induced delayed cracking, *Metallurgical and Materials Transactions A*, 1983, Vol. 14, No 11, 2357–2362.
- [11] Wang Z.F. et al.: Dependence of acoustic emission for low strength steels upon the embrittlement and the plastic zone reduction at the crack tip during corrosion fatigue crack propagation, *Fatigue Fract. Eng. Mater. Struc*, 1993, Vol. 16, No 4, 441–451.
- [12] Merson E.D. et al.: Effect of strain rate on acoustic emission during hydrogen assisted cracking in high carbon steel, *Mater. Sci. Eng. A*, 2012, Vol. 550, 408–417.
- [13] Wang Z.F., Zhu Z., Ke W.: Behavior of acoustic emission for low-strength structural steel during fatigue and corrosion fatigue, *Metall. Mater. Trans. A*, 1991, Vol. 22, No 11, 2677–2680.
- [14] Zharkova N.A., Botvina L.R., Tyutin M.R.: Damage accumulation stages in a low-carbon steel during uniaxial tension, *Russian Metallurgy*, 2007, No 3, 223–229.
- [15] Dedhia D.D., Wood W.E.: Application of acoustic emission analysis to hydrogen-assisted cracking, *Materials Science and Engineering*, 1981, Vol. 49, No 3, 263–273.
- [16] Troiano A.R.: The role of hydrogen and other interstitials in the mechanical behavior of metals, *Transactions of ASM*, 1960, Vol. 52, No 1, 54–80.
- [17] Bhattacharya A.K., Parida N., Gope P.C.: Monitoring hydrogen embrittlement cracking using acoustic emission technique, *J. Mat. Sci*, 1992, Vol. 27, No 6, 1421–1427.
- [18] Vinogradov A., Nadtochiy M., Hashimoto S. M.S.: Correlation between spectral parameters of acoustic emission during plastic deformation of Cu and Cu-Al single and polycrystals, *Materials Transactions*, 1995, Vol. 36, No 3, 426–431.
- [19] Kudryavtsev V.N. et al.: Detection of hydrogen embrittlement of a carbon steel by acoustic emission, *Corrosion*, 1981, Vol. 37, No 12, 690–695.
- [20] Botvina L., Tetyueva T., Ioffe A.: Stages of multiple fracture of low-alloy steels in a hydrogen sulfide medium, *Metal Sci. Heat Treat.*, 1998, Vol. 40, No 2, 61–70.
- [21] Teoh H.B., Ono K. Fracture-Induced Acoustic Emission during Slow Bend Tests of A533B Steel, *J. Acoustic Emission*, 1987, Vol. 6, No 1, 1–12.
- [22] Ono K., Yamamoto M.: Anisotropic Mechanical and Acoustic Emission Behavior of A533B Steels, *Materials Science and Engineering*, 1981, Vol. 47, 247–263.
- [23] Wadley H.N.G., Scruby C.B., Sinclair J.E.: Acoustic emission source characterization, *The J. Acoust. Soc. Am.*, 1980, Vol. 68, No S1, S103–S104.

EFFECT OF TEMPERATURE ON MICROSTRUCTURE EVOLUTION IN TRIP/TWIP STEELS DURING TENSILE DEFORMATION

M. Linderov¹, C. Segel², A. Vinogradov¹, A. Weidner², H. Biermann²

¹Laboratory of Physics of Strength of Materials and Intelligent Diagnostic Systems, Togliatti State University, Togliatti, Russia, dartvi@gmail.com

²Institute of Materials Engineering, Freiberg Technical University, Freiberg, Germany, christian.segel@iwt.tu-freiberg.de

ABSTRACT

The model austenitic stainless TRIP/TWIP steels have an outstanding combination of strength and ductility, depending on chemical composition and loading conditions. The critical factor, which strongly affects all deformation-induced processes in metastable steels is temperature. To get a better insight into the effect of temperature on kinetics of deformation processes in Fe-Cr-Mn-Ni TRIP/TWIP steels with different content of Ni (6 and 9%) controlling the degree of stability of the initial austenitic structure, an acoustic emission (AE) technique was used during uniaxial tension at two different temperatures - ambient and 373K. The in-situ AE results are paired with detailed SEM investigations using the electron backscattered diffraction (EBSD) technique to identify the martensitic phase transformation and for visualisation of the deformed dislocation microstructures. The cluster analysis of the AE "streaming" signal recorded continuously during tension test has revealed an excellent correlation with synergistic complexity of involved deformation mechanisms in various combinations: dislocation slip, martensitic α' transformation, and twinning.

Key words: TRIP steels, TWIP steel, acoustic emission, cluster analysis, martensitic transformation, scanning electron microscopy.

1. Introduction

Among other engineering steels, modern high alloyed metastable austenitic steels have an outstanding combination of mechanical properties including a high strength and ductility, Fig. 1 [1]. The deformation behavior CrMnNi-steels will be determined by characteristic deformation mechanism like the TRIP effect (TRansformation Induced Plasticity), the TWIP effect (TWinning Induced Plasticity) and the gliding and cross slipping of dislocations. All this

deformation mechanism influences significantly the deformation characteristics and mechanical behaviour of the steel.

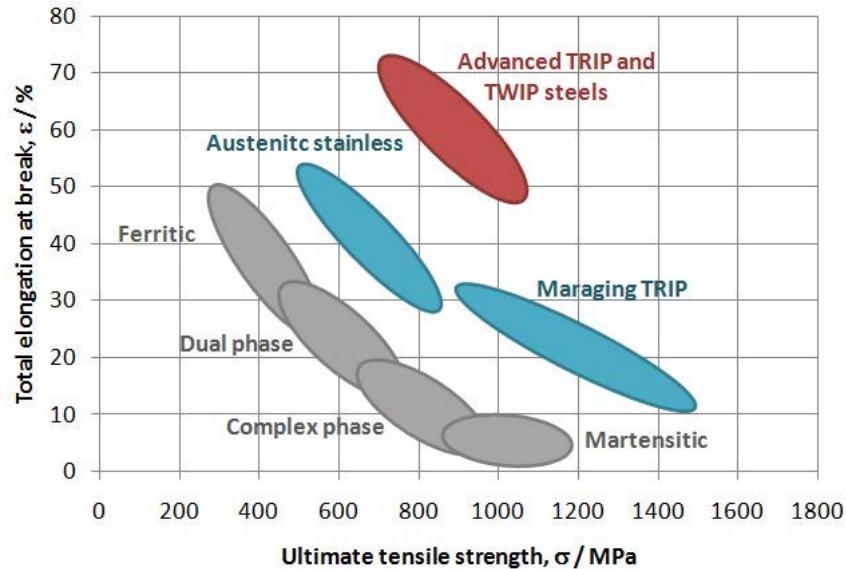


Fig.1. Range of mechanical properties of TRIP/TWIP steels in comparison with other modern engineering steels (Adapted from [2])

The TRIP effect is characterized by a deformation-induced martensitic phase transformation under loading. The transformation from the metastable austenitic phase γ (FCC) involves the formation of deformation bands which are characterized by an intermediate structure with a high density of parallel stacking faults which is often associated with the so-called ϵ -martensite (HCP) and a α' -martensite (BCC) structure. In the literature the TRIP effect in metastable stainless steels will be described by a sequence of the martensitic transformation like $\gamma \rightarrow \epsilon \rightarrow \alpha$. The TWIP effect increases significantly the plasticity and the flow stress. The reason is that twins act as a barrier for gliding dislocations. The susceptibility of steel to TRIP or TWIP effect can be controlled by alloying which controls the stacking fault energy (SFE) and the austenitic stability, and thus determines the deformation mechanisms active under different temperatures and strain rates [3]. For instance, the increase of the temperature results in higher austenite stability and, thus, reduces the propensity to the martensitic phase transformation.

Using a model family of high-alloyed 16Cr-6Mn- x Ni cast steels (composition in wt. %) exhibiting the TRIP and/or TWIP effect [4-6] depending on the amount of Ni x varied between 3 and 9 wt.%, it has been demonstrated that the steel with the low nickel content exhibits profuse α' -martensite formation whereas the steel with the highest nickel content shows intensive twinning. Comprehensive understanding of the synergistic interplay between the primary mechanisms involved into complexity of plastic deformation – dislocation slip, twinning and martensitic transformation - at elevated temperature is still lacking. The present work aims at reducing this obvious deficit in knowledge.

Aiming at clarifying on the effect of temperature on the deformation behavior of austenitic stainless steels, we used the same methodology as in the previous paper [7]: the detailed statistical and cluster analysis of the AE time-series in real time scale is backed by comprehensive post-mortem characterization of the deformation microstructure by high-resolution EBSD (electron back scattering diffraction) technique enabled in modern SEM (scanning electron microscopy) facilities.

2. Experimental

Flat tensile specimens with a rectangular cross section of $8 \times 4 \text{ mm}^2$ and a gauge length of 35 mm were machined from the plates cast as shown in Fig. 2. Their chemical compositions and SFE γ_{SF} are summarised in Table 1. Here M_s is calculated from the chemical composition as described in the experimentally-based approach in ref. [8, 9]; γ_{SF} is calculated according to [8, 9] on basis of the stacking fault energy of pure iron ($36\text{-}42 \text{ mJ/m}^2$) taking into account the influence of the alloying elements.

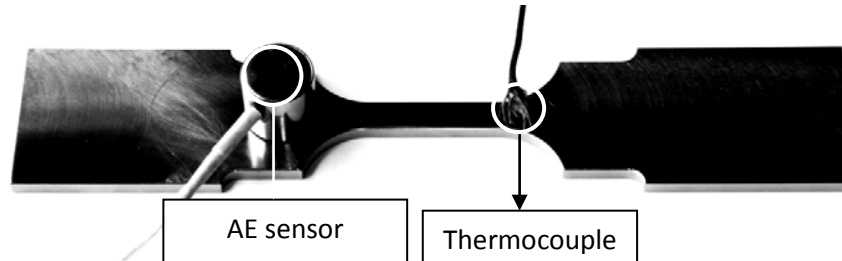


Fig. 2. Tensile specimen shape with the PAC WD sensor on a shoulder part.

The details of the AE experimental setup based on the 18 bit PCI-2 (Physical Acoustics Corp., USA) data acquisition board operated in a threshold-less continuous mode with 2 Msamples/s data rate have been given in [7]. The WD FS63 sensor (PAC, USA) was clamped to the shoulder part, Fig.2, of the specimen using machine oil as a coupling medium.

The AE signal from the sensor output was amplified by 60 dB by a low-noise PAC 2/4/6 preamp and passed through the 30-1000 kHz band-pass filter before acquisition. For tests at the elevated temperature a thermocouple was welded to the specimen in the intimate vicinity to the gauge part.

Table 1. Chemical composition and the stacking fault energy of the tested Cr-Mn-Ni steels

Steel	Chemical composition (wt.-%)							Stacking fault energy $\gamma_{SF} \text{ (mJ/m}^2\text{)}$
	C	Cr	Mn	Ni	Si	Al	N	
16Cr-6Mn-9Ni	0.04	15.3	5.8	8.6	0.9	0.07	0.05	15.4 - 21.4
16Cr-6Mn-6Ni	0.08	16.0	6.0	6.1	1.0	0.05	0.05	9.6 - 15.6

The specimens were deformed in tension using a screw-driven frame (Zwick 1476, Germany) at room temperature (RT) and $100 \text{ }^\circ\text{C}$ under crosshead displacement control at the nominal strain rate of $3 \times 10^{-3} \text{ s}^{-1}$.

For the post-experimental SEM observations the gauge parts of the specimens were mechanically and vibration polished to a mirror-like finish. Vibro-polishing for 24 h with $0.02 \text{ }\mu\text{m}$ grade colloidal silica was employed at the last stage of preparation. The BSE and EBSD investigations were carried out using a field emission scanning electron microscope (MIRA 3 XMU, TESCAN, Czech Republic) powered by the OIMTM-technology from EDAX/TSL.

3. Results of AE analysis

3.1. Acoustic emission behaviour

Loading diagrams of the model TRIP/TWIP steels at room temperature and at 373 K synchronized with AE data are shown in Fig. 3 where AE is represented by the energy E (*per realization* of 1 ms duration) and median frequency f_m of the power spectral density (PSD) function. The temperature exerts a strong effect on the hardening behaviour. Furthermore, this effect is more pronounced in the metastable 16Cr-6Mn-6Ni steel than in the relatively stable 16Cr-6Mn-9Ni steel having a higher stacking fault energy, Table 1.

As can be seen from Fig. 3, AE in both TRIP/TWIP steels consists of high-amplitude bursts, arising on a background of a noise-like continuous signal, cf. [7]. Typically to pure fcc metals and alloys where plastic deformation is mediated by dislocation slip, the AE level rapidly increases after the beginning of loading around the yield stress and then reduces smoothly until fracture. However, importantly is that the behaviour of the median frequency f_m in the deforming stable and metastable steels, 16Cr-6Mn-9Ni and 16Cr-6Mn-6Ni, respectively, is quite specific and is not similar to what is typically observed during hardening of pure fcc metals. The f_m magnitude exhibits a clearly pronounced maximum on the early deformation stage of both steels at both testing temperatures, Fig. 3, unlike pure fcc metals such as Cu or Ni where the AE spectrum commonly shifts to higher frequencies during uniform of deformation where hardening is mediated primarily (or entirely) by dislocation slip and interaction between dislocations. This specific behaviour of the AE PSD function is a clear indicator of the operating sources other than dislocation slip. The most obvious candidates for those sources are mechanical twins and phase transformation the distinction between which can be quantified with a help from an AE cluster analysis as is outlined in the next section.

3.2. Kinetics of different deformation mechanisms probed by AE cluster analysis

Different AE mechanisms are assumed to generate different waveforms, which then can be, in principle, distinguished by their characteristic shapes of the Fourier power spectral density (PSD) function. Based on this idea, a new “evolutionary” clustering algorithm (ASK-adaptive sequential k -means) has been proposed recently by Pomponi and Vinogradov [10] and proved effective to classify the AE signals with different power spectral density functions associated with different emitting sources [11]. The mathematical details of the method used are given in [10]. Importantly is that the method is data driven and the number of clusters to be created does not have to be specified in advance. Since the AE acquisition starts a few seconds before the loading starts, the beginning of the AE streaming record includes a considerable amount of data pertinent to the laboratory noise only. These data are used to tune the algorithm and to verify if it works correctly. Figure 4 shows the results of application of this approach with a Kullback-Leibler divergence used as a measure of inter-cluster distance and a measure of dissimilarity between different clusters compared by the shapes of their normalized AE power spectral density (PSD). If compared to the results reported in [7] for the same type steels tested under the same conditions but with another type sensors, it is importantly to notice that despite some unavoidable differences of the power distributions caused by different sensors responses, the general trends in the behaviour of normalized PSDs, Fig. 3, in different samples are quite comparable and the kinetics of evolution of different AE mechanisms at room temperature appears to be similar, Fig. 4. One can see that at the beginning of the AE recording a single cluster corresponding to the background noise is recognized in all specimens. This cluster is substituted for the AE –pertinent clusters as soon as loading begins (the moment when loading starts is indicated by arrows in Fig. 4). These AE-pertinent clusters are however different for different steels under different testing temperatures.

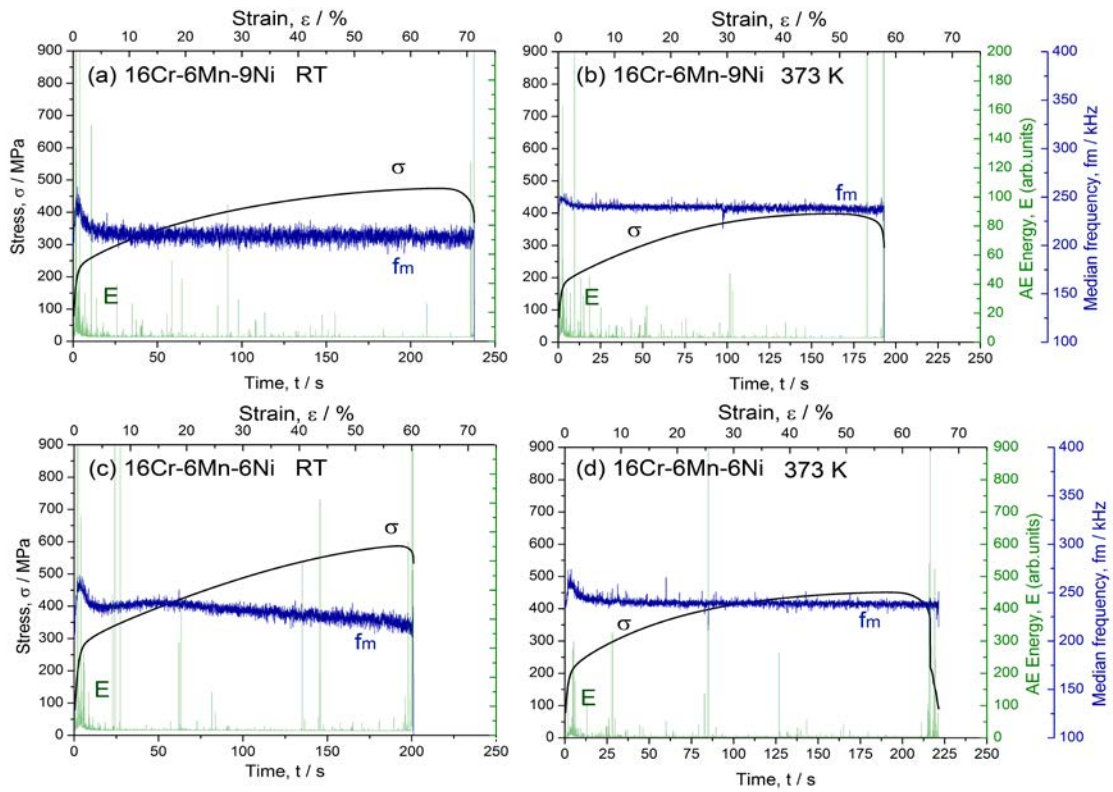


Fig. 3. Stress-strain curves plotted together with the average AE energy E and the median frequency f_m for three types of austenitic cast steel with 16% Cr 6% Mn and 6 and 9% Ni tested at room temperature and at 373 K with a strain rate of $3 \times 10^{-3} \text{ s}^{-1}$

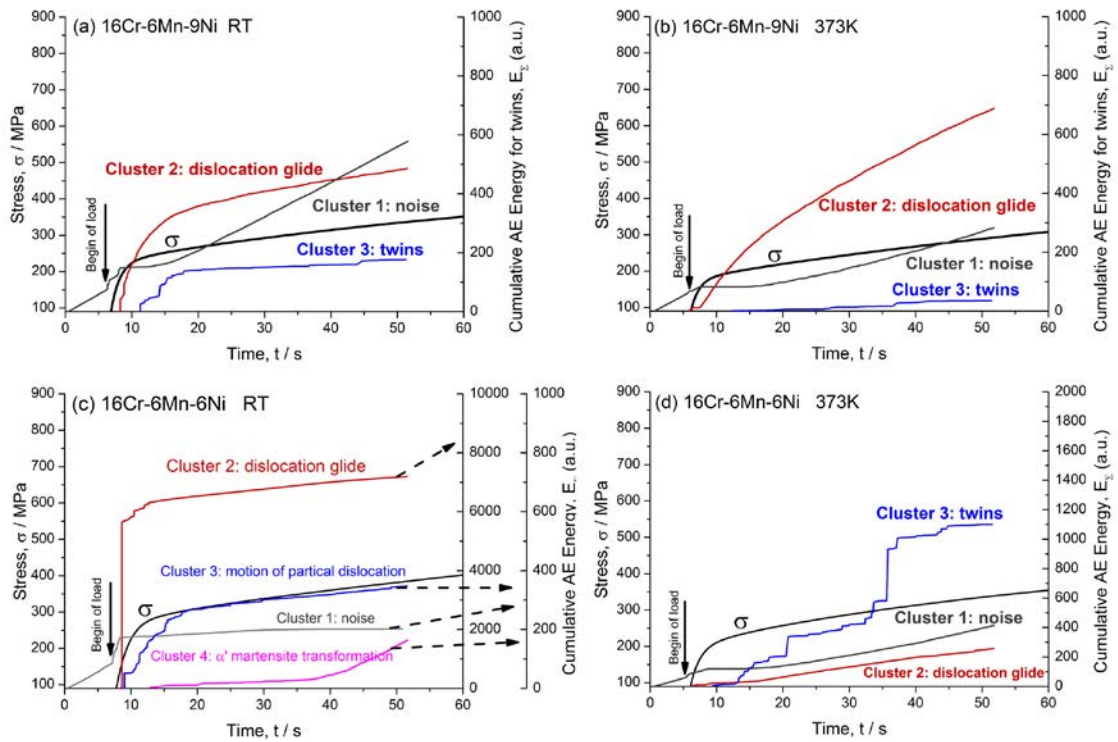


Fig. 4. The kinetics of different AE mechanisms during deformation of Fe-Cr-Mn-Ni stainless steels, which is reconstructed with a help of the AE clustering procedure ASK developed in [10].

First of all the significant amount of burst type AE with high peak amplitude corresponding to mechanical twinning is observed in the 16Cr-6Mn-9Ni steel and this is correctly recognized by the clustering procedure used due to fine differences in the AE PSD. In the metastable 16Cr-6Mn-6Ni, the phase transformation commences already at small plastic strains at the beginning of deformation. The transformation starts as a cooperative motion of Shockley partials resulting in the bundles of stacking faults associated with the hcp ϵ -martensite (see discussion in the next section). Shortly after the formation of deformation bands consisting of finely spaced stacking faults, the α' -martensite forms at the intersections between the bands and then extends along the whole deformation band with progressively increasing volume fraction. Although the elementary slip of lattice dislocations generates a much weaker AE than the cooperative motion of Shockley partials and the AE which mechanical twins produce, the contribution of the ordinary dislocations to resultant plastic strain cannot be overestimated and this contribution is recognized by the AE technique too quite reasonably: AE due to dislocation slip is featured by low amplitude and energy, but due to a huge number of moving dislocation segments the overall energy associated with the low amplitude but continuous AE appears to be even higher than that of twinning or martensitic transformation.

3.3. Microstructural Observations and deformation mechanisms

The detailed SEM observations of the austenitic steels after deformation have been reported on several occasions [3]. In the present work we focus on the changes which the microstructures undergo during plastic deformation at the elevated temperature. The phase transformations responsible for the TRIP effect, or twinning responsible for the TWIP effect, in austenitic steels under load have been fairly well understood with regard to the effect of Ni content and the temperature, which have a crucial effect on the SFE and the underlying deformation mechanisms.

The deformation mechanism, which exerts the most significant impact on the overall mechanical response of the steel 16Cr6Mn9Ni with a reasonably stable microstructure, is the mechanical twinning, Figs. 5 and 6. The deformation microstructure of steels with the TWIP effect is characterized by arrays of mechanically-induced twin layers with a nanometer thickness. Bundles of numerous twins are regularly observed in the primary and secondary twinning systems. The twins in the primary twin system extend across the whole grain from one grain boundary to the other unlike the twins in the secondary system where they are confined to the space between the primary twins. The number of twins in the bundles of primary twins is appreciably larger than that in the secondary where the length and thickness of twin bands is notably smaller than those in the primary system. The phase maps show a nearly complete austenitic microstructure in the field of view. A little amount of a bcc phase, which is highlighted in blue, Fig. 5a, is associated with the δ -ferrite remaining in the matrix after manufacturing and should not be mixed up with α' martensite which is also indexed as a bcc phase on the phase map in the 16Cr-6Mn-6Ni steel. With increasing temperature to 373 K the significant changes in the twinning activity are observed, i.e. the density of twins decreases strongly with increasing temperature in the stable 16Cr-6Mn-9Ni steel but it increases notably in the 16Cr-6Mn-6Ni steel, exhibiting transition from TRIP to TWIP effect. In fact, the deformation of type of the latter metastable steel is particularly complex, involving a variety of mechanisms operating concurrently. During deformation at room temperature, the metastable steel 16Cr-6Mn-6Ni exhibits a complex combination of a martensitic α' transformation, which occurs through the intermediate ϵ phase transformation $\gamma \rightarrow \epsilon \rightarrow \alpha'$, and twinning. Additionally, both these mechanisms occur on a background of conventional dislocation slip. In the electron backscatter diffraction (EBSD) micrograph the deformation bands are clearly visible. No direct transformation $\gamma \rightarrow \alpha'$ from the austenite phase to α' -martensite was observed in the matrix aside from deformation bands.

The use of the crystallographic orientation in the inverse pole figure (IPF) colouring on the orientation image map makes a clear distinction between the matrix and the twins having a specific orientation relation, Fig. 5 (the twin boundaries are highlighted in red) for both steels. When testing temperature increases to 373 K, the martensitic transformation ceases to occur and the TRIP effect vanishes. On the other hand, the density of twins increases significantly. With the increasing deformation temperature to 373 K the metastable steel changed the major deformation mechanism significantly. At high temperature, the steel has a higher austenitic stability and thus shows no remarkable martensitic phase transformation at 373 K during tensile test. The most pronounced deformation mechanism at 373 K is the strain-induced twinning.

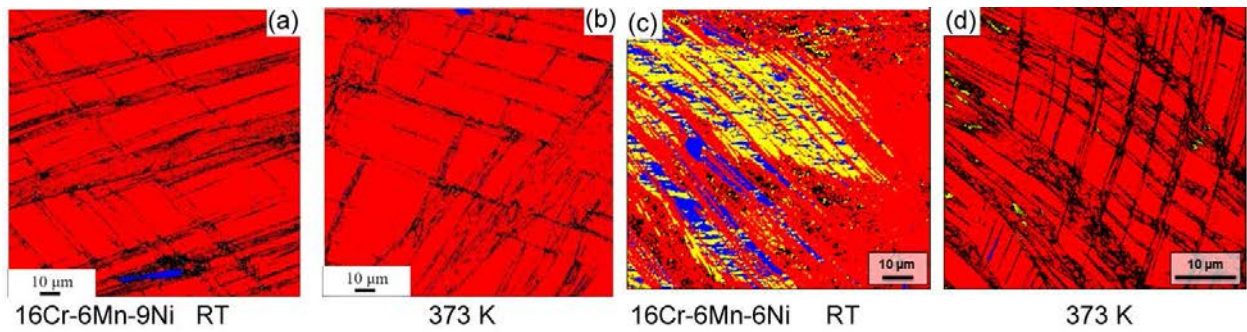


Fig. 5. OIM phase map in tw austenitic steels after formation and room temperature and 373 K. Red –fcc austenitic phase, yellow – hcp phase corresponding to the ϵ martensite in the 16Cr-6Mn-6Ni steel and blue – bcc phase corresponding to the residual δ -ferrite in the 16Cr-6Mn-9Ni steel and to the α' - martensite in 16Cr-6Mn-6Ni steel, respectively. The loading axis is horizontal.

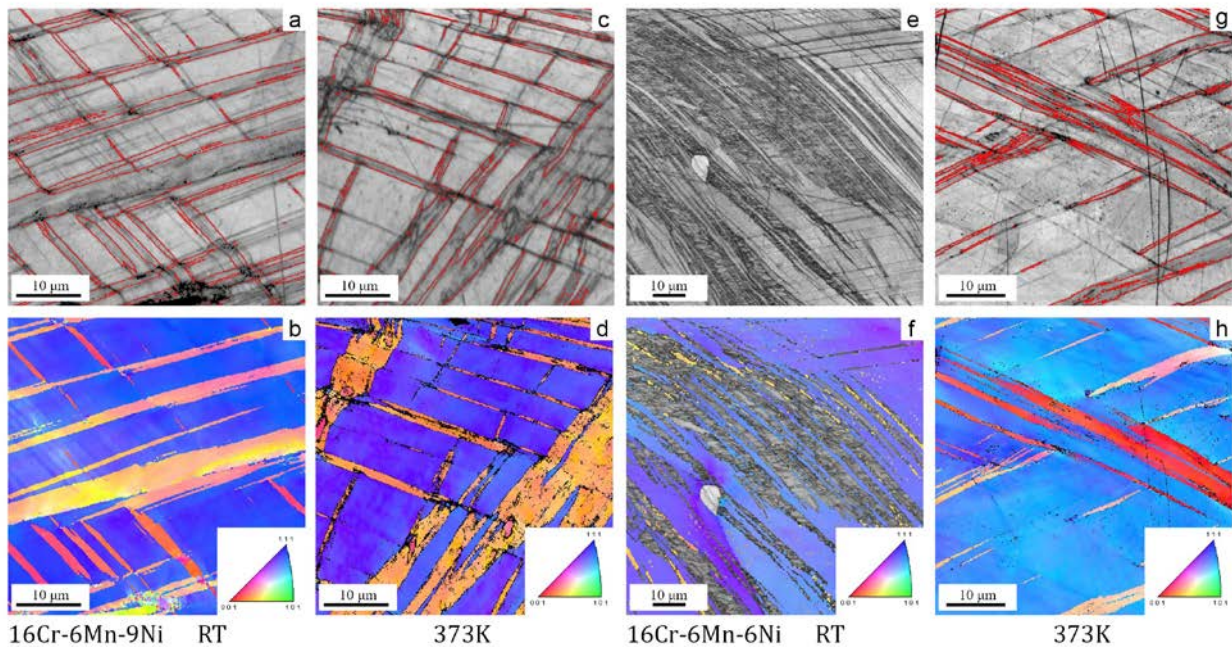


Fig. 6. SEM/EBSD images showing the deformation microstructures of the 16Cr-6Mn-9Ni steel (a-d) and 16Cr-6Mn-6Ni (e-h) after tensile testing to fracture at RT (a-b) and (e-f) and 373 K (c-d) and (g-h), respectively: image quality maps with highlighted coherent twin boundaries having a rotation angle of 60° along the $\{111\}$ plane (red coloured) (a,c,e,f) and the corresponding inverse pole figure map inked according to the surface normal direction (b,d,f,h). The loading axis is horizontal.

4. Conclusions

The acoustic emission technique was used in the present work to highlight the complexity in kinetics of multiple mutually interacting mechanisms involved into plastic deformation of model metastable austenitic Fe-16Cr-6Mn-xNi TRIP/TWIP steels with x=6 and 9 wt.% of Ni at room temperature and 373 K. Different microstructure-related major mechanisms of plastic deformation are identified as major AE sources with a help of a robust non-supervised signal categorization technique grouping AE signals with similar power spectral densities. Specifically, it is found that AE follows the behaviour of dislocation slip and twinning in the stable 16Cr-6Mn-9Ni steel. At 373 K the amount (number fraction) of mechanical twins reduced while the role of the dislocation slip in the overall plastic deformation increased. In the metastable 16Cr-6Mn-9Ni steel, besides the dislocation slip, the complexity of the involved deformation mechanisms involves a combination of a martensitic α' transformation, which occurs through the intermediate ε phase transformation $\gamma \rightarrow \varepsilon \rightarrow \alpha'$, and twinning with different proportions at room temperature and 373 K. The transition between TRIP and TWIP effects is well identified by the AE technique when temperature increased from ambient to 373 K. All major results of AE analysis appeared in excellent agreement with microstructural EBSD and ECCI observations.

Financial support from the German Research Foundation (DFG) through the CRC 799 contract and by the Russian Ministry of Education and Science (grant-in-aid 11.G34.31.0031) is greatly appreciated. One of the authors (ML) gratefully acknowledges the hospitality of the Institute of Materials Engineering, Freiberg Technical University. Special thanks go to Mr. G. Schade for his skillful help with experiments.

6. References

- [1] De Cooman BC. et al: High Mn TWIP Steels for Automotive Applications, in: New Trends and Developments in Automotive System Engineering (Chiaberge M, editor.), InTech, New York, 2011, 101-128.
- [2] Hickel T. et al.: Advancing density functional theory to finite temperatures: methods and applications in steel design. *J of Phys: Condensed Matter*, Vol. 24, 2012, 053202.
- [3] Biermann H, Solarek J, Weidner A.: SEM investigation of high-alloyed austenitic stainless cast steels with varying austenite stability at room temperature and 100°C, *Steel Research International*, Vol. 83, No. 6, 2012, 512-520.
- [4] Weiß A, et al.: Nichtrostender austenitischer Stahlformguss, Verfahren zu dessen Herstellung, und seine Verwendung, German patent WO 002008009722A1.
- [5] Weiß A, Gutte H, Jahn A, Scheller PR.: Stainless steels with TRIP/TWIP/SBIP effect, *Materialwissenschaft und Werkstofftechnik*, Vol. 40, No. 6, 2009, 606-611.
- [6] Jahn A, et al.: Mechanical properties of high alloyed cast and rolled CrMnNi TRIP steels with varying Ni contents, *Proceedings of the 8th ESOMAT*, Prague, 2009, 05013.
- [7] Vinogradov A, et al.: Kinetics of deformation processes in high-alloyed cast transformation-induced plasticity/twinning-induced plasticity steels determined by acoustic emission and scanning electron microscopy: Influence of austenite stability on deformation mechanisms, *Acta Materialia*, Vol. 61, No. 7, 2013, 2434-2449.
- [8] Jahn A, et. al.: Influence of manganese and nickel on the α' martensite transformation temperatures of high alloyed Cr-Mn-Ni steels, *Steel Res. Int.*, Vol. 82, No. 9, 2011, 1108.
- [9] Dai QX, et al.: Structural parameters of the martensite transformation for austenitic steels, *Materials Characterization*, Vol. 49, No. 4, 2013, 367-371.
- [10] Pomponi E, Vinogradov A.: A real-time approach to acoustic emission clustering. *Mech. Syst. Signal Proc.*, 2013 (doi 10.1016/j.ymsp.2013.03.017).
- [11] Takeda R, Kaneko Y, Merson DL, Vinogradov A.: Cluster analysis of acoustic emissions measured during deformation of duplex stainless steels, *Materials Transactions*, Vol. 54, No. 4, 2013, 532-539.

INVESTIGATING THE PRESENCE OF CRACKS IN TOOL STEEL INSERTS BY USING ACOUSTIC EMISSION METHOD

Tomaž Kek¹, Dragan Kusić², Rajko Svečko³, Aleš Hančič² and Janez Grum¹

¹ University of Ljubljana, Faculty of Mechanical Engineering
Aškerčeva 6, 1000 Ljubljana, Slovenia, tomaz.kek@fs.uni-lj.si, janez.grum@fs.uni-lj.si

² TECOS Slovenian Tool and Die Development Centre
Kidričeva 25, 3000 Celje, Slovenia, dragan.kusic@tecos.si, ales.hancic@tecos.si

³ University of Maribor, Faculty of Electrical Engineering and Computer Science
Smetanova 17, 2000 Maribor, Slovenia, rajko.svecko@uni-mb.si

ABSTRACT

In daily industrial production of different plastic products we often have to deal with various errors that practically occur on the mold primarily as a result of material wear and tear, improper storage and improper settings on the injection molding machine. In the testing phase of plastic materials we use many times different inserts that are made from standard tool steels, such as OCR12VM. In case of tool steel inserts after some years of usage a few micro-cracks can occur in the early stage, which can later quickly spread according to the applied loading. With the help of different non-destructive testing methods we know that we can most certainly detect possible formation of cracks on the tool steel inserts. Therefore the purpose of this paper is to present a detailed review of the applicability of acoustic emission (AE) method for the detection of cracks on the tool steel insert during a regular molding production cycle of standard test specimens. In this paper, we focused exclusively on the acoustic emission signal acquisition by using two resonant 150 kHz piezoelectric AE sensors on such tool steel inserts that are already affected by macro-cracks. On such tool steel insert the obtained acoustic emission results were compared with those obtained from a brand new tool steel insert. The final obtained acoustic emission results on the crack defected tool steel insert revealed as expected that the energy and intensity of the captured AE signals is higher compared with the ones that were captured on the brand new engraving insert under same processing conditions.

Key words: Acoustic emission, tool steel insert, cracks, test specimens, PZT sensors.

1. Introduction

Injection molding is a well known plastic manufacturing process where heated molten plastic material is forced into a mold cavity under high pressure. The plastic material solidifies into a shape that has conformed to the contour of the mold. Nowadays it is still regarded as the most important and very popular manufacturing process because of simple operation steps. A typical production cycle begins when the mold closes, followed by the injection of the plastic into the

mold cavity. Once the cavity is filled, additional pressure compensates the material shrinkage. In the next step, the screw turns, feeding the next shot to the front screw tip. This causes the screw to retract as the next cycle is almost prepared. Once the molded part is sufficiently cooled, the mold opens and the part is finally ejected. An example of a typical injection molding machine is shown in Fig. 1. Like in all today's industrial manufacturing processes, injection molding process can produce plastic parts which have poor quality and therefore are characterized as bad ones. In the field of injection molding during long term production first signs of micro-cracks can occur on the mold that usually causes production of bad parts. In such cases if a proper inspection inside the company is not provided then a whole series of freshly produced parts can be rejected. For a production company this can lead to a heavy economical loss. Location and advancement of a possible crack on the tool steel insert can be detected by the use of acoustic emission technique as already reported by many researchers [1-5]. The primary objective of monitoring the crack advancement with acoustic emission method is to obtain useful information about the quality of tool steel inserts which guarantees good quality of the produced test specimens.



Fig. 1: Example of a typical injection molding machine.

2. Experimental procedure

Acoustic emission signals were captured during the production cycle of standard test specimens that are intended for shrinkage evaluation of various plastic materials. The main aim was to analyze the influence of a possible crack located in tool steel insert on the captured acoustic emission signals. After finishing the first experimental part on a tool steel insert with a macro-crack we repeated the experiment under same processing conditions also on the brand new tool steel insert. In this way the captured acoustic emission signals could be compared. The captured acoustic emission signals were then correlated with the quality of the produced test specimens. Acoustic emission measurement system AMSY-5 from Vallen-Systeme GmbH was used for capturing and analyzing the AE signals. Two piezoelectric AE sensors VS150-M (resonant at 150 kHz) were mounted with silicone grease with two sensor holders on the tool steel insert from both sides. Both PZT sensors were connected via two preamplifiers AEP4 with a fixed gain of 40dB on the first and second channel of AMSY-5 measurement system. In the evaluation stage of acquired AE signals we focused closely on their maximal amplitudes and energy values during filling and packing stage. CAD model of the tool steel insert for production of standard test specimens is shown in Fig. 2.

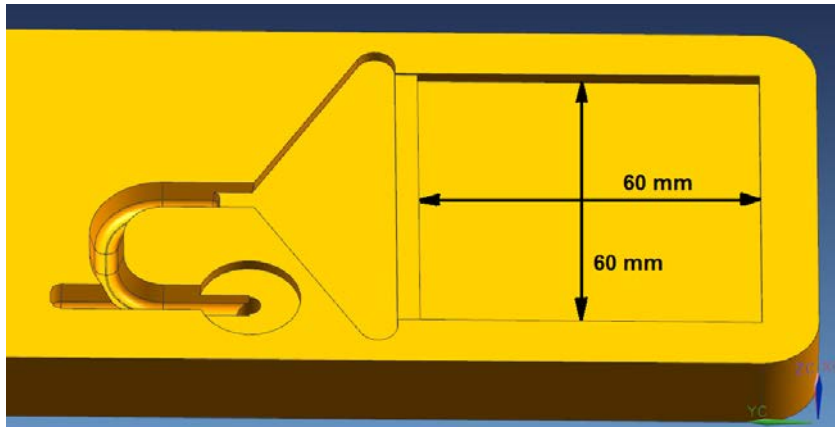


Fig. 2: CAD model of the tool steel insert that was used for experiments.

If we want to produce standard test specimens with good quality then the process parameters must be correctly set. Before the start of the experiment, it was necessary to select and fix the following process parameters: injection pressure was set to 1100 bar in the course of the experiment, holding pressure was set to 500 bar. On the new tool steel insert the melt temperature in cylinder has been set to 230 °C and the injection speed was set to 50 mm/s. On the tool insert with a macro-crack the melt temperature was set to 240 °C and the injection speed was 45 mm/s. The main criterion for the quality of produced test specimens was chosen to be the size of the shrinkage in longitudinal and transverse direction of the melt flow.

3. Experimental results

In the first part, we carried out the first experiments on a brand new tool steel insert. Later in the second part of experiments a tool steel insert with visible sign of macro-crack was used. In both cases to provide similar processing conditions, we used the same polypropylene material from Sirmax manufacturer (H40 C2 FNAT), which is mainly used in the automotive industry. After the test specimens were produced, they were scanned with an optical 3D digitizer ATOS II SO after 24 hours. This industrial 3D optical digitizer has two high-resolution CCD cameras (1280x1024 pixels) as shown in Fig. 3.



Fig. 3: Optical 3D digitizer ATOS II SO with two high-resolution CCD cameras.

Once the test specimens are digitized the measured data can be saved and used later on. Usually we are interested in individual measuring values and sections across the test specimen. Larger deviations and/or dimensional changes compared to the nominal ones are easy to verify and to control. Optical 3D Digitizer is based on the principle of capturing images through the camera, which then through an appropriate program prepares a computer model. The accuracy that can be achieved with these digitizers depends largely on the quality of the camera, which records the desired object. Of course, in a very small precision scale the accuracy itself also depends on the wavelength of the light. The biggest advantage of 3D digitizer from Fig. 3 lies in extremely rapid procedure of digitizing and excellent precision (precision declared for very small objects are up to 2 microns). Example of produced and later scanned test specimens on a brand new tool steel insert and insert with a visible macro-crack is shown in Fig. 4.

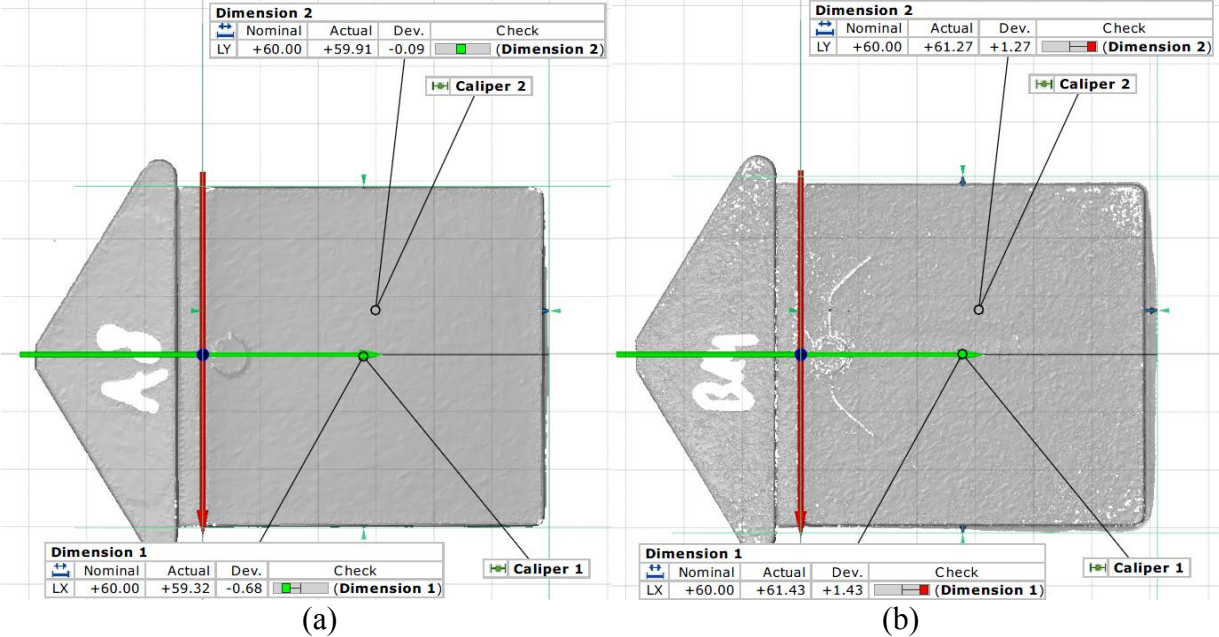
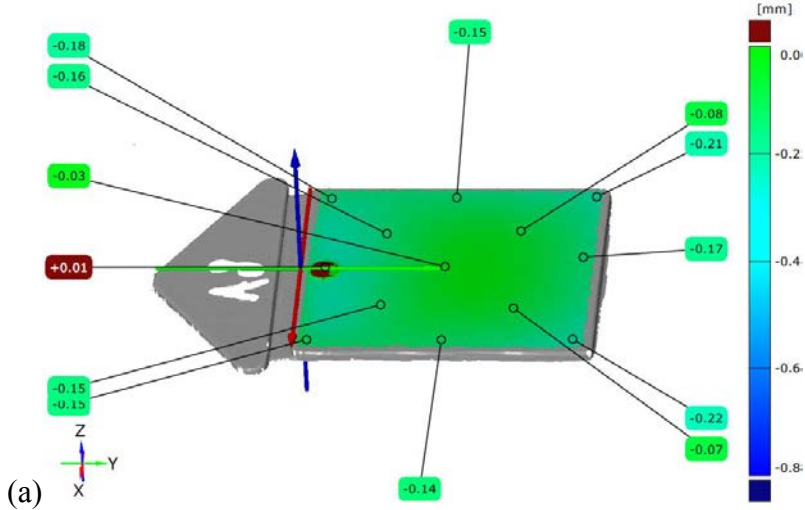


Fig. 4: Scanned test specimens (a) specimen 8 produced on a new tool steel insert, (b) specimen 14 produced on a tool steel insert with visible sign of macro-crack.

As can be seen from Fig. 4b the test specimen 14 has a clearly visible macro-crack. Also both dimensions are outside of the nominal 60 mm in the longitudinal (1.27 mm) and transverse (1.43 mm) direction. From Fig. 4a we can see that the produced test specimen 8 is within the prescribed tolerances (59.91 mm in length and 59.32 mm in width) and with no visible defects.



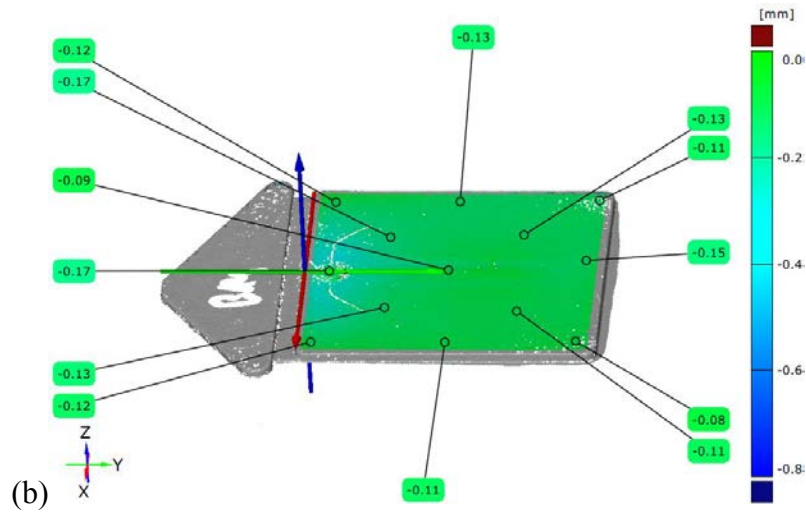


Fig. 5: Measuring surface deviations on (a) test specimen 8 produced on new tool steel insert, (b) test specimen 14 produced on tool steel insert with visible sign of macro-crack.

A good advantage of scanning the test specimens is the fact that quality of surface and its deviation can be compared to the flat (ideal) surface as shown in Fig. 5. By comparing both scanned test specimens in Fig. 5 we can notice on Fig. 5b that there are significant surface deviations in regards to the ideal surface, which are within the range of 0.17 mm exactly on the place of macro-cracks. The acoustic emission signal intensity is proportional to signal energy [6-7] and defined by an integral of signal square

$$E_{AE} = \int_0^{\infty} |V(t)|^2 dt \quad (1)$$

Amplitudes of the acoustic emission signals can be given in the form of a voltage, but it is usually converted into decibels by the following equation

$$A_{AE} = 20 \log \left(\frac{|V(t)|}{V_r} \right) \quad (2)$$

whereas $V(t)$ is the maximal measured voltage of AE signal and V_r is the reference input voltage on preamplifier, which was in our case equal to 0.001 mV. By measuring the simple waveform parameters such as energy, amplitude, hits, counts etc. on acquired AE signals, we can obtain useful information about the AE source intensity and its seriousness. In this way we can determine if the tool steel inserts quality is still good and if it's necessary to be replaced in the forthcoming future. Acoustic emission energy measurements are also important especially in those cases when the measured AE signal amplitudes are low. By squaring the captured AE signal burst a simple pulse is produced and consequently the hit counting is simplified, which is clearly visible in Fig. 6. The peak AE signal amplitudes are normally related to the intensity of one or more AE sources, which are in our case macro-cracks located on the tool steel insert. In the past research works [6] correlations between total counts, count rate and various fracture mechanics parameters (like for example the stress intensity factor) have been established and can be expressed by following equation

$$N \cong K^n \quad (3)$$

where K is the stress intensity factor, N is the total number of counts and n is a constant value between 2 and 10. The fatigue crack propagation rate is defined by

$$\frac{dN}{dc} \cong \frac{da}{dc} \quad (4)$$

where a is the crack size, c is the number of cycles and N is the total number of counts.

Filling phase (1)	Holding phase (2)	Cooling phase, mold opening and specimen ejection phase (3)
----------------------	----------------------	--

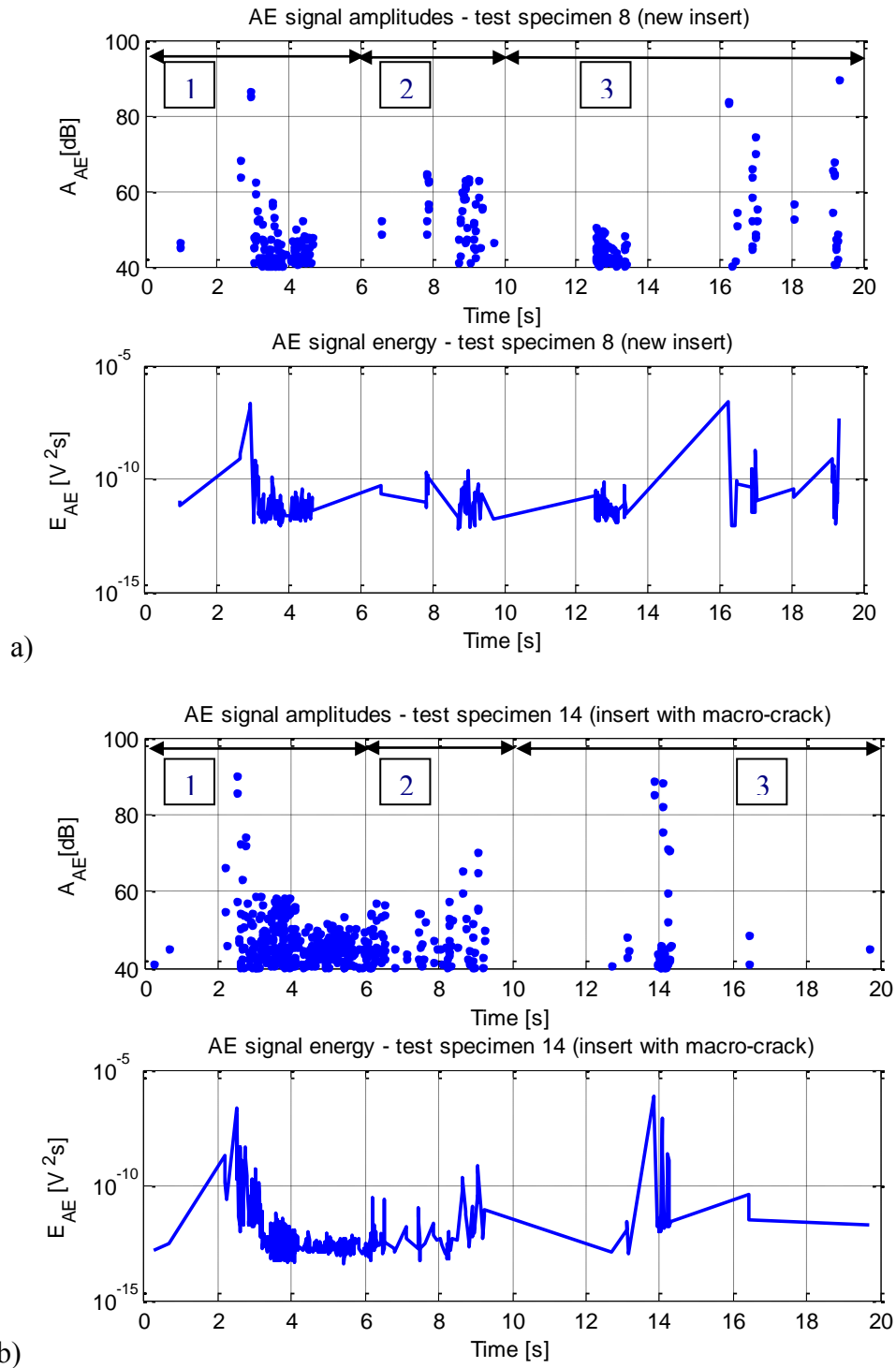


Fig. 6: Captured AE signals during production of (a) test specimen 8 (new insert), (b) test specimen 14 (insert with macro-crack).

Figure 6 shows the amplitudes and AE signal energy during the production of test specimens 8 and 14. On the tool steel insert with macro-crack a significant increase in the number of detected AE signals in filling phase can be seen (Fig. 7a), which is due to the filling of polymer melt through macro-cracks until the test specimen is filled. Even better, this transition of melt through macro-cracks is evident in Fig. 7b, where rapid transitions of AE signal from 0.2 mV (46dB) up to 0.81 mV (58.2 dB) can be clearly seen.

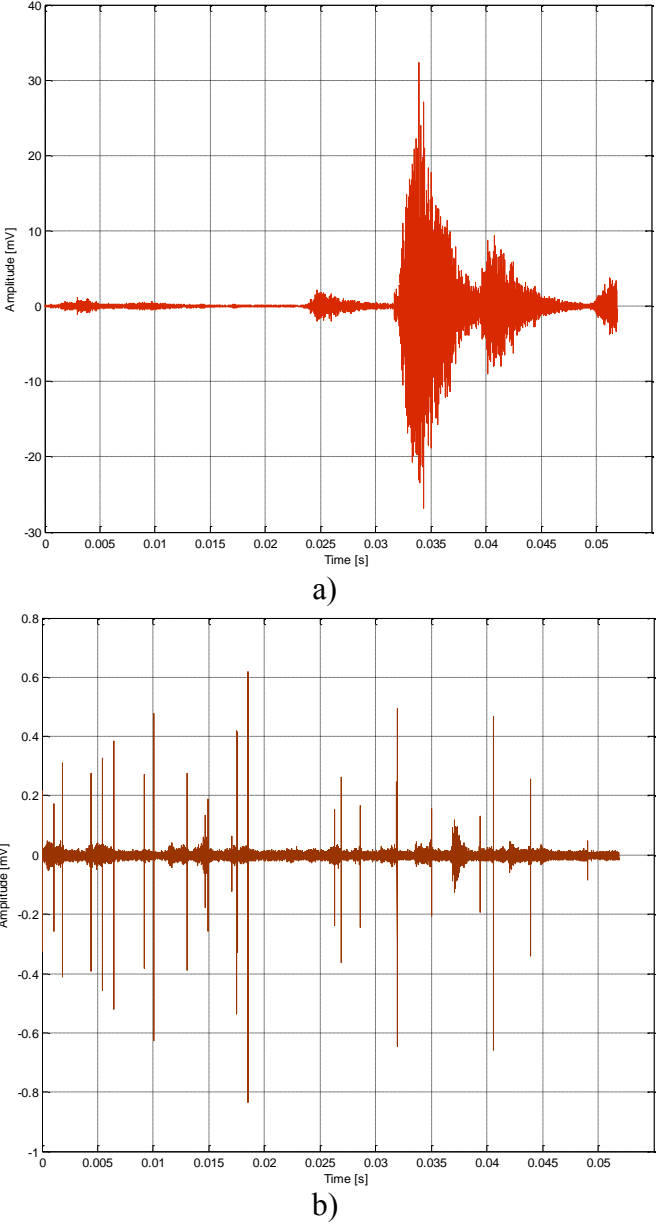


Fig. 7: Maximal amplitude values of captured AE signals during production of test specimen 14 (a) injection phase 1100 bar, (b) holding phase 500 bar.

Based on a detailed comparison of captured AE signals from Fig. 6 on both tool steel inserts, we found that higher number of AE signals was present during the production of test specimen 14 on tool steel insert with visible signs of macro-cracks. During production of test specimen 14 we can obviously notice higher amplitude and energy values of captured AE signal in filling and packing phase (Fig. 7).

4. Conclusions

The aim of this research work was to determine to which extent is it possible with AE method to detect the presence of macro-cracks on engraving tool steel inserts by conducting a closer comparison of captured AE signals obtained from new tool steel insert under same processing conditions. From our experimental results we were able to obtain useful information about the presence of macro-cracks during production of standard test specimens. We have found in the filing stage during production of test specimens on both inserts that there was more apparent difference in the number of detected AE signals during the injection phase of commercial polypropylene material in favor of the tool steel insert with visible sign of macro-cracks. The results clearly show also the difference in the maximum amplitudes during filling and holding phase, as well as in energies of captured AE signals. As could be seen from the practically obtained results from captured AE signals we can successfully use the AE method for detecting fractures on tool steel inserts, which is one of the important advantages of this nondestructive testing method.

Acknowledgement

The research work was partly financed by the European Union, European Social Fund, and by the Slovenian Ministry for Higher Education, Science and Technology.

5. References

- [1] Cao J., Luo H., Han Z.: Acoustic emission source mechanism analysis and crack length prediction during fatigue crack propagation in 16Mn steel and welds, *Procedia Engineering*, Vol. 27, 2012, 1524-1537.
- [2] Biancolini M.E., Brutti C., Paparo G., Zanini A.: Fatigue cracks nucleation on steel, acoustic emission and fractal analysis, *International Journal of Fatigue*, Vol. 28, 2006, 1820-1825.
- [3] Moorthy V., Jayakumar T., Raj B.: Influence of micro structure on acoustic emission behavior during stage 2 fatigue crack growth in solution annealed, thermally aged and weld specimens of AISI type 316 stainless steel, *Materials Science and Engineering: A*, Vol. 212, 1996, 273-280.
- [4] Mukhopadhyay C.K., Sasikala G., Jayakumar T., Raj B.: Acoustic emission during fracture toughness tests of SA333 Gr.6 steel, *Engineering Fracture Mechanics*, Vol. 96, 2012, 294-306.
- [5] Berkovits A., Fang D.: Study of fatigue crack characteristics by acoustic emission, *Engineering Fracture Mechanics*, Vol. 51, 1995, 401-416.
- [6] Vallen H.: *Acoustic Emission Testing: Fundamentals, Equipment, Applications*, Vol. 6, Castell Publication Inc., Wuppertal, 2006.
- [7] Miller R. K., Hill E.v.K., Moore P. O.: *Nondestructive Testing Handbook*, Third edition, Vol. 6, *Acoustic Emission Testing*, American Society for Nondestructive Testing, Inc., 2005.

ACOUSTIC EMISSION DURING SHORT-TERM ELECTROCHEMICAL CORROSION TESTING: LSP EFFECT ON PITTING CORROSION

Uroš Trdan¹, Janez Grum²

¹Faculty of Mechanical Engineering, Laboratory for Materials Testing and Heat Treatment
Aškerčeva 6, 1000 Ljubljana, Slovenia, uros.trdan@fs.uni-lj.si

²Faculty of Mechanical Engineering, Laboratory for Materials Testing and Heat Treatment
Aškerčeva 6, 1000 Ljubljana, Slovenia, janez.grum@fs.uni-lj.si

ABSTRACT

Acoustic emission (AE) during accelerated potentiostatic corrosion measurements in a 0.6 M NaCl naturally aerated aqueous solution was used to study localised corrosion phenomena of non-treated and Laser Shock Peened (LSP) aluminium alloy. Correlations between LSP parameters, anodic current density and characteristics of AE events were observed and analysed. Obvious beneficial effect of preliminary LSP treatment was confirmed, with reduction of both, i.e. current density and AE activity, indicating improved corrosion resistance of investigated alloy. Results revealed three different populations of AE events during the potentiostatic sweep at -700 mV_{SCE} , which differ significantly in the waveform, amplitude, signal duration and rise time. First population of AE bursts, with low emissivity are the results of the initiation step of pitting corrosion, whereas the second population appeared due to propagation of pits revealed higher amplitude and longer AE bursts. However, the most emissive source was found to be due to evolution of hydrogen bubbles (population 3), with highest amplitude and the longest duration of AE signals. Results confirmed the important potential of AE in the detection and characterization of localised corrosion even at extremely accelerated corrosion tests.

Key words: *Acoustic emission (AE), Pitting corrosion, Laser Shock Peening (LSP), Al alloy.*

1. Introduction

Corrosion damage represents one of the most important problems in existing structural parts. Although aluminium alloys covers a broad field of various applications owing to low weight, good mechanical properties and high corrosion resistance, in aggressive environment these alloys undergo a localized corrosion [1, 2] and stress corrosion cracking [3]. However, localized forms of corrosion are rather complex and consists various steps and electrochemical reactions. In this aspect, implementation of *in-situ* corrosion with non-destructive testing (NDT) methods enables early detection with ameliorated understanding of corrosion phenomena [4]. For the last two decades Acoustic Emission (AE) has been used to monitor the severity of corrosion. Compared to the conventional NDT methods, it is less intrusive and has the advantage of real-

time measurement [5]. Acoustic emission is based on the rapid release of energy inside the material (*film rupture, corrosion propagation, etc.*) which in-turn generates transient elastic (*acoustic*) waves that are detected by a piezoelectric sensor and then further analysed. AE has already been proved as a powerfully tool for early-stage detection of various localised corrosion modes, such as exfoliation corrosion [6], pitting corrosion [7, 8] and stress corrosion cracking [9, 10].

It is worth-noting that even aluminium parts exposed to the demanding conditions frequently requires an adequate surface treatment. Recently, laser shock peening (*LSP*) has attracted a global interest and has been accepted as the substitute of conventional Shot Peening. LSP surface treatment is a versatile, fast emerging and promising technique which involves underwater sample irradiation with laser pulses of short duration at a level of nanoseconds and a power density of several GW/cm^2 , with high laser pulse repetition rate. Specific condition enables plasma generation at the moment of the interaction of laser light and propagation of shock impact waves in the material [2, 11]. It was confirmed that LSP has the ability to improve both, i.e. mechanical properties [11, 12] and corrosion resistance [1, 13].

However, until now there is little report on the study of different LSP parameters on AE activity during electrochemical corrosion process. Thus, this work is focused to obtain correlation among AE burst and anodic current density in order to establish the impact of various LSP treatment parameters' on corrosion resistance during accelerated potentiostatic tests and to identify population of specific AE sources.

2. Experimental procedure

2.1 Specimen preparation & Laser Shock Peening set-up

In this study commercial aluminium alloy AA6082-T651 was used. Prior to LSP treatment specimens were cut along the longitudinal (*L*) and long-transverse (*LT*) directions from a 10 mm thick rolled plate and thoroughly degreased with acetone and then rinsed with deionised water. Laser shock Peening was performed using a Q-switched Nd:YAG laser operating at 10 Hz with a wavelength of 1064 nm in a water confinement regime, without ablative coating (*LSP_{wC}*). FWHM of the pulses was 10 ns, where a convert lens system delivered 2.8 J. In this study, the influence of different pulse density and power density was evaluated. Pulse density was controlled with a 2D motion velocity system and was set to three levels, i.e. 900, 1600 and 2500 pulses/ cm^2 . Power density was controlled with a spot diameter, i.e. 1.5 mm at $15.8 \text{ GW}/\text{cm}^2$, 2.0 mm at $8.9 \text{ GW}/\text{cm}^2$ and 2.5 mm at $5.7 \text{ GW}/\text{cm}^2$, respectively. First numeral of specimen designation is relating to pulse density and the second one power density; for example LSP 2-3 denotes the specimen treated with 1600 pulses/ cm^2 and $5.7 \text{ GW}/\text{cm}^2$.

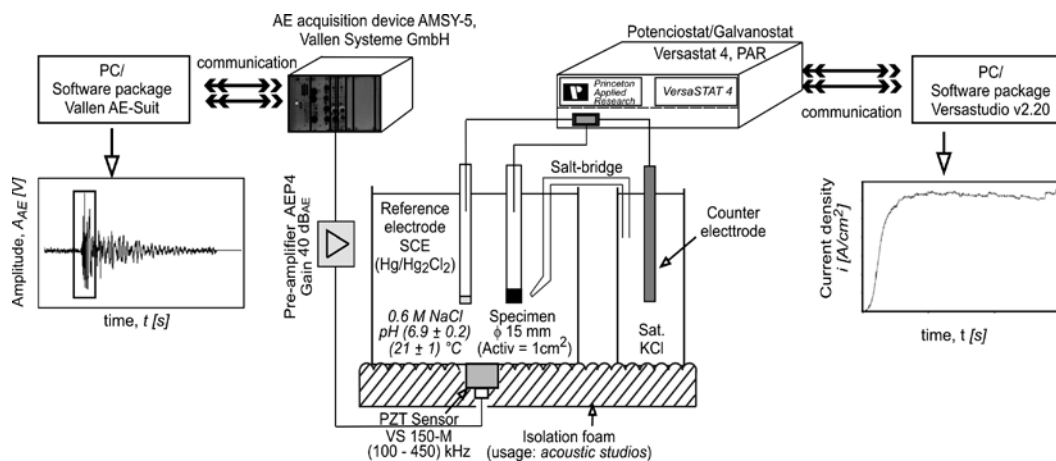


Fig. 1: Schematic presentation of the measurement system.

2.2 Electrochemical Potentiostatic and Acoustic Emission monitoring

In-situ detection of Acoustic Emission (AE) during potentiostatic (PS) experiments were performed prior to and after LSP surface pre-treatments. The experimental set-up is shown on Fig. 1. All the results reported here were conducted in a freshly prepared naturally aerated, near natural ($\text{pH}=6.9\pm 0.2$; $T=21\pm 1$ °C) 0.6 M NaCl solution, prepared with deionized water. The applied potential of -700 mV_{SCE} ($SCE=+242$ mV vs. SHE) was controlled by a PAR Versastat-4 potentiostat/galvanostat/ZRA. A classic three-electrode electrochemical cell was used, where a saturated calomel electrode (SCE) was employed as the reference electrode. In order to avoid acoustic noise induced by hydrogen evolution (*bubbles*) during potentiostatic corrosion tests, corrosion cell set-up was altered. For this purpose the counter electrode was connected to the corrosion cell via a salt bridge. Immediately, prior to each corrosion experiment, specimens were carefully cleaned and degreased. Procedure of preparation steps were the same as described in ref. [1], with EIS evaluation. The exposed working electrode, i.e. specimen was equal to 1 cm². Instrumentation for AE detection consisted of an acquisition device AMSY5 (*Vallen Systeme*), pre-amplifier (AEP4, gain 40 dB) and a contact piezoelectric transducer (PZT) VS150-M, with a frequency range from 100 kHz to 450 kHz. On the basis of the preliminary test the threshold for all AE measurements was set to 40 dB.

Taking into consideration the investigations by Bellenger et al. [6] and Kim et al [14]: following AE features were studied:

- number of events – N_{AE} : number of AE signals detected (*discontinuous emission*),
- Amplitude – A_{AE} [dB]: maximal (peak) amplitude of the considered AE burst,
- Rise time – $t_{R,AE}$: time interval between first and last threshold crossing,
- Counts number – CNTS: number of threshold crossings for a given AE burst,
- Duration – t_{AE} : time interval between first and last threshold crossing.

3. Results and discussion

Evolution of detected acoustic emission events (*peak amplitude*) and anodic current density during the PS test for the specimens treated with highest power density (15.8 GW/cm²) and various pulse densities (1–900 p/cm²; 2–1600 p/cm²; 3–2500 p/cm²) is shown on Fig. 2.

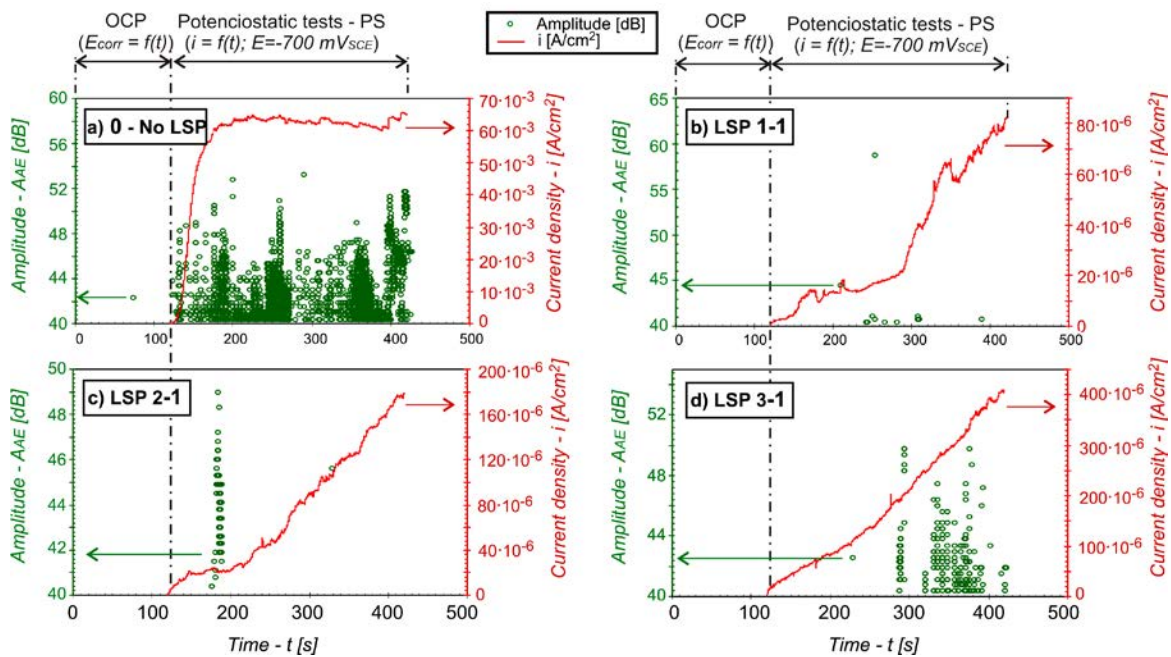


Fig. 2. Evolution of AE activity and anodic current density during potentiostatic tests in a 0.6 M NaCl near-natural naturally aerated solution (*Note: y-axis scales are not unified*).

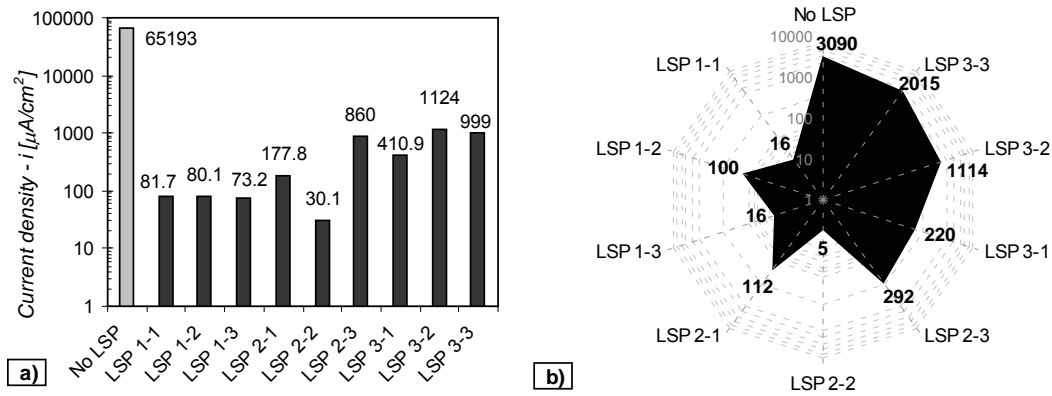


Fig. 3. Comparison of: a) anodic current density – i [$\mu\text{A}/\text{cm}^2$] and b) number of events – N_{AE} .

During the first sequence of the test, corresponding to OCP test ($t \leq 120$ s) AE activity is expectedly very low. It seems that in the case when no external polarisation is involved, aluminium oxide/passive film offers more or less effective barrier against corrosion attack in the aggressive chloride environment. On the contrary, the second sequence (120 s $\leq t \leq 420$ s), during external polarisation at potentiostatic test at -700mV_{SCE} , revealed a strong correlation among detected AE events and anodic current density. From the results obtained it is obvious that the untreated specimen exhibits the highest AE activity with highest anodic current density, suggesting lower corrosion resistance compared to the LSP treated specimens.

Results of anodic current density and number of detected AE events during PS test are shown in Fig. 3a and 3b, respectively. The results confirmed significant influence of LSP treatment parameters.

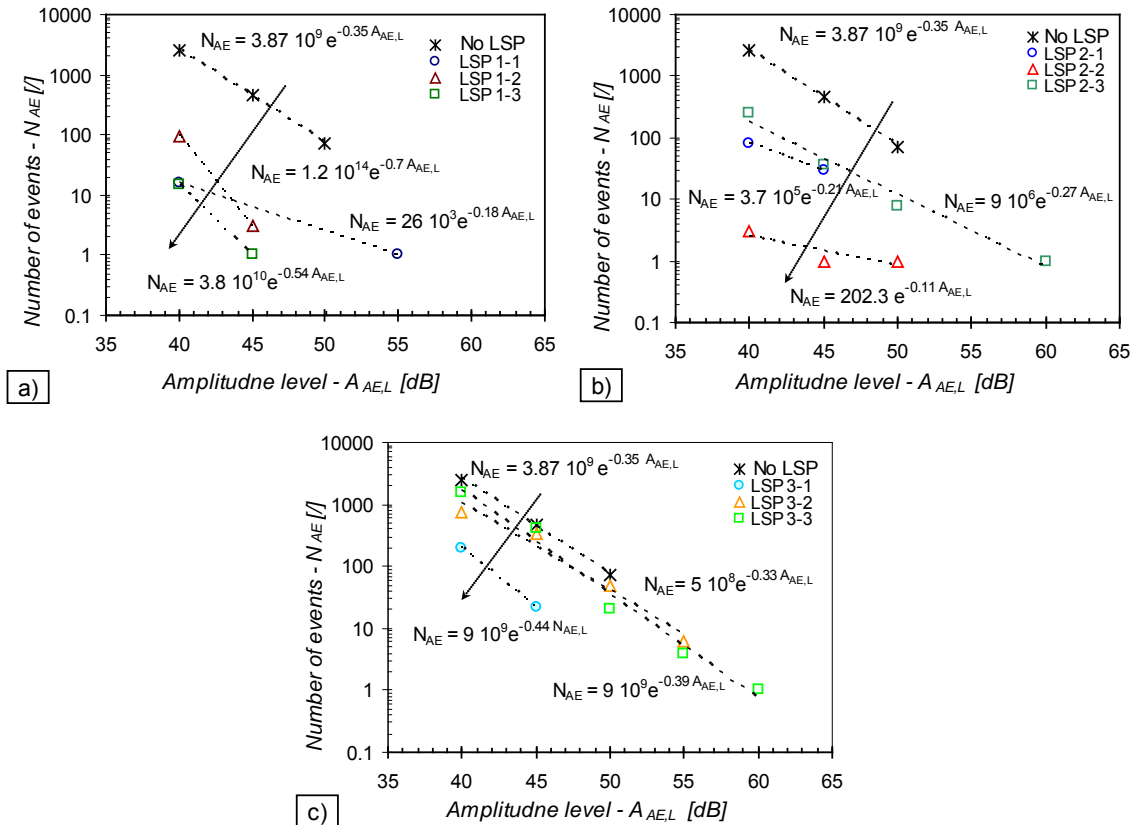


Fig. 4. Number of AE events inside specific amplitude levels during PS corrosion test; a) Untreated (0) & LSP - 900 p/cm², b) 0 & LSP - 1600 p/cm² and c) 0 & LSP - 2500 p/cm².

One should note that analysis of current density (*Fig. 3a*) confirmed the lowest value of $30.1 \mu\text{A}/\text{cm}^2$ with LSP 2-2 specimen. Compared to the untreated specimen ($65193 \mu\text{A}/\text{cm}^2$) results presents current density reduction of factor 2166! However, analysis confirmed that inside specific LSP group, the highest anodic current density values are obtained with the specimens treated with highest pulse density ($2500 \text{ pulses}/\text{cm}^2 \rightarrow \text{LSP 3-X}$). These is probably associated with the highest degree of surface micro-roughening and largest LSP-affected craters due to ablation, plasma generation and mechanical hardening effect of induced shock waves.

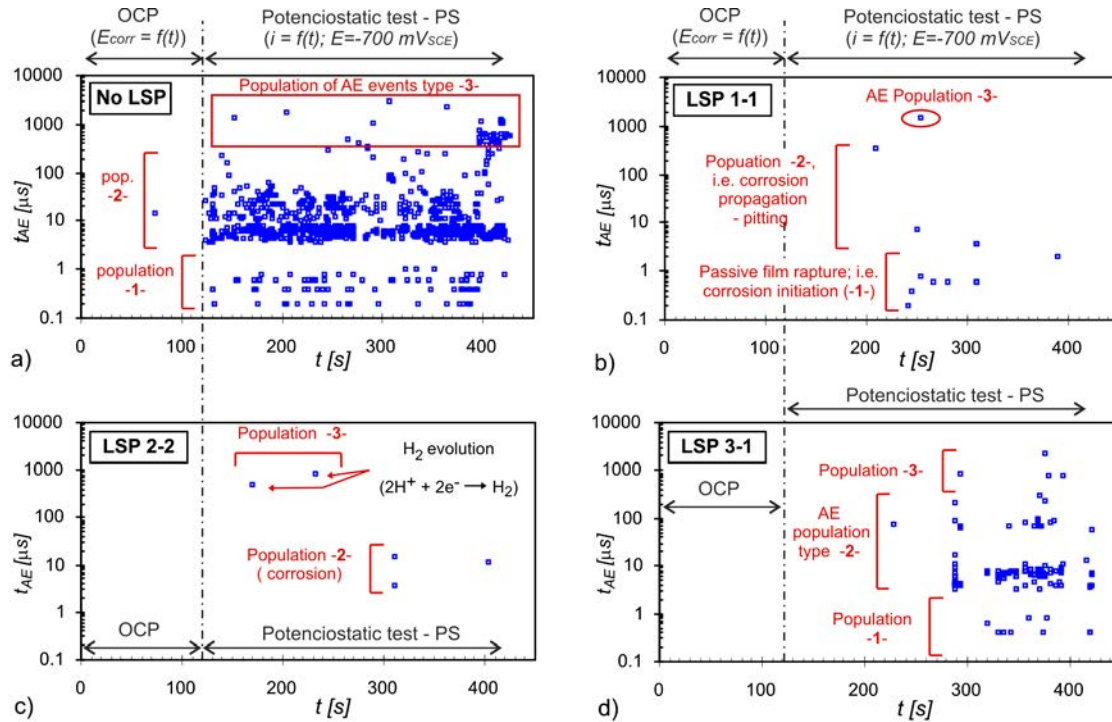


Fig. 5. Evolution of AE durations of untreated and LSP treated specimens which had the lowest AE activity within LSP group (unified pulse density).

From the number of detected AE events, good correlation with current density is observed. It can be noted that the number of detected AE events was the highest for the untreated specimen and was equal to 3090. This is followed by specimen LSP 3-3 with 2015 AE bursts. The lowest AE activity was once again achieved with specimen LSP 2-2, with only 5 detected AE bursts.

Amplitude distributions of detected AE events, for various surface pre-treatments are presented in Fig. 4. The amplitudes of AE events from 40 dB to 60 dB were classified into 5 amplitude levels $A_{AE,L}$, increments being equal to 5 dB. Thus, the number of AE events at amplitude level of 40 dB represents the total number of AE events equal or higher to 45 dB and lower than 50 dB ($45 \leq A_{AE} [\text{dB}] < 50$).

In the investigation by Kek et al. [15] dependence of the number of AE events (N_{AE}) and the amplitude levels $A_{AE,L}$ was successfully described with an exponential function.

Measurement results in this study also confirmed an overall trend, i.e. lower distance of an exponential trend line from the starting-point of the coordinate system, indicating improved corrosion resistance (lower AE activity) of LSP treated specimens.

Results once again confirm the beneficial effect of preliminary LSP treatment on improvement of corrosion resistance of investigated aluminium alloy. According to our previous publications [1, 16] it has been shown that LSP clearly enables more difficult penetration of water molecules, oxygen and Cl^- ions due to the development of compressive residual stresses and more chemically stable passive/oxide and more compact film on the specimen surface due to surface ablation, plasma generation and hardening effect of shock waves.

In order to characterize and to evaluate population of AE source more precisely, complementary analyses of the amplitude, duration and waveforms were performed.

Fig. 5 shows evolution of AE activity, i.e. duration of specific AE events of untreated and three LSP treated specimen which had the lowest AE activity within unified pulse density, respectively. It is worth nothing that the untreated specimens' exhibits much larger number of AE events within each population, compared to the LSP treated ones, indicating the most severe corrosion attack. Furthermore, the results of the AE duration during PS tests demonstrates that the highest differences among untreated and LSP treated specimens exists within the second population of AE events, i.e. active material dissolution.

Results of the present study confirmed the presence of three (3) populations of AE events, which distinguishes in amplitude - A_{AE} , duration - t_{AE} , rise time - $t_{R,AE}$ and threshold crossings - $CNTS$:

- I. The first population, noted -1-, consists of AE signals with short duration (0.1 - 2 μ s), low distribution and of low amplitude, i.e. in the range 40 dB – 44 dB. This population of AE events appeared to be related to the *initiation step of localized pitting corrosion*, or to say the *rupture of the protective passive film*.
- II. Second population -2- are related to the 2nd step of corrosion, i.e. *formation and propagation of corrosion pits*. These AE events are of grater amplitude, with longer duration, in the range from 2.5 μ s to 300 μ s.
- III. Signals related to population -3- (Fig. 6) appeared as the most emissive AE source, with the highest amplitude, short rise time and exceptionally long duration ($t \leq 5$ ms). This AE signals are associated with the *evolution of hydrogen bubbles inside the corrosion pits*.

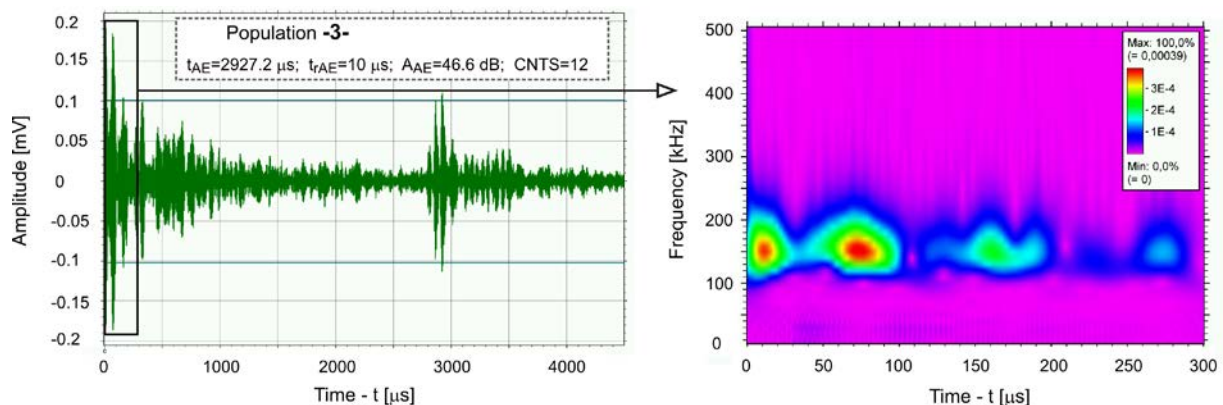


Fig. 6. Evolution of AE burst waveform (on left) and spectrograph (right) of AE population -3-.

Analysis of specific population of AE sources confirmed that the population distinguish especially in the duration time and waveforms. This effect is attributed to the different acoustic emission sources, or to say different direction of energy release. Furthermore, the results obtained indicate that the most vivid difference between untreated and LSP treated specimens are in the cumulative number of AE burst belonging to population -2-.

Such results are understandable due to the fact that untreated specimen suffered from the highest corrosion attack and anodic current density during PS test. During this step corrosion in the form of active dissolution of Al matrix in the proximity of cathodic precipitates of $Al_x(Fe,Mn)$ occurred [1, 16].

Analysis revealed that the emissivity of AE events sources are in the following order (*from lower to higher*): Population -1- (*passive film rupture/corrosion initiation*) < Population -2- (*corrosion initiation*) < Population -3- (*hydrogen evolution /release of hydrogen bubbles*), of which waveform and spectrograph are presented in Fig. 6.

Furthermore, it has been demonstrated that almost perfect correlation exists between acoustic activity and current density during accelerated potentiostatic tests at $-700 \text{ mV}_{\text{SCE}}$. However, in order to characterize more precisely corrosion pit morphology evolution and detected AE signals, further experiments with *in-situ* observation of the specimens by high speed camera/microscope during electrochemical corrosion testing would be highly recommend.

4. Conclusions

Simultaneous (*in-situ*) use of acoustic emission (AE) during accelerated electrochemical potentiostatic (PS) tests was found to be a reliable method for early detection of pitting corrosion of investigated Al alloy and for general monitoring of corrosion activity.

AE activity showed good correlation between this activity (N_{AE} & A_{AE}) and advance of pitting corrosion by the transients of current density. The analysis revealed that general correlation exists, i.e. more of AE bursts (N_{AE}) detected \leftrightarrow higher the current density (lower corrosion resistance).

Analysis of AE signal characteristics revealed three explicit populations of detected AE bursts. Furthermore, detailed analysis has confirmed that the most energetic, i.e. the most emissive AE source belongs to hydrogen evolution, which had the amplitude of up to 47 dB and AE signal duration of almost 5 ms. Nevertheless, due to the complexity associated with hydrogen evolution and nature of the acoustic emission, additional visual observation of the specimens during corrosion testing would be strongly recommended.

5. References

- [1] Trdan U., Grum, J., Corrosion Science, Vol. 59, 2012, 324–333.
- [2] Trdan U., Ocaña J.L., Grum J., J. Mech. Eng., Vol. 57, No. 5, 2011, 385–393.
- [3] Yue T.M., Yan L.J., Chan C.P., Applied Surface Science, Vol. 252, 2006, 5026–5034.
- [4] Boinet M., Bernard J., Chatenet M., Dalard F., Maximovitch S., Electrochimica Acta, Vol. 55, 2010, 3454–3463.
- [5] Prateepasen A.: Pitting Corrosion Monitoring Using Acoustic Emission, Pitting Corrosion, (Bensalah N., ed.), ISBN: 978-953-51-0275-5, *InTech*, 2012.
- [6] Bellanger F., Mazille H., Idrissi H., NDT&E International Vol.35, 2002, 385–392.
- [7] Fregonese M., Idrissi H., Mazille H., Renaud L., Cetre Y., Corrosion Science, Vol. 43, No. 4, 2001, 627–641.
- [8] Mazille H., Rothea R., Tronel C., Corrosion Science, Vol. 37, No. 9, 1995, 1365–1375.
- [9] Kovac J., Alaux C., Marrow T.J., Govekar E., Legat A. Corrosion Science, Vol. 52, 2010, 2015–2025
- [10] Lapitz P., Ruzzante J., Alvarez M.G., Corrosion Science, Vol. 49, 2007, 3312–3325
- [11] Trdan U., Porro J.A., Ocaña J.L., Grum J., Surface & Coatings Technology, Vol. 208, 2012, 109–116.
- [12] Altenberger I., Nalla R.K., Sano Y., Wagner L., Ritchie R.O., International Journal of Fatigue, Vol. 44, 2012, 292–302.
- [13] Krawiec H., Vignal V., Amar H., Peyre P., Corrosion Science, Vol. 53, 2011, 3215–3221.
- [14] Kim, Y.P. Fregonese M., Mazille H., Feron D., Santarini D., Corrosion Science Vol. 48, 2006, 3945–3959.
- [15] Kek T., Grum J., Int. Journal of Machine Tools & Manufacture, Vol. 49, 2009, 8–12.
- [16] Trdan U., Žagar S., Grum J., Ocaña J.L., Int. Journal of Struct. Integ., Vol. 2, 2011, 9–21.

DETECTION AND PROCESSING OF SOUND SIGNALS IN STEEL QUENCHING

Franc Ravnik*, Janez Grum

University of Ljubljana, Faculty of Mechanical Engineering, Aškerčeva 6, 1000 Ljubljana
franc.ravnik@fs.uni-lj.si; janez.grum@fs.uni-lj.si

ABSTRACT

In the production of machine components a manufacturing process often ends with heat treatment such as quenching by tempering. Generation of internal stresses during heat treatment and residual stresses present thereafter frequently result in non-uniform hardness and depth of a quenched layer, which produces distortion of a machine component and generation of residual stresses. The choice of optimum parameters of a quenching process and monitoring of the process itself ensures the achievement of the specified hardness and residual stress at the surface of the machine component. The paper treats an experimental setup comprising detection of acoustic emission in the course of quenching. Due to heat transfer from a specimen to a quenching medium, film boiling and nucleate boiling occur round a heated object, which strongly affects quenching. An investigation of acoustic emission in the quenching process was carried out with cylindrical specimens made of chrome-molybdenum heat-treatment steel 42CrMo4. The cylindrical specimens of two shapes were quenched in five different recommended quenching media. Sound-pressure signals demonstrated by different amplitudes depending on time at different frequencies are shown in 3D diagrams. It has turned out that an analysis of acoustic-emission signals can provide useful information that confirms differences occurring in quenching with different quenching media and under different quenching conditions. The quenching results obtained from acoustic-emission signals during the quenching process can be confirmed by variations of residual stresses and hardness in the cross section. The results confirm the applicability of the new approach to the control of steel quenching.

Keywords: Acoustic emission, Acoustic spectrograph, Cooling rate, Polymeric solution, Quenching, Sound pressure level, Vapour film

1. Introduction

A purpose of quenching is to provide a cooling rate higher than the upper critical cooling rate in a certain depth of a machine component in order to obtain desired mechanical properties. The mechanical properties obtained are then verified by hardness measurement at the surface, i.e. by measuring through-depth hardness of the machine component. Critical cooling rates with carbon steels and low-alloy steels can be achieved by cooling a machine component from the austenitic microstructure, which is obtained by immersion into fluid quenching media such as water, oil, polymeric water solutions, and emulsions.

During the quenching process in liquids the occurrence of three phases of heat transport of the heated machine component, which is conditioned by quenching parameters and workpiece properties, is characteristic.

In the initial phase of machine-component immersion, a stable vapour film of a fluid quenching medium forms around the workpiece, so that the heat transfer to the quenching medium is considerably slowed down. In further cooling the vapour film gradually decays so that a phase of nucleate boiling occurs at some parts of the workpiece surface having a temperature lower than the Leidenfrost temperature. In nucleate boiling, a surface section wets with the liquid quenching medium and the heat transfer from the workpiece increases. At lower temperatures, a third phase of convective cooling occurs at the interface. The three phases are characterized by different modes of heat transfer, which contributes to different cooling intensities.

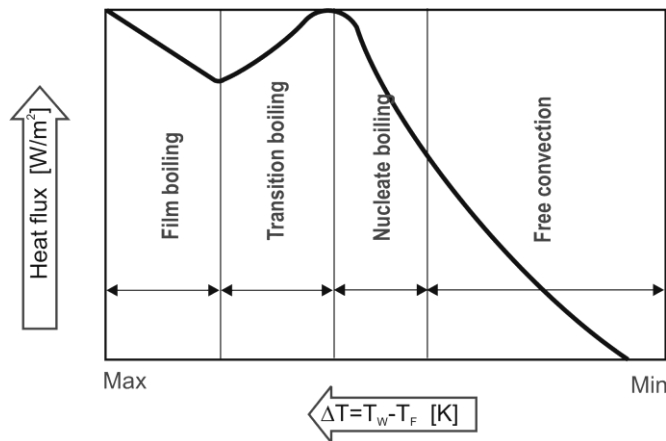


Fig. 1. Nukiyama boiling curve and different stages of boiling (heat transfer).

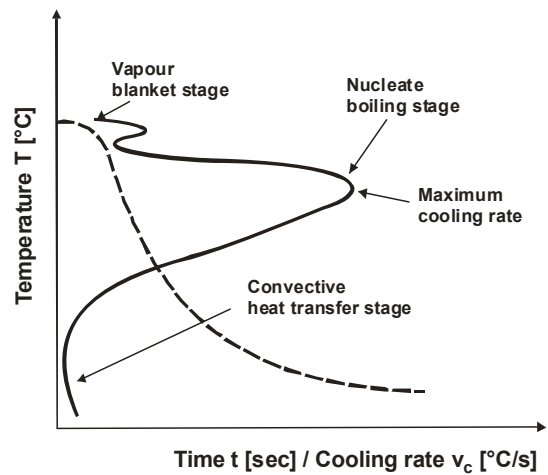


Fig. 2. Cooling rate and temperature during quenching.

With exacting workpiece shapes it often occurs during heat treatment, i.e. during workpiece cooling, that all the three phases occur simultaneously, which, however, produces considerable thermal stresses and also an explicit influence on microstructural stresses, which leads to distortion, or even to distortion and cracking, of the workpiece. Steel quenching starts at the austenitizing temperature of a given steel, the quenching process in fluid quenching media always being accompanied by an evaporation phase of the medium in contact with the workpiece surface, since a boiling point of most of quenching media ranges between 100 °C and 300 °C at normal pressure.

Liberation of steam bubbles is a function of their size, which produces sound phenomena in the liquid, which are the strongest at the transition between film boiling and nucleate boiling of the quenching medium. Detection of acoustic signals and their analysis can, therefore, provide useful information on the quenching process.

The Minnaert model of frequency of bubble formation during immersion quenching of the workpiece indicates a relation between a bubble size and the frequency of bubble formation. In the initial phase of nucleate boiling, bubbles of smaller diameters form and their frequency is higher, and vice versa, when nucleate boiling of the quenching medium is nearing its end. Such conditions can be achieved in quenching in water and in polymeric water solutions of different concentrations.

Minnaert's frequency of oscillation bubble:

$$\omega_M = \frac{1}{R_o} \sqrt{\frac{3\chi \cdot p_0}{\rho}} \quad [1]$$

where:

p_0 [N/m²] ... is hydrostatic pressure of the liquid around the bubble in conditions of static equilibrium,

χ [] polytropic coefficient,
 R_0 [m] radius of the bubble in the equilibrium and
 ρ [kg/m³] the density of the liquid

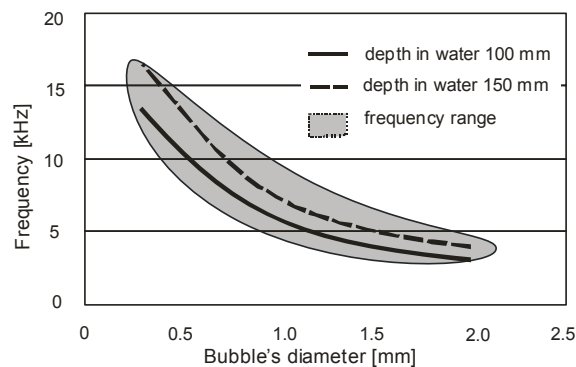


Fig. 3. Expected frequency of nucleate formation as a function of nucleate size with chosen immersion depth of specimen

Consequently, a measuring setup is adapted to the expected frequency of sound phenomena. Thus it should be known which frequencies of bubble formation and decay occur predominantly in the range of hearing and which slightly below this threshold.

Sound phenomena depend to a large extent on the temperature occurring at the workpiece surface during the quenching process and a momentary temperature of the quenching medium. Thus it is necessary that a signal detected with a hydrophone during the quenching process follows the Minnaert model of formation of bubbles and sound signals in the quenching medium. The conditions at which the signals were detected can be monitored with temperature measurement in the specimen during the quenching process. The phenomena occurring at the workpiece/medium interface should then be logically interrelated in film boiling, including additional sound effects due to material failure.

2. Experimental procedure

Because of an influence of the workpiece surface temperature on the occurrence of film boiling and nucleate boiling, an experimental procedure was elaborated for temperature monitoring in the cylindrical specimens and on-line detection of sound signals in the entire temperature range of the quenching process.

2.1. Experimental setup

The designed experimental setup comprises two independent setups, i.e.:

- a setup for monitoring the temperatures at the surface and in the core during quenching and monitoring of the temperature of the medium itself (Fig. 4);
- a setup for detection and processing acoustic-emission signals (Fig. 4).

The experimental setup for detecting AE signals in wetting processes is to be independent from the type of quenching medium used and of the quenching mode. Although the quenching process takes some seconds or even up to several minutes, the experimental system should register individual events sensed up to 0.1 second or less.

Fig. 4 shows the experimental setup for detecting AE signals during quenching. It comprises a vertically adjustable hydrophone carrier providing a stable position perpendicular to the specimen surface, and a small wire basket enabling fast and simple putting of a specimen in a stable position to provide quenching free of additional heat removal. The specimen/basket contact is realized in three points only so that the unwanted heat transfer to the cold basket is

prevented. A heated specimen is transferred from a quenching furnace with special pliers as fast as possible so that heat transfer is as small as possible. The specimen is set in a measuring position with regard to the hydrophone position in the quenching medium. The entire equipment is immersed in a container having the form of a glass aquarium having convex walls and filled with the quenching medium. A preliminary test showed that a 6 mm thick soft rubber lining, which considerably reduces reflection of sound signals from the container walls, considerably reduces noise.

The measuring setup for detection and processing of AE signals comprises:

- A hydrophone suitable for laboratory and industrial applications. Its high sensibility permits sound capturing in liquids, in frequency ranges from 0.1 Hz to 180 kHz, in a wide range of working temperatures between 40 °C and 80 °C (for short periods even up to 120 °C).
- A multi-channel measuring amplifier/pre-amplifier which is suitable for measuring sound emission and is also used in vibration measurements.
- A two-channel Sound Blaster card enables analogous/digital transformation of the signal captured and permits 16- or 24-bit sampling of velocity up to 96 kHz.
- The program package SpectraLAB, specially designed for the detection, recording and processing of sound signals in their original and digitized form, permits subsequent evaluation and monitoring of events in the specimen during quenching.
- A notebook with Intel® Pentium® M Processor 1.6 MHz, and 760 MB RAM. Operating system: MS Windows XP Professional 2002.

In addition to acoustic emission, temperature variations at the specimen surface and in the core, and quenching-medium temperatures prior to, during and after quenching were monitored too.

Each of the ten specimens was equipped with two thermocouples, the first being 2 mm below the surface and the second one in the core centre, i.e. in the specimen axis.

The measuring setup for monitoring temperature variations at the specimen surface and in its comprised:

- Thermocouples, mounted near the surface and in the core, for measuring temperature variations during quenching;
- SCIXI 16-bit USB I/O platform for signal processing which enables the detection of temperature signals with a 16-bit resolution and sampling rate of up to 200 kHz;
- Software for monitoring time-dependent temperature.

Within the experimental setup for temperature measurements in the specimen, a temperature of the quenching medium prior to, during, and after quenching was measured too, using a digital thermometer, model 30, a product of Macken Instruments Inc.

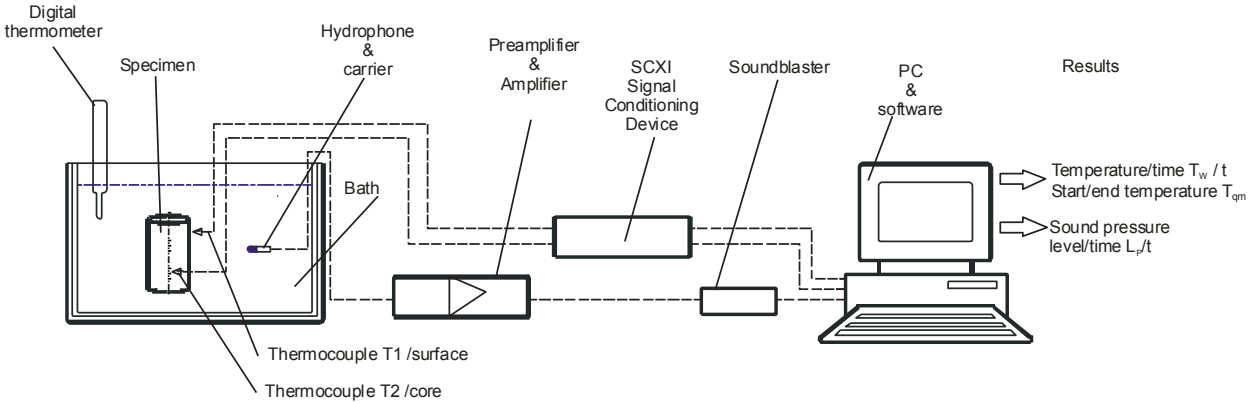


Fig. 4. Experimental setup for detection of temperature measurement signals during quenching and experimental setup for detection of AE signals during quenching

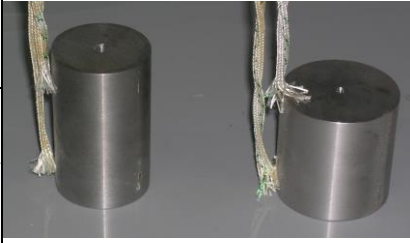
2.2. Specimen material and size

Low-alloy Cr-Mo heat-treatable steel AISI 4140 was selected for the specimens. This steel shows high hardness after heat treatment of even up to 57 HRC. It is characterized by good through-hardening and high strength after heat treatment [Grum et al, 1998]. For this reason, it is widely used in the production of static- and dynamical-load components of vehicles, motors, and machine components with a large cross section.

Specimen form

Test specimens had a form of a cylinder with diameters of 45 mm and 53.5 mm and a height that provides the same mass, i.e. 0.92 kg. A ratio between the specimen volume and area was taken into account since it affects the cooling rate with the same specimen mass. Table 1 shows two different cylindrical specimens (A and B) with different P/V ratios.

Table 1: Specimen form and size

Spec. type	Diameter D [mm]	Length L [mm]	Mass M [kg]		Area	Volume	P/V
					P [cm ²]	V [cm ³]	--
A	φ 45.0	75.0	0.92		138	119	1.16
B	φ 53.5	53.5	0.92		132	119	1.11

2.3. Quenching medium

For the steel chosen an adequate quenching medium and a suitable quenching mode ensuring a cooling rate slightly higher than the critical one should be used. Thus the required through-specimen hardness and strength can be obtained, and internal stresses can be optimized in the specimen during quenching and distortion with residual stresses as a result of quenching. In accordance with steel manufacturer's recommendations, five types of quenching media were chosen for quenching steel 42CrMo4; they are given in Table 2.

Table 2: Quenching medium

Quenching medium	Ratio		
	Water	Aquatensid BW	"Olmakal Rapid 90"
Pure water	100 %	--	--
5% polymeric water solution	95 %	5 %	--
10% polymeric water solution	90 %	10 %	--
15% polymeric water solution	85 %	15 %	--
"Olmakal Rapid 90" oil	--	--	100 %

2.4. Procedure

A cold specimen was introduced in the furnace preheated to a temperature around 600 °C. Then progressive heating of the specimen to the austenitizing temperature, i.e. 850 °C, followed in accordance with manufacturer's recommendations. When the temperature became stable, the specimen was quickly moved with the pliers to a quenching bath to be quenched in the different quenching media.

During the experiment the specimen was fixed in a stable position to ensure identical quenching conditions for all the specimens and to reduce noise that could generate due to stirring of the quenching medium. The initial quenching-medium temperature amounted to 18 °C, whereas the final temperature varied due to the different specific heat of the quenching media used. It varied in dependence of the quenching medium used. It was the lowest with pure water and highest with oil. The volume of the quenching medium in the container was always the same, i.e. 14 l.

At the IBM notebook two program packages, i.e. "*SpectraLAB*" for sound-signal processing and "*Temperature*" program for temperature-signal processing, were running simultaneously at platform LabView. The captured sound signals were subsequently evaluated with the same program package, i.e. "*SpectraLAB*", and the temperature signals with MS EXCEL.

3. Results

The results on the sound pressure are represented in diagrams showing the varying sound pressure level L_p in dependence of frequency and time.

The sound power at a certain point indicates the relation between the instantaneous pressure and the ambient pressure. The sound pressure (p) is expressed in [Pa]. A reference value of the sound-pressure for liquids p_{ref} is equal to 10^{-6} Pa. The sound-pressure level L_p is defined by:

$$L_p = 10 \cdot \log \frac{p^2}{p_{ref}^2} = 20 \cdot \log \frac{p}{p_{ref}} \quad [\text{dB}] \quad (1)$$

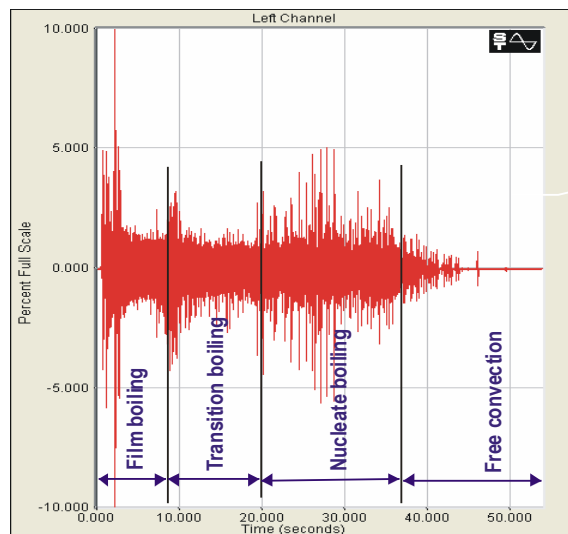


Fig. 5 Typical time series diagram of sound pressure signals.

- The diagram of time intervals displays the raw digitized audio data with the amplitude shown on the vertical axis and time on the horizontal axis in linear view. The amplitude ratio between maximum level at the start of the quenching process and background noise level at the very end of the process is sufficient to identify different stages of the quenching process (Fig. 5).
- Signal processing software enables spectrogram view as calculated time record of sound signals. Digitized audio signal is passed through a math algorithm known as a Fast Fourier Transform (FFT) which converts the signal from the time domain (amplitude-vs-time) to the frequency domain (amplitude-vs-frequency). This view displays the spectral data over time with the amplitude shown in colour in which frequency is seen as the ordinate value and signal intensity as color intensity: cold - blue color → low intensity; hot - red color → strong intensity (Fig. 7b).

- The calculated average spectrum shows relative amplitude level dependent on the frequency. This view is a two-dimensional plot of the spectrum. The horizontal axis shows the frequency and the vertical axis shows the amplitude of each frequency line (Fig. 6A, Fig. 6B).

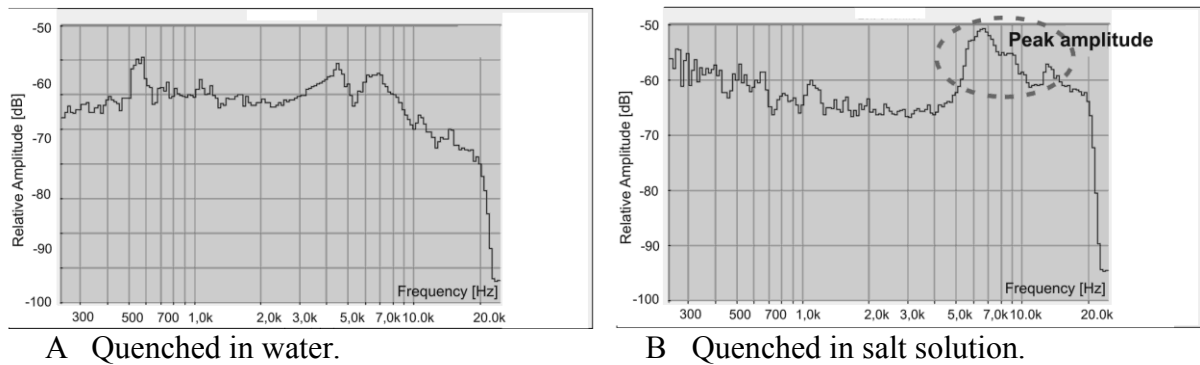
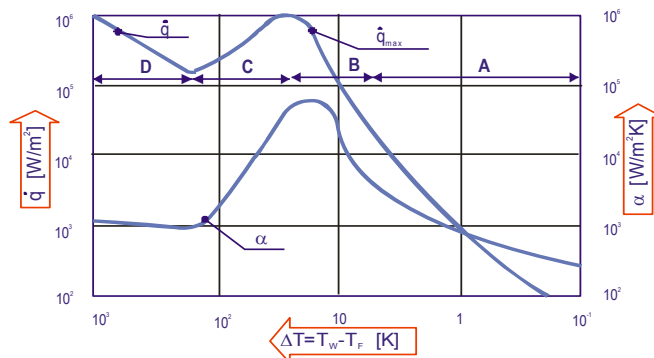


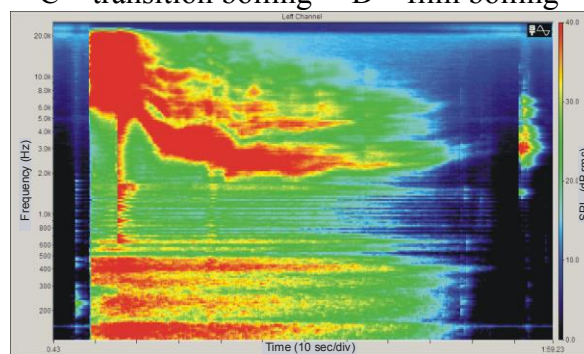
Fig. 6 The average spectrum of type A samples.

3.1. Comparison of spectrograms

The comparison of spectrograms obtained in quenching of the specimens of different forms and the same mass in different quenching media indicates an important characteristic of the spectrograms, a differentiation in sound intensity. The differences of sound emission intensity and duration during quenching distinctively depend on the specimen mass and the type of quenching medium used (Fig. 8). As the specimen-surface wetting occurs simultaneously at different sections of the specimen surface, all regions of Nukiyama boiling curve from the beginning to the end of cooling can be differentiated. The Nukiyama curve in Fig. 7a shows the heat flow as a function of the temperature difference between the specimen temperature T_w and the quenching-medium temperature T_f .



A – free convection B – nucleate boiling a)
 C – transition boiling D – film boiling



b)

Fig. 7. Comparison between Nukiyama boiling curve (a) and spectrogram during cooling (b) at specimen of ϕ 53.5 mm quenched in 10% polymeric water solution

3.2. Analysis of an acoustic spectrum

A spectrogram is a time record of sound signals, from which a frequency is evident as a value at the ordinate and signal intensity as colour intensity (cold, blue colour - low intensity, hot, red colour – strong intensity).

The spectrogram of the quenching process shows the presence of low frequencies at the beginning of the process, i.e. in the first 10 seconds, when using water as a quenching medium. Intense sound pulses occur due to the formation and decay of the vapour film. Their frequency gradually reduces due to a decreasing cooling rate.

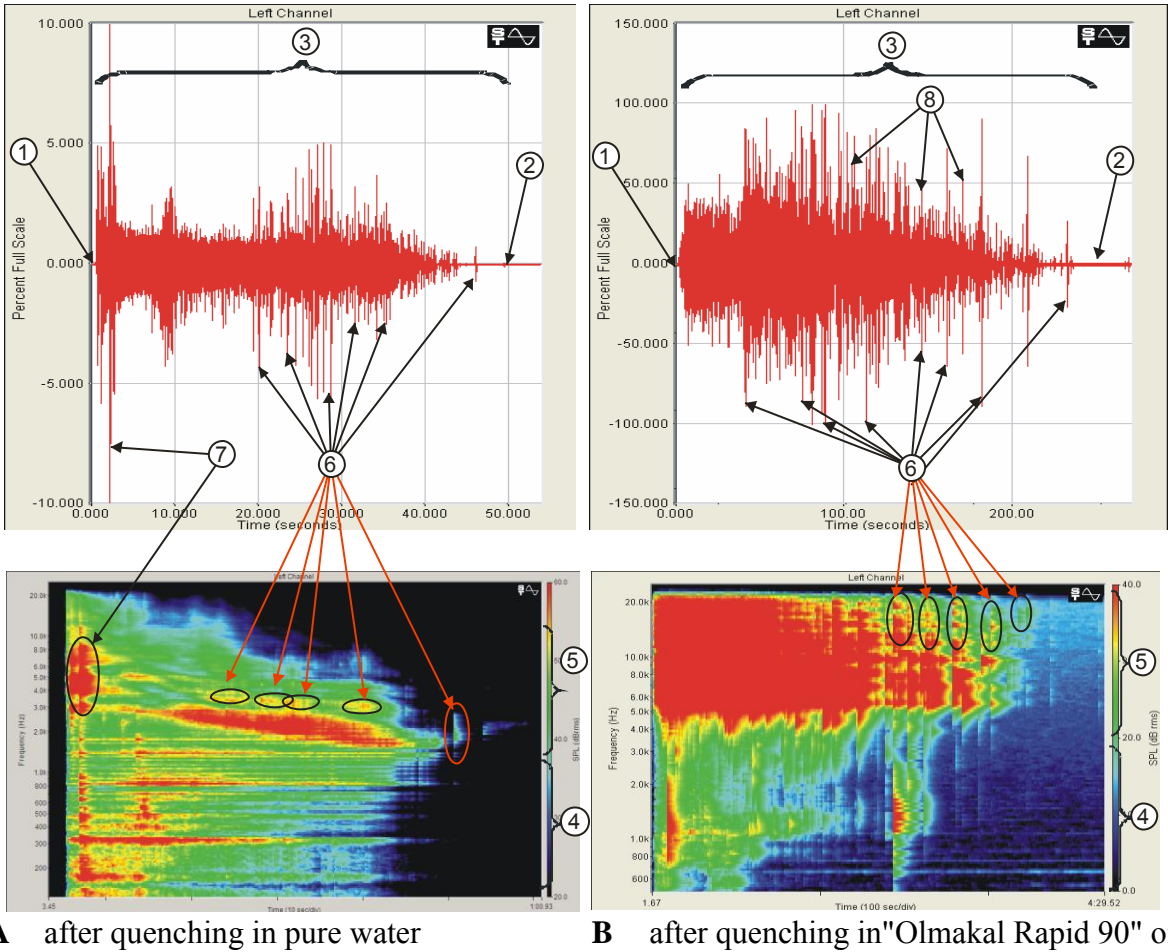


Fig. 8. Acoustic signal obtained in quenching of specimen of ϕ 45 mm in pure water (A) and "Olmakal Rapid 90" oil (B).

The analysis of the acoustic spectrum obtained during quenching comprises detection of sound emission and transformation into a voltage signal. It provides detailed information on individual events in the quenching medium used. Fig. 4 shows two records of voltage signals detected with the hydrophone and shown in the spectrogram giving the frequency of events during nucleate boiling. Although the signal of the ϕ 45 mm specimen quenched in pure water and the one quenched in the "Olmakal Rapid 90" oil (Fig. 8) differ considerably, following may be concluded:

- The beginning of quenching is described by the signals of different frequencies which in their amplitude differ from the environmental noise (Fig. 8, area 1);

- The end of quenching is described by the signal having intensity comparable to that of the environmental noise, which means that the number and intensity of the signals with regard to the frequency and their intensity reduces. Determination of the end of cooling is of subjective nature and cannot be made by means of the spectrogram. (Fig. 8, area 2);
- The process duration is the difference between the beginning and end of quenching; wherefrom an average cooling rate can be established (Fig. 8, area 3);
- From the voltage signal detected with the hydrophone and from the spectrogram, two characteristic areas can be determined:
 - * an area of lower frequencies, i.e. up to 1 kHz in water quenching, and up to 2 kHz in oil quenching, where only the amplitude is changing (Fig. 8, area 4), and
 - * an area of higher frequencies, i.e. up to 18 kHz in water quenching, and up to 20 kHz in oil quenching, where the signal frequency is changing as well (Fig. 8, area 5).
- Individual peaks of higher sound-emission intensity given by a voltage signal of higher frequencies (up to 6 kHz in water quenching, and up to 14 kHz in oil quenching) due to surface oxidation and oxide cracking (scale) at the surface (Fig. 8, area 6) are identified. In sound emission there are also short-time peaks of high intensity with frequencies of up to 12 kHz in water quenching as a result of too high a cooling rate (Fig. 8, area 7).
- The individual peaks of high intensity with lower frequencies are a result of steam bubbles escaping from a drillhole of 4 mm in diameter at the upper specimen plane, which are particularly distinct in oil quenching (Fig. 8, area 8).

In general, it can be concluded that characteristic changes at the specimen/quenching-medium interface could be determined from the detected sound emission during quenching.

3.3. Temperature measurement

Fig. 9 shows cooling curves at the surface for type A specimen (ϕ 45 mm) quenched in all five quenching media. The temperature was measured near the surface and in the core, but only surface temperature was taken into account when describing the interface phenomena.

Water quenching is more intense, which means that the cooling from the quenching temperature to the boiling point of water only takes a few seconds (4.5 seconds at the surface and 6.5 seconds in the core), whereas the cooling to a temperature of 40 °C at the surface takes 52 seconds, the core temperature being lower by approximately 10 °C.

Oil quenching is slower, i.e. cooling from the quenching temperature to a temperature of 400°C takes approximately 10 seconds (10.8 seconds at the surface and 11.8 seconds in the core), whereas cooling to 50 °C at the surface takes 322 seconds, the core temperature being lower by approximately 2 °C.

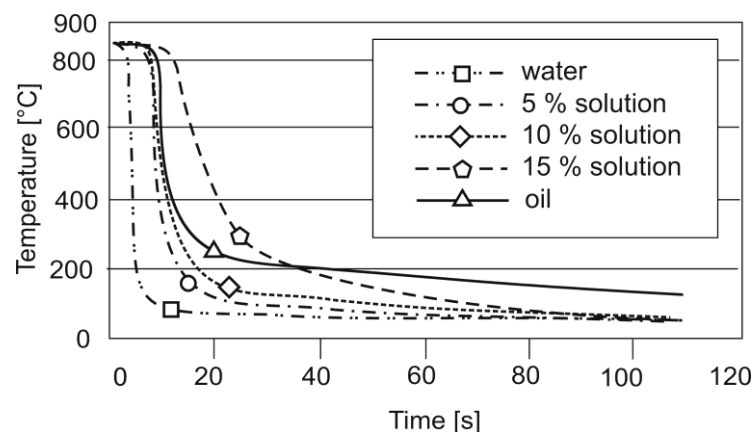


Fig. 9 Temperature variation at specimen surface of 45 mm in diameter during quenching in different quenching media.

4. Conclusions

The paper treats the signals captured through sound emission measurements which occur during the steel quenching in different quenching media. The sound pressure signal, represented as the amplitude and duration of the signal during quenching, was captured by the hydrophone. During the recording of the sound pressure the signal shape changes as the vapour film phase on the specimen surface is formed and the nucleate boiling phase on the specimen/quenching-medium interface enters. Sound emission analysis provides a new approach to processing, evaluation and optimization of the quenching process. The sound-pressure signals described with the voltage-signal amplitude were detected with the hydrophone and shown in diagrams as time-dependent amplitude. The analysis results confirm that there are important differences in the amplitude and frequency of the detected signals, indicated by the formation and decay of the vapour film at the specimen surface as well the occurrence of nucleate boiling at the specimen/quenching-medium interface during quenching. The sound emission occurring during quenching is found predominantly in the hearing section of the spectrum; therefore, detecting emission is efficient since the phenomena at the interface can be monitored. The phenomena at the interface play an important role in the heat removal from the workpiece, which means that quenching effects with deviations in hardness and residual stresses in the cylindrical specimens can also be taken into account. The investigation performed shows that the proposed experimental system for detecting acoustic emission and temperature in the specimen provides useful information from the voltage signal even though the quenching phenomena happen quickly. The analysis of the results offers an interesting new approach to evaluation and, more importantly, to monitoring, controlling and optimizing the entire quenching process.

5. References

- [1.] Tensi, H. M. (1992): Wetting kinematics. Eds: Liščić, B.; Tensi, H. M.; Luty, W.: Theory and Technology of Quenching, A handbook, Springer-Verlag, Berlin, 481 pp.
- [2.] Tensi, H.M., and G.E. Totten (1996): "Development of the Understanding of the Influence of Wetting Behaviour on Quenching and the Merits in these Developments of Prof. Imao Tamura", *Proceedings of the 2nd International Conference on Quenching and the Control of Distortion*, Nov. 4-7, 1996.
- [3.] Grum J., Božič S. (2003): Acoustic emission during quenching of 42CrMo4 steel, *Proceedings of the Fourth International Conference on Quenching and the Control of Distortion*, Beijing
- [4.] GRUM, Janez, RAVNIK, Franc. Investigation of sound phenomena during quenching process. *Int. J. Mater. Prod. Technol.*, 2006, vol. 27, no. 3/4, str. 266-288. [COBISS.SI-ID 9847835]
- [5.] Čudina M. (2001): Technical Acoustics - Measuring, evaluation and decreasing noise and vibration (*in Slovene: Tehnična akustika – merjenje, vrednotenje in zmanjševanje hrupa in vibracij*), University of Ljubljana, Faculty of Mechanical Engineering
- [6.] Grum J., Božič S. (1999): Influence of various quenching oils and polymeric water solutions on mechanical properties of steel, ASM Heat Treating Society, The 3rd International Conference on Quenching and Control of Distortion, Eds.: G.E. Totten, B. Liščić, H.M. Tensi, Prague, Czech Republic, 530-541.
- [7.] Grum J., Božič S. Zupančič M., (1999): Influence of quenching process parameters on residual stresses in steels, ASM Heat Treating Society, The 3rd International Conference on Quenching and Control of Distortion, Eds.: G.E. Totten, B. Liščić, H.M. Tensi, Prague, Czech Republic, 530-541.
- [8.] Grum J., Božič S., Lavrič R. (1998): Influence of Mass of Steel and a Quenching Agent on Mechanical Properties of Steel, Heat Treating, *Proceedings of the 18th Conference*,

- Including the Liu Dai Memorial Symposium, ASM International, The Materials Information Society, Eds.: R.A. Wallis, H.V. Walton, 645-654.
- [9.] Leighton T. G. (2001): The Acoustic Bubble, Academic Press, 613 p.
- Macherauch E., Vohringer O. (1992): Residual Stresses After Quenching, Eds.: B. Liščić, H.M. Tensi, W. Luty: Theory and Technology of Quenching, A Handbook, Springer-Verlag Berlin, Heidelberg, 117-181.